Flexoelectric Effect of Heterogeneous Structure and Its Multiscale Topology Optimization

Xing Chen

Université Gustave Eiffel

Flexoelectric Effect of Heterogeneous Structure and its Multiscale Topology Optimization

Thèse de doctorat de l'Université Gustave Eiffel

École doctorale : Sciences, Ingénierie et Environnement
Spécialité de doctorat : MÉCANIQUE
Unité de recherche : Laboratoire Modélisation et Simulation Multi-Echelle

Thèse présentée et soutenue à l'Université Gustave Eiffel, le 26/06/2024, par :

XING CHEN

Composition du Jury

Yong PENG Professor, Central South University, China	Président du jury
Jean-François GANGHOFFER Professeur des universités, Université de Lorraine, France	Rapporteur
Michel DEVEL Professeur des universités, Université Bourgogne Franche-Comté, France	Rapporteur

Encadrement de la thèse

Julien YVONNET Professeur des Université, Université Gustave Eiffel, France	Directeur de thèse
Song YAO Professor, Central South University, China	Co-directeur de thèse

Acknowledgment

I would like to express my deepest gratitude to my PhD supervisor, Professor Julien YVONNET, for his invaluable guidance, unwavering support, and profound expertise throughout the journey of completing this thesis. Prof. Yvonnet's mentorship has been instrumental in shaping the trajectory of my research and academic growth. His insightful feedback, constructive suggestions, and encouragement have been a constant source of motivation, pushing me to strive for excellence in all aspects of my research endeavors.

I extend my sincere gratitude to my co-supervisor in China, Professor Song YAO, for his unwavering support, guidance, and mentorship throughout the entirety of my doctoral research. Prof. Yao' expertise and encouragement have played an instrumental role in shaping the direction and success of this thesis. His mentorship has inspired me to push the boundaries of knowledge and pursue excellence in my work.

I would also like to express my appreciation to Prof. Harold Park for his invaluable contributions to our scientific discussions during our collaborations.

Furthermore, I am grateful to my friends and colleagues in Université Gustave Eiffel. They are Dr. Pengfei Li, Dr. Yi Wu, Mr. Bing He, Dr. Thanh Tung Nguyen, Dr. Weizhi Luo, Mr. Zhonghua Li, Mr. Yiming Ren, Mr. Amritesh Sinha, Mr. Zakaria Chafia, Mr. Souhail Chaouch and Mr. Matthieu Noel.

I would like to express my appreciation to the jury members, Prof. Jean-François Ganghoffer, Prof. Michel Devel and Prof. Yong Peng.

I am deeply grateful to my family for their unwavering support and encouragement.

Finally, I wish to acknowledge the financial support from the China Scholarship Council and Central South University.

"Citation"

Abstract

Over the past few decades, flexoelectricity has attracted growing interest as a means of converting ambient vibratory energy into electric power. Flexoelectricity is an electromechanical phenomenon that associates electric fields with deformation gradients, and inversely induces mechanical deformation for an electric field gradient. This phenomenon is inherent in all dielectric materials, and can be significant at very small scales. The universality and remarkable size-effects of flexoelectricity are promising for the design of advanced nano/micro electromechanical systems. However, flexoelectricity is intrinsically weak in natural materials, posing a major challenge for its practical application to real systems. In this thesis, in order to fully exploit the potential of flexoelectric properties, we propose techniques for modeling and designing flexoelectric composites, for applications to energy harvesting systems converting vibrations into electric current.

The methodologies proposed in this thesis are numerical approaches to modeling flexoelectricity in micro and macro structures. We first develop direct and converse flexoelectricity homogenization models for microstructures composed of heterogeneous piezoelectric constituent phases. A C^1-continuity model for multiple patches is constructed within an isogeometric analysis (IGA) framework to model the dynamic frequency response of flexoelectric structures with complex geometries, and where the inertial effect of deformation gradients is included. Next, we develop a topology optimization framework for microstructures and flexoelectric structures. These topology optimization and numerical homogenization techniques are then coupled to design microstructures containing piezoelectric two-phase materials with a view to maximizing macroscopic direct and converse flexoelectric properties, in both static and dynamic settings.

Finally, we extend the topology optimization method to the nonlinear large deformation framework to model and design flexible flexoelectric energy harvesting systems, in order to exploit interactions between size effects and large deformations and increase electromechanical coupling factors.

Résumé

Au cours des dernières décennies, la flexoélectricité a suscité un intérêt croissant pour convertir l'énergie vibratoire ambiante en énergie électrique. La flexoélectricité est un phénomène électromécanique qui associe des champs électriques à des gradients de déformation et induit inversement une déformation mécanique pour un gradient de champ électrique. Ce phénomène est inhérent à tous les matériaux diélectriques, et peut être significatif aux très petites échelles. L'universalité et le remarquable effet d'échelle de l'effet flexoélectrique sont prometteurs pour la conception de systèmes électromécaniques nano/micro avancés. Cependant, l'effet flexoélectrique est intrinsèquement faible dans les matériaux naturels, ce qui pose un défi majeur pour son application pratique à des systèmes réels. Dans cette thèse, afin d'exploiter pleinement le potentiel des propriétés flexoélectriques, nous proposons des techniques de modélisation et de conception de composites flexoélectriques, pour des applications à des systèmes de récupération dénergie convertissant vibrations en courant électrique.

Les méthodologies proposées dans cette thèse sont des approches numériques pour modéliser la flexoélectricité dans les micro et macro structures. Nous développons d'abord un modèle d'homogénéisation de la flexoélectricité directe et converse pour les microstructures composées de phases constitutives piézoélectriques hétérogènes. Un modèle de continuité C^1 pour patchs multiples est construit dans un cadre d'analyse isogéométrique (IGA) pour modéliser la réponse dynamique en fréquence des structures flexoélectriques avec des géométries complexes, et où l'effet d'inertie des gradients de déformation est inclus. Ensuite, nous développons un cadre d'optimisation topologique pour les microstructures et structures flexoélectriques. Ces techniques d'optimisation topologique et d'homogénéisation numérique sont alors couplées pour concevoir des microstructures contenant des matériaux biphasés piézoélectriques en vue de maximiser les propriétés flexoélectriques directes et inverses macroscopiques, dans des cadres statiques et dynamiques.

Nous étendons enfin la méthode d'optimisation topologique au cadre non linéaire en grandes déformations pour modéliser et concevoir systèmes de récupération d'énergie souples flexoélectriques, afin d'exploiter les interactions entre les effets de taille et les grandes déformations et augmenter les facteurs de couplage électromécaniques.

Contents

List of Figures

List of Tables

Publications

Journals

1. Chen X, Yao S, Yvonnet J. Nonlinear topology optimization of flexoelectric soft dielectrics at large deformation. Computer Methods in Applied Mechanics and Engineering, 2024, 427: 117005

2. Chen X, Yao S, Yvonnet J. Multiscale topology optimization of an electromechanical dynamic energy harvester made of non-piezoelectric material. Structural and Multidisciplinary Optimization, 2024, 67(5):66.

3. Chen X, Yao S, Yvonnet J. Dynamic analysis of flexoelectric systems in the frequency domain with isogeometric analysis. Computational Mechanics, 2023,71:353366.

4. Chen X, Yvonnet J, Park H S, Yao S. Enhanced converse flexoelectricity in piezoelectric composites by coupling topology optimization with homogenization. Journal of Applied Physics, 2021, 129 (24):245104.

5. Chen X, Yvonnet J, Yao S, Park H S. Topology optimization of flexoelectric composites using computational homogenization. Computer Methods in Applied Mechanics and Engineering, 2021, 381(1):113819.

6. Yvonnet J, Chen X, Sharma P. Apparent Flexoelectricity due to Heterogeneous Piezoelectricity. Journal of Applied Mechanics, 2020, 87(11):111003.

International Conferences

1. Chen X, Yvonnet J, Yao S. "Topology optimization of dynamic flexoelectric structures by isogeometric analysis", the 15th World Congress on Structural and Multidisciplinary Optimization, 2023, Cork, Ireland, Oral presentation.

Introduction

In recent decades, wireless sensor network (WSN) technology has found extensive applications across healthcare, infrastructure monitoring, environmental protection, and various other domains [1, 2]. The primary power source for sensor nodes continues to be chemical batteries. However, traditional batteries present environmental concerns, limited operational lifespan, and high maintenance costs [3]. The necessity of battery replacement or recharging within large-scale sensor networks poses significant challenges and expenses. The quest for minimizing power consumption in WSNs is paramount, driving advancements in device miniaturization. Integrating batteries into microsystems is typically challenging, prompting a shift towards self-powered electronic devices. Harvesting and converting ambient environmental energy stands as a crucial and efficient method for sustainable green power in wireless and portable devices [4, 5, 6]. A variety of energy forms abound in the environment, including mechanical energy, acoustics, wind energy, thermal energy, nuclear energy, solar energy, and chemical energy, among others. Among these, mechanical energy enjoys the broadest distribution and can conveniently power most low-consumption applications such as remote sensor networks, biomedical implants, and portable electronics [7]. Moreover, it boasts benefits of prolonged sustainability and environmental friendliness. Consequently, the development of vibration energy harvesters has surged rapidly as an alternative to conventional battery power sources [8], supplying energy to numerous wireless sensors and low-power consumption devices [9]. Numerous methods exist for converting mechanical vibration energy into electrical power. These methods adhere to the principle of energy transformation, categorizing vibration energy devices into three main types: piezoelectric transduction [10, 11], electrostatic transduction [12, 13], and electromagnetic transduction [14]. When comparing electromagnetic and electrostatic devices, piezoelectric energy harvesters (PEH, as schematically illustrated in Fig. 1) stand out due to their higher energy density and conversion efficiency, making them particularly adept at harvesting vibration energy. This superiority arises from the inherent capability of piezoelectric materials to directly convert applied strain energy into electric power. As a result, such devices feature compact and simpler architectures compared to their electromagnetic and electrostatic counterparts. Furthermore, they can be manufactured using micromachining techniques and seamlessly integrated into monolithic micro-electro-mechanical systems (MEMS).

Piezoelectric energy harvesters leverage the unique piezoelectric effect exhibited by certain materials, converting vibrational energy into electrical energy. This effect arises from the electromechanical coupling within piezoelectric materials, where applying mechanical stress generates electric polarization, and conversely, applying an electric field induces mechanical deformation, as schematically illustrated in Fig. 2. However, despite its potential, the piezoelectric effect faces several limitations: (1) the piezoelectric effect exists only in dielectric materials whose crystals are non-centrosymmetric, limiting the selection of suitable materials; (2) piezoelectric materials are susceptible to electrical fatigue, characterized by a decrease in polarization after numerous switching cycles [15]; (3) elevated temperatures beyond the Curie point can trigger phase transitions in most piezoelectric materials, diminishing their piezoelectric properties due to increased lattice symmetry; (4) many high-performance piezoelectric materials incorporate lead, a hazardous substance harmful to both human health and the environment [16]. These shortcomings of piezoelectric materials limit their in-depth applications in certain fields, par-

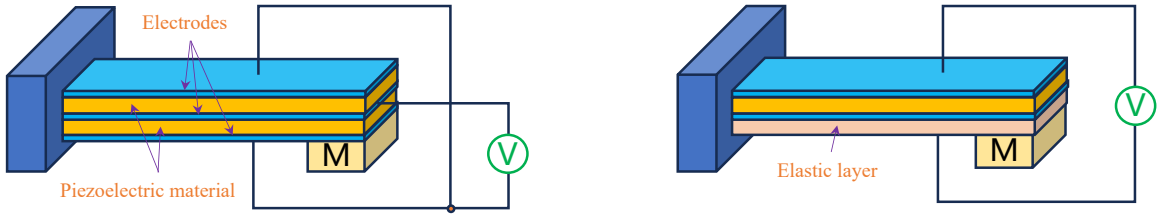

(a) (b)

Figure 1: Schematics of piezoelectric energy harvesters: (a) bimorph structure; (b) unimorph structure

ticularly in fields where electromechanical systems are advancing toward miniaturization and integration at nanometer scales. In the process of exploring electromechanical coupling materials with both high polarization properties and high stability, the flexoelectric effect has attracted more and more attention.

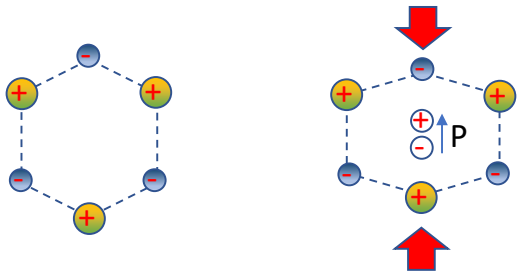

(a) (b)

Figure 2: Schematics of piezoelectric effect for non-centrosymmetric crystals: (a) undeformed and unpolarized state; (b) polarization induced by uniform deformation

Flexoelectricity stands out as an electromechanical phenomenon that couples electric fields with strain gradients and inversely induces mechanical strain by electric field gradients. Non-uniform deformation (strain gradient) breaks the local symmetry of the material crystal, causing the positive and negative charge centers of the lattice to shift and produce dipoles, resulting in the formation of polarization phenomena, as schematically illustrated in Fig. 3. Theoretically, all dielectric materials are capable of producing flexoelectric effects, and flexoelectric effects are not limited by Curie temperature and can be used in high temperature applications. Flexoelectricity can be considered as size-dependent electromechanical coupling due to the fact that its contribution becomes significant and even dominant at lower scales where the strain gradient effect becomes more profound as the material dimensions shrink to micro- and nano-levels. The universality and outstanding scaling effect of the flexoelectric effect made it a desirable property for advanced nano/micro-electromechanical systems (N/MEMS). The gradient coupling property of the flexoelectric effect makes it show a very high sensitivity to the bending strain or curvature change of the structure, and this property is especially important in signal sensing and energy harvesting, which is mainly based on bending vibration deformation. One of the

most important studies and applications of the flexoelectric effect is the flexoelectric energy harvester, which captures the bending vibration energy and converts it into electrical energy.

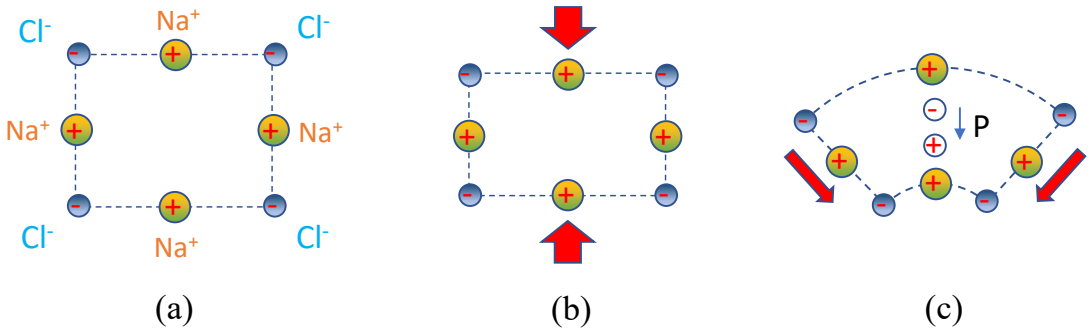

Figure 3: Schematics of flexoelectric effect for dielectric material: (a) undeformed and unpolarized state; (b) uniformly deformed but unpolarized state; (c) polarization induced by non-uniform deformation

The flexoelectric effect is present in all dielectric materials, however, the price of this ubiquity is that the flexoelectric effect is weak in natural materials. Therefore, the intriguing challenges in the field of flexoelectricity revolve around the exploration of advanced materials featuring heightened flexoelectric properties and the creation of engineered structures that optimize electromechanical coupling through a synergistic utilization of both flexoelectric and piezoelectric effects. In contrast to the traditional design approach[17, 18, 19, 20], topology optimization technique [21, 22, 23] is a structural design method based on mathematical optimization theory, aiming at determining the optimal material distribution to maximize specific properties. Topology optimization can be employed as a powerful tool for the design of fine and complex flexoelectric structures, which provides technical support for the enhancement of material flexoelectric properties and structural electromechanical coupling efficiency.

Motivation

The universality and outstanding scaling effect of the flexoelectric effect are promising for designing advanced nano/micro electromechanical systems (N/MEMS). However, the inherent weakness of the flexoelectric effect in natural materials presents a significant obstacle to the practical application of flexoelectricity. To fully exploit the potential of flexoelectric properties, we focus on designing high-performance flexoelectric composites and improving the electromechanical coupling efficiency of flexoelectric structures. Flexoelectric effect can be enhanced by increasing the strain gradients in dielectric materials and leveraging the scale effect of flexoelectricity. These challenges and characteristics of flexoelectric effect serve as primary motivations for our research in this dissertation. More specifically, the motivations can be summarized as follows:

- Recent research has brought attention to how flexoelectricity can mimic piezoelectricity. In this thesis, we explore the potential of leveraging piezoelectric materials to generate a significantly enhanced flexoelectric response. We investigate the use of architectured materials comprising diverse piezoelectric phases with the goal of achieving a substantial emergent flexoelectric effect, potentially surpassing the inherent flexoelectricity of the materials. At the beginning of the thesis, a computational homogenization framework for effective flexoelectric materials is lacking. Such a framework is essential for examining and optimizing the applications mentioned above without the necessity of solving the full heterogeneous structure.

- In materials or composites exhibiting an effective flexoelectric response, polarization can be triggered by local strain gradients. Typically, these effects remain subtle under static conditions. However, when subjected to dynamic loads, significantly larger effects can arise, presenting opportunities for energy harvesters that convert mechanical vibrations into electrical energy. In numerical analyses, a key challenge encountered by traditional finite element formulations when exploring the flexoelectric effect is the requirement for C^1 continuity to accurately interpolate the strain gradient from the displacement variable.
- The effective direct and converse flexoelectric properties of periodic piezoelectric composites can be tuned to be much higher than the constituents, by creating a heterogeneity through asymmetric geometric inclusions and multiple constitutive materials, which motivates our research in optimization designs of flexoelectric properties in piezoelectric microstructures by combining topology optimization with computational homogenization.
- In the realm of flexoelectric composites, research has concentrated on developing piezoelectric composites using non-piezoelectric materials, driven by earlier work [24, 25]. Traditional piezoelectric composites usually include lead-containing PZT for higher permittivity. Piezoelectric responses can be achieved in these composites made of purely flexoelectric materials, which are comparable to common single-phase piezoelectrics.
- Soft dielectrics have distinctive capability to produce extensive deformations. This characteristic holds the potential for achieving more significant electric responses, attributed to the presence of larger strain gradients. Besides, the reduction of structural dimensions to the micro and nanoscale facilitates nonlinearity, enabling the more accessible production of large strain gradients, thereby contributing to the increasing improvement of the flexoelectric effect.

Objectives

This thesis aims to address these questions described above through the following objectives:

- Establish a computational homogenization framework for periodic composites composed of heterogeneous piezoelectric phases, taking into account direct and converse flexoelectric effect. The approach should enable the prediction of direct and converse flexoelectric properties of homogeneous microstructures, whatever their shape and material.
- Develop a C^1-continuous Isogeometric analysis (IGA) framework with one or more patches for the dynamic frequency response of flexoelectric structures with complex geometries, where the inertial effect of deformation gradients is included. The methodology must satisfy the requirement for C^1-continuity of the approximated displacement field for the fourth-order PDE of flexoelectricity, for structures with general or even complex geometries.
- Formulate a topology optimization framework for designing periodic piezoelectric microstructures with larger direct and converse flexoelectric constants.
- Propose a multiscale topology optimization method for designing flexoelectric microstructures made of non-piezoelectric materials and electromechanical energy harvesting systems to efficiently convert mechanical vibrations into electrical energy.
- Develop a nonlinear topology optimization framework for flexoelectric soft dielectrics at finite strains to take full advantage of the interaction between the size effect and large deformations, and increase the electromechanical coupling factors of structures.

Outline of the dissertation

The contents of this thesis are organized as follows:

Chapter 1 presents an overview of experimental measurements, microscopic and phenomenological theory, and computational models for the flexoelectric effect. We then review the theory, methods and applications of topological optimization techniques used in the design of flexoelectric structures. In Chapter 2, we develop a homogeneous direct/converse flexoelectric-piezoelectric model for microstructures composed of heterogeneous piezoelectric phases, which enables the prediction of effective direct and converse flexoelectric coefficients for piezoelectric composite materials. In Chapter 3, a C^1-continuous single/multiple-patch isogeometric analysis framework for the dynamic frequency response of flexoelectric structures with complex geometries is developed. The inertial effect of deformation gradients is taken into account. In Chapter 4, we propose a topology optimization framework for the design of piezoelectric composites microstructures to maximize the direct flexoelectric properties of piezoelectric composites. This framework is then extended to improve the converse flexoelectricity of microstructures. In Chapter 5, a multiscale topology optimization method for the design of flexoelectric microstructures made of non-piezoelectric materials in electromechanical systems is proposed for designing energy harvesting systems that convert mechanical vibrations into electrical energy. In Chapter 6, we establish a nonlinear topology optimization framework for flexoelectric soft dielectrics in finite strains to take full advantage of the interaction between the size effect and large deformations, thereby increasing the electromechanical coupling factors of structures. We end this manuscript with some conclusions and perspectives

Chapter 1

Literature review

In this chapter, an overview of experimental measurements, microscopic and phenomenological theory, and computational models for flexoelectric effect is presented. We then sort out the theory, methods and applications of topology optimization technology, and finally review the research work on topology optimization employed in the design of flexoelectric structures.

1.1 Flexoelectric effect

Flexoelectricity, which refers to the linear relationship between electrical polarization and strain gradient, was first predicted by Mashkevich and Tolpygo [26] in the 1950s and then observed experimentally by Scott [27] and Bursian [28]. Kogan [29] formulated the first phenomenological theory of flexelectricity and estimated the range of values for flexoelectric coefficients. The first microscopic description on dynamic flexoelectricity was addressed by Harris [30]. In 1968, Mindlin proposed a phenomenological framework to describe the linear response of stress (or strain) to a polarization gradient, which was later recognized as converse flexoelectricity [31]. The initial microscopic calculations of the coefficients governing flexoelectricity were conducted by Askar et al. [32] in 1970 based on a theory of lattice dynamics for the shell model of cubic ionic crystals. Indenbom et al. [33] were the first to adopt the term "flexoelectricity" for the solid phase, by borrowing it from the liquid crystals community. Earlier work categorized flexoelectricity as an effect similar to piezoelectricity or simply called it as "nonlocal piezoelectric effect". It was not until 1985 that Tagantsev [34, 35, 36] proved through phenomenological and microscopic methods in his research that the flexoelectric effect has a more complex mechanism and can exist in non-piezoelectric materials. Since then, the flexoelectric effect has been completely distinguished from the piezoelectric effect. For an extended period following that, the observed weak effect resulted in limited interest in bulk flexoelectricity, with only a few studies being relevant to ferroelectric materials [28, 37]. By the turn of the century, Cross and Ma [17, 18, 38, 39] conducted a series of systematic experimental studies for the flexoelectric effect in ferroelectric ceramics, pioneered a classical method of measuring the longitudinal flexoelectric coefficient, i.e. compressed truncated pyramid structure. They discovered that the flexoelectric effect in certain ferroelectric materials is much higher than the theoretically estimated magnitudes. These experimental results, in return, revitalized theoretical exploration of flexoelectricity, especially in developing an advanced first-principles framework [40, 41, 42] and enhancing the description within continuum mechanics [34, 35].

1.1.1 Experimental studies

Although experimental evidence of the flexoelectric effect in solids dates back to the 1960s [30], it wasn't until the early 2000s that Ma and Cross conducted a systematic measurement of flexoelectricity. The initial approach involves dynamically bending the material within a

cantilever-beam geometry to induce a transverse strain gradient, as shown in Fig. 1.1(a). This method has been applied to systematically quantify the transverse flexoelectric coefficient μ_{12} in a number of perovskite ceramics [17, 38, 39, 43]. Variations of the method involving four-point bending (Fig. 1.1(b)) and three-point bending (Fig. 1.1(c)) geometries have also been successfully employed. Quasi-static four-point bending is also designed for the measurement of the transverse flexoelectric coefficient, while it can produce a significantly larger strain gradient within the sample compared to cantilever bending, enabling the exploration of nonlinear flexoelectric behaviors under a large load. Another method for measuring direct flexoelectricity involves uniaxial compression of a truncated pyramid-shaped sample [20], as schematically illustrated in Fig. 1.1(d). Arising from their different areas, the stress disparity between the top and bottom surfaces of the truncated pyramid establishes a longitudinal strain gradient, leading to the generation of a flexoelectric polarization. However, in practice, the pyramid-compression approach is complicated due to the strongly inhomogeneous nature of the strain gradient. In principle, it is possible to determine efficiently the complete flexoelectric components of a cubic-symmetric insulator by carefully designed experimental frameworks [19]. However, the flexoelectric coefficients measured through these macroscopic methods often represent effective properties which may comprise various flexoelectric contributions or encompass multiple components of the flexoelectric tensor.

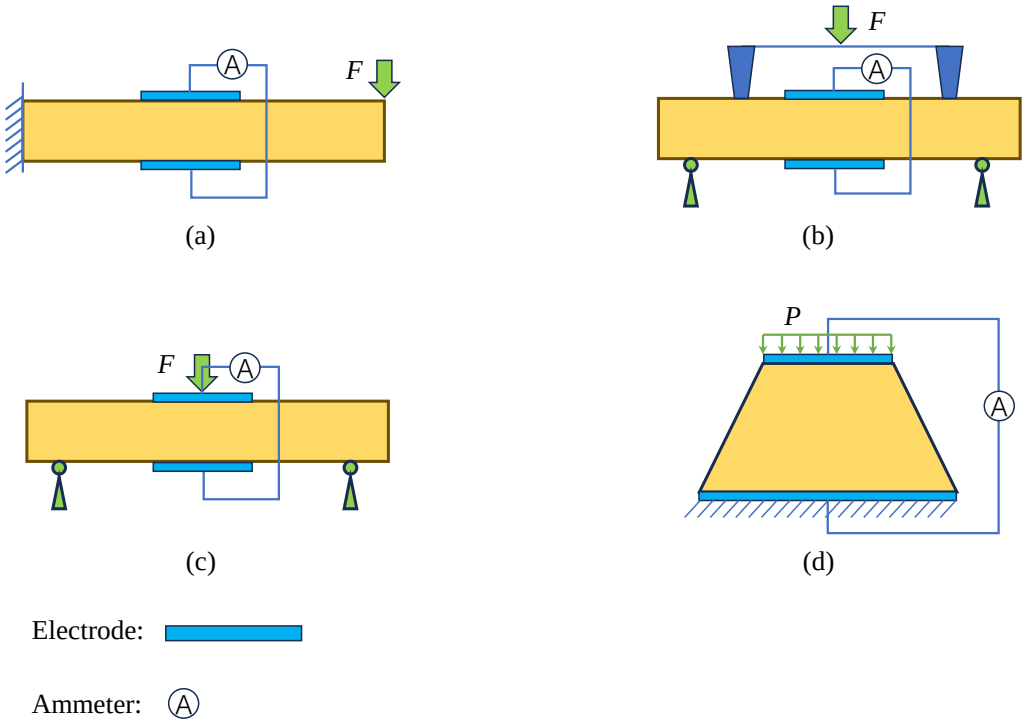

Figure 1.1: Schematics of experimental setup for measurements of flexoelectric coefficients: (a) Cantilever beam bending [17]; (b) four-point bending [18]; (c) three-point bending [19]; (d) truncated pyramid compression [20].

Conversely, a practical method for measuring the flexoelectric property entails utilizing the converse flexoelectric effect, where applying a bias across the structure results in a non-uniform electric field distribution that induces strain within the sample. Building on this concept, Cross and coworkers [44] applied a graded electric field across a truncated pyramid-shaped sample and thus to estimate the flexoelectric coefficient of (Ba,Sr)TiO_3. Zubko [19] utilized a dynamic mechanical analyzer in a three-point bending (shown in Fig. 1.1(c)) configuration to induce flexoelectric polarization in non-piezoelectric $SrTiO_3$ single crystals, measuring all three flex-

oelectric tensor components as $\mu_{1111} = 2$ nC/m, $\mu_{1122} = 7$ nC/m and $\mu_{1212} = 5.8$ nC/m. Recently, a comprehensive comparison of the three bending methods (as schematically illustrated in Fig. 1.1(a), (b) and (c)) for measuring transverse flexoelectric coefficients was conducted [45]. Additionally, Shu [46] employed the converse flexoelectric effect to measure the shear flexoelectricity of (Ba,Sr)TiO_3 (BST) ceramics, utilizing a pyramid sample with electrodes on the two sloping sides.

Numerous studies are dedicated to ferroelectrics due to their significant flexoelectricity, and this property is directly proportional to the dielectric permittivity [34, 35]. Cross et al. conducted measurements on the flexoelectric coefficients of various ferroelectrics by different methods. Based on cantilever bending, they obtained the transverse flexoelectricity μ_{1122} as: 4 μC/m for Pb(Mg,Nb)O_3 (PMN) [17], 50 μC/m for $BaTiO_3$ [39], 100 μC/m for (Ba,Sr)TiO_3 (BST) [38], 1.4 μC/m for Pb(Zr,Ti)O_3 (PZT) while 1.5 μC/m when using four-point bending method [18, 47], respectively. They also measured (Pb,Sr)TiO_3 as longitudinal $\mu_{1111} =$ 150 μC/m by pyramid compression [20]. The BST was observed to have significantly enhanced flexoelectricity. Due to ecological considerations for next-generation electronic devices, the lead-free nature of BST has attracted substantial research interest in BST-based systems. In addition to ferroelectrics, polymers and elastomers have also been investigated. The inherent flexibility of these materials renders them potentially appealing candidates for future flexoelectric devices, thus sparking numerous studies on flexoelectricity in polymers. For instance, in the case of polyvinylidene fluoride (PVDF), reported flexoelectric coefficients vary between 13 nC/m and 80 μC/m [48, 49, 50, 51].

Despite substantial experimental and theoretical endeavors, accurately quantifying the flexoelectric response remains a formidable challenge. A well-known order-of-magnitude discrepancy exists between theoretically estimated and experimentally measured flexoelectric coefficients. In the paraelectric phase of many perovskite oxides, experimental measurements of the flexoelectric coefficient reach up to several tens of μC/m and more, whereas theoretical estimations suggest that intrinsic flexoelectricity should not exceed several nC/m. The mechanism underlying the flexoelectricity of perovskite ceramics remains poorly understood. In response, recent studies have made efforts to address this issue through both experimental endeavors [52, 53, 54, 55, 56, 57] and theoretical investigations [58, 59, 60, 61, 62].

Several factors contribute to the disparity in flexoelectric coefficients. In certain scenarios, macroscopic symmetry breaking can occur and make a substantial contribution to the overall flexoelectric response [17, 53, 55]. Yurkov and Tagantsev [61] theoretically demonstrated that the surface contribution, encompassing both surface piezoelectricity and surface flexoelectricity, to the flexoelectric response is significant and comparable to that of the bulk. Abdollahi [60] found the flexoelectric effect is sensitive to sample geometry, and the simplification of strain gradients made in most experimental measurements for flexoelectricity may lead to overestimation of flexoelectric coefficients. Abdollahi [63] also proposed that the asymmetric distribution of the piezoelectric coefficient could result in an apparent flexoelectric response. Additionally, Morozovska [64] explored the idea that dynamic flexoelectricity might contribute to the substantial static flexoelectric effect observed in spatially inhomogeneous samples.

1.1.2 Microscopic theory

At micro scale, the bulk flexoelectric response can be separated into the ionic and electronic contributions [65], attributed to the redistribution of bound and free charges in response to strain gradient. The former was quantified based on the lattice dynamics of the shell model [32] and rigid-ion model [34, 35], while the description of the latter was made by Resta [40] and Hong [66], extending classical piezoelectric theory [67] to the flexoelectric effect. The microscopic theory quantifies the intrinsic flexoelectric coefficients, facilitates the validation of experimental measurements, and holds the potential for designing new materials with desired

flexoelectric properties.

The microscopic theories of flexoelectricity can be categorized into two main types: the classical microscopic theory, which concentrates on the ionic contribution to flexoelectricity through lattice mechanics approaches, and the first-principles theories, which explicitly consider both ionic and electronic contributions. To understand the ionic contribution, we briefly discuss rigid-ion model developed by Tagantsev [34, 35]. For a deformed crystalline lattice, the i-th component of the displacement $w_{n,i}$ of the n-th atom, can be expressed as:

$$w_{n,i} = w_{n,i}^{ext} + w_{n,i}^{int} = \int_{x_j^0}^{R_j} u_{i,j} \mathrm{d}x_j + w_{n,i}^{int} \tag{1.1}$$

where x_j^0 and R_j are respectively the coordinates of an immobile reference point and the n-th atom before the deformation. $w_{n,i}^{ext}$ represents the atomic displacement induced the unsymmetrized external strain $u_{i,j}$ under the elastic medium approximation. For a material with centrosymmetric crystals, the external strain alone is adequate to characterize all atomic displacements induced by a uniform deformation. As illustrated in Fig. 1.2, centrosymmetry is preserved under the homogeneous deformation, and the displacements of the atoms satisfy $\bar{w}^{ext} = \delta e_1$. However, for inhomogeneous deformation or non-centrosymmetric crystals, the actual atomic displacements will include an additional component termed the internal displacement w^{int} (commonly referred to as internal strain) [68]. The internal displacement can be approximated by the strain tensor and the strain gradient in a linear relationship of lowest order

$$w_{n,i}^{int} = B_{n,i}^{jk} \varepsilon_{jk} + N_{n,i}^{jkl} \varepsilon_{jk,l} \tag{1.2}$$

where $B_{n,i}^{jk}$ and $N_{n,i}^{jkl}$ are the internal strain tensors with respect to strain and strain gradient, respectively. They can be calculated by lattice dynamics theory [68]. For a body with point charge Q_n on coordinates $R_{n,i}$, its polarization induced by inhomogeneous deformation can be expressed as

$$\delta P_i = \frac{1}{V_{def}} \sum_n Q_n (R_{n,i} + w_{n,i}) - \frac{1}{V} \sum_n Q_n R_{n,i} \tag{1.3}$$

where V and V_{def} are the volume of crystal before and after the deformation, respectively. Substituting (1.1) into (1.3), we arrive at

$$\delta P_i = \frac{1}{V_{def}} \sum_n Q_n B_{n,i}^{jk} \varepsilon_{jk} + \frac{1}{V} \sum_n Q_n N_{n,i}^{jkl} \varepsilon_{jk,l} + \delta P_i^{ext} \tag{1.4}$$

Then the flexoelectric coefficient μ_{ijkl} is written as

$$\mu_{ijkl} = \frac{1}{V} \sum_n Q_n N_{n,i}^{jkl} \tag{1.5}$$

where the summation is performed over the ions within a unit cell of volume V. The first term in right of (1.4) is the piezoelectricity, while the last term induced by the external strain and the volume change of the crystal, is associated with the surface flexoelectric effect.

The rigid-ion model relies on the point-charge assumption, emphasizing the dominant role of ions in flexoelectric response, while the impact of electronic charge density redistribution is excluded. Some theoretical work focused on the electronic part, and they suggest a significant curvature-induced polarization to flexelectric response [69, 70]. Still others considered both contributions implicitly but did not distinguish them [32, 41].

Two branches have emerged in the development of first-principles flexoelectricity theory: charge-density response functions and current-density response functions. The first attempt at

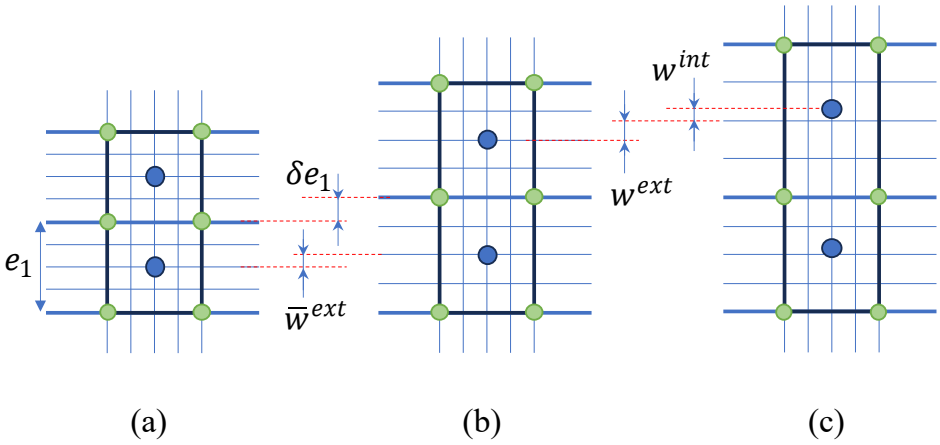

Figure 1.2: Schematic of atomic displacements for centrosymmetric diatomic lattice: (a) undeformed state; (b) homogeneous deformation; (c) inhomogeneous deformation.

a first-principles calculation of flexoelectric coefficients for bulk materials was carried out for $BaTiO_3$ and $SrTiO_3$ by Hong [41], later they developed a general and unified first-principles theory of piezoelectric and flexoelectric tensor with explicit consideration of electronic and ions contributions [66]. Resta [40] developed a first-principles theory of flexoelectricity toward understanding the longitudinal electronic contribution to flexoelectricity in bulk crystals. Shortly afterwards, Hong and Vanderbilt [66] extended this theory to general insulators and implemented it to calculate FECs for a variety of materials, from elementary insulators to perovskites. Stengel [42] formulated an alternative version of the first-principles theory of flexoelectricity using density-functional perturbation theory (DFPT). Recently, leveraging electronic-structure methods, they have uncovered two distinct electronic and one lattice-mediated contributions to the flexoelectric response in 2D materials, both derived entirely from first principles [71]. Based on the analytical long-wavelength extension of DFPT, Royo et al. [72] proposed a approach to calculate the lattice-mediated contributions to the bulk flexoelectric tensor, and validated it on the representative cubic crystals and the tetragonal low-temperature polymorph of $SrTiO_3$.

1.1.3 Macroscopic and phenomenological theory

The macroscopic or phenomenological theory of the bulk flexoelectric effect in crystals is rooted in the thermodynamics of a dielectric. It introduces a flexoelectric contribution into the total free energy to explain the electric polarization induced by bending in non-piezoelectric materials [34, 35]. The presentation will first adopt the LGD (Landau-Ginzburg-Devonshire) theory of ferroelectric materials, exploring its applications in predicting and elucidating flexoelectric-related behaviors across diverse systems. Following this, we will provide a concise summary of the general continuum mechanics theory of flexoelectricity, originating from Mindlin's seminal work on the polarization gradient-strain coupling in elastic dielectrics.

Within the framework of the phenomenological thermodynamic theory for ferroelectrics (LGD theory), the total free energy, including all the flexoelectric contribution, is expressed as:

$$\begin{aligned} W = \int \Big(& a_{ij}P_iP_j + a_{ijkl}P_iP_jP_kP_l - \beta_{ijkl}\varepsilon_{ij}P_kP_l + \frac{1}{2}b_{ijkl}P_{i,j}P_{k,l} + \frac{1}{2}c_{ijkl}\varepsilon_{ij}\varepsilon_{kl} \\ & - \frac{1}{2}\varepsilon_0\kappa_{ij}E_iE_j - P_iE_i + \frac{1}{2}f_{ijkl}(P_{i,j}\varepsilon_{kl} - P_i\varepsilon_{kl,j}) \Big) \mathrm{d}\Omega \end{aligned} \tag{1.6}$$

where the second and fourth order a are the Landau-Devonshire coefficients. P_i is polarization β_{ijkl} is an electrostrictive tensor. b_{ijkl} is polarization gradient coupling tensor. c_{ijkl} is elastic stiffness tensor. ε_0 is the dielectric permittivity of the vacuum, and κ_{ij} is the background relative dielectric permittivity tensor. f_{ijkl} is the flexoelectric coupling tensor. E_i is the total electric field. ε_{ij} is symmetric strain tensor. The energy related to flexoelectric contribution is obtained as

$$f^{flexo} = \frac{1}{2} f_{ijkl}(P_{i,j}\varepsilon_{kl} - P_i\varepsilon_{kl,j}) \tag{1.7}$$

By the variation of the free energy $\frac{\delta W}{\delta P_i} = 0$ and some algebraic operations, we obtain the relation of flexoelectric tensor and the flexocoupling tensor as

$$\mu_{ijkl} = \frac{1}{2}(a_{ij} - \beta_{ijpq}\varepsilon_{pq})^{-1}\varepsilon_0 f_{ijkl} \tag{1.8}$$

The dynamic flexoelectric effect [34, 35], a distinct mechanism, showcases the influence of flexoelectricity on the dynamic behaviors of a dielectric, and can be expressed as

$$P_i = \mu_{ij}^{dyn}\frac{\partial^2 u_j}{\partial t^2} \tag{1.9}$$

where μ_{ij}^{dyn} is the second-rank tensor of dynamic flexoelectric effect. u_i and t are displacement and time, respectively. To consider all the interaction, the kinetic energy K is given as

$$K = \int \left(\frac{\rho}{2}\left(\frac{\partial u_i}{\partial t}\frac{\partial u_i}{\partial t} + L_{ij}\frac{\partial P_i}{\partial t}\frac{\partial P_j}{\partial t} + M_{ij}\frac{\partial P_i}{\partial t}\frac{\partial u_j}{\partial t}\right)\right)\mathrm{d}\Omega \tag{1.10}$$

where ρ is density of material. M_{ij} is the dynamic flexoelectric tensor [73] and L_{ij} is polarization dynamics tensor. The Lagrangian of the ferroelectric can be written as

$$\mathcal{L} = \int \mathrm{d}t\Big(W - K\Big) \tag{1.11}$$

Then the motion equation can be obtained by the Euler-Lagrange equation

$$\frac{\mathrm{d}}{\mathrm{d}t}\left(\frac{\partial \mathcal{L}}{\partial \dot{\boldsymbol{q}}}\right) - \frac{\partial \mathcal{L}}{\partial \boldsymbol{q}} = 0 \tag{1.12}$$

where $\boldsymbol{q}$ represents P_i and u_i. $\dot{(\cdot)}$ is time derivative. Then the relation is obtained as

$$\mu_{ij}^{dyn} = \frac{1}{2}(a_{in} - \beta_{inkl}\varepsilon_{kl})^{-1}M_{nj} \tag{1.13}$$

The LGD theory of flexoelectricity can be used to explain and predict various phenomena associated with flexoelectricity. In the LGD phenomenological framework, it has been demonstrated that flexoelectric coupling significantly impacts various properties of nanoferroics [74]. Catalan et al. [75] and illustrated that the flexoelectric effect contributes to the smearing of the dielectric constant near the Curie temperature and influences the thickness-dependent coercive fields and remnant polarization. Additionally, surface stress and surface polarization have also been incorporated into a theoretical flexoelectricity model for dielectrics [76].

The continuum theory of flexoelectricity is completed by incorporating higher-order and nonlocal mechanical and electromechanical couplings into the internal energy, as well as defining governing equations and boundary conditions. The internal energy density U can be defined as [77]

$$U = \frac{1}{2}a_{ij}P_iP_j + \frac{1}{2}b_{ijkl}P_{i,j}P_{k,l} + \frac{1}{2}c_{ijkl}\varepsilon_{ij}\varepsilon_{kl} + f^I_{ijkl}P_iu_{j,kl} + d_{ijkl}P_{i,j}\varepsilon_{kl} + \frac{1}{2}g_{ijklmn}u_{i,jk}u_{l,mn} \tag{1.14}$$

where f^I_{ijkl} and d_{ijkl} are direct and converse flexoelectric tensor, respectively. g_{ijklmn} represents strain gradient tensor. The constitutive equations can be derived as

$$\tau_{ijk} = \frac{\partial U}{\partial u_{i,jk}},\ \sigma_{ij} = \frac{\partial U}{\partial \varepsilon_{ij}},\ P_i = \frac{\partial U}{\partial E_i},\ Q_{ij} = \frac{\partial U}{\partial E_{i,j}} \tag{1.15}$$

where σ_{ij} and E_i are stress and electric field, respectively. While τ_{ijk} and Q_{ij} can be regarded as hyper-stress and hyper-electric-field. In a body occupying a volume V bounded by interface Γ, and surrounded by an outer vacuum V', the equilibrium equations can be obtained by Toupin's variational principle [78] as

$$(\sigma_{ij} - \tau_{ijk,k})_{,j} + b_i = 0 \tag{1.16}$$

$$E_{ij,j} + E_i - \phi_{,i} + E^0_i = 0 \tag{1.17}$$

$$-\varepsilon_0 \phi_{,ii} + P_{i,i} = 0 \text{ in V} \tag{1.18}$$

$$\phi_{,ii} = 0 \text{ in V'} \tag{1.19}$$

where b_i and E^0_i are the external body force and electric field, respectively. $-\phi_{,i}$ is the Maxwell macroscopic field. The boundary conditions on Γ are given by

$$n_i(\sigma_{ij} - \tau_{ijk,k}) = t_j \tag{1.20}$$

$$n_i E_{ij} = 0 \tag{1.21}$$

$$n_i([[-\varepsilon_0 \phi_{,ii}]] + P_{i,i}) = 0 \tag{1.22}$$

where t_i is the surface traction, n_i is the normal unit vector of surface, and the symbol $[[\cdot]]$ denotes the field jump at the interfaces of V and V'. The equilibrium equations (1.16)-(1.19) with the constitutive equations (1.15) and boundary conditions (1.20)-(1.22) complete the continuum theory of flexoelectricity.

Continuum flexoelectricity theory has been extended to incorporate multiple physical and chemical couplings. Liu [79] proposed a general energy formulation of continuum electro-elasticity and magneto-electro-elasticity for various hard and soft functional materials. Giannakopoulos [80] developed a dynamic magneto-flexo-electric theory for dielectric solids by introducing a new theoretical framework which incorporates both gradients of electric polarization and flexoelectricity due to strain gradients and also includes a weak coupling with the magnetic field. Another approach involves developing the nonlinear theory of flexoelectricity tailored for soft materials experiencing large deformations [81]. Additionally, endeavors have been undertaken to investigate flexoelectric coupling in dynamic effect. Deng examined the output power density and conversion efficiency of flexoelectric energy harvesters [15], and studied the impact of the flexo-dynamic effects on nanoscale energy harvesters [82]. Baroudi [83] analyzed analytically the static and dynamic responses of nanobeam with different boundary conditions. The surface and size effects were introduced to the dynamic response of flexoelectric systems [84, 85, 86]. Nguyen [87] investigated the influence of dynamic flexoelectric effect on the natural frequency of both the Timoshenko and Euler-Bernoulli beams, where the flexo-dynamic term and dynamic polarization were both considered. Other studies incorporating nonlinear effects in dynamic response of flexoelectric systems can be found in [88, 89, 90, 91, 92].

1.1.4 Computational modeling of flexoelectricity

Modeling flexoelectricity involves solving the boundary value problem described in equations (1.15)-(1.22) within the framework of phenomenological continuum theory. Several investigations have concentrated on addressing the fourth-order partial differential equations associated with flexoelectricity in solids. These efforts include analytical models applied to simplified geometries [24, 76, 77, 93]. Based on beam and plate assumptions, extensive works have studied

the static and dynamic behaviors on Euler-Bernoulli beams [15, 94, 95], Timoshenko beams [87], Kirchhoff plates [96, 97]. Approximate solutions under restrictive assumptions may result in under- or over-estimation of the flexoelectric effect. Furthermore, flexoelectricity tends to be more pronounced in complex geometries that promote strain gradients, where analytical solutions are not available. As a consequence, various numerical approaches were developed to solve the boundary value problems of flexoelectricity in general geometries.

As in strain gradient elasticity, the main difficulty is that the fourth-order nature of the flexoelectric partial differential equation requires C^1 continuity in the approximation of the displacement field. Abdollahi et al. [98] firstly employed the local maximum-entropy (LME) meshfree method to solve this issue, allowing to interpret the flexoelectric responses in the cantilever bending and pyramid compression. In virtue of meshfree method, Abdollahi et al. also explored the effect of flexoelectricity on mechanical and electromechanical properties in several complex structures [60, 99]. However, due to LMS shape functions lack the Kronecker delta property, it needs additional steps to impose Dirichlet boundary conditions. Therefore, further research on flexoelectricity using meshfree methods is required. Alternatively, Mao et al. [100] developed a mixed finite element formulation for both piezoelectric and flexoelectric effects, which allows to use C^0-continuous interpolation functions in finite element method (FEM) instead of C^1. The method was then utilized to flexoelectricty in 3D systems [101]. Nanthakumar et al. [102] employed a nine-noded quadrilateral element to solve the flexoelectric PDEs and optimize the electromechanical coupling factor of flexoelectric structures. In mixed FEM formulation, the mechanical degrees of freedom include both displacements and relaxed displacement gradients, with kinematic constraints enforced through Lagrange multipliers. The primary advantage of mixed finite element methods lies in their simplicity when imposing higher-order Dirichlet boundary conditions, facilitated by the inclusion of displacement gradient degrees of freedom. Isogeometric analysis (IGA) [103] is robust and suitable approach for flexoelectric-related problems, whose basis function fulfills the C^1-continuity requirement, as in [104, 105, 106, 107]. Moreover, Yvonnet and Liu [108] modeled flexoelectricity in soft dielectrics with finite deformation, where the C^1 requirement is satisfied by Argyris triangular elements.

Recently, due to the potential on inducing larger strain gradient, several studies have concentrated on tackling the complexities of nonlinear flexoelectric models undergoing large deformation. Yvonnet [108] proposed a numerical finite element framework aimed at modeling and solving the response of nonlinear soft dielectrics, considering the effects of Maxwell stress and flexoelectricity at finite strains. Tran Quoc Thai [105] presented an isogeometric approach for flexoelectricity in soft dielectric materials subjected to finite deformations, taking into account Maxwell stresses on the surface between two different media. After then, a staggered explicit-implicit isogeometric formulation based on large strain kinematics was proposed for soft dielectrics [109]. Codony [110] developed equilibrium equations describing the flexoelectric effect in soft dielectrics under large deformations based on isogeometric analysis. Deng [111] delved into the impact of geometric nonlinearity on flexoelectricity in soft dielectrics under large deformation by using a mixed finite element formulation.

1.2 Topology optimization

Broadly speaking, structural optimization encompasses three key components: topology optimization (TO), shape optimization and size optimization. Among these, TO is considered the conceptual design phase in structural optimization, and is recognized as an important and superior optimization approach but with more challenges. The primary objective of TO is to determine the distribution of material within a specified domain without pre-existing knowledge in order to achieve the best structural performance.

The origin of topology optimization can be traced back to the pioneering work of Michell in 1904 [112], where he established optimality criteria for the least weight design of truss structures based on a continuum description. Inspired by Michell's theory, Prager and Rozvany formulated the minimum-weight analytical solution of elastic and plastic grillages [113, 114]. Cheng and Olhof [115, 116] were pioneers in addressing the numerical structural optimization of continuum structures, where they considered the stiffness optimization for solid elastic plates, with the plate thickness as the design variable. However, the solid-void binary design for structural optimization is known as being ill-posed, within the continuum framework. Kohn and Strang [117] demonstrated that achieving optimal material distribution requires relaxing the design space. They utilized a continuous composite material description to replace the point-wise material or void description traditionally represented in a single-scale discretized manner. This continuous composite was characterized by unit cells based on homogenization theory. Following this, Bendsøe and Kikuchi [118] extended the problem to optimize the sizes and orientations of porous microstructures, which formulated the computational framework for homogenization-based topology optimization of continuum structures. Since then, TO has attracted a growing attention among researches from academic studies to engineering applications.

TO approaches can be broadly categorized into two families: density-based methods (DBM) and boundary-based methods (BBM). Density-based methods encompass the Solid Isotropic Material with Penalization (SIMP) method [21, 22, 23] and the Evolutionary Structural Optimization (ESO) method [119]. On the other hand, boundary-based methods include the Level-set method (LSM) [120, 121], the phase field method [122], and the recently introduced Moving Morphable Components/Voids (MMC/V) method [123, 124]. Several review papers have delved into specific TO methods, such as SIMP [125], ESO [126, 127], and LSM [128]. A critical review comparison on various methods, with advantages and drawbacks, can be found in [129]. A survey on the applications of TO to a broad variety of problems including mechanical and thermal loads of structures, fluid flow, dynamics, acoustics and biomechanics can be referred to [130]. A comprehensive review of educational articles on structural optimization is provided in [131]. In addition to structures, TO can also be employed in architected and multifunctional materials design via combining with multi-scale method [132, 133, 134]. More recently, the development of TO toward additive manufacturing provides an advanced integrated design and manufacturing technique for innovative and high-performance structures, which presents a wide prospect in industrial application [135].

1.2.1 Density-based methods

Due to the numerical difficulties introduced by the homogenization approach in earlier efforts to optimize structural topology, the SIMP method or power-law approach as a robust alternative was suggested [136, 137]. In this framework, the material distribution in the discretized domain Ω is represented by a scalar field i.e. relative density ρ_i per element or node. The solid is represented by $\rho_i = 1$, while void $\rho_i = 0$. The local material properties are interpolated with respect to the local density in a continuous manner, using penalty exponents to enforce local densities to converge to values close to 0 (void) or 1 (solid), e.g.

$$E(\rho_e) = \rho_e^p E_0 \tag{1.23}$$

where p is the penalization parameter and E_0 is the Young's modulus of solid phase. The optimization problem with $p = 1$ corresponds to the "variable-thickness-sheet" problem. However, when $p > 1$, it penalizes intermediate thicknesses or densities, favoring 0-1 solutions. If the value of p is too low or too high, it results in either excessive grey scale or rapid convergence to local minima. While $p = 3$ has been proven to exhibit good convergence towards nearly 0-1 solutions in most cases [23]. In the case of complex multiphysics and multimaterial problems, one can choose suitable penalization factors by considering theoretical material bounds [138].

A general mathematical model of topology optimization can be described as follows: find the material distribution $\boldsymbol{\rho}$ that minimizes the objective c, i.e.

$$\begin{aligned} \text{Min}: \quad & c(\mathbf{U}(\boldsymbol{\rho}),\boldsymbol{\rho}) \\ \text{S.t.}: \quad & \hat{C}_0 = \int_\Omega \rho(\boldsymbol{x})\mathrm{d}V - V_0 \le 0,\ \boldsymbol{x}\in\Omega \\ : \quad & \hat{C}_1 = \mathbf{KU}-\mathbf{F} = 0 \\ : \quad & \hat{C}_j(\mathbf{U}(\boldsymbol{\rho}),\boldsymbol{\rho}) \le 0,\ j = 2,...,M \\ & 0 < \rho_i \le 1,\ \ i = 1,2,...,N \end{aligned} \tag{1.24}$$

where the objective function $c(\mathbf{U}(\boldsymbol{\rho}),\boldsymbol{\rho})$, for example, can be the strain energy $c = \mathbf{U}^T\mathbf{KU}$ for the classic compliance optimization problem. $\mathbf{KU} = \mathbf{F}$ is the discrete system of the specific mechanical or physical state equations by the Finite Element Method. V_0 is the remaining material volume. In (1.24), it comprises $M+1$ constraints, allowing for the incorporation of additional design criteria to enhance the alignment of the optimization problem with practical requirements.

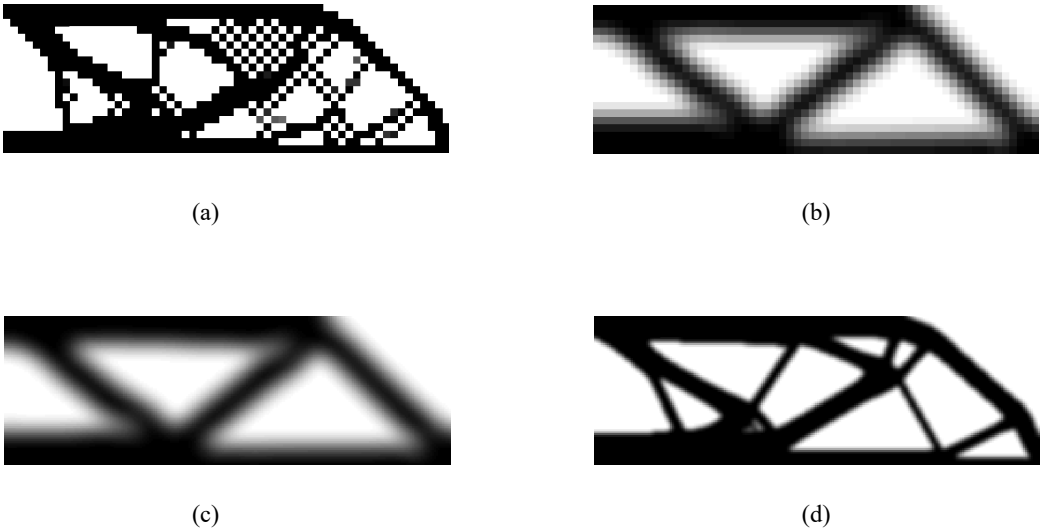

(a) (b) (c) (d)

Figure 1.3: Illustration of checkerboard and mesh-dependence in an example of half-MBB: (a) optimized structure with checkerboard, discretized by 20×60 elements ; (b) optimized structure by density filter with filtering radius r_{min}, discretized by 40×120 elements; (c) optimized structure by density filter with r_{min}, discretized by 80×240 elements; (d) optimized structure by density filter with $1/2r_{min}$, discretized by 80×240 elements

Optimized solutions in the SIMP method are well-known to exhibit numerical artifacts (shown in Fig. 1.3), such as checkerboards, mesh dependency and zig-zag boundary, attributed to the strong reliance on finite element discretization (more details refer to [139]). To ensure well-posed and mesh-independent solutions, one needs to introduce restriction. Restriction methods for SIMP problems were divide into sensitivity and density filters. The sensitivity or density filter defines the physical element sensitivity or density as a weighted average of their neighbors within a circle in 2D or sphere in 3D with specified radius r_{min}.

$$\frac{\tilde{\partial}c}{\partial\rho_i} = \frac{\sum_{j\in N_{e,i}} w_j\rho_j\frac{\partial c}{\partial\rho_j}}{\rho_i\sum_{j\in N_{e,i}} w_j} \tag{1.25}$$

$$\tilde{\rho}_i = \frac{\sum_{j\in N_{e,i}} w_j\rho_j}{\rho_e\sum_{j\in N_{e,i}} w_j} \tag{1.26}$$

where $N_{e,i}$ is the neighbors set of element i within the filter domain. w_j is the weight defined as $w_j = r_{min} - |\boldsymbol{x}_i - \boldsymbol{x}_j|$, wherein $|\boldsymbol{x}_i - \boldsymbol{x}_j|$ is Euclidean distances of two elements. An alternative to density filter in (1.26) is Helmholtz type partial differential equation [140] defined as

$$-r^2\Delta\tilde{\rho} + \tilde{\rho} = \rho \tag{1.27}$$

where r is a length parameter that can be related to the radius r_{min}. The optimized structures with the density filter are shown in Fig. 1.3(b)-(d), where the checkerboard pattern is no longer present. However, it's important to note that the use of filters introduces a grey zone between solid and void regions. To address the grey-scale issue related to the discussed filtering strategies, projection schemes, such as various Heaviside projections in (1.28), have been introduced. Interested readers are referred to the paper [141].

$$\bar{\tilde{\rho}} = \frac{\tanh(\beta\eta_0) + \tanh\beta(\tilde{\rho}_i - \eta_0)}{\tanh(\beta\eta_0) + \tanh\beta(1-\eta_0)} \tag{1.28}$$

where η_0 is the threshold value to transfer the intermediate density to 1 or 0, while β controls the slope of the smooth Heaviside function. The impact of these two parameters can be intuitively seen in Fig. 1.4. The sensitivity of the compliance in (1.24) with respect to the original design variables is computed by the chain rules as

$$\frac{\partial c}{\partial \rho_j} = \frac{\partial c}{\partial \bar{\tilde{\rho}}_j}\frac{\partial \bar{\tilde{\rho}}_j}{\partial \tilde{\rho}_j}\frac{\partial \tilde{\rho}_j}{\partial \rho_j} \tag{1.29}$$

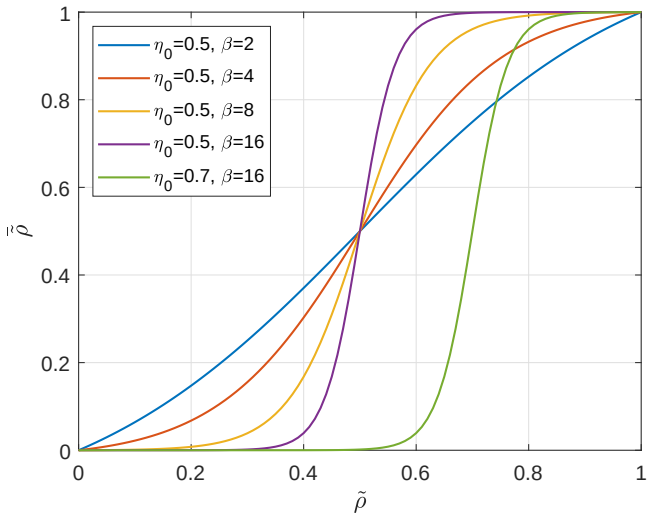

Figure 1.4: Heaviside projection with different thresholds

To resolve the optimization problem in (1.24), its Lagrangian equation is formulated as

$$L = c + \lambda_0\hat{C}_0 + \lambda_j\hat{C}_j,\ j = 1,...M \tag{1.30}$$

where λ are Lagrangian multipliers. For all density-based approaches, a common characteristic is their representation of smooth and differentiable problems, allowing for efficient solutions using well-established and gradient-based optimization techniques. For simplicity, we only consider the compliance with a volume fraction constraint, and give a heuristic updating scheme for the design variables based on standard Optimality Criteria method [112, 142, 143],

$$\rho_i^{(n+1)} = \begin{cases} \max(\rho_{min}, \rho_i^{(n)} - m), & if\ \rho_i^{(n)}B_i^{\eta} \le \max(\rho_{min}, \rho_i^{(n)} - m) \\ \rho_i^{(n)}B_i^{\eta}, & if\ \max(\rho_{min}, \rho_i^{(n)} - m) < \rho_i^{(n)}B_i^{\eta} < \min(1, \rho_i^{(n)} + m) \\ \min(1, \rho_i^{(n)} + m), & if\ \rho_i^{(n)}B_i^{\eta} \ge \min(1, \rho_i^{(n)} + m) \end{cases} \tag{1.31}$$

where m is a positive move-limit, $\eta(=0.5)$ is a numerical damping coefficient and the optimality condition B_i is written as

$$B_i = \frac{-\frac{\partial c}{\partial \rho_i}}{\lambda_0 \frac{\partial \hat{C}_0}{\partial \rho_i}} \tag{1.32}$$

Optimality Criteria method is easy and efficient optimizer to solve the single-constraint problem, but may not be suitable for those with multiple constraints. As an alternative, the Method of Moving Asymptotes (MMA) [144] is effective in tackling multi-constraint optimization problems.

1.2.2 Level-set method

Level set method (LSM), initially introduced by Osher and Sethian [145] to address moving interface problems, have since been well-developed and extensively applied across a wide range of research areas. In Level-set-based topology optimization (LSM-TO) [120, 121], the structure undergoing optimization is implicitly represented by a dynamic boundary embedded in a scalar function known as the higher-dimension level set function ψ, where the zero-level set denotes the structural boundaries. The movement of the design boundaries driven by a relevant speed function of the embedding space can be tracked to capture changes in the shape and topology of the structure. The void phase is depicted by the negative level set, while positive values represent solids within the design domain, i.e. (1.33). Consequently, the level-set model can be referred to as an implicit boundary representation model.

$$\rho = \begin{cases} 0, & \text{if } \psi(\boldsymbol{x}) < 0 \text{ for } \forall \boldsymbol{x} \in \Omega \\ 1, & \text{if } \psi(\boldsymbol{x}) \geq 0 \text{ for } \forall \boldsymbol{x} \in \Omega. \end{cases} \tag{1.33}$$

A surface defined by a level-set model can be regarded as an iso-surface embedded in 3D, and the dynamic model to process structural optimization can be given as a time-varying level set function, i.e

$$S = \{\boldsymbol{x}(t) : \psi(\boldsymbol{x}(t), t) = a\} \tag{1.34}$$

where a is iso-value. Differentiating (1.34), the Hamilton-Jacobi equation can be obtained as

$$\frac{\partial \psi(\boldsymbol{x}, t)}{\partial t} + \nabla \psi(\boldsymbol{x}, t) \frac{\mathrm{d}\boldsymbol{x}}{\mathrm{d}t} = 0 \tag{1.35}$$

The $v = \frac{\mathrm{d}\boldsymbol{x}}{\mathrm{d}t}$ denotes the speed function, which can be chosen as the shape derivative of the augmented Lagrange multiplier formulations for the optimization with constraints [120, 146].

LSM-TO defines precisely the geometry and topology of the structure via a solid-void interface throughout the optimization process. However, these direct methods have limitations as algorithms are unable to create new holes in the level set function away from free boundaries, typically outside a design domain. Resulting solutions are highly dependent on the initial state of the design problem, as noted in previous studies [147, 148]. Additionally, conventional level-set methods explicitly solve the Hamilton-Jacobi partial differential equation (PDE) to control structural boundaries, leading to time step restrictions and the need for frequent reinitialization of level set functions. To overcome these challenges, various alternative formulations have been suggested [149, 150, 151, 152, 153], with the notable advantage that many of them can handle the emergence of new holes without relying on a topological derivative.

1.2.3 Other types

In addition to the methods detailed previously, many other efficient topology optimization methods have been also developed. Xie and Steven [119] introduced the evolutionary structural optimization approach, evolving from initial unidirectional "hard-kill" strategies (removing elements with the lowest sensitivity of compliance) to more flexible bi-directional schemes [126, 154] where the removed elements can be reintroduced if considered rewarding. While this method may appear to involve discrete 0-1 design, it actually utilizes gradients derived from continuous variable assumptions in conjunction with discrete design changes or sharp projections. In phase field-based TO [122, 155, 156], the optimal design can be updated by the steady state of the phase transition described by the generalized Cahn-Hilliard equation. All the previously mentioned methods that depend on finite elements describe structural topology to some extent based on elements or nodes, including LSM-TO and phase field-based TO. In contrast, Moving Morphable Components-based Topology Optimization (MMC) [123, 124] achieves structural topology optimization by optimizing geometric characteristic parameters of the pre-existing morphable components, such as the shape, length, thickness, and orientation as well as the layout (connectivity). Importantly, MMC enables components to overlap, facilitating the change and optimization of the structural layout. To handle mesh capable of representing smooth and precise boundaries, researchers have employed diverse generalized and adaptive finite element schemes in conjunction with level set methods, such as the extended finite element method (XFEM) [157, 158], local remeshing schemes [159] and isogeometric analysis [160, 161].

While gradient-based topology optimization techniques have witnessed successful advancements, there is a consistent presence of papers advocating optimization approaches grounded in non-gradient topology optimization approaches, including Genetic Algorithms, Ant Colonies, Particle Swarms, and others [162]. In recent years, there has been a significant emphasis on integrating machine learning/deep learning with topology optimization [163]. In these methods, the update of the design variables (pseudo-density) in the conventional topology optimization method is transformed into the update of the parameters of various neural networks.

1.3 Topology optimization in flexoelectric structures

More recently, topology optimization has emerged as a promising method for improving the apparent flexoelectricity and Electromechanical Coupling Factors in piezoelectric and flexoelectric structures. Several works have been dedicated to the optimization of structures and metamaterials with flexoelectricity and piezoelectricity. At structure level, Ghasemi et al. [104, 164] proposed an optimization design methodology for piezoelectric/flexoelectric materials, employing IsoGeometric Analysis (IGA) and the level-set topology optimization approach, and successfully applied it to the multi-material design of flexoelectric composites. Nanthakumar [102] et al. have developed a level-set based topology optimization to maximize the electromechanical coupling factor of flexoelectric nanostructures, by solving the flexoelectric PDEs through a mixed finite element formulation. López [165] et al. developed a shape and topology optimization method based on an isogeometric phase field to improve the effective electromechanical coupling factor of flexoelectric structures. Zhang [166] et al proposed an explicit topology optimization to improve the electromechanical coupling factors and effective electric polarization of flexoelectric nanostructures, using the Moving Morphable Void and IGA-based approach. At microstructure level, Chen [167, 168] et al. have developed a topology optimization framework aimed at designing periodic composites comprising piezoelectric constituents, resulting in an increase in direct and converse flexoelectric constants, where a Representative Volume Element (RVE)-based computational homogenization was employed to estimate the effective flexoelectric properties. Greco [169] proposed a computational framework to perform topol-

ogy optimization of the representative volume element of flexoelectric metamaterials by using a Cartesian B-spline method. The topology optimization of nonlinear flexoelectric structures is now beginning to emerge. Zhuang [170] developed a topology optimization procedure to design optimal layouts of nonlinear geometric flexoelectric structures undergoing large displacement. Ortigosa [171] introduced an topology optimization approach for designing flexoelectric energy harvesters at finite strains.

The utilization of flexoelectric effects is linked to the generation of significant strain gradients in dielectric materials, relying on two fundamental characteristics: the scaling effect and the symmetry-breaking effect. The flexoelectric effect becomes increasingly prominent at microscale level, attributed to the strain gradient effect becomes more profound as the material dimensions shrink to micro- and nano-levels. The symmetry-breaking nature of the flexoelectricity has brought more phenomena or physical properties beyond electromechanical applications, such as pyroelectricity [172] and bulk photovoltaic effect [173], triggered by a controlled graded field in the system. The universality and outstanding scaling effect of the flexoelectric effect made it a desirable property for advanced nano/micro-electromechanical systems (N/MEMS).

Exploiting flexoelectric effects at the microscale enables us to design new flexoelectric structures. Flexoelectric structures are often made from one single material but with specially designed shape from which substantial gradients can be generated. There are many interesting designs of flexoelectric structures include the multilayered cantilevers [174, 175], circular rings [176, 177], truncated pyramid cantilever [178] and architected structures [179, 180, 181, 182]. At the macroscopic length scale, it is usually difficult to create large strain gradients within a rigid solid. However, substantial mechanical deformation can be generated through the flexible material or soft dielectrics. The flexible electronic devices integrate the flexoelectric material with a soft matrix to realize large electromechanical responses for energy harvesting and converting [183, 184, 185].

In the realm of flexoelectric composites, researches have concentrated on developing piezoelectric composites using non-piezoelectric materials, driven by earlier work [24, 25]. Traditional piezoelectric composites usually include lead-containing PZT for higher permittivity [16]. Piezoelectric responses, achieved in these composites made of purely flexoelectric materials, can be comparable to common single-phase piezoelectrics. Non-piezoelectric flexoelectric materials can serve as low-cost, lead-free alternatives to traditional piezoelectric materials, thereby promoting the sustainability of electromechanical applications.

In this thesis, to fully exploit the potential of flexoelectric properties, we focus on designing high-performance flexoelectric composites and enhancing the electromechanical coupling efficiency of flexoelectric structures. The presented framework involves the following new contributions: (1) we develop a homogeneous direct/converse flexoelectric-piezoelectric model for microstructures consisting of heterogeneous piezoelectric constitutive phases, which enables the prediction of effective direct and converse flexoelectric coefficients for piezoelectric composites; (2) a C^1-continuous one/multi-patch Isogeometric Analysis framework for the dynamic frequency response of flexoelectric structures with complex geometries has been proposed, where the inertial effect of deformation gradients is included; (3) a homogeneous topology optimization framework is proposed for designing microstructures containing two-phase materials to maximize the effective direct and inverse flexoelectric properties of piezoelectric composites; (4) a multiscale topology optimization method for designing flexoelectric metamaterials made of non-piezoelectric materials and electromechanical energy harvesting systems is proposed to efficiently convert mechanical vibrations into electrical energy; (5) we propose a nonlinear topology optimization framework for flexoelectric soft dielectrics at finite strain to fully leverage the interplay between size effect and large deformation, thereby increasing the electromechanical coupling factors of the structures.

Chapter 2

Apparent direct and converse flexoelectricity of heterogeneous piezoelectric composites

Recent research has brought attention to how flexoelectricity can mimic piezoelectricity. In this chapter, we explore the potential of leveraging piezoelectric materials to generate a significantly enhanced flexoelectric response. We investigate the use of architectured materials comprising diverse piezoelectric phases with the goal of achieving a substantial emergent flexoelectric effect, potentially surpassing the inherent flexoelectricity of the materials. Currently, a computational homogenization framework for effective flexoelectric materials is lacking. Such a framework is essential for examining and optimizing the applications mentioned above without the necessity of solving the full heterogeneous structure.

We begin by introducing the fundamental concepts of computational homogenization, taking the elastic problem as an illustrative example. With the computational homogenization framework, we then establish the effective behavior over a Mindlin strain gradient medium that is augmented with energetic terms related to the electromechanical coupling characteristic of direct and converse flexoelectricity. A finite element procedure is then developed to calculate the various related homogeneous tensors within a Representative Volume Element (RVE), encompassing the fourth-order direct and converse flexoelectric tensor and all other higher order electromechanical coupling terms. By creating a heterogeneity through asymmetric geometric inclusions and multiple constitutive materials, the direct and converse flexoelectric responses can be tuned to much higher than the constituents.

This chapter is adapted from the published articles [167, 168, 179].

2.1 Fundamental concepts of computational homogenization

In this section, the fundamental principles of computational homogenization within the framework of linear elasticity are presented: the establishment of the effective elastic modulus for a heterogeneous medium under steady-state conditions. The notion of Representative Volume Element (RVE) is introduced. To illustrate, we examine the comparatively straightforward scenario of linear elasticity in order to demonstrate the process of defining effective properties.

An RVE is the minimal material volume which must include a large number of the composite microheterogeneities (grains, inclusions, etc), in order to be representative enough for determining the effective properties of the homogenized macroscopic model [186] (schematically in Fig. 2.1). Nevertheless, it should be notably smaller than the macroscopic structural dimensions, such that the scale separation is enabled. The effective properties are determined by spatially averaging the associated internal fields over an RVE, wherein the internal fields are acquired by solving a series of boundary value problems with test loadings [187].

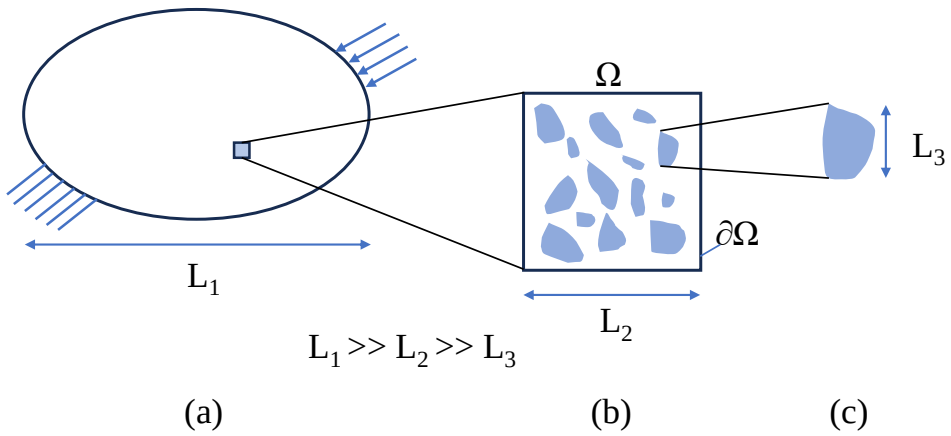

Figure 2.1: (a) Heterogeneous material; (b) Representative Volume Element; (c) Inclusions.

2.1.1 Linear elasticity problem

We consider a volume element $\Omega \in \mathbb{R}^d$ $(d = 2,3)$ made of heterogeneous material, with a boundary $\partial\Omega$. We assume that the homogeneous strain $\overline{\epsilon}$ across the entire body generates a homogeneous stress referred to as $\overline{\sigma}$, then the homogenized (or effective) constitutive equations establish the relationship between $\overline{\varepsilon}$ and $\overline{\sigma}$. σ and ε are respectively the local stress and strain fields within a volume element. The local strain field is assumed to be the superposition of a macroscopic strain $\overline{\varepsilon}$ and of a microscopic fluctuation $\tilde{\varepsilon}$:

$$\varepsilon(\boldsymbol{x}) = \overline{\varepsilon} + \tilde{\varepsilon}(\boldsymbol{x}),\ \forall \boldsymbol{x} \in \Omega \tag{2.1}$$

Taking spatial average of (2.1), we have

$$\begin{aligned}\langle \varepsilon(\boldsymbol{x}) \rangle &= \overline{\varepsilon} + \langle \tilde{\varepsilon}(\boldsymbol{x}) \rangle = \overline{\varepsilon} + \frac{1}{\Omega}\int_\Omega \tilde{\varepsilon}(\boldsymbol{x}) \mathrm{d}\Omega \\ &= \overline{\varepsilon} + \frac{1}{2\Omega}\int_\Omega (\nabla \tilde{\mathbf{u}}(\boldsymbol{x}) + \nabla^T \tilde{\mathbf{u}}(\boldsymbol{x})) \mathrm{d}\Omega \end{aligned} \tag{2.2}$$

where $\langle \cdot \rangle = \frac{1}{\Omega}\int_\Omega \cdot \mathrm{d}\Omega$. $\tilde{\mathbf{u}}$ is a periodic fluctuating displacement. Thus, the spatial average of $\tilde{\mathbf{u}}$ is zero, i.e. $\langle \varepsilon(\boldsymbol{x}) \rangle = \overline{\varepsilon}$.

There are three types of boundary conditions imposed on $\partial\Omega$ to estimate the homogeneous properties of RVE and for which the Hill condition is satisfied [188].

(1) Kinematic Uniform Boundary Conditions (KUBC): the displacement $\mathbf{u}(\boldsymbol{x})$ is prescribed at point $\boldsymbol{x} \in \partial\Omega$, such that:

$$\mathbf{u}(\boldsymbol{x}) = \overline{\varepsilon} \cdot \boldsymbol{x},\ \forall \boldsymbol{x} \in \partial\Omega \tag{2.3}$$

(2) Static Uniform Boundary Conditions (SUBC): the traction is imposed at the boundary,

$$\sigma(\boldsymbol{x}) \cdot \boldsymbol{n} = \overline{\sigma} \cdot \boldsymbol{n},\ \forall \boldsymbol{x} \in \partial\Omega \tag{2.4}$$

(3) Periodic Boundary Conditions (PBC): the displacement $\mathbf{u}(\boldsymbol{x})$ over $\partial\Omega$ takes the form,

$$\mathbf{u}(\boldsymbol{x}) = \overline{\varepsilon} \cdot \boldsymbol{x} + \tilde{\mathbf{u}},\ \forall \boldsymbol{x} \in \partial\Omega \tag{2.5}$$

where $\tilde{\mathbf{u}}$ is the periodic fluctuating displacement.

2.1.2 Average strain and average stress theorems

For simplification, we consider two-phase RVE as shown in Fig. 2.1, defined in a domain $\Omega = \Omega_1 \cup \Omega_2$. The following procedure can be extended to N-phase heterogeneous body. The average stain theorem is obtained by the spatial average of local strain field [189], and can be derived by using divergence theorem and (2.3):

$$\begin{aligned}
\langle \boldsymbol{\varepsilon}(\boldsymbol{x}) \rangle =& \frac{1}{2\Omega} \int_{\Omega} (\nabla \mathbf{u}(\boldsymbol{x}) + \nabla^T \mathbf{u}(\boldsymbol{x})) \mathrm{d}\Omega \\
=& \frac{1}{2\Omega} \left\{ \int_{\Omega_1} (\nabla \mathbf{u}(\boldsymbol{x}) + \nabla^T \mathbf{u}(\boldsymbol{x})) \mathrm{d}\Omega + \int_{\Omega_2} (\nabla \mathbf{u}(\boldsymbol{x}) + \nabla^T \mathbf{u}(\boldsymbol{x})) \mathrm{d}\Omega \right\} \\
=& \frac{1}{2\Omega} \left\{ \int_{\partial\Omega_1} (\mathbf{u} \otimes \mathbf{n} + \mathbf{n} \otimes \mathbf{u}) \mathrm{d}\Gamma + \int_{\partial\Omega_2} (\mathbf{u} \otimes \mathbf{n} + \mathbf{n} \otimes \mathbf{u}) \mathrm{d}\Gamma \right\} \\
=& \frac{1}{2\Omega} \{ \int_{\partial\Omega} (\mathbf{u} \otimes \mathbf{n} + \mathbf{n} \otimes \mathbf{u}) \mathrm{d}\Gamma + \int_{\partial\Omega_1 \cap \partial\Omega_2} (\mathbf{u}^1 \otimes \mathbf{n} + \mathbf{n} \otimes \mathbf{u}^1) \mathrm{d}\Gamma \\
& - \int_{\partial\Omega_1 \cap \partial\Omega_2} (\mathbf{u}^2 \otimes \mathbf{n} + \mathbf{n} \otimes \mathbf{u}^2) \mathrm{d}\Gamma \} \\
=& \frac{1}{2\Omega} \left\{ \int_{\partial\Omega} (\mathbf{u} \otimes \mathbf{n} + \mathbf{n} \otimes \mathbf{u}) \mathrm{d}\Gamma + \int_{\partial\Omega_1 \cap \partial\Omega_2} ([[\mathbf{u}]] \otimes \mathbf{n} + \mathbf{n} \otimes [[\mathbf{u}]]) \mathrm{d}\Gamma \right\} \\
=& \frac{1}{2\Omega} \left\{ \int_{\Omega} (\nabla (\overline{\boldsymbol{\varepsilon}} \cdot \boldsymbol{x}) + \nabla^T (\overline{\boldsymbol{\varepsilon}} \cdot \boldsymbol{x})) \mathrm{d}\Omega + \int_{\partial\Omega_1 \cap \partial\Omega_2} ([[\mathbf{u}]] \otimes \mathbf{n} + \mathbf{n} \otimes [[\mathbf{u}]]) \mathrm{d}\Gamma \right\} \\
=& \overline{\boldsymbol{\varepsilon}} + \frac{1}{2\Omega} \int_{\partial\Omega_1 \cap \partial\Omega_2} ([[\mathbf{u}]] \otimes \mathbf{n} + \mathbf{n} \otimes [[\mathbf{u}]]) \mathrm{d}\Gamma
\end{aligned} \tag{2.6}$$

where $[[\mathbf{u}]]$ describes the displacement jump at the interfaces of Ω_1 and Ω_2. Only if the interface of the material is perfectly bonded, we have

$$\overline{\boldsymbol{\varepsilon}} = \langle \boldsymbol{\varepsilon}(\boldsymbol{x}) \rangle = \frac{1}{2\Omega} \int_{\partial\Omega} (\mathbf{u} \otimes \mathbf{n} + \mathbf{n} \otimes \mathbf{u}) \mathrm{d}\Gamma \tag{2.7}$$

Again we consider a body with SUBC traction $\mathbf{t} = \overline{\boldsymbol{\sigma}} \cdot \mathbf{n}$. We give the identity as ($\mathbf{f}$, body force):

$$\nabla \cdot (\boldsymbol{\sigma} \otimes \boldsymbol{x}) = (\nabla \cdot \boldsymbol{\sigma}) \otimes \boldsymbol{x} + \boldsymbol{\sigma} \cdot \nabla \boldsymbol{x} = -\mathbf{f} \otimes \boldsymbol{x} + \boldsymbol{\sigma} \tag{2.8}$$

Substituting (2.8) into the definition of the average stress, we obtain

$$\begin{aligned}
\langle \boldsymbol{\sigma} \rangle &= \frac{1}{\Omega} \int_{\Omega} \{ \nabla \cdot (\boldsymbol{\sigma} \otimes \boldsymbol{x}) + \mathbf{f} \otimes \boldsymbol{x} \} \mathrm{d}\Omega \\
&= \frac{1}{\Omega} \int_{\partial\Omega} (\boldsymbol{\sigma} \otimes \boldsymbol{x}) \cdot \mathbf{n} \mathrm{d}\Gamma + \frac{1}{\Omega} \int_{\Omega} \mathbf{f} \otimes \boldsymbol{x} \mathrm{d}\Omega \\
&= \frac{1}{\Omega} \int_{\partial\Omega} (\overline{\boldsymbol{\sigma}} \otimes \boldsymbol{x}) \cdot \mathbf{n} \mathrm{d}\Gamma + \frac{1}{\Omega} \int_{\Omega} \mathbf{f} \otimes \boldsymbol{x} \mathrm{d}\Omega \\
&= \frac{1}{\Omega} \int_{\Omega} \nabla \cdot (\overline{\boldsymbol{\sigma}} \otimes \boldsymbol{x}) \mathrm{d}\Omega + \frac{1}{\Omega} \int_{\Omega} \mathbf{f} \otimes \boldsymbol{x} \mathrm{d}\Omega \\
&= \overline{\boldsymbol{\sigma}} + \frac{1}{\Omega} \int_{\Omega} \mathbf{f} \otimes \boldsymbol{x} \mathrm{d}\Omega
\end{aligned} \tag{2.9}$$

In the case of no body force, $\mathbf{f} = \mathbf{0}$, then

$$\overline{\boldsymbol{\sigma}} = \langle \boldsymbol{\sigma} \rangle = \frac{1}{\Omega} \int_{\partial\Omega} (\boldsymbol{\sigma} \otimes \boldsymbol{x}) \cdot \mathbf{n} \mathrm{d}\Gamma \tag{2.10}$$

2.1.3 Hill-Mandel Energy Condition

The Hill-Mandel lemma plays a fundamental role in determining the effective properties of heterogeneous materials. It states that the spatial average of the microscopic (virtual) internal work equals the macroscopic (virtual) internal force work:

$$\langle \boldsymbol{\sigma} : \varepsilon \rangle = \overline{\boldsymbol{\sigma}} : \overline{\varepsilon} \tag{2.11}$$

To prove (2.11), we consider a body with perfectly bonded interfaces among the microscopic constituents and no body force $\nabla \cdot \boldsymbol{\sigma} = \mathbf{0}$. Multiplying the traction $\boldsymbol{\sigma} \cdot \mathbf{n}$ by the displacement vector $\mathbf{u}$ and integrating over boundary $\partial\Omega$, we have

$$\int_{\partial\Omega} \mathbf{u} \cdot \boldsymbol{\sigma} \cdot \mathbf{n} \mathrm{d}\Gamma = \int_{\Omega} \nabla(\mathbf{u} \cdot \boldsymbol{\sigma}) \mathrm{d}\Omega = \int_{\Omega} \nabla \mathbf{u} : \boldsymbol{\sigma} \mathrm{d}\Omega = \int_{\Omega} \varepsilon : \boldsymbol{\sigma} \mathrm{d}\Omega \tag{2.12}$$

Introducing boundary conditions (2.3), then

$$\begin{aligned} &\int_{\partial\Omega} \mathbf{u} \cdot \boldsymbol{\sigma} \cdot \mathbf{n} \mathrm{d}\Gamma = \int_{\partial\Omega} \overline{\varepsilon} \cdot \boldsymbol{x} \cdot \boldsymbol{\sigma} \cdot \mathbf{n} \mathrm{d}\Gamma = \int_{\Omega} \nabla(\overline{\varepsilon} \cdot \boldsymbol{x} \cdot \boldsymbol{\sigma}) \mathrm{d}\Omega \\ &= \int_{\Omega} \nabla(\overline{\varepsilon} \cdot \boldsymbol{x}) : \boldsymbol{\sigma} \mathrm{d}\Omega = \overline{\varepsilon} : \int_{\Omega} \boldsymbol{\sigma} \mathrm{d}\Omega = \overline{\varepsilon} : \overline{\boldsymbol{\sigma}} \cdot \Omega \end{aligned} \tag{2.13}$$

From (2.12) and (2.13), we finally obtain

$$\overline{\boldsymbol{\sigma}} : \overline{\varepsilon} = \frac{1}{\Omega} \int_{\Omega} \boldsymbol{\sigma} : \varepsilon \mathrm{d}\Omega = \langle \boldsymbol{\sigma} : \varepsilon \rangle \tag{2.14}$$

2.1.4 Effective elastic tensor

(1) Strain approach

We assume the fourth-order elastic tensor $\mathbb{C}(\boldsymbol{x})$ is constant within each phase of the heterogeneous body. The local problem where the RVE is subjected to a homogeneous strain field is defined as

$$\nabla \cdot \boldsymbol{\sigma}(\boldsymbol{x}) = \mathbf{0}, \ \forall \boldsymbol{x} \in \Omega \tag{2.15}$$

$$\boldsymbol{\sigma}(\boldsymbol{x}) = \mathbb{C}(\boldsymbol{x}) : \varepsilon(\mathbf{u}(\boldsymbol{x})) \tag{2.16}$$

The homogeneous strain $\overline{\varepsilon}$ imposed on the RVE boundary can be considered as a thermal strain and can be decomposed into elementary strain states [190]:

$$\overline{\varepsilon}_{kl} = \overline{\varepsilon}_{ij} I_{kl}^{ij}, \ I_{kl}^{ij} = \frac{1}{2}(\delta_{ik}\delta_{jl} + \delta_{il}\delta_{jk}) \tag{2.17}$$

where δ_{ij} is the Kronecker delta. The solution $\mathbf{u}$ can be expanded using the superposition principle as a linear combination the homogeneous strain tensor as

$$u_k = \overline{\varepsilon}_{ij} u_k^{ij} \tag{2.18}$$

then

$$\varepsilon(\mathbf{u}) = \varepsilon(\overline{\varepsilon}_{ij} \mathbf{u}^{ij}) = \varepsilon(\mathbf{u}^{ij}) \overline{\varepsilon}_{ij} \tag{2.19}$$

Substituting (2.19) into (2.16) and taking the space averaging, we obtain the macroscopic constitutive relationship as

$$\langle \boldsymbol{\sigma}(\boldsymbol{x}) \rangle = \left\langle \mathbb{C}(\boldsymbol{x}) : \varepsilon(\mathbf{u}^{ij}) \right\rangle : \overline{\varepsilon} \tag{2.20}$$

then we have:

$$\overline{\mathbb{C}}^{\varepsilon}_{ijkl} = \left\langle \mathbb{C}_{ijpq}\boldsymbol{\varepsilon}_{pq}(\mathbf{u}^{kl}) \right\rangle \tag{2.21}$$

An alternative definition of $\overline{\mathbb{C}}^{\varepsilon}$ can be obtained from Hill-Mandel energy condition. By using (2.19), it's derived as

$$\overline{\boldsymbol{\sigma}} : \overline{\boldsymbol{\varepsilon}} = \overline{\boldsymbol{\varepsilon}} : \overline{\mathbb{C}}^{\varepsilon} : \overline{\boldsymbol{\varepsilon}} \tag{2.22}$$

$$\langle \boldsymbol{\sigma} : \boldsymbol{\varepsilon} \rangle = \overline{\boldsymbol{\varepsilon}} : \left\langle \boldsymbol{\varepsilon}(\mathbf{u}^{ij}) : \mathbb{C} : \boldsymbol{\varepsilon}(\mathbf{u}^{kl}) \right\rangle : \overline{\boldsymbol{\varepsilon}} \tag{2.23}$$

$$\overline{\mathbb{C}}^{\varepsilon} = \left\langle \boldsymbol{\varepsilon}(\mathbf{u}^{ij}) : \mathbb{C} : \boldsymbol{\varepsilon}(\mathbf{u}^{kl}) \right\rangle \tag{2.24}$$

(2) Stress approach

The local problem defined in (2.15)-(2.16) can be imposed a homogeneous stress filed on the boundary. Then the solution can be expressed by a linear combination of the macroscopic stress components as:

$$\boldsymbol{\sigma}_{ij}(\boldsymbol{x}) = \boldsymbol{\sigma}^{kl}_{ij}(\boldsymbol{x})\overline{\boldsymbol{\sigma}}_{kl} \tag{2.25}$$

In term of (2.16), we have

$$\boldsymbol{\varepsilon}(\boldsymbol{x}) = \mathbb{C}^{-1} : \boldsymbol{\sigma}(\boldsymbol{x}) : \overline{\boldsymbol{\sigma}} \tag{2.26}$$

and taking the spatial average over Ω, considering the macroscopic stress-strain constitutive law, we obtain

$$\overline{\mathbb{C}}^{\sigma}_{ijkl} = \left\langle \mathbb{C}^{-1}_{ijpq}\boldsymbol{\sigma}^{pq}_{kl}(\boldsymbol{x}) \right\rangle^{-1} \tag{2.27}$$

Similarly to the strain approach, an alternative definition of $\overline{\mathbb{C}}^{\sigma}$ can be obtained from the Hill-Mandel lemma as

$$\overline{C}^{\sigma}_{pqrs} = \left\langle \boldsymbol{\sigma}^{pq}_{ij}\mathbb{C}^{-1}_{ijkl}\boldsymbol{\sigma}^{rs}_{kl}(\boldsymbol{x}) \right\rangle^{-1} \tag{2.28}$$

2.2 Micro scale problem of flexoelectricity

In this section, we present an extension of the previous homogenization scheme to electromechanical media with strain gradients, including the effects of electric field gradients (converse flexoelectric behavior).

2.2.1 Local problem on the RVE

We consider a periodic composite (see Fig. 2.2(a)) assumed to be characterized by a Representative Volume Element (RVE) (see Fig. 2.2(c)). The RVE is defined in a domain $\Omega \in \mathbb{R}^d$ whose external boundary is denoted by $\partial\Omega$. The characteristic size of the RVE is ℓ. The RVE is assumed to be subjected to four homogeneous fields: a strain $\overline{\boldsymbol{\varepsilon}}$, a strain gradient $\overline{\nabla\boldsymbol{\varepsilon}}$, an electric field $\overline{\mathbf{E}}$ and an electric field gradient $\overline{\nabla\mathbf{E}}$, which are prescribed through boundary conditions. The different phases of the RVE are assumed to be linear piezoelectric and characterized by an elastic tensor $\mathbb{C}^k$, a dielectric tensor $\boldsymbol{\alpha}^k$ and a piezoelectric tensor $\mathcal{E}^k$, $k = 1, ..., N_p$, with N_p the number of phases.

The energy density function (electrical enthalpy density) of a piezoelectric material is defined by:

$$W = \frac{1}{2}\boldsymbol{\varepsilon}(\mathbf{x}) : \mathbb{C}(\mathbf{x}) : \boldsymbol{\varepsilon}(\mathbf{x}) - \mathbf{E}(\mathbf{x}) \cdot \mathcal{E}(\mathbf{x}) : \boldsymbol{\varepsilon}(\mathbf{x}) - \frac{1}{2}\mathbf{E}(\mathbf{x}) \cdot \boldsymbol{\alpha}(\mathbf{x}) \cdot \mathbf{E}(\mathbf{x}) \tag{2.29}$$

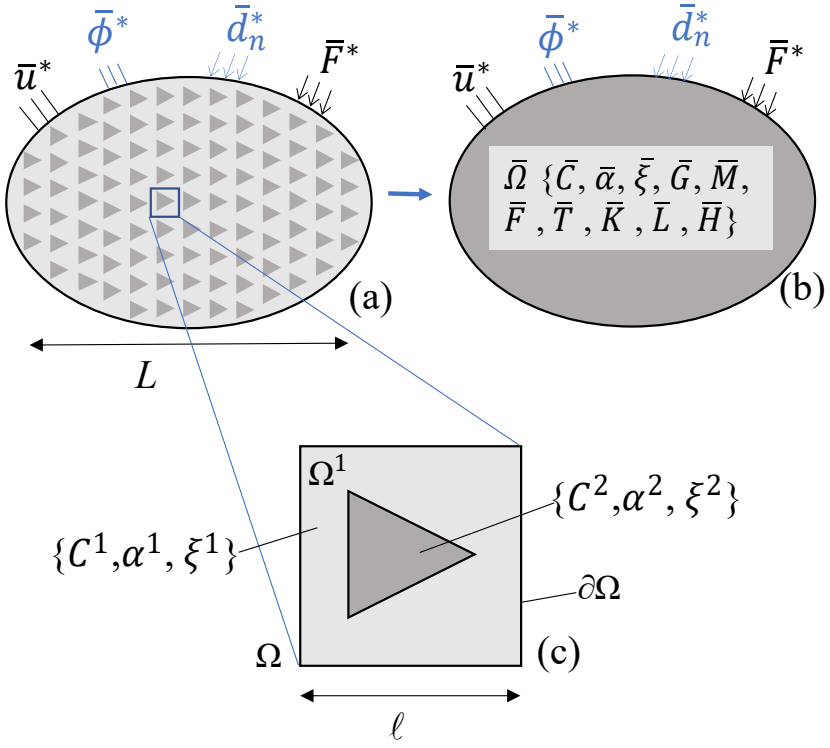

Figure 2.2: (a) Periodic heterogeneous structure; (b) Equivalent piezo-flexoelectric homogeneous structure; (c) RVE model.

where $\mathbb{C}$ is the fourth-order elastic tensor, α is the second-order dielectric tensor, $\mathcal{E}$ is the third-order piezoelectric tensor and $\mathbf{x}$ denotes coordinates. Then the Cauchy stress $\boldsymbol{\sigma}$ and the electric displacement $\mathbf{d}$ are defined by:

$$\boldsymbol{\sigma}(\mathbf{x}) = \frac{\partial W}{\partial \varepsilon} = \mathbb{C}(\mathbf{x}) : \varepsilon(\mathbf{x}) - \mathcal{E}(\mathbf{x}) \cdot \mathbf{E}(\mathbf{x}) \tag{2.30}$$

$$\mathbf{d}(\mathbf{x}) = -\frac{\partial W}{\partial \mathbf{E}} = \mathcal{E}(\mathbf{x}) : \varepsilon(\mathbf{x}) + \boldsymbol{\alpha}(\mathbf{x}) \cdot E(\mathbf{x}) \tag{2.31}$$

A displacement quadratic boundary condition (QBC) has been introduced to prescribe an effective strain and strain gradient [191]:

$$\mathbf{u}(\mathbf{x}) = \overline{\varepsilon} \cdot \mathbf{x} + \frac{1}{2}\overline{\mathcal{G}} : \mathbf{x} \otimes \mathbf{x} + \tilde{\mathbf{u}}(\mathbf{x}) \; on \; \partial\Omega \tag{2.32}$$

where $\overline{\mathcal{G}}$ is the macroscopic second gradient of displacements and the symbol $\overline{\square}$ represents homogeneous field,

$$\mathcal{G}_{ijk} = \frac{\partial^2 u_i}{\partial x_j \partial x_k} \tag{2.33}$$

and $\tilde{\mathbf{u}}(\mathbf{x})$ is either zero or periodic on $\partial\Omega$.

The effective electric field can be computed by prescribing the following electric potential quadratic boundary conditions over the RVE:

$$\phi(\mathbf{x}) = -\bar{\mathbf{E}} \cdot \mathbf{x} - \frac{1}{2}\overline{\nabla \mathbf{E}} : \mathbf{x} \otimes \mathbf{x} + \tilde{\phi}(\mathbf{x}) \text{ on } \partial\Omega \tag{2.34}$$

where $\tilde{\phi}(\mathbf{x})$ is either zero or a periodic fluctuation on $\partial\Omega$.

The electric field vector E_j, the strain tensor ε_{ij} and strain-gradient tensor $\nabla\varepsilon_{ijk}$ are defined as

$$E_j = -\frac{\partial \phi}{\partial x_j} \tag{2.35}$$

$$\varepsilon_{ij} = \frac{1}{2}\left(\frac{\partial u_i}{\partial x_j} + \frac{\partial u_j}{\partial x_i}\right) \tag{2.36}$$

$$\nabla\varepsilon_{ijk} = \frac{\partial \varepsilon_{ij}}{\partial x_k} = \frac{1}{2}\left(\frac{\partial u_i}{\partial x_j x_k} + \frac{\partial u_j}{\partial x_i x_k}\right) \tag{2.37}$$

The strain gradient differs from the second gradient of displacement, their relation can be derived as:

$$\nabla\varepsilon_{(ij)k} = \frac{1}{2}\left(\frac{\partial u_i}{\partial x_j x_k} + \frac{\partial u_j}{\partial x_i x_k}\right) = \frac{1}{2}\left(\mathcal{G}_{ijk} + \mathcal{G}_{jik}\right) \tag{2.38}$$

$$\begin{aligned}
\mathcal{G}_{i(jk)} &= \frac{\partial^2 u_i}{\partial x_j \partial x_k} \\
&= \frac{1}{2}\left(\frac{\partial^2 u_i}{\partial x_j \partial x_k} + \frac{\partial^2 u_i}{\partial x_j \partial x_k} + \frac{\partial^2 u_j}{\partial x_i \partial x_k} - \frac{\partial^2 u_j}{\partial x_i \partial x_k} + \frac{\partial^2 u_k}{\partial x_i \partial x_j} - \frac{\partial^2 u_k}{\partial x_i \partial x_j}\right) \\
&= \frac{1}{2}\left(\frac{\partial^2 u_i}{\partial x_j \partial x_k} + \frac{\partial^2 u_j}{\partial x_i \partial x_k}\right) + \frac{1}{2}\left(\frac{\partial^2 u_i}{\partial x_k \partial x_j} + \frac{\partial^2 u_k}{\partial x_i \partial x_j}\right) - \frac{1}{2}\left(\frac{\partial^2 u_j}{\partial x_k \partial x_i} + \frac{\partial^2 u_k}{\partial x_j \partial x_i}\right) \\
&= \nabla\varepsilon_{ijk} + \nabla\varepsilon_{ikj} - \nabla\varepsilon_{jki}
\end{aligned} \tag{2.39}$$

where the notation $(\cdot\cdot)$ on the subscript of $\nabla\varepsilon_{(ij)k}$ and $\mathcal{G}_{i(jk)}$ stands for the minor symmetries. In this chapter, the theoretical derivation are demonstrated in strain gradient elasticity, whereas the boundary conditions needed for the homogenization scheme are more natural in formulation for second gradient of displacements. The macroscopic second gradient of displacements can be expressed as a function of the homogeneous strain gradient tensor $\overline{\nabla\varepsilon}$:

$$\overline{\mathcal{G}}_{ijk} = \overline{\nabla\varepsilon}_{ijk} + \overline{\nabla\varepsilon}_{ikj} - \overline{\nabla\varepsilon}_{jki} \tag{2.40}$$

One obvious issue with conditions (2.32) and (2.34) arise when considering a homogeneous RVE characterized by a elastic, piezoelectric and dielectric tensors $\mathbb{C}^1$, $\mathcal{E}^1$ and $\boldsymbol{\alpha}^1$. In that case, and for $\overline{\varepsilon} = 0$ and $\overline{\mathbf{E}} = 0$, it is expected that the electric field and local strain solutions within the RVE should be equal to:

$$\varepsilon(\mathbf{x}) = \overline{\nabla\varepsilon} \cdot \mathbf{x}, \quad \forall \mathbf{x} \in \Omega. \tag{2.41}$$

$$\mathbf{E}(\mathbf{x}) = \overline{\nabla\mathbf{E}} \cdot \mathbf{x}, \quad \forall \mathbf{x} \in \Omega. \tag{2.42}$$

However generally (2.41) and (2.42) is not a statically admissible solution for boundary conditions (2.32) and (2.34) since:

$$\nabla \cdot \left(\mathbb{C}^1 : \left[\overline{\nabla\varepsilon}\,\mathbf{x}\right] - \mathcal{E}^1 \cdot \left[\overline{\nabla\mathbf{E}}\,\mathbf{x}\right]\right) \neq 0 \tag{2.43}$$

and

$$\nabla \cdot \left(\mathcal{E}^1 : \left[\overline{\nabla\varepsilon}\,\mathbf{x}\right] + \boldsymbol{\alpha}^1 \cdot \left[\overline{\nabla\mathbf{E}}\,\mathbf{x}\right]\right) \neq 0. \tag{2.44}$$

The inequalities (2.43)-(2.44) hold because in the present work $\overline{\nabla\varepsilon}$ and $\overline{\nabla\mathbf{E}}$ can be chosen arbitrarily. Therefore, as observed in [192, 193], fluctuations remain even when the local continuum is homogeneous, leading to persistent non-physical gradient effects. Indeed, when the local medium is Cauchy homogeneous, there is no dependence on an internal length and the overall medium cannot be of generalized type. To cure this problem, and following the analysis conducted in [194, 195], we propose to prescribe body forces in addition to QBC (2.32) and (2.34) to enforce a constant strain gradient and electric-field gradient within the RVE when the material is homogeneous. The new localization problem involves solving the equilibrium equation:

$$\nabla\cdot\boldsymbol{\sigma}(\mathbf{x}) = \mathbf{f}(\overline{\nabla\varepsilon},\overline{\nabla\mathbf{E}})\ \forall\mathbf{x}\in\Omega, \tag{2.45}$$

and

$$\nabla\cdot\mathbf{d}(\mathbf{x}) = r(\overline{\nabla\varepsilon},\overline{\nabla\mathbf{E}})\ \forall\mathbf{x}\in\Omega, \tag{2.46}$$

where

$$\mathbf{f}(\overline{\nabla\varepsilon},\overline{\nabla\mathbf{E}}) = \nabla\cdot\left(\mathbb{C}^0(\mathbf{x}) : (\overline{\nabla\varepsilon}\cdot\mathbf{x}) - \mathcal{E}^0(\mathbf{x})\cdot(\overline{\nabla\mathbf{E}}\cdot\mathbf{x})\right) \tag{2.47}$$

and

$$r(\overline{\nabla\varepsilon},\overline{\nabla\mathbf{E}}) = \nabla\cdot\left(\mathcal{E}^0(\mathbf{x}) : (\overline{\nabla\varepsilon}\cdot\mathbf{x}) + \boldsymbol{\alpha}^0(\mathbf{x})\cdot(\overline{\nabla\mathbf{E}}\cdot\mathbf{x})\right). \tag{2.48}$$

In the definition of $\mathbf{f}$ and r, $\mathbb{C}^0(\mathbf{x})$, $\mathcal{E}^0(\mathbf{x})$ and $\boldsymbol{\alpha}^0(\mathbf{x})$ are arbitrary elastic, piezoelectric and dielectric tensor fields which have to be specified. At this point, and without loss of generality, we assume a two-phase composite whose elastic properties are described by $\mathbb{C}^1$ and $\mathbb{C}^2$, and where piezoelectric properties are defined by $\mathcal{E}^1$ and $\mathcal{E}^2$, and the dielectric properties are defined by $\boldsymbol{\alpha}^2$ and $\boldsymbol{\alpha}^1$; in which the phase 1 has the highest volume fraction. The RVE is piezoelectric-homogeneous if either (a) the volume fraction of phase 2 goes to zero, i.e. $f^1\to 1$, or (b) if the contrast between phase properties goes to one, i.e. $\|\mathbb{C}^2\|\to\|\mathbb{C}^1\|$, $\|\mathcal{E}^2\|\to\|\mathcal{E}^1\|$ and $\|\boldsymbol{\alpha}^2\|\to\|\boldsymbol{\alpha}^1\|$. For each of these three conditions, the tensors $\mathbb{C}^0(\mathbf{x})$, $\mathcal{E}^0(\mathbf{x})$ and $\boldsymbol{\alpha}^0(\mathbf{x})$ should satisfy:

$$\mathbb{C}^0(\mathbf{x})\to\mathbb{C}^1 \quad \text{if} \begin{cases} f^1\to 1, \\ \text{or } \|\mathbb{C}^2\|\to\|\mathbb{C}^1\| \end{cases} \tag{2.49}$$

and

$$\mathcal{E}^0(\mathbf{x})\to\mathcal{E}^1 \quad \text{if} \begin{cases} f^1\to 1, \\ \text{or } \|\mathcal{E}^2\|\to\|\mathcal{E}^1\|. \end{cases} \tag{2.50}$$

and

$$\boldsymbol{\alpha}^0(\mathbf{x})\to\boldsymbol{\alpha}^1 \quad \text{if} \begin{cases} f^1\to 1, \\ \text{or } \|\boldsymbol{\alpha}^2\|\to\|\boldsymbol{\alpha}^1\|. \end{cases} \tag{2.51}$$

Several choices are possible to respect conditions (2.49)-(2.51), such as (among others): pointwise body force correction, $\mathbb{C}^0(\mathbf{x})=\mathbb{C}(\mathbf{x})$, $\mathcal{E}^0(\mathbf{x})=\mathcal{E}(\mathbf{x})$, $\boldsymbol{\alpha}^0(\mathbf{x})=\boldsymbol{\alpha}(\mathbf{x})$, effective body force correction, $\mathbb{C}^0(\mathbf{x})=\overline{\mathbb{C}}$ and $\mathcal{E}^0(\mathbf{x})=\overline{\mathcal{E}}$ and $\boldsymbol{\alpha}^0(\mathbf{x})=\overline{\boldsymbol{\alpha}}$, or null body force (standard QBC) $\mathbb{C}^0(\mathbf{x})=\mathbb{O}$, $\mathcal{E}^0(\mathbf{x})=\mathbb{O}$ and $\boldsymbol{\alpha}^0(\mathbf{x})=\mathbb{O}$. These different choices have been compared in the elastic case in [195], and there is still no definitive answer to the best choice. The standard solution is simple but induces the mentioned spurious strain gradient effects in the case of homogeneous domains, as discussed in [195]. The effective body forces solution is consistent with asymptotic analysis [194] and removes these spurious effects but induces divergence of

effective properties in case of infinite contrasts of properties between phases. A more detailed discussion can be found in [195]. In spite of these remaining issues, we adopt the effective body forces solution in the present work. Then, defining $\mathbb{C}^0 = \overline{\mathbb{C}}$, $\mathcal{E}^0 = \overline{\mathcal{E}}$ and $\boldsymbol{\alpha}^0 = \overline{\boldsymbol{\alpha}}$ (defined respectively by Eqs. (2.86), (2.87) and (2.88)) and introducing them in (2.47) and (2.48), we obtain the local problem as:

$$\nabla \cdot \boldsymbol{\sigma}(\mathbf{x}) = \mathbf{f}(\overline{\nabla \varepsilon}, \overline{\nabla \mathbf{E}}),\ \mathbf{x} \in \Omega \tag{2.52}$$

$$\nabla \cdot \mathbf{d}(\mathbf{x}) = \mathbf{r}(\overline{\nabla \varepsilon}, \overline{\nabla \mathbf{E}}),\ \mathbf{x} \in \Omega \tag{2.53}$$

where

$$f_i = C^0_{ijkl}\overline{\nabla \varepsilon}_{klj} - \mathcal{E}^0_{ijk}\overline{\nabla E}_{kj} \tag{2.54}$$

$$r = \mathcal{E}^0_{ijk}\overline{\nabla \varepsilon}_{jki} + \alpha^0_{ij}\overline{\nabla E}_{ji} \tag{2.55}$$

2.2.2 Finite element discretization of local RVE equation

In the following, we present the Finite Element discretization for localization problem defined in (2.52)-(2.53). The 2D plane strain condition is considered.

The weak form associated with the coupled problem (2.52)-(2.53)-(2.32)-(2.34) is to find $\mathbf{u} \in \{\mathbf{u} = \bar{\mathbf{u}}^* \text{ on } \partial\Omega_{\mathrm{u}}, \mathbf{u} \in \mathbf{H}^1(\Omega)\}$ and $\phi \in \{\phi = \bar{\phi}^* \text{ on } \partial\Omega_\phi, \phi \in \mathbf{H}^1(\Omega)\}$ such that [179]

$$\int_\Omega d_{k,k}\delta\phi_i \mathrm{d}\Omega = -\int_\Omega \{\overline{\mathcal{E}}_{ijk}\overline{\nabla \varepsilon}_{ijk}x_k + \overline{\alpha}_{kj}\overline{\nabla E}_{jk}x_k\}\delta\phi_{i,i}\mathrm{d}\Omega \tag{2.56}$$

$$\int_\Omega \sigma_{ij,j}\delta u_i \mathrm{d}\Omega = \int_\Omega \{\overline{C}_{ijkl}\overline{\nabla \varepsilon}_{klj}x_j - \overline{\mathcal{E}}_{ijk}\overline{\nabla E}_{kj}x_j\}\varepsilon_{ij}(\delta u_i)\mathrm{d}\Omega \tag{2.57}$$

for all $\delta\mathbf{u} \in \{\delta\mathbf{u} = 0 \text{ on } \partial\Omega_u, \delta\mathbf{u} \in \mathbf{H}^1(\Omega)\}$ and $\delta\phi \in \{\delta\phi = 0 \text{ on } \partial\Omega_\phi, \delta\phi \in \mathbf{H}^1(\Omega)\}$. Substituting Eq. (2.30) and (2.31) into Eq. (2.56) and (2.57) yields:

$$\int_\Omega (\mathcal{E}_{ijk}\varepsilon_{ij}(u_i) + \alpha_{kj}E_j(\phi))\delta\phi_{i,i}\mathrm{d}\Omega = -\int_\Omega \{\overline{\mathcal{E}}_{ijk}\overline{\nabla \varepsilon}_{ijk}x_k + \overline{\alpha}_{kj}\overline{\nabla E}_{jk}x_k\}\delta\phi_{i,i}\mathrm{d}\Omega \tag{2.58}$$

$$\int_\Omega (C_{ijkl}\varepsilon_{kl}(u_k) - \mathcal{E}_{ijk}E_k(\phi))\varepsilon_{ij}(\delta u_i)\mathrm{d}\Omega = \int_\Omega \{\overline{C}_{ijkl}\overline{\nabla \varepsilon}_{klj}x_j - \overline{\mathcal{E}}_{ijk}\overline{\nabla E}_{kj}x_j\}\varepsilon_{ij}(\delta u_i)\mathrm{d}\Omega \tag{2.59}$$

We adopt the same finite element discretization for the approximation of the displacement field $\mathbf{u}$ and of the electric field ϕ. Using 8-node element, the two finite element approximate field ($\mathbf{u}^h$, ϕ^h) can be expressed as:

$$\mathbf{u}^h(\mathbf{x}) = \mathbf{N}_u(\mathbf{x})\mathbf{u}_e;\ \phi^h(\mathbf{x}) = \mathbf{N}_\phi(\mathbf{x})\phi_e \tag{2.60}$$

$$\delta\mathbf{u}^h(\mathbf{x}) = \mathbf{N}_u(\mathbf{x})\delta\mathbf{u}_e;\ \delta\phi^h(\mathbf{x}) = \mathbf{N}_\phi(\mathbf{x})\delta\phi_e \tag{2.61}$$

and their derivatives as,

$$\nabla\mathbf{u}^h(\mathbf{x}) = \mathbf{B}_u(\mathbf{x})\mathbf{u_i};\ \nabla\phi^h(\mathbf{x}) = \mathbf{B}_\phi(\mathbf{x})\phi_i \tag{2.62}$$

$$\nabla\delta\mathbf{u}^h(\mathbf{x}) = \mathbf{B}_u(\mathbf{x})\delta\mathbf{u_i};\ \nabla\delta\phi^h(\mathbf{x}) = \mathbf{B}_\phi(\mathbf{x})\delta\phi_i \tag{2.63}$$

$\mathbf{B}_\phi$ and $\mathbf{B}_u$ are the matrices containing the gradient of the corresponding basis functions N_ϕ and N_u which are given by

$$\mathbf{B}_\phi = \begin{bmatrix} \frac{\partial N_1}{\partial x} & \cdots & \frac{\partial N_n}{\partial x} \\ \frac{\partial N_1}{\partial y} & \cdots & \frac{\partial N_n}{\partial y} \end{bmatrix},\ \mathbf{B}_u = \begin{bmatrix} \frac{\partial N_1}{\partial x} & \cdots & \frac{\partial N_n}{\partial x} & 0 & \cdots & 0 \\ 0 & \cdots & 0 & \frac{\partial N_1}{\partial y} & \cdots & \frac{\partial N_n}{\partial y} \\ \frac{\partial N_1}{\partial y} & \cdots & \frac{\partial N_n}{\partial y} & \frac{\partial N_1}{\partial x} & \cdots & \frac{\partial N_n}{\partial x} \end{bmatrix} \tag{2.64}$$

By substituting the above discrete approximation in Eq. (2.58) and (2.59), we obtain the linear system of coupling equations:

$$\begin{bmatrix} \mathbf{K}_{\phi\phi} & \mathbf{K}_{\phi u} \\ -\mathbf{K}_{u\phi} & \mathbf{K}_{uu} \end{bmatrix} \begin{bmatrix} \boldsymbol{\phi} \\ \boldsymbol{u} \end{bmatrix} = \begin{bmatrix} \mathbf{F}_{\phi} \\ \mathbf{F}_{u} \end{bmatrix} \tag{2.65}$$

with

$$\mathbf{K}_{\phi\phi} = \int_{\Omega} (\mathbf{B}_{\phi})^T [\boldsymbol{\alpha}] \mathbf{B}_{\phi} \mathrm{d}\Omega, \tag{2.66}$$

$$\mathbf{K}_{\phi u} = -\int_{\Omega} (\mathbf{B}_{\phi})^T [\mathcal{E}] \mathbf{B}_{u} \mathrm{d}\Omega, \tag{2.67}$$

$$\mathbf{K}_{uu} = \int_{\Omega} (\mathbf{B}_{u})^T [\mathbf{C}] \mathbf{B}_{u} \mathrm{d}\Omega, \tag{2.68}$$

$$\mathbf{F}_{\phi} = \int_{\Omega} (\mathbf{B}_{\phi})^T \{[\overline{\mathcal{E}}][\boldsymbol{\eta}] + [\overline{\alpha}][\boldsymbol{\kappa}]\} \mathrm{d}\Omega, \tag{2.69}$$

$$\mathbf{F}_{u} = \int_{\Omega} (\mathbf{B}_{u})^T \{[\overline{\mathbf{C}}][\boldsymbol{\eta}] - [\overline{\mathcal{E}}]^T [\boldsymbol{\kappa}]\} \mathrm{d}\Omega, \tag{2.70}$$

where,

$$[\boldsymbol{\eta}] = \begin{bmatrix} \overline{\nabla\varepsilon}_{111} x_1 + \overline{\nabla\varepsilon}_{112} x_2 \\ \overline{\nabla\varepsilon}_{221} x_1 + \overline{\nabla\varepsilon}_{222} x_2 \\ \overline{\nabla\varepsilon}_{121} x_1 + \overline{\nabla\varepsilon}_{122} x_2 \end{bmatrix} \tag{2.71}$$

and

$$[\boldsymbol{\kappa}] = \begin{bmatrix} \overline{\nabla E}_{11} x_1 + \overline{\nabla E}_{12} x_2 \\ \overline{\nabla E}_{21} x_1 + \overline{\nabla E}_{22} x_2 \end{bmatrix} \tag{2.72}$$

2.3 Effective piezo-flexoelectric model

2.3.1 Macroscopic model

We define the total energy density $\overline{W}$ for an electromechanical system where all couplings between strains $\overline{\varepsilon}$, electric field $\overline{E}$, strain gradient $\overline{\nabla\varepsilon}$ and electric field gradient $\overline{\nabla E}$ are taken into account:

$$\begin{aligned} \overline{W} =& \frac{1}{2}\overline{\mathbb{C}}_{ijkl}\overline{\varepsilon}_{ij}\overline{\varepsilon}_{kl} - \frac{1}{2}\overline{\alpha}_{ij}\overline{E}_i\overline{E}_j - \overline{\mathcal{E}}_{ijk}\overline{E}_i\overline{\varepsilon}_{jk} \\ &+ \frac{1}{2}\overline{\mathbb{G}}_{ijklmn}\overline{\nabla\varepsilon}_{ijk}\overline{\nabla\varepsilon}_{lmn} + \overline{\mathbb{F}}_{ijkl}\overline{E}_i\overline{\nabla\varepsilon}_{jkl} + \overline{\mathbb{M}}_{ijklm}\overline{\varepsilon}_{ij}\overline{\nabla\varepsilon}_{klm} \\ &- \overline{\mathbb{T}}_{ijk}\overline{E}_i\overline{\nabla E}_{jk} - \overline{\mathbb{K}}_{ijkl}\overline{\varepsilon}_{ij}\overline{\nabla E}_{kl} - \frac{1}{2}\overline{\mathbb{L}}_{ijkl}\overline{\nabla E}_{ij}\overline{\nabla E}_{kl} - \overline{\mathbb{H}}_{ijklm}\overline{\nabla E}_{ij}\overline{\nabla\varepsilon}_{klm} \end{aligned} \tag{2.73}$$

In Eq. (2.73), $\overline{\mathbb{C}}$, $\overline{\alpha}$ and $\overline{\mathcal{E}}$ denote the effective fourth-order elastic, second-order dielectric and third-order piezoelectric tensors, respectively. The term $\overline{\mathbb{F}}$ denotes the effective fourth-order flexoelectric tensor, while $\overline{\mathbb{M}}$ and $\overline{\mathbb{G}}$ correspond to higher-order strain gradient elastic tensors (see e.g. [195]). The term $\overline{\mathbb{K}}$ is the so-called converse flexoelectric tensor. Here, we emphasize that $\overline{\mathbb{F}}$ and $\overline{\mathbb{K}}$ are considered independent tensors, meaning the relation $\overline{\mathbb{K}}_{ijkl} = \overline{\mathbb{F}}_{jkil}$ does not hold strictly.

We note that there are several new coupling tensors in the above energy density expression, whose interpretation is as follows: $\overline{\mathbb{T}}$ denotes the relation between an additional polarization

(electric field) and an electric field gradient; $\overline{\mathbb{L}}$ denotes the relation between a polarization gradient (or electric field gradient) and an electric field gradient and $\overline{\mathbb{H}}$ denotes the relation between a polarization gradient (or electric field gradient) and a strain gradient.

The effective stress tensor $\overline{\sigma}$, effective electric displacement $\overline{d}$, effective hyperstress tensor $\overline{S}$ and hyper-electric displacement $\overline{P}$ associated with energy density function (2.73) are defined as:

$$\overline{\sigma}_{ij} = \frac{\partial \overline{W}}{\partial \overline{\varepsilon}_{ij}}, \quad \overline{d}_i = -\frac{\partial \overline{W}}{\partial \overline{E}_i}, \quad \overline{S}_{ijk} = \frac{\partial \overline{W}}{\partial \overline{\nabla \varepsilon}_{ijk}}, \quad \overline{P}_{ij} = -\frac{\partial \overline{W}}{\partial \overline{\nabla E}_{ij}} \tag{2.74}$$

The corresponding expressions for the stress $\overline{\sigma}$, the electric displacement $\overline{d}$, the hyperstress $\overline{S}$ and hyper electric displacement $\overline{P}$ are provided by:

$$\overline{\sigma}_{ij} = \overline{\mathbb{C}}_{ijkl}\overline{\varepsilon}_{kl} - \overline{\mathcal{E}}_{kij}\overline{E}_k + \overline{\mathbb{M}}_{ijklm}\overline{\nabla \varepsilon}_{klm} - \overline{\mathbb{K}}_{ijkl}\overline{\nabla E}_{kl} \tag{2.75}$$

$$\overline{d}_i = \overline{\mathcal{E}}_{ijk}\overline{\varepsilon}_{jk} + \overline{\alpha}_{ij}\overline{E}_j - \overline{\mathbb{F}}_{ijkl}\overline{\nabla \varepsilon}_{jkl} + \overline{\mathbb{T}}_{ijk}\overline{\nabla E}_{jk} \tag{2.76}$$

$$\overline{S}_{ijk} = \overline{\mathbb{M}}_{lmijk}\overline{\varepsilon}_{lm} + \overline{\mathbb{F}}_{lijk}\overline{E}_l + \overline{\mathbb{G}}_{ijklmn}\overline{\nabla \varepsilon}_{lmn} + \overline{\mathbb{H}}_{lmijk}\overline{\nabla E}_{lm} \tag{2.77}$$

$$\overline{P}_{ij} = \overline{\mathbb{K}}_{klij}\overline{\varepsilon}_{kl} + \overline{\mathbb{T}}_{kij}\overline{E}_k - \overline{\mathbb{H}}_{ijklm}\overline{\nabla \varepsilon}_{klm} + \overline{\mathbb{L}}_{ijkl}\overline{\nabla E}_{kl} \tag{2.78}$$

Taking the spatial average of (2.29) we obtain:

$$\langle W \rangle = \frac{1}{2}\langle \mathbb{C}_{ijkl}\varepsilon_{ij}\varepsilon_{kl} \rangle - \langle \mathcal{E}_{ijk}\varepsilon_{ij}E_k \rangle - \frac{1}{2}\langle \alpha_{ij}E_iE_j \rangle \tag{2.79}$$

where $\langle \cdot \rangle = \frac{1}{\Omega}\int_\Omega \cdot \, \mathrm{d}\Omega$ denotes the volume average over Ω.

Solving the linear localization problem (2.52)-(2.53)-(2.32)-(2.34) by using the superposition principle, the local strain field $\varepsilon(\mathbf{x})$ and the local electric field $\mathbf{E}(\mathbf{x})$ can be obtained as:

$$\varepsilon_{ij} = A^0_{ijkl}\overline{\varepsilon}_{kl} + B^0_{ijk}\overline{E}_k + \tilde{A}^1_{ijklm}\overline{\nabla \varepsilon}_{klm} + \tilde{B}^1_{ijkl}\overline{\nabla E}_{kl}, \tag{2.80}$$

$$E_i = D^0_{ijk}\overline{\varepsilon}_{jk} + h^0_{ij}\overline{E}_j + \tilde{D}^1_{ijkl}\overline{\nabla \varepsilon}_{jkl} + \tilde{h}^1_{ijk}\overline{\nabla E}_{jk} \tag{2.81}$$

where

$$\tilde{A}^1_{ijklm} = A^1_{ijklm} - A^0_{ijkl}x_m \tag{2.82}$$

$$\tilde{D}^1_{ijkl} = D^1_{ijkl} - D^0_{ijk}x_l \tag{2.83}$$

$$\tilde{B}^1_{ijkl} = B^1_{ijkl} - B^0_{ijk}x_l \tag{2.84}$$

$$\tilde{h}^1_{ijk} = h^1_{ijk} - h^0_{ij}x_k \tag{2.85}$$

are corrected terms to remove local spurious fluctuations in the case of homogeneous RVEs [179, 195].

The strain solutions and electric field solutions are calculated by:

i) A^0_{ijkl}, B^0_{ijk}, A^1_{ijklm} and B^1_{ijkl} are the strain solution $\varepsilon_{ij}(x)$ obtained by solving the problems (2.52)-(2.53)-(2.34)-(2.32) with $\overline{\varepsilon}_{kl} = \frac{1}{2}(e_k \otimes e_l + e_l \otimes e_k)$, $\overline{E}_k = e_k$, $\overline{\nabla \varepsilon}_{klm} = \frac{1}{2}(e_k \otimes e_l + e_l \otimes e_k) \otimes e_m$, $\overline{\nabla E}_{kl} = e_k \otimes e_l + e_l \otimes e_k$, respectively.

ii) D^0_{ijk}, h^0_{ij}, D^1_{ijkl} and h^1_{ijk} are the electric field solution $E_i(x)$ obtained by solving the problems (2.52)-(2.53)-(2.34)-(2.32) with $\overline{\varepsilon}_{jk} = \frac{1}{2}(e_j \otimes e_k + e_k \otimes e_j)$, $\overline{E}_j = e_j$, $\overline{\nabla\varepsilon}_{jkl} = \frac{1}{2}(e_j \otimes e_k + e_k \otimes e_j) \otimes e_l$,$\overline{\nabla E}_{jk} = e_j \otimes e_k + e_k \otimes e_j$, respectively.

The terms e_i are unitary basis vectors. The Finite Element discretization procedure is used to solve (2.52)-(2.53)-(2.34)-(2.32) is recalled in Section 2.2.2.

Substituting Eq.(2.80) and (2.81) into Eq.(2.79). According to Hill-Mandel lemma, the volume average of microscopic energy over the RVE could be identified with a strain gradient macroscopic elastic energy, i.e. $\langle W \rangle = \overline{W}$, the effective operators are obtained as:

$$\overline{\mathbb{C}}_{ijkl} = \langle A^0_{ijpq} C_{pqrs} A^0_{rskl} - 2A^0_{ijpq} \mathcal{E}_{pqr} D^0_{rkl} - D^0_{ijp} \alpha_{pq} D^0_{qkl} \rangle \tag{2.86}$$

$$\overline{\mathcal{E}}_{ijk} = \langle -A^0_{ijpq} C_{pqrs} B^0_{rsk} + A^0_{ijpq} \mathcal{E}_{pqr} h^0_{rk} + D^0_{ijp} \mathcal{E}_{pqr} B^0_{qrk} + D^0_{ijp} \alpha_{pq} h^0_{qk} \rangle \tag{2.87}$$

$$\overline{\alpha}_{ij} = \langle -B^0_{ipq} C_{pqrs} B^0_{rsj} + 2h^0_{ip} \mathcal{E}_{pqr} B^0_{qrj} + h^0_{ip} \alpha_{pq} h^0_{qj} \rangle \tag{2.88}$$

$$\overline{\mathbb{F}}_{ijkl} = \langle B^0_{ipq} C_{pqrs} \tilde{A}^1_{rsjkl} - h^0_{ip} \mathcal{E}_{pqr} \tilde{A}^1_{qrjkl} - B^0_{ipq} \mathcal{E}_{pqr} \tilde{D}^1_{rjkl} - h^0_{ip} \alpha_{pq} \tilde{D}^1_{qjkl} \rangle \tag{2.89}$$

$$\overline{\mathbb{M}}_{ijklm} = \langle A^0_{ijpq} C_{pqrs} \tilde{A}^1_{rsklm} - D^0_{ijp} \mathcal{E}_{pqr} \tilde{A}^1_{qrklm} - A^0_{ijpq} \mathcal{E}_{pqr} \tilde{D}^1_{rklm} - D^0_{ijp} \alpha_{pq} \tilde{D}^1_{qklm} \rangle \tag{2.90}$$

$$\overline{\mathbb{G}}_{ijklmn} = \langle \tilde{A}^1_{ijkpq} C_{pqrs} \tilde{A}^1_{rslmn} - 2\tilde{D}^1_{ijkp} \mathcal{E}_{pqr} \tilde{A}^1_{qrlmn} - \tilde{D}^1_{ijkp} \alpha_{pq} \tilde{D}^1_{qlmn} \rangle \tag{2.91}$$

$$\overline{\mathbb{T}}_{ijk} = \langle B^0_{ipq} C_{pqrs} \tilde{B}^1_{rsjk} - h^0_{ip} \mathcal{E}_{pqr} \tilde{B}^1_{qrjk} - B^0_{ipq} \mathcal{E}_{pqr} \tilde{h}^1_{rjk} - h^0_{ip} \alpha_{pq} \tilde{h}^1_{qjk} \rangle \tag{2.92}$$

$$\overline{\mathbb{K}}_{ijkl} = \langle -A^0_{ijpq} C_{pqrs} \tilde{B}^1_{rskl} + D^0_{ijp} \mathcal{E}_{pqr} \tilde{B}^1_{qrkl} + A^0_{ijpq} \mathcal{E}_{pqr} \tilde{h}^1_{rkl} + D^0_{ijp} \alpha_{pq} \tilde{h}^1_{qkl} \rangle \tag{2.93}$$

$$\overline{\mathbb{L}}_{ijkl} = \langle \tilde{B}^1_{ijpq} C_{pqrs} \tilde{B}^1_{rskl} - 2\tilde{h}^1_{ijp} \mathcal{E}_{pqr} \tilde{B}^1_{qrkl} - \tilde{h}^1_{ijp} \alpha_{pq} \tilde{h}^1_{qkl} \rangle \tag{2.94}$$

$$\overline{\mathbb{H}}_{ijklm} = \langle -\tilde{B}^1_{ijpq} C_{pqrs} \tilde{A}^1_{rsklm} + \tilde{B}^1_{ijpq} \mathcal{E}_{pqr} \tilde{D}^1_{rklm} + \tilde{h}^1_{ijp} \mathcal{E}_{pqr} \tilde{A}^1_{qrklm} + \tilde{h}^1_{ijp} \alpha_{pq} \tilde{D}^1_{qklm} \rangle \tag{2.95}$$

2.3.2 Numerical calculation of the effective tensors

The 2D vector form associated with the components of strain ε, strain gradient tensor $\nabla\varepsilon$ and electric strain gradient $\nabla\mathbf{E}$ can be defined respectively as:

$$[\varepsilon] = \begin{bmatrix} \varepsilon_{11} \\ \varepsilon_{22} \\ \varepsilon_{12} \end{bmatrix} = \begin{bmatrix} \frac{\partial u_1}{\partial x_1} \\ \frac{\partial u_2}{\partial x_2} \\ \frac{1}{2}(\frac{\partial u_1}{\partial x_2} + \frac{\partial u_2}{\partial x_1}) \end{bmatrix} \tag{2.96}$$

$$[\nabla\varepsilon] = \begin{bmatrix} \nabla\varepsilon_{111} \\ \nabla\varepsilon_{221} \\ 2\nabla\varepsilon_{122} \\ \nabla\varepsilon_{222} \\ \nabla\varepsilon_{112} \\ 2\nabla\varepsilon_{121} \end{bmatrix} = \begin{bmatrix} \frac{\partial^2 u_1}{\partial x_1^2} \\ \frac{\partial^2 u_2}{\partial x_1 \partial x_2} \\ \frac{\partial^2 u_1}{\partial x_2^2} + \frac{\partial^2 u_2}{\partial x_1 \partial x_2} \\ \frac{\partial^2 u_2}{\partial x_2^2} \\ \frac{\partial^2 u_1}{\partial x_1 \partial x_2} \\ \frac{\partial^2 u_1}{\partial x_1 \partial x_2} + \frac{\partial^2 u_2}{\partial x_1^2} \end{bmatrix} \tag{2.97}$$

$$[\nabla\mathbf{E}] = \begin{bmatrix} \nabla E_{11} \\ \nabla E_{22} \\ 2\nabla E_{12} \end{bmatrix} = \begin{bmatrix} \frac{\partial E_1}{\partial x_1} \\ \frac{\partial E_2}{\partial x_2} \\ \frac{\partial E_1}{\partial x_2} + \frac{\partial E_2}{\partial x_1} \end{bmatrix} \tag{2.98}$$

where the symmetries of effective tensors $\overline{\boldsymbol{\alpha}}$, $\overline{\mathcal{E}}$, $\overline{\mathbb{C}}$, $\overline{\mathbb{F}}$, $\overline{\mathbb{M}}$, $\overline{\mathbb{G}}$, $\overline{\mathbb{T}}$, $\overline{\mathbb{K}}$, $\overline{\mathbb{L}}$ and $\overline{\mathbb{H}}$ are taken into account,

$$\overline{\alpha}_{ij} = \overline{\alpha}_{ji}, \overline{\mathcal{E}}_{ijk} = \overline{\mathcal{E}}_{ikj}, \overline{\mathbb{F}}_{ijkl} = \overline{\mathbb{F}}_{ikjl} \tag{2.99}$$

$$\overline{\mathbb{M}}_{ijklm} = \overline{\mathbb{M}}_{jiklm} = \overline{\mathbb{M}}_{ijlkm} \tag{2.100}$$

$$\overline{\mathbb{C}}_{ijkl} = \overline{\mathbb{C}}_{klij} = \overline{\mathbb{C}}_{jikl} = \overline{\mathbb{C}}_{ijlk} \tag{2.101}$$

$$\overline{\mathbb{G}}_{ijklmp} = \overline{\mathbb{G}}_{lmpijk} = \overline{\mathbb{G}}_{jiklmp} = \overline{\mathbb{G}}_{ijkmlp} \tag{2.102}$$

$$\overline{\mathbb{T}}_{ijk} = \overline{\mathbb{T}}_{ikj} \tag{2.103}$$

$$\overline{\mathbb{K}}_{ijkl} = \overline{\mathbb{K}}_{jikl} = \overline{\mathbb{K}}_{ijlk} \tag{2.104}$$

$$\overline{\mathbb{L}}_{ijkl} = \overline{\mathbb{L}}_{klij} = \overline{\mathbb{L}}_{jikl} = \overline{\mathbb{L}}_{ijlk} \tag{2.105}$$

$$\overline{\mathbb{H}}_{ijklm} = \overline{\mathbb{H}}_{jiklm} = \overline{\mathbb{H}}_{ijlkm} \tag{2.106}$$

The above effective tensors are written in matrix form as,

$$[\overline{\alpha}] = \begin{bmatrix} \overline{\alpha}_{11} & \overline{\alpha}_{12} \\ \overline{\alpha}_{21} & \overline{\alpha}_{22} \end{bmatrix} \tag{2.107}$$

$$[\overline{\mathbb{C}}] = \begin{bmatrix} \overline{C}_{1111} & \overline{C}_{1122} & \overline{C}_{1112} \\ \overline{C}_{1122} & \overline{C}_{2222} & \overline{C}_{2212} \\ \overline{C}_{1112} & \overline{C}_{2212} & \overline{C}_{1212} \end{bmatrix} \tag{2.108}$$

$$[\overline{\mathcal{E}}] = \begin{bmatrix} \overline{\mathcal{E}}_{111} & \overline{\mathcal{E}}_{221} & \overline{\mathcal{E}}_{121} \\ \overline{\mathcal{E}}_{112} & \overline{\mathcal{E}}_{222} & \overline{\mathcal{E}}_{122} \end{bmatrix} \tag{2.109}$$

$$[\overline{\mathbb{F}}] = \begin{bmatrix} \overline{F}_{1111} & \overline{F}_{1221} & \overline{F}_{1122} & \overline{F}_{1222} & \overline{F}_{1112} & \overline{F}_{1121} \\ \overline{F}_{2111} & \overline{F}_{2221} & \overline{F}_{2122} & \overline{F}_{2222} & \overline{F}_{2112} & \overline{F}_{2121} \end{bmatrix} \tag{2.110}$$

$$[\overline{\mathbb{M}}] = \begin{bmatrix} \overline{M}_{11111} & \overline{M}_{11221} & \overline{M}_{11122} & \overline{M}_{11222} & \overline{M}_{11112} & \overline{M}_{11121} \\ \overline{M}_{22111} & \overline{M}_{22221} & \overline{M}_{22122} & \overline{M}_{22222} & \overline{M}_{22112} & \overline{M}_{22121} \\ \overline{M}_{12111} & \overline{M}_{12221} & \overline{M}_{12122} & \overline{M}_{12222} & \overline{M}_{12112} & \overline{M}_{12121} \end{bmatrix} \tag{2.111}$$

$$[\overline{\mathbb{G}}] = \begin{bmatrix} \overline{G}_{111111} & \overline{G}_{111221} & \overline{G}_{111122} & \overline{G}_{111222} & \overline{G}_{111112} & \overline{G}_{111121} \\ \overline{G}_{221111} & \overline{G}_{221221} & \overline{G}_{221122} & \overline{G}_{221222} & \overline{G}_{221112} & \overline{G}_{221121} \\ \overline{G}_{122111} & \overline{G}_{122221} & \overline{G}_{122122} & \overline{G}_{122222} & \overline{G}_{122112} & \overline{G}_{122121} \\ \overline{G}_{222111} & \overline{G}_{222221} & \overline{G}_{222122} & \overline{G}_{222222} & \overline{G}_{222112} & \overline{G}_{222121} \\ \overline{G}_{112111} & \overline{G}_{112221} & \overline{G}_{112122} & \overline{G}_{112222} & \overline{G}_{112112} & \overline{G}_{112121} \\ \overline{G}_{121111} & \overline{G}_{121221} & \overline{G}_{121122} & \overline{G}_{121222} & \overline{G}_{121112} & \overline{G}_{121121} \end{bmatrix} \tag{2.112}$$

$$[\overline{\mathbb{T}}] = \begin{bmatrix} \overline{T}_{111} & \overline{T}_{122} & \overline{T}_{112} \\ \overline{T}_{211} & \overline{T}_{222} & \overline{T}_{212} \end{bmatrix} \tag{2.113}$$

$$[\overline{\mathbb{K}}] = \begin{bmatrix} \overline{K}_{1111} & \overline{K}_{1122} & \overline{K}_{1112} \\ \overline{K}_{2211} & \overline{K}_{2222} & \overline{K}_{2212} \\ \overline{K}_{1211} & \overline{K}_{1222} & \overline{K}_{1212} \end{bmatrix} \tag{2.114}$$

$$[\overline{\mathbb{L}}] = \begin{bmatrix} \overline{L}_{1111} & \overline{L}_{1122} & \overline{L}_{1112} \\ \overline{L}_{2211} & \overline{L}_{2222} & \overline{L}_{2212} \\ \overline{L}_{1211} & \overline{L}_{1222} & \overline{L}_{1212} \end{bmatrix} \tag{2.115}$$

$$[\overline{\mathbb{H}}] = \begin{bmatrix} \overline{H}_{11111} & \overline{H}_{11221} & \overline{H}_{11122} & \overline{H}_{11222} & \overline{H}_{11112} & \overline{H}_{11121} \\ \overline{H}_{22111} & \overline{H}_{22221} & \overline{H}_{22122} & \overline{H}_{22222} & \overline{H}_{22112} & \overline{H}_{22121} \\ \overline{H}_{12111} & \overline{H}_{12221} & \overline{H}_{12122} & \overline{H}_{12222} & \overline{H}_{12112} & \overline{H}_{12121} \end{bmatrix} \tag{2.116}$$

After discretization, the local strain and electric fields defined respectively in Eqs. (2.80) and (2.81) can expressed as:

$$\varepsilon(\mathbf{x}) = \mathbf{A}^0(\mathbf{x}) : \overline{\varepsilon} + \mathbf{B}^0(\mathbf{x}) \cdot \overline{\mathbf{E}} + \{\mathbf{A}^1(\mathbf{x}) - \mathbf{A}^0(\mathbf{x}) \otimes \mathbf{x}\} \vdots \overline{\nabla\varepsilon} + \{\mathbf{B}^1(\mathbf{x}) - \mathbf{B}^0(\mathbf{x}) \otimes \mathbf{x}\} : \overline{\nabla\mathbf{E}}, \tag{2.117}$$

$$\mathbf{E}(\mathbf{x}) = \mathbf{D}^0(\mathbf{x}) : \overline{\varepsilon} + \mathbf{h}^0(\mathbf{x}) \cdot \overline{\mathbf{E}} + \{\mathbf{D}^1(\mathbf{x}) - \mathbf{D}^0(\mathbf{x}) \otimes \mathbf{x}\} \vdots \overline{\nabla\varepsilon} + \{\mathbf{h}^1(\mathbf{x}) - \mathbf{h}^0(\mathbf{x}) \otimes \mathbf{x}\} : \overline{\nabla\mathbf{E}} \tag{2.118}$$

We define the above displacement and electric fields matrices as:

$$\begin{aligned} &\mathbf{U}_u = [\mathbf{u}^1, \mathbf{u}^2, \mathbf{u}^3]; \mathbf{V}_u = [\mathbf{u}^4, \mathbf{u}^5]; \mathbf{W}_u = [\mathbf{u}^6, \mathbf{u}^7, \mathbf{u}^8, \mathbf{u}^9, \mathbf{u}^{10}, \mathbf{u}^{11}]; \\ &\mathbf{Z}_u = [\mathbf{u}^{12}, \mathbf{u}^{13}, \mathbf{u}^{14}] \end{aligned} \tag{2.119}$$

$$\begin{aligned} &\mathbf{U}_\phi = [\phi^1, \phi^2, \phi^3]; \mathbf{V}_\phi = [\phi^4, \phi^5]; \mathbf{W}_\phi = [\phi^6, \phi^7, \phi^8, \phi^9, \phi^{10}, \phi^{11}]; \\ &\mathbf{Z}_\phi = [\phi^{12}, \phi^{13}, \phi^{14}] \end{aligned} \tag{2.120}$$

Table 2.1: Elementary solution corresponding to the activated strain, electric potential and strain gradient components

Field	$(\overline{\varepsilon}_{11},\overline{\varepsilon}_{22},\overline{\varepsilon}_{12})$	$(\overline{E_1},\overline{E_2})$	$(\overline{\nabla\varepsilon}_{111},\overline{\nabla\varepsilon}_{221},\overline{\nabla\varepsilon}_{122},\overline{\nabla\varepsilon}_{222},\overline{\nabla\varepsilon}_{112},\overline{\nabla\varepsilon}_{121})$	$(\overline{\nabla E}_{11},\overline{\nabla E}_{22},\overline{\nabla E}_{12})$
$\mathbf{u}^1,\phi^1$	(1,0,0)	(0,0)	(0,0,0,0,0,0)	(0,0,0)
$\mathbf{u}^2,\phi^2$	(0,1,0)	(0,0)	(0,0,0,0,0,0)	(0,0,0)
$\mathbf{u}^3,\phi^3$	$(0,0,\frac{1}{2})$	(0,0)	(0,0,0,0,0,0)	(0,0,0)
$\mathbf{u}^4,\phi^4$	(0,0,0)	(1,0)	(0,0,0,0,0,0)	(0,0,0)
$\mathbf{u}^5,\phi^5$	(0,0,0)	(0,1)	(0,0,0,0,0,0)	(0,0,0)
$\mathbf{u}^6,\phi^6$	(0,0,0)	(0,0)	(1,0,0,0,0,0)	(0,0,0)
$\mathbf{u}^7,\phi^7$	(0,0,0)	(0,0)	(0,1,0,0,0,0)	(0,0,0)
$\mathbf{u}^8,\phi^8$	(0,0,0)	(0,0)	(0,0,1,0,0,0)	(0,0,0)
$\mathbf{u}^9,\phi^9$	(0,0,0)	(0,0)	(0,0,0,1,0,0)	(0,0,0)
$\mathbf{u}^{10},\phi^{10}$	(0,0,0)	(0,0)	(0,0,0,0,1,0)	(0,0,0)
$\mathbf{u}^{11},\phi^{11}$	(0,0,0)	(0,0)	(0,0,0,0,0,1)	(0,0,0)
$\mathbf{u}^{12},\phi^{12}$	(0,0,0)	(0,0)	(0,0,0,0,0,0)	(1,0,0)
$\mathbf{u}^{13},\phi^{13}$	(0,0,0)	(0,0)	(0,0,0,0,0,0)	(0,1,0)
$\mathbf{u}^{14},\phi^{14}$	(0,0,0)	(0,0)	(0,0,0,0,0,0)	(0,0,1)

and

$$\begin{aligned}
\mathbf{W}_u^x &= [x\mathbf{u}^1, y\mathbf{u}^1, x\mathbf{u}^2, y\mathbf{u}^2, x\mathbf{u}^3, y\mathbf{u}^3] \\
\mathbf{W}_\phi^x &= [x\phi^1, y\phi^1, x\phi^2, y\phi^2, x\phi^3, y\phi^3] \\
\mathbf{Z}_u^x &= [x\mathbf{u}^4, y\mathbf{u}^5, x\mathbf{u}^5 + y\mathbf{u}^4] \\
\mathbf{Z}_\phi^x &= [x\phi^4, y\phi^5, x\phi^5 + y\phi^4]
\end{aligned} \tag{2.121}$$

The displacement fields $\mathbf{u}^i$ and the electric potential fields ϕ^i are the vector columns containing respectively the nodal displacement and electric potentials solution of the localization problems Eq. (2.52)-(2.53)-(2.34)-(2.32) with the boundary conditions described in Table 2.1.

In terms of the above definition and finite element discretization, we obtain:

$$\mathbf{A}^0(\mathbf{x}) = \mathbf{B}_u(\mathbf{x})\mathbf{U}_u; \quad \mathbf{B}^0(\mathbf{x}) = \mathbf{B}_u(\mathbf{x})\mathbf{V}_u; \quad \mathbf{B}^1(\mathbf{x}) = \mathbf{B}_u(\mathbf{x})\mathbf{Z}_u \tag{2.122}$$

$$\mathbf{A}^1(\mathbf{x}) = \mathbf{B}_u(\mathbf{x})\mathbf{W}_u; \quad \mathbf{A}_x^0(\mathbf{x}) = \mathbf{B}_u(\mathbf{x})\mathbf{W}_u^x; \quad \mathbf{B}_x^0(\mathbf{x}) = \mathbf{B}_u(\mathbf{x})\mathbf{Z}_u^x \tag{2.123}$$

$$\mathbf{D}^0(\mathbf{x}) = -\mathbf{B}_\phi(\mathbf{x})\mathbf{U}_\phi; \quad \mathbf{h}^0(\mathbf{x}) = -\mathbf{B}_\phi(\mathbf{x})\mathbf{V}_\phi; \quad \mathbf{h}^1(\mathbf{x}) = -\mathbf{B}_\phi(\mathbf{x})\mathbf{Z}_\phi \tag{2.124}$$

$$\mathbf{D}^1(\mathbf{x}) = -\mathbf{B}_\phi(\mathbf{x})\mathbf{W}_\phi; \quad \mathbf{D}_x^0(\mathbf{x}) = -\mathbf{B}_\phi(\mathbf{x})\mathbf{W}_\phi^x; \quad \mathbf{h}_x^0(\mathbf{x}) = -\mathbf{B}_\phi(\mathbf{x})\mathbf{Z}_\phi^x \tag{2.125}$$

and

$$\tilde{\mathbf{A}}^1(\mathbf{x}) = \mathbf{A}^1(\mathbf{x}) - \mathbf{A}_x^0(\mathbf{x}); \quad \tilde{\mathbf{B}}^1(\mathbf{x}) = \mathbf{B}^1(\mathbf{x}) - \mathbf{B}_x^0(\mathbf{x}) \tag{2.126}$$

$$\tilde{\mathbf{D}}^1(\mathbf{x}) = \mathbf{D}^1(\mathbf{x}) - \mathbf{D}_x^0(\mathbf{x}); \quad \tilde{\mathbf{h}}^1(\mathbf{x}) = \mathbf{h}^1(\mathbf{x}) - \mathbf{h}_x^0(\mathbf{x}) \tag{2.127}$$

By introducing Eqs. (2.122)-(2.127) into Eqs. (2.86)-(2.95), we can obtain the discretization forms of the effective tensors.

$$[\overline{\mathbb{C}}] = \langle (\mathbf{A}^0)^T[\mathbf{C}]\mathbf{A}^0 - 2(\mathbf{A}^0)^T[\mathcal{E}]\mathbf{D}^0 - (\mathbf{D}^0)^T[\boldsymbol{\alpha}]\mathbf{D}^0 \rangle \tag{2.128}$$

$$[\overline{\boldsymbol{\alpha}}] = \langle -(\mathbf{B}^0)^T[\mathbf{C}]\mathbf{B}^0 + 2(\mathbf{h}^0)^T[\mathcal{E}]\mathbf{B}^0 + (\mathbf{h}^0)^T[\boldsymbol{\alpha}]\mathbf{h}^0 \rangle \tag{2.129}$$

$$[\overline{\mathcal{E}}] = \langle -(\mathbf{A}^0)^T[\mathbf{C}]\mathbf{B}^0 + (\mathbf{A}^0)^T[\mathcal{E}]\mathbf{h}^0 + (\mathbf{D}^0)^T[\mathcal{E}]\mathbf{B}^0 + (\mathbf{D}^0)^T[\boldsymbol{\alpha}]\mathbf{h}^0 \rangle \tag{2.130}$$

$$[\overline{\mathbb{F}}] = \langle (\mathbf{B}^0)^T[\mathbf{C}]\tilde{\mathbf{A}}^1 - (\mathbf{h}^0)^T[\mathcal{E}]\tilde{\mathbf{A}}^1 - (\mathbf{B}^0)^T[\mathcal{E}]\tilde{\mathbf{D}}^1 - (\mathbf{h}^0)^T[\boldsymbol{\alpha}]\tilde{\mathbf{D}}^1 \rangle \tag{2.131}$$

$$[\overline{\mathbb{M}}] = \langle (\mathbf{A}^0)^T[\mathbf{C}]\tilde{\mathbf{A}}^1 - (\mathbf{D}^0)^T[\mathcal{E}]\tilde{\mathbf{A}}^1 - (\mathbf{A}^0)^T[\mathcal{E}]\tilde{\mathbf{D}}^1 - (\mathbf{D}^0)^T[\boldsymbol{\alpha}]\tilde{\mathbf{D}}^1 \rangle \tag{2.132}$$

$$[\overline{\mathbb{G}}] = \langle (\tilde{\mathbf{A}}^1)^T[\mathbf{C}]\tilde{\mathbf{A}}^1 - 2(\tilde{\mathbf{D}}^1)^T[\mathcal{E}]\tilde{\mathbf{A}}^1 - (\tilde{\mathbf{D}}^1)^T[\boldsymbol{\alpha}]\tilde{\mathbf{D}}^1 \rangle \tag{2.133}$$

$$[\overline{\mathbb{T}}] = \langle (\mathbf{B}^0)^T[\mathbf{C}]\tilde{\mathbf{B}}^1 - (\mathbf{h}^0)^T[\mathcal{E}]\tilde{\mathbf{B}}^1 - (\mathbf{B}^0)^T[\mathcal{E}]\tilde{\mathbf{h}}^1 - (\mathbf{h}^0)^T[\boldsymbol{\alpha}]\tilde{\mathbf{h}}^1 \rangle \tag{2.134}$$

$$[\overline{\mathbb{K}}] = \langle -(\mathbf{A}^0)^T[\mathbf{C}]\tilde{\mathbf{B}}^1 + (\mathbf{D}^0)^T[\mathcal{E}]\tilde{\mathbf{B}}^1 + (\mathbf{A}^0)^T[\mathcal{E}]\tilde{\mathbf{h}}^1 + (\mathbf{D}^0)^T[\boldsymbol{\alpha}]\tilde{\mathbf{h}}^1 \rangle \tag{2.135}$$

$$[\overline{\mathbb{L}}] = \langle (\tilde{\mathbf{B}}^1)^T[\mathbf{C}]\tilde{\mathbf{B}}^1 - 2(\tilde{\mathbf{h}}^1)^T[\mathcal{E}]\tilde{\mathbf{B}}^1 - (\tilde{\mathbf{h}}^1)^T[\boldsymbol{\alpha}]\tilde{\mathbf{h}}^1 \rangle \tag{2.136}$$

$$[\overline{\mathbb{H}}] = \langle -(\tilde{\mathbf{B}}^1)^T[\mathbf{C}]\tilde{\mathbf{A}}^1 + (\tilde{\mathbf{B}}^1)^T[\mathcal{E}]\tilde{\mathbf{D}}^1 + (\tilde{\mathbf{h}}^1)^T[\mathcal{E}]\tilde{\mathbf{A}}^1 + (\tilde{\mathbf{h}}^1)^T[\boldsymbol{\alpha}]\tilde{\mathbf{D}}^1 \rangle \tag{2.137}$$

2.4 Numerical examples

2.4.1 Direct flexoelectricity of composite with piezoelectric phases

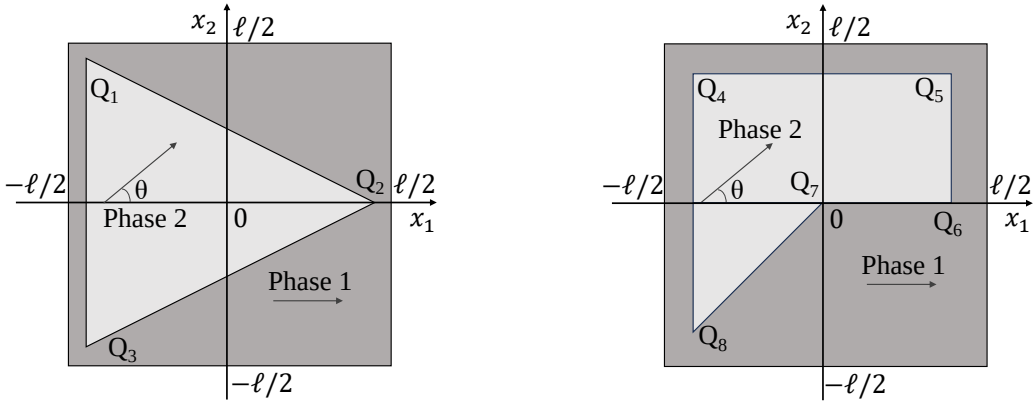

(a) (b)

Figure 2.3: Unit cell with: (a) triangular inclusion; (b) asymmetric inclusion.

In this first example, we investigate the effective flexoelectric properties of a two-phase periodic composite comprised of piezoelectric materials. The Representative Volume Elements

(RVEs) are constructed using periodic unit cells. The RVEs with two distinct geometric inclusions are examined: one featuring triangular inclusion (Fig. 2.3(a)) and another exhibiting a fully asymmetric design as illustrated in Fig. 2.3(b). The geometric description of the different inclusions in Fig. 2.3 is given as: $Q_1 = (-a\ell, a\ell)$, $Q_2 = (a\ell, 0)$, $Q_3 = (-a\ell, -a\ell)$, $Q_4 = (-b\ell, b\ell)$, $Q_5 = (b\ell, b\ell)$, $Q_6 = (b\ell, 0)$, $Q_7 = (0,0)$, and $Q_8 = (-b\ell, -b\ell)$. Here, the parameters $a = \sqrt{0.8}/2$ and $b = 0.4$ are selected such that the inclusions of both unit cells are of the same volume fraction $f = 0.4$. Both geometries are chosen to confine symmetrical number, thereby enhancing the influence of gradient effects. The RVE is assumed to be composed of $N \times N$ periodic unit cells, and the length of the RVE is $L = N\ell$, where $\ell = 1$mm.

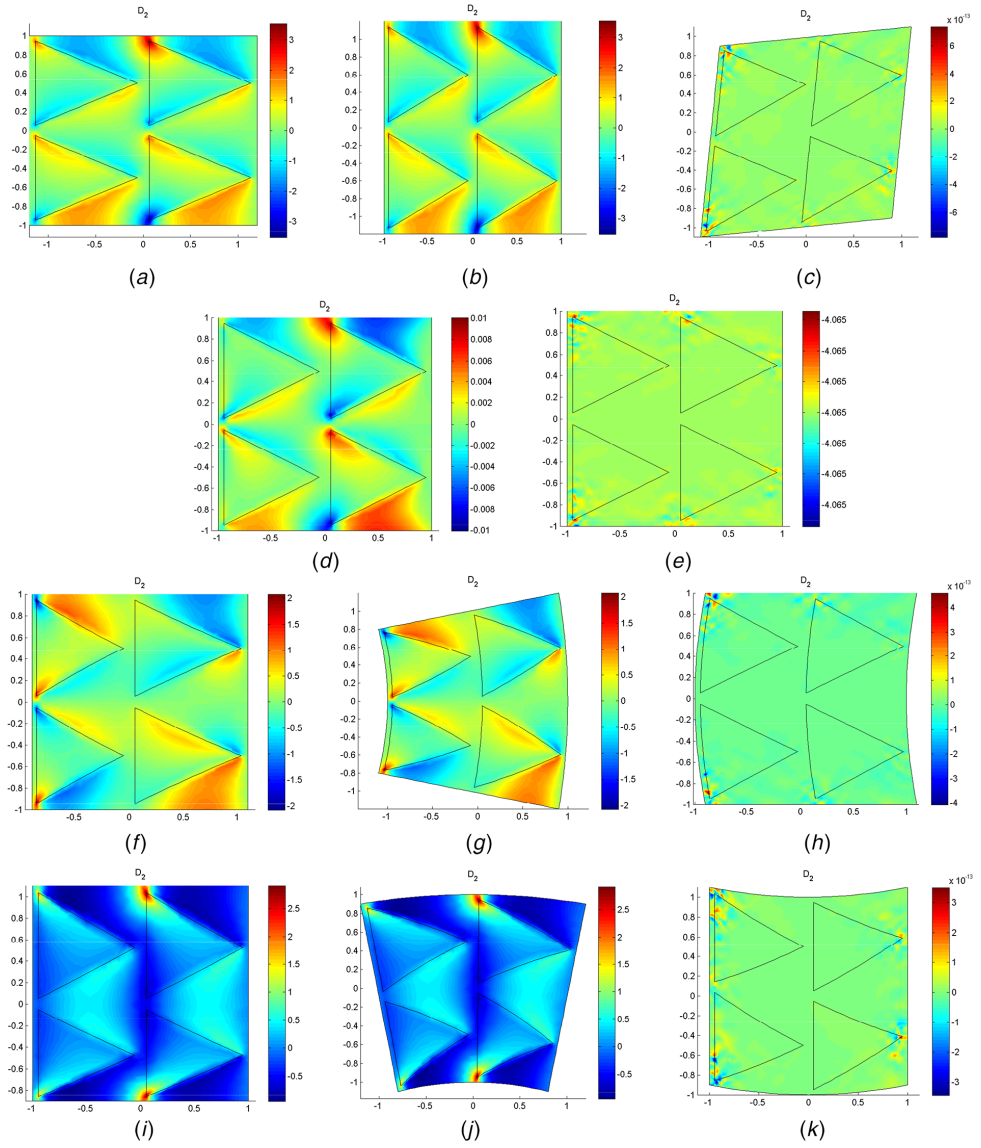

Figure 2.4: $d_2(x)$ electric displacement field in deformed ($\times 0.2$) configurations for RVE with triangular inclusions: (a) $\overline{\varepsilon} = [1;0;0]$, $\overline{\nabla\varepsilon} = 0$, $\overline{E} = 0$; (b) $\overline{\varepsilon} = [0;1;0]$, $\overline{\nabla\varepsilon} = 0$, $\overline{E} = 0$; (c) $\overline{\varepsilon} = [0;0;1]$, $\overline{\nabla\varepsilon} = 0$, $\overline{E} = 0$; (d) $\overline{\varepsilon} = 0$, $\overline{\nabla\varepsilon} = [1;0;0;0;0;0]$, $\overline{E} = 0$; (e) $\overline{\varepsilon} = 0$, $\overline{\nabla\varepsilon} = [0;1;0;0;0;0]$, $\overline{E} = 0$; (f) $\overline{\varepsilon} = 0$, $\overline{\nabla\varepsilon} = [0;0;1;0;0;0]$, $\overline{E} = 0$; (g) $\overline{\varepsilon} = 0$, $\overline{\nabla\varepsilon} = [0;0;0;1;0;0]$, $\overline{E} = 0$; (h) $\overline{\varepsilon} = 0$, $\overline{\nabla\varepsilon} = [0;0;0;0;1;0]$, $\overline{E} = 0$; (i) $\overline{\varepsilon} = 0$, $\overline{\nabla\varepsilon} = [0;0;0;0;0;1]$, $\overline{E} = 0$; (j) $\overline{\varepsilon} = 0$, $\overline{\nabla\varepsilon} = 0$, $\overline{E} = [1;0]$; (k) $\overline{\varepsilon} = 0$, $\overline{\nabla\varepsilon} = 0$, $\overline{E} = [0;1]$.

It is assumed that both phases consist of the same piezoelectric material, but there is a rotation mismatch between the main directions of the crystal in two phases by an angle θ. Thus, the different mechanical, dielectric, and piezoelectric tensors are assumed to be completely anisotropic, which results in a material heterogeneity. The matrix (phase 1 in Fig. 2.3)

is supposed filled by a transversely anisotropic ceramic (lead zirconium titanate) whereby an orientation of the piezoelectric crystal main direction is along x_1. The material parameters are given in (2.138)-(2.140) in 2D form.

$$[\mathbf{C}^1] = \begin{bmatrix} 131.39 & 83.237 & 0 \\ 83.237 & 154.837 & 0 \\ 0 & 0 & 35.8 \end{bmatrix} (\text{GPa}), \tag{2.138}$$

$$[\boldsymbol{\alpha}^1] = \begin{bmatrix} 2.079 & 0 \\ 0 & 4.065 \end{bmatrix} (\text{nC} \cdot \text{m}^{-1} \cdot \text{V}^{-1}), \tag{2.139}$$

$$[\mathcal{E}^1] = \begin{bmatrix} -2.120582 & -2.120582 & 0 \\ 0 & 0 & 0 \end{bmatrix} (\text{C} \cdot \text{m}^{-2}). \tag{2.140}$$

The main orientation of crystal in the inclusion differs from that of the matrix phase by an angle of θ, thus the properties of the inclusion are defined according to

$$\alpha^2_{ij} = R_{ip} R_{jq} \alpha^1_{pq} \tag{2.141}$$

$$e^2_{ijk} = R_{ip} R_{jq} R_{kr} e^1_{pqr} \tag{2.142}$$

$$C^2_{ijkl} = R_{ip} R_{jq} R_{kr} R_{ls} C^1_{pqrs} \tag{2.143}$$

with the rotation matrix:

$$R = \begin{bmatrix} \cos(\theta) & -\sin(\theta) \\ \sin(\theta) & \cos(\theta) \end{bmatrix} \tag{2.144}$$

For illustration, the local electric displacement states in the deformed configurations corresponding to the elementary loads are depicted in Fig. 2.4. We proceed to examine the convergence of the effective flexoelectric properties concerning the number of unit cells N along each direction within the RVE. The triangular unit cell (Fig. 2.3(a)) is chosen here and the mismatch angle $\theta = \pi$. Results for the components F_{1221} and F_{2112} are provided in Fig. 2.5. We can observe a rapid convergence of the effective flexoelectric properties as the number of unit cells increases.

Next, we only compute the evolution of the coefficients F_{1221}, F_{2221}, F_{1112} and F_{2112} with respect to the mismatch angle for both triangular and asymmetric unit cells, due to these coefficients represent the polarization induced by bending. Other coefficients are associated with polarization induced by more intricate strain gradient modes, which can be challenging to practically acquire.

From Fig. 2.6(a) (triangular unit cell), our first observation is that, when $\theta = 0$ (representing a homogeneous medium), the flexoelectric effects naturally vanish as expected. In this scenario, the components F_{1221} and F_{2112} reach their maximum values when $\theta = \pi$, aligning both crystal phases in the same main direction but with coefficients of opposite signs. Conversely, the other components F_{2221} and F_{1112} exhibit significantly smaller values in comparison to F_{1221} and F_{2112}, displaying local minima. Moving on to Fig. 2.6(b) (asymmetric unit cell), we note that the components F_{1221} and F_{2112} exhibit two extrema, with F_{1221} reaching its maximum at approximately $\theta \approx 1.2\pi$.

Comparing the two cases, we observe a noteworthy difference in the maximum value of the coefficient F_{2112}, which signifies the change in polarization along the x_2 direction induced by bending around an out-of-plane axis x_3 (illustrated in Fig. 2.4(j)). Specifically, the triangular inclusion exhibits a higher value of 0.124×10^{-3} C/m, surpassing the 0.090×10^{-3} C/m found in the asymmetric case. This comparison illustrates the potential for a significant increase in flexoelectric effects by judiciously selecting a directional mismatch between crystal orientations and shapes. Additionally, it is noteworthy that these obtained values are considerably higher when compared to naturally occurring flexoelectric materials like $BaTiO_3$, whose flexoelectric coefficients typically fall within the order of 10^{-5} C/m.

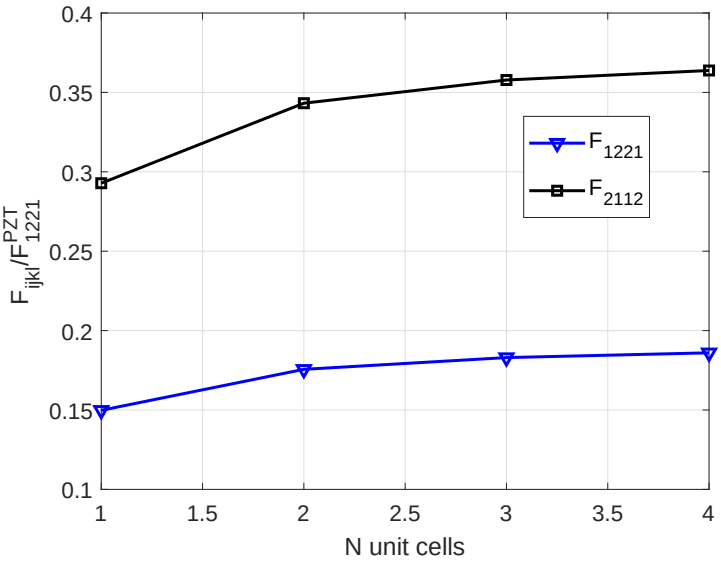

Figure 2.5: Convergence of effective flexoelectric properties with the number of unit cells in the RVE

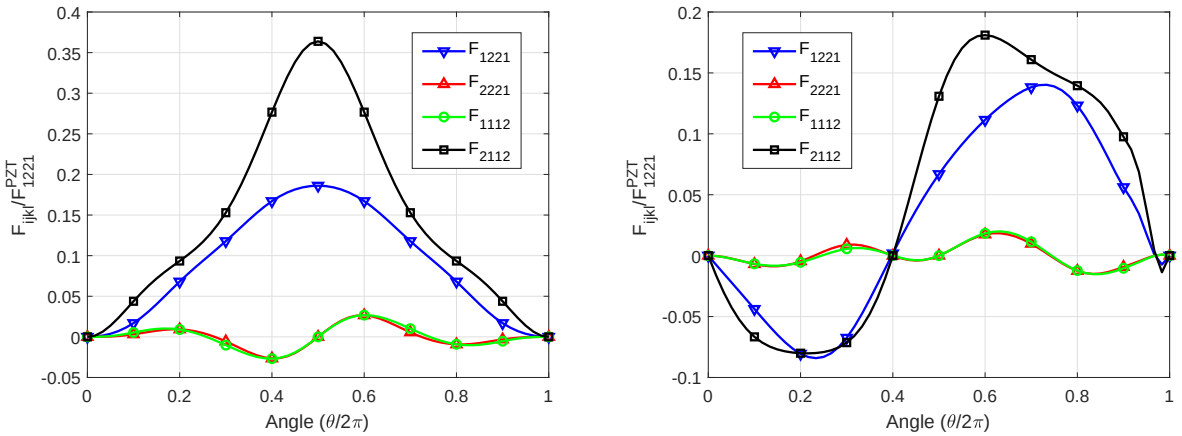

Figure 2.6: (a) Evolution of effective flexoelectric components with respect to the mismatch angle for the RVE with: (a) triangular inclusions and (b) asymmetric inclusions.

2.4.2 Converse flexoelectricity of composite with piezoelectric phases

In this example, we investigate the significance of the converse flexoelectric and other higher order electromechanical coupling terms in a piezoelectric composite. Only the RVE with triangular inclusion (depicted in Fig. 2.3 (a)) is considered. Each phase is made of PZT (lead zirconium titanate ceramics), but the main orientation of the crystal in both phase is rotated by a mismatch angle $\theta \in [0, 2\pi]$ to create a heterogeneity. The mechanical, dielectric and piezoelectric properties of the PZT matrix phase are same as the previous example and given in (2.138)-(2.140). Similarly, the inclusion phases are obtained by the material rotation formula (2.141)-(2.144).

In Fig. 2.7(a), we compute the evolution of the components of the converse flexoelectric tensor $\overline{\mathbb{K}}$ with respect to the mismatch angle θ. The values are normalized with respect to the flexoelectric component F_{1221} of PZT to evaluate their significance. We can notice that the components $\overline{K}_{1111}$, $\overline{K}_{1112}$, $\overline{K}_{2211}$ and $\overline{K}_{1212}$ are of the same order (or higher) than the direct flexoelectric coefficients of its constituents for almost all mismatch angles. The components

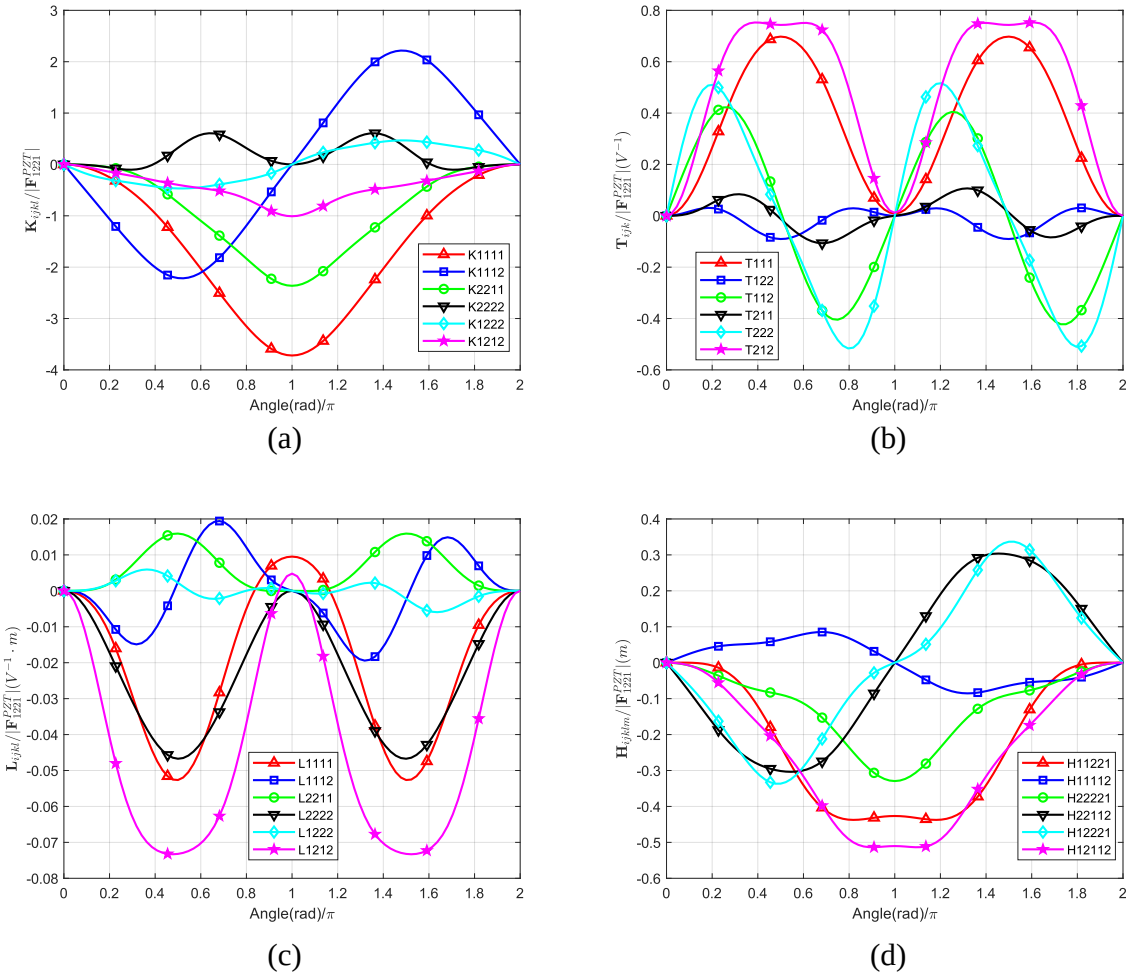

Figure 2.7: Evolution of the components of the effective converse flexoelectric tensor $\overline{\mathbb{K}}$ and of higher order electromechanical coupling term $\overline{\mathbb{T}}$, $\overline{\mathbb{L}}$ and $\overline{\mathbb{H}}$ with respect to the mismatch angle in the piezoelectric composite with triangular inclusions: (a) $\overline{\mathbb{K}}$; (b) $\overline{\mathbb{T}}$; (c) $\overline{\mathbb{L}}$; (d) $\overline{\mathbb{H}}$.

$\overline{K}_{1111}$, $\overline{K}_{2211}$ and $\overline{K}_{1212}$ exhibit an extremum of 0.1860×10^{-3} C $\cdot$ m^{-1}, 0.1181×10^{-3} C $\cdot$ m^{-1} and 0.0504×10^{-3} C $\cdot$ m^{-1}, respectively around $\theta = \pi$, while for $\overline{K}_{1112}$ this extremum is 0.111×10^{-3} C $\cdot$ m^{-1} around $\theta = \frac{\pi}{2}, \frac{3\pi}{2}$. These results clearly demonstrate that the converse flexoelectric coefficients in piezoelectric composites can make an important contribution to the electromechanical response of the structure and cannot be ignored.

The evolution of the components of the other higher order electromechanical terms $\overline{\mathbb{T}}$, $\overline{\mathbb{L}}$ and $\overline{\mathbb{H}}$ with respect to the mismatch angle θ are computed and shown in Figs. 2.7(b), 2.7(c) and 2.7(d), respectively. Here again, these values are normalized with respect to the flexoelectric properties of PZT to evaluate their significance. The extremum of components $\overline{T}_{111}$, $\overline{T}_{222}$, $\overline{T}_{112}$ and $\overline{T}_{212}$ are comparable to the direct flexoelectric coefficient of PZT. For $\overline{\mathbb{H}}$, the extrema of the components $\overline{H}_{11221}$ $\overline{H}_{12112}$ $\overline{H}_{22112}$ and $\overline{H}_{12221}$ are close to the half of the direct flexoelectric coefficient of PZT. However, the effective tensor $\overline{\mathbb{L}}$ has much smaller components values as compared to local flexoelectric properties and only plays a negligible role here. Therefore, these results demonstrate that the higher order electromechanical terms $\overline{\mathbb{H}}$ and $\overline{\mathbb{T}}$ can make a significant contribution to the electromechanical response of piezoelectric composites. More specifically, the coefficients $\overline{T}_{ijk}$ are associated with additional polarization/electric displacement induced by the electric field gradient, and thus characterize the importance of these additional effects on the flexoelectric behavior. Taking these new terms into account in the modeling and simulation of flexoelectric structures may help to design new flexoelectric-based

sensors and actuators based on the mechanical and electrical gradient effects.

2.5 Conclusion

In this chapter, we have proposed a computational homogenization framework for composites made of piezoelectric phases and having an apparent flexoelectric behavior. The effective model takes into account both direct and converse flexoelectric effects, as well as all other higher order electromechanical coupling terms related to electric and electric gradient fields. In contrast to previous works, the present framework allows evaluating the full anisotropic direct and converse flexoelectric tensors and all other higher order electromechanical coupling tensors associating with electric and electric gradient fields, by means of finite element numerical calculations over RVEs, and this for morphologies of phases having arbitrary local geometries. Additionally, we have devised an effective mechanical and electric body forces correction which goal is to eliminate the spurious effects that were inherent in strain gradient and electric gradient numerical homogenization schemes.

Numerical investigations have been conducted to evaluate the evolution of direct and converse flexoelectric coefficients with regards to the local material properties and geometry of the composite phases. The results show that the apparent converse flexoelectric coefficients in a composite made of periodic triangular inclusions have the same order of magnitude as the direct flexoelectric properties of the local constituents. We demonstrate that a significant enhancement in flexoelectric effects can be achieved by appropriately selecting a mismatch in crystal directions and shapes, showing the potential of the approach for optimization-based design of efficient flexoelectric systems and concomitant applications in fields such as energy harvesting, sensors and actuators etc, that will be discussed in the next chapters. Furthermore, we have shows that the other higher order coupling terms, i.e., that relate the electric field to an applied electric field gradient and the strain gradient (bending) to the electric field gradient have non-negligible values as compared to the flexoelectric coefficients, and can make a significant contribution to the electromechanical response of piezoelectric composites.

Chapter 3

Dynamic analysis of flexoelectric effects in complex geometric structures

In materials or composites with an effective flexoelectric response, a polarization can be induced by local strain gradients. In general, these effects are small in the static regime. However, larger effects may be induced by dynamic loads, and can be used in energy harvesters converting mechanical vibrations into electrical energy. In this chapter, we developed an isogeometric analysis (IGA) framework to solve the dynamic response of flexoelectric energy harvesters for arbitrary geometries, in the frequency domain, including strain gradient inertial effects. As compared to the previous related works available in the literature, the IGA discretization is proposed here for the first time to solve dynamic flexoelectric problems in the frequency domain. The conditions of both open and close-circuits are formulated. The numerical methodology is used to evaluate the sensitivity of different parameters such as load resistors, flexoelectric coefficients and dynamic scale parameter on the frequency response of output voltage, power and displacements of a beam-like structure with structural geometrical features, to evaluate the potential of the proposed IGA approach, and its advantages for h- and p-refinements when considering complex geometries.

Isogeometric analysis offers an effective and flexible method for achieving high-smoothness approximations, which guarantee C^1 continuity of the physical domain to tackle the 4th-order flexoelectric partial differential equations. However, the tensor product structure of the parameter space of a patch makes it poorly suited for representing complex, multiple connected domains. These multi-patch constructions in isogeometric analysis are at most C^0-continuity. To construct C^1-continuity among patch common interfaces, the concept of geometric continuity of surfaces is introduced. The C^1-continuity of isogeometric functions is achieved by ensuring that their geometric smoothness of the same order as that of their graph surfaces. We present the construction of a C^1 continuous isogeometric functions for multi-patch domains based on the approaches of [196, 197, 198]. Finally, a beam with 4 circular voids, comprised of 18 patches, is fabricated to ensure C^1 continuity. The dynamic effects of the beam with flexoelectricity are also examined. A part of this chapter is adapted from our published article [107].

3.1 Static flexoelectricity

The equations governing the static flexoelectric equilibrium are first reviewed. An open domain $\Omega \subset \mathbb{R}^2$ is considered, with boundary $\partial\Omega$. The boundary is composed of Dirichlet and Neumann parts, which are denoted by $\partial\Omega_u$ and $\partial\Omega_t$ for the displacement problem, respectively, and $\partial\Omega_\phi$ and $\partial\Omega_D$ for the electric problem, respectively, such as $\partial\Omega_u \cup \partial\Omega_t = \partial\Omega$, $\partial\Omega_u \cap \partial\Omega_t = \emptyset$ and $\partial\Omega_\phi \cup \partial\Omega_D = \partial\Omega$, $\partial\Omega_\phi \cap \partial\Omega_D = \emptyset$. In the following, bold symbols denote vectors or tensors, while non-bold symbols denote scalars or tensor components.

The electric enthalpy density h^* of a linear electromechanical system, where piezoelectricity

and flexoelectricity are both taken into account, is expressed by [15, 98, 199]:

$$h^* = \frac{1}{2}\mathbb{C}_{ijkl}\varepsilon_{ij}\varepsilon_{kl} - \frac{1}{2}\alpha_{ij}E_iE_j - e_{ijk}E_k\varepsilon_{ij} - \mu_{ijkl}E_i\nabla\varepsilon_{jkl} + \frac{1}{2}\mathbb{G}_{ijklmn}\nabla\varepsilon_{ijk}\nabla\varepsilon_{lmn} \tag{3.1}$$

In Eq. (3.1), $\mathbb{C}$, $\boldsymbol{\alpha}$ and $\mathbf{e}$ denote the fourth-order elastic, second-order dielectric and third-order piezoelectric tensors, respectively, $\boldsymbol{\mu}$ denotes the fourth-order flexoelectric tensor, while $\mathbb{G}$ is the sixth-order strain gradient elastic tensor. Note that in this chapter, for the sake of simplicity, we did not include converse flexoelectric terms. The reader can refer to Chapter 2 for the complete converse flexoelectric model.

The strain tensor ε, the strain-gradient tensor $\nabla\varepsilon$ and the electric field vector $\mathbf{E}$ are defined in (2.35)-(2.37) of Chapter 2.

Then the constitutive equations are obtained by:

$$\sigma_{ij} = \frac{\partial h^*}{\partial \varepsilon_{ij}} = \mathbb{C}_{ijkl}\varepsilon_{kl} - e_{kij}E_k \tag{3.2}$$

$$d_i = -\frac{\partial h^*}{\partial E_i} = \alpha_{ij}E_j + e_{ijk}\varepsilon_{jk} + \mu_{ijkl}\nabla\varepsilon_{jkl} \tag{3.3}$$

$$\tau_{ijk} = \frac{\partial h^*}{\partial \nabla\varepsilon_{ijk}} = \mathbb{G}_{ijklmn}\nabla\varepsilon_{lmn} - \mu_{ijkl}E_l \tag{3.4}$$

where the $\boldsymbol{\sigma}$, $\mathbf{d}$ and $\boldsymbol{\tau}$ denote stress, electric displacement and hyperstress tensors, respectively. The equations of the dielectric problem without free charge and mechanical problem without body force are given by [24]

$$d_{i,i} = 0 \text{ in } \Omega \tag{3.5}$$

$$\sigma_{ij,j} - \tau_{ijk,jk} = 0 \text{ in } \Omega \tag{3.6}$$

The problem is completed by boundary conditions for the electric problem as

$$\phi = \phi^d \text{ on } \partial\Omega_\phi \tag{3.7}$$

$$d_i n_i = -D_n^d \text{ on } \partial\Omega_D \tag{3.8}$$

where ϕ^d and D_n^d are the prescribed electric potential and surface charge density and $\mathbf{n}$ is the unitary normal vector to the boundary $\partial\Omega$. The mechanical boundary conditions are given by (see e.g. [98]):

$$u_i = u_i^d \text{ on } \partial\Omega_u \tag{3.9}$$

$$t_k = n_j\left(\sigma_{jk} - \tau_{ijk,i}\right) - D_j\left(n_i\tau_{ijk}\right) = F_k^d \text{ on } \partial\Omega_t \tag{3.10}$$

where $\mathbf{u}^d$ and $\mathbf{F}^d$ are the prescribed mechanical displacements and tractions, and $D_j(.) = \frac{\partial(.)}{\partial x_j} - n_j n_q \frac{\partial(.)}{\partial x_q}$. Due to strain gradients, additional boundary conditions are considered:

$$u_{i,j}n_j = v_i^d \text{ on } \partial\Omega_v \tag{3.11}$$

$$n_i n_j \tau_{ijk} = r_k^d \text{ on } \partial\Omega_r \tag{3.12}$$

with $\partial\Omega_v \cup \partial\Omega_r = \partial\Omega$, $\partial\Omega_v \cap \partial\Omega_r = \emptyset$. Here, we assume natural boundary conditions on $\partial\Omega_v$ and $\partial\Omega_r$, i.e. $\mathbf{v}^d = \mathbf{r}^d = 0$.

3.2 Dynamic flexoelectricity

The total electric enthalpy H, the kinetic energy K, the Rayleigh dissipation $\tilde{R}$ and the external work W^{ext} are expressed by [98, 200] .

$$H = \int_{\Omega} h^{*} \mathrm{d}\Omega \tag{3.13}$$

$$K = \int_{\Omega} \{\frac{1}{2}\rho \dot{u}_i \dot{u}_i + \frac{1}{2}\ell_d^2 \dot{u}_{i,j}\dot{u}_{i,j}\}\mathrm{d}\Omega \tag{3.14}$$

$$\tilde{R} = \int_{\Omega} \frac{1}{2} V_{ij}\dot{u}_i \dot{u}_j \mathrm{d}\Omega \tag{3.15}$$

$$W^{ext} = \int_{\partial\Omega_t} F_i^d u_i \mathrm{d}S - \int_{\partial\Omega_D} D_n^d \phi \mathrm{d}S \tag{3.16}$$

Above, ρ is the density, $\dot{(.)}$ indicates time derivative, ℓ_d is dynamic scaling parameter (micro inertia characteristic length). The term $\ell_d^2 \dot{u}_{i,j}\dot{u}_{i,j}$ is a dynamic term associated with the strain gradient problem [200, 201] and $\mathbf{V}$ denotes viscous damping coefficients. Let us group all unknown quantities, respectively the displacement vector $\mathbf{u}$ and the potential ϕ in a vector $\mathbf{q}$. From the Hamilton's principle, the following Lagrangian equations are obtained, taking into account dissipation due to viscous damping terms:

$$\frac{\mathrm{d}}{\mathrm{d}t}\left(D_{\delta\dot{\mathbf{q}}}L\right) - D_{\delta\mathbf{q}}L + D_{\delta\dot{\mathbf{q}}}R = W^{ext} \tag{3.17}$$

where $D_{\delta\mathbf{v}}f(\mathbf{u})$ is the directional derivative, expressed by

$$D_{\delta\mathbf{v}}f(\mathbf{u}) = \left[\frac{\mathrm{d}f(\mathbf{u}+\alpha\delta\mathbf{v})}{\mathrm{d}\alpha}\right]_{\alpha=0} \tag{3.18}$$

and $D_{\mathbf{q}} = D_{\delta\mathbf{u}} + D_{\delta\phi}$, $D_{\dot{\mathbf{q}}} = D_{\delta\dot{\mathbf{u}}}$ and

$$L = K - H \tag{3.19}$$

We have, using (3.14):

$$D_{\dot{\mathbf{q}}}L = D_{\dot{\mathbf{u}}}L = \int_{\Omega} D_{\dot{\mathbf{u}}}K\mathrm{d}\Omega = \int_{\Omega} \{\rho\dot{u}_i\delta\dot{u}_i + \ell_d^2\dot{u}_{i,j}\delta\dot{u}_{i,j}\}\mathrm{d}\Omega \tag{3.20}$$

Then,

$$\frac{\mathrm{d}}{\mathrm{d}t}\left(D_{\dot{\mathbf{q}}}L\right) = \int_{\Omega} \{\rho\ddot{u}_i\delta\dot{u}_i + \ell_d^2\ddot{u}_{i,j}\delta\dot{u}_{i,j}\}\mathrm{d}\Omega \tag{3.21}$$

and

$$D_{\delta L} = -D_{\delta \mathbf{u}} H - D_{\delta \phi} H \quad . \tag{3.22}$$

We have, using (3.1)-(3.13):

$$D_{\delta \mathbf{u}} H = \int_{\Omega} \{ \mathbb{C}_{ijkl} \varepsilon_{ij} \delta \varepsilon_{kl} - e_{ijk} \delta \varepsilon_{ij} E_k - \mu_{ijkl} E_i \delta \nabla \varepsilon_{jkl} + \mathbb{G}_{ijklmn} \nabla \varepsilon_{ijk} \delta \nabla \varepsilon_{lmn} \} \mathrm{d}\Omega \tag{3.23}$$

$$D_{\delta \phi} H = \int_{\Omega} \{ \alpha_{ij} E_i \delta \phi_{,j} + e_{ijk} \varepsilon_{ij} \delta \phi_{,k} + \mu_{ijkl} \delta \phi_{,i} \nabla \varepsilon_{jkl} \} \mathrm{d}\Omega \tag{3.24}$$

and

$$D_{\delta \dot{\mathbf{q}}} \tilde{R} = D_{\delta \dot{\mathbf{u}}} \tilde{R} = \int_{\Omega} V_{ij} \dot{u}_i \delta u_j \mathrm{d}\Omega \tag{3.25}$$

We finally obtain the weak forms:

$$\int_{\Omega} \{ \sigma_{ij} \delta \varepsilon_{ij} + \tau_{ijk} \delta \nabla \varepsilon_{ijk} + \rho \ddot{u}_i \delta u_i + \ell_d^2 \ddot{u}_{i,j} \delta u_{i,j} + V_{ij} \dot{u}_i \delta u_j \} \mathrm{d}\Omega = \int_{\partial \Omega_t} F_i^d \delta u_i \mathrm{d}S \tag{3.26}$$

$$\int_{\Omega} d_i \delta \phi_{,i} \mathrm{d}\Omega = \int_{\partial \Omega_D} D_n^d \delta \phi \mathrm{d}S \tag{3.27}$$

with $\delta \varepsilon_{ij} = \frac{1}{2} \left(\delta u_{i,j} + \delta u_{j,i} \right)$ and $\delta \nabla \varepsilon_{ijk} = \frac{1}{2} \left(\delta u_{i,jk} + \delta u_{j,ik} \right)$.

3.3 IGA discretization of dynamic flexoelectric equations

3.3.1 Concepts of IsoGeometric Analysis (IGA)

The flexoeoectric problem requires at least C^1 continuity of displacement fields due to the strain gradient terms in (3.26). Different approaches have been proposed in the literature, as described in the introduction. In this work, we use Isogeometric Analysis (IGA) [103] for the discretization of the dynamic flexoelectric problem in the frequency domain. In isogeometric analysis, the NURBS (Non-Uniform Rational B-Spline) are used to construct curves, surface and solid, and NURBS basis functions are employed to approximate the physical fields like the displacements (see e.g. [103, 202, 203]). The geometry and physical field construction of NURBS surfaces is illustrated in Fig. 3.1.

The fundamental concept of Isogeometric Analysis is the utilization of NURBS not only as a technology for discretizing geometry but also as a tool for discretizing the analysis. NURBS are built from B-splines. To construct a B-spline, a knot vector in one dimension must be specified and is defined as a non-decreasing set of parameter values $\boldsymbol{\xi} = \{\xi_1, \xi_2, ..., \xi_{n+p+1}\}$, where $\xi_i \in \mathbb{R}$ is i-th knot index, p is the polynomial order, and n is the number of basis function. The knot vector partitions the parameter space into intervals usually referred to as knot spans. Knot vectors can be uniform when knots are evenly distributed in the parameter space. Conversely they become non-uniform when the spacing of knots is non-uniform. Knot values may be repeated, and the repeated number of a particular knot value is referred to as a knot with a certain multiplicity k. Typically, an open knot vector is utilized where its first and last knots appear $k = p + 1$ times.

B-Spline basis functions are recursively defined using the Cox-de Boor formula [204] and start with piecewise constants functions ($p = 0$):

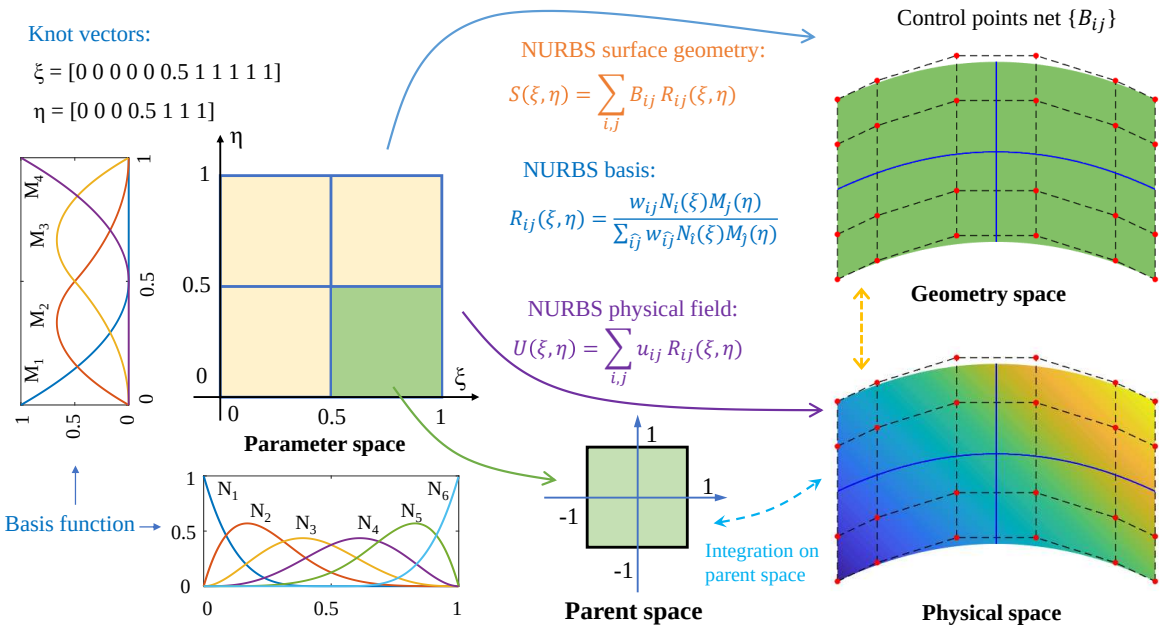

Figure 3.1: Schematic illustration of NURBS surface model. Open knot vectors and high order continuous basis functions are used.

$$N_{i,0}=\begin{cases}0, & if\ \xi_i\le\xi\le\xi_{i+1}\\ 1, & \text{otherwise.}\end{cases} \tag{3.28}$$

For $p=1,2,...$, we have

$$N_{i,p}(\xi)=\frac{\xi-\xi_i}{\xi_{i+p}-\xi_i}N_{i,p-1}(\xi)+\frac{\xi_{i+p+1}-\xi}{\xi_{i+p+1}-\xi_{i+1}}N_{i+1,p-1}(\xi) \tag{3.29}$$

NURBS are formed through rational functions of B-spline. The projective transformation of a B-spline curve yields a rational polynomial of the form $C_R(\xi)=f(\xi)/g(\xi)$, where $f(\xi)$ and $g(\xi)$ are piecewise polynomials. We get the NURBS curve $C(\xi)$ by performing exactly the same projective transformation to the B-spline curve $C^w(\xi)$. Given a knot vector $\boldsymbol{\xi}=\{\xi_1,\xi_2,...,\xi_{n+p+1}\}$, and a control net of points $B_i\in\mathbb{R}^d$ (d is dimension), the control points B_i are derived from the projective control points B_i^w in $\mathbb{R}^{d+1}$ by the following relations:

$$(B_i)_j=(B_i^w)_j/w_i,\ \ j=1,...,d \tag{3.30}$$

$$w_i=(B_i^w)_{d+1} \tag{3.31}$$

where $(B_i)_j$ is the j-th component of the vector B_i. w_i is referred to as the i-th positive weight and the subscript $d+1$ means the $(d+1)$-th component of projective control points.

We define the weighting function $W(\xi)$:

$$W(\xi)=\sum_{i=1}^{n}N_{i,p}(\xi)w_i \tag{3.32}$$

The NURBS curve obtained as:

$$C(\xi)=\frac{C^w(\xi)}{W(\xi)}=\sum_{i=1}^{n}\frac{N_{i,p}(\xi)w_iB_i}{\sum_{j=1}^{n}N_{j,p}(\xi)w_j} \tag{3.33}$$

The NURBS basis functions are given by

$$R_{i,p}(\xi) = \frac{N_{i,p}(\xi)w_i}{W(\xi)} = \frac{N_{i,p}(\xi)w_i}{\sum_{j=1}^{n} N_{j,p}(\xi)w_j} \tag{3.34}$$

It is worth noting that when all the weights are equal, the NURBS basis degenerate to the B-Spline basis. With this procedure, NURBS surfaces $S(\xi,\eta)$ and solids $V(\xi,\eta,\zeta)$ can be defined analogously by extending the rational basis functions to 2D and 3D as:

$$S(\xi,\eta) = \sum_{i=1}^{n}\sum_{j=1}^{m} R_{i,j}^{p,q}(\xi,\eta)\mathbf{B}_{i,j} \tag{3.35}$$

and

$$V(\xi,\eta,\zeta) = \sum_{i=1}^{n}\sum_{j=1}^{m}\sum_{k=1}^{l} R_{i,j,k}^{p,q,r}(\xi,\eta,\zeta)\mathbf{B}_{i,j,k} \tag{3.36}$$

where $\mathbf{B}_{i,j}$ and $\mathbf{B}_{i,j,k}$ are respectively the 2D and 3D coordinates of the control points. The rational terms $R_{i,j}^{p,q}$ and $R_{i,j,k}^{p,q,r}$ are provided by

$$R_{i,j}^{p,q}(\xi,\eta) = \frac{N_i(\xi)M_j(\eta)w_{i,j}}{\sum_{\hat{i}=1}^{n}\sum_{\hat{j}=1}^{m} N_{\hat{i},p}(\xi)M_{\hat{j},q}(\eta)w_{\hat{i},\hat{j}}} \tag{3.37}$$

and

$$R_{i,j,k}^{p,q,r}(\xi,\eta,\zeta) = \frac{N_i(\xi)M_j(\eta)L_k(\zeta)w_{i,j,k}}{\sum_{\hat{i}=1}^{n}\sum_{\hat{j}=1}^{m}\sum_{\hat{k}=1}^{m} N_{\hat{i},p}(\xi)M_{\hat{j},q}(\eta)L_{\hat{k},q}(\zeta)w_{\hat{i},\hat{j},\hat{j}}} \tag{3.38}$$

where $N_{i,p}(\xi)$ and $M_{i,q}(\eta)$, $L_{k,r}(\zeta)$ are univariate B-Spline basis of order p, q and r corresponding to knot vectors $\boldsymbol{\xi}$, $\boldsymbol{\eta}$ and $\boldsymbol{\zeta}$, respectively.

In the previous content, we appreciate how NURBS construct geometry. We then proceed to introduce the use of NURBS as a discretization tool for structural analysis, so called Isogeometric Analysis. A schematic illustration of Isogeometric Analysis is presented in Fig. 3.1 for a NURBS surface. Parameter space schematically shown in Fig. 3.1 is formed by considering only the non-zero intervals between knot values. The regions bounded by knot lines with non-zero knot values subdivide element domains. The NURBS mapping of Eq. (3.35) transform coordinates in the parameter space to the physical space. For analysis to be performed we require the definition of a parent space $\tilde{\Omega} = [-1,1]^d$, $d = 1,2,3$, where the use of numerical integration routines are often defined over the interval $[-1,1]$ for each direction. The fields in physical questions (e.g., displacement, temperature, electric potential, etc.) are represented in terms of the same basis functions as the geometry. The coefficients of the basis functions are the degrees-of-freedom, or control variables.

3.3.2 Discretization of flexoelectric equations

In this work, the IGA discretization for the problem defined in (3.26)-(3.27) is presented with 2D plane strain assumption. The displacement $\mathbf{u}$ and electric potential ϕ fields are both approximated using NURBS according to

$$\mathbf{u}(\mathbf{x}) = \sum_{i=1}^{n}\sum_{j=1}^{m} R_{i,j}^{p,q}(\xi,\eta)u_{ij}^{e} = \boldsymbol{N}_u\boldsymbol{u}^e \tag{3.39}$$

$$\phi(\mathbf{x}) = \sum_{i=1}^{n}\sum_{j=1}^{m} R_{i,j}^{p,q}(\xi,\eta)\phi^{e} = \boldsymbol{N}_\phi\boldsymbol{\phi}^e \tag{3.40}$$

defining the following vectors:

$$\mathbf{u}^e = \left[u_x^1, u_x^2, ..., u_x^n, u_y^1, u_y^2, ..., u_y^n\right] \tag{3.41}$$

$$\boldsymbol{\phi}^e = \left[\boldsymbol{\phi}^1, \boldsymbol{\phi}^2, ..., \boldsymbol{\phi}^n\right] \tag{3.42}$$

$$[\boldsymbol{\varepsilon}] = [\varepsilon_{11}, \varepsilon_{22}, 2\varepsilon_{12}] \tag{3.43}$$

$$[\nabla\boldsymbol{\varepsilon}] = [\nabla\varepsilon_{111}, \nabla\varepsilon_{221}, 2\nabla\varepsilon_{122}, \nabla\varepsilon_{222}, \nabla\varepsilon_{112}, 2\nabla\varepsilon_{121}] \tag{3.44}$$

and the different following quantities are obtained from the shape function derivatives by

$$[\boldsymbol{\varepsilon}] = \boldsymbol{B}_u \boldsymbol{u}^e \tag{3.45}$$
$$\boldsymbol{E} = -\boldsymbol{B}_\phi \boldsymbol{\phi}^e \tag{3.46}$$
$$[\nabla\boldsymbol{\varepsilon}] = \boldsymbol{H}_u \boldsymbol{u}^e \tag{3.47}$$

where $\boldsymbol{B}_u$, $\boldsymbol{B}_\phi$ and $\boldsymbol{H}_u$ are shape function derivative matrices, given by

$$\boldsymbol{B}_\phi = \begin{bmatrix} \frac{\partial N_\phi^1}{\partial x} & \cdots & \frac{\partial N_\phi^n}{\partial x} \\ \frac{\partial N_\phi^1}{\partial y} & \cdots & \frac{\partial N_\phi^n}{\partial y} \end{bmatrix}, \ \boldsymbol{B}_u = \begin{bmatrix} \frac{\partial N_u^1}{\partial x} & \cdots & \frac{\partial N_u^n}{\partial x} & 0 & \cdots, & 0 \\ 0 & \cdots & 0 & \frac{\partial N_u^1}{\partial y} & \cdots & \frac{\partial N_u^n}{\partial y} \\ \frac{\partial N_u^1}{\partial y} & \cdots & \frac{\partial N_u^n}{\partial y} & \frac{\partial N_u^1}{\partial x} & \cdots & \frac{\partial N_u^n}{\partial x} \end{bmatrix} \tag{3.48}$$

$$\boldsymbol{H}_u = \begin{bmatrix} \frac{\partial^2 N_u^1}{\partial x^2} & \cdots & \frac{\partial^2 N_u^n}{\partial x^2} & 0 & \cdots & 0 \\ 0 & \cdots & 0 & \frac{\partial^2 N_u^1}{\partial x \partial y} & \cdots & \frac{\partial^2 N_u^n}{\partial x \partial y} \\ \frac{\partial^2 N_u^1}{\partial y^2} & \cdots & \frac{\partial^2 N_u^n}{\partial y^2} & \frac{\partial^2 N_u^1}{\partial x \partial y} & \cdots & \frac{\partial^2 N_u^n}{\partial x \partial y} \\ 0 & \cdots & 0 & \frac{\partial^2 N_u^1}{\partial y^2} & \cdots & \frac{\partial^2 N_u^n}{\partial y^2} \\ \frac{\partial^2 N_u^1}{\partial x \partial y} & \cdots & \frac{\partial^2 N_u^n}{\partial x \partial y} & 0 & \cdots & 0 \\ \frac{\partial^2 N_u^1}{\partial x \partial y} & \cdots & \frac{\partial^2 N_u^n}{\partial x \partial y} & \frac{\partial^2 N_u^1}{\partial x^2} & \cdots & \frac{\partial^2 N_u^n}{\partial x^2} \end{bmatrix} \tag{3.49}$$

and $\mathbf{u}^e$ and $\boldsymbol{\phi}^e$ denote the nodal displacements and potentials, respectively.

When only static equilibrium is considered, substituting (3.2)-(3.4) and (3.39)-(3.47) into (3.26)-(3.27) yields a discrete system of algebraic equations in the form:

$$\begin{aligned} &\int_\Omega (\delta\boldsymbol{u}^e)^T \{(\boldsymbol{B}_u^T \mathbb{C} \boldsymbol{B}_u \boldsymbol{u}^e + \boldsymbol{H}_u^T \mathbb{G} \boldsymbol{H}_u \boldsymbol{u}^e) + (\delta\boldsymbol{u}^e)^T (\boldsymbol{B}_u^T \boldsymbol{e} \boldsymbol{B}_\phi \boldsymbol{\phi}^e + \boldsymbol{H}_u^T \boldsymbol{\mu} \boldsymbol{B}_\phi \boldsymbol{\phi}^e)\} \mathrm{d}\Omega \\ &= \int_{\partial\Omega_t} (\delta\boldsymbol{u}^e)^T \boldsymbol{N}_u^T F_i^d \mathrm{d}S \end{aligned} \tag{3.50}$$

$$\int_\Omega (\delta\boldsymbol{\phi}^e)^T (\boldsymbol{B}_\phi^T \boldsymbol{\alpha} \boldsymbol{B}_\phi \boldsymbol{\phi}^e + \boldsymbol{B}_\phi^T \boldsymbol{e} \boldsymbol{B}_u \boldsymbol{u}^e - \boldsymbol{B}_\phi^T \boldsymbol{\mu} \boldsymbol{H}_u \boldsymbol{u}^e) \mathrm{d}\Omega = -\int_{\partial\Omega_D} (\delta\boldsymbol{\phi}^e)^T \boldsymbol{N}_\phi^T D_n^d \mathrm{d}S \tag{3.51}$$

We write the discrete system by the matrix form as:

$$\begin{bmatrix} \mathbf{K}_{uu} & \mathbf{K}_{u\phi} \\ -\mathbf{K}_{u\phi}^T & \mathbf{K}_{\phi\phi} \end{bmatrix} \begin{bmatrix} \mathbf{u} \\ \boldsymbol{\phi} \end{bmatrix} = \begin{bmatrix} \mathbf{f}_u \\ \mathbf{f}_\phi \end{bmatrix} \tag{3.52}$$

with

$$\mathbf{K}_{uu} = \int_{\Omega} [\boldsymbol{B}_u^T \mathbb{C} \boldsymbol{B}_u + \boldsymbol{H}_u^T \mathbb{G} \boldsymbol{H}_u] \mathrm{d}\Omega \tag{3.53}$$

$$\mathbf{K}_{u\phi} = \int_{\Omega} [\boldsymbol{B}_\phi^T \mathbf{e} \boldsymbol{B}_u + \boldsymbol{B}_\phi^T \boldsymbol{\mu} \boldsymbol{H}_u] \mathrm{d}\Omega \tag{3.54}$$

$$\mathbf{K}_{\phi\phi} = \int_{\Omega} [\boldsymbol{B}_\phi^T \boldsymbol{\alpha} \boldsymbol{B}_\phi] \mathrm{d}\Omega \tag{3.55}$$

$$\mathbf{f}_u = \int_{\Omega} \mathbf{N}_u^T \mathbf{F}^d \mathrm{d}S \tag{3.56}$$

$$\mathbf{f}_\phi = -\int_{\Omega} \mathbf{N}_\phi^T D_n^d \mathrm{d}S \tag{3.57}$$

Moreover, the material parameters $\mathbb{C}$, $\boldsymbol{e}$, $\boldsymbol{\alpha}$, $\boldsymbol{\mu}$ and $\mathbb{G}$ can be defined in the matrix form [60, 179] as

$$\mathbb{C} = \begin{bmatrix} c_{11} & c_{12} & 0 \\ c_{12} & c_{22} & 0 \\ 0 & 0 & c_{44} \end{bmatrix}, \quad \boldsymbol{e} = \begin{bmatrix} e_{111} & e_{122} & e_{112} \\ e_{211} & e_{222} & e_{212} \end{bmatrix}, \quad \boldsymbol{\alpha} = \begin{bmatrix} \alpha_{11} & 0 \\ 0 & \alpha_{33} \end{bmatrix} \tag{3.58}$$

$$\boldsymbol{\mu} = \begin{bmatrix} \mu_{1111} & \mu_{1221} & \mu_{1122} & \mu_{1222} & \mu_{1112} & \mu_{1121} \\ \mu_{2111} & \mu_{2221} & \mu_{2122} & \mu_{2222} & \mu_{2112} & \mu_{2121} \end{bmatrix} \tag{3.59}$$

For the sake of simplicity, we assume the matrix $\mathbf{G}$ is in the form:

$$\mathbb{G} = \ell^2 \begin{bmatrix} c_{11} & 0 & 0 & c_{12} & 0 & 0 \\ 0 & c_{22} & c_{12} & 0 & 0 & 0 \\ 0 & c_{12} & c_{11} & 0 & 0 & 0 \\ c_{12} & 0 & 0 & c_{22} & 0 & 0 \\ 0 & 0 & 0 & 0 & c_{44} & 0 \\ 0 & 0 & 0 & 0 & 0 & c_{44} \end{bmatrix} \tag{3.60}$$

3.3.3 Discretization of dynamic flexoelectricity in the frequency domain

When dynamic terms are taken into account, introducing (3.39)-(3.47) into (3.26)-(3.27) yields the following discrete set of time-differential equations:

$$\begin{cases} \mathbf{M}\ddot{\mathbf{u}} + \mathbf{D}\dot{\mathbf{u}} + \mathbf{K}_{uu}\mathbf{u} + \mathbf{K}_{u\phi}\boldsymbol{\phi} = \mathbf{f}_\mathbf{u} \\ -\mathbf{K}_{u\phi}^T\mathbf{u} + \mathbf{K}_{\phi\phi}\boldsymbol{\phi} = \mathbf{f}_\phi \end{cases} \tag{3.61}$$

where the mass matrix $\mathbf{M}$ and damping matrix $\mathbf{D}$ are defined by

$$\mathbf{M} = \int_{\Omega} \rho \{\boldsymbol{N}_u^T \boldsymbol{N}_u + \ell_d^2 \tilde{\boldsymbol{B}}_u^T \tilde{\boldsymbol{B}}_u\} \mathrm{d}\Omega \tag{3.62}$$

$$\mathbf{D} = \int_{\Omega} \mathbf{N}_u^T \mathbf{V} \mathbf{N} \mathrm{d}\Omega \tag{3.63}$$

with

$$\tilde{\boldsymbol{B}}_u = \begin{bmatrix} \frac{\partial N_u^1}{\partial x} & \cdots & \frac{\partial N_u^n}{\partial x} & 0 & \cdots, & 0 \\ 0 & \cdots & 0 & \frac{\partial N_u^1}{\partial y} & \cdots & \frac{\partial N_u^n}{\partial y} \\ \frac{\partial N_u^1}{\partial y} & \cdots & \frac{\partial N_u^n}{\partial y} & 0 & \cdots & 0 \\ 0 & \cdots & 0 & \frac{\partial N_u^1}{\partial x} & \cdots & \frac{\partial N_u^n}{\partial x} \end{bmatrix} \tag{3.64}$$

Following classical approaches, the matrix $\mathbf{D}$ is approximated by

$$\mathbf{D} = \beta_1 \mathbf{M} + \beta_2 \mathbf{K}_{uu} \tag{3.65}$$

Above, β_1 and β_2 are constants computed by [15]:

$$\begin{bmatrix} \beta_1 \\ \beta_2 \end{bmatrix} = \frac{2\omega_1\omega_2}{\omega_1^2 - \omega_2^2} \begin{bmatrix} -\omega_2 & \omega_1 \\ \frac{1}{\omega_2} & -\frac{1}{\omega_1} \end{bmatrix} \begin{bmatrix} \xi_1 \\ \xi_2 \end{bmatrix} \tag{3.66}$$

where ξ_1 and ξ_2 are two damping ratios, and ω_1 and ω_2 are the first two resonance frequencies of the structure.

The displacement field, the potential and the external forces are assumed to be in the form:

$$\mathbf{u} = \tilde{\mathbf{u}} e^{j\omega t},\ \phi = \tilde{\phi} e^{j\omega t},\ \mathbf{f_u} = \tilde{\mathbf{f}}_u e^{j\omega t} \tag{3.67}$$

where j is the complex number and ω is the frequency. In the case of an open circuit, $\mathbf{f}_\phi = \mathbf{0}$. Introducing (3.67) in (3.61), we obtain:

$$\begin{bmatrix} \left(\mathbf{K}_{uu} + j\omega\mathbf{D} - \omega^2\mathbf{M}\right) & \mathbf{K}_{u\phi} \\ -\mathbf{K}_{u\phi}^T & \mathbf{K}_{\phi\phi} \end{bmatrix} \begin{bmatrix} \tilde{\mathbf{u}} \\ \tilde{\phi} \end{bmatrix} = \begin{bmatrix} \tilde{\mathbf{f}}_u \\ \mathbf{0} \end{bmatrix} \tag{3.68}$$

In this work, boundary conditions associated with a close circuit, as illustrated in Fig. 3.4(b), are considered. Following [102], we have:

$$\dot{\mathbf{f}}_\phi = \frac{\hat{\phi}}{R} \tag{3.69}$$

where R is the resistor value and $\hat{\phi}$ is the vector of nodal potentials where the resistor is connected. The vector $\hat{\phi}$ is related to the global unknown vector $\tilde{\phi}$ through a matrix $\mathbf{T}$ such that $\hat{\phi} = \mathbf{T}\tilde{\phi}$ and which contains mainly zeros and ones. Deriving the last equation of (3.61) with respect to time we obtain:

$$-\mathbf{K}_{u\phi}^T \dot{\mathbf{u}} + \mathbf{K}_{\phi\phi}\dot{\phi} = \dot{\mathbf{f}}_\phi \tag{3.70}$$

Then, using (3.67) and (3.69), it yields:

$$-j\omega\mathbf{K}_{u\phi}^T \tilde{\mathbf{u}} + j\omega\mathbf{K}_{\phi\phi}\tilde{\phi} = \frac{\hat{\phi}}{R} \tag{3.71}$$

The new linear system to be solved for a given frequency ω is given by:

$$\begin{bmatrix} \mathbf{K}_{uu} + j\omega\mathbf{D} - \omega^2\mathbf{M} & \mathbf{K}_{u\phi} \\ -\mathbf{K}_{u\phi}^T & \mathbf{K}_{\phi\phi} - \frac{\mathbf{T}}{j\omega R} \end{bmatrix} \begin{bmatrix} \tilde{\mathbf{u}} \\ \tilde{\phi} \end{bmatrix} = \begin{bmatrix} \tilde{\mathbf{f}}_u \\ \mathbf{0} \end{bmatrix} \tag{3.72}$$

3.4 C^1-continuous Isogeometric analysis on multiple patches

It is crucial to guarantee C^1 continuity of the physical domain when tackling the 4th-order flexoelectric partial differential equations. Isogeometric analysis offers a valuable method for achieving high-smoothness approximations. Nevertheless, the tensor product structure of the parameter space of a patch makes it poorly suited for representing complex, multiply connected domains. On these geometries, multiple parameter spaces (patches) are used to describe the physical domain, resulting in a loss of continuity occurring at the patch interfaces. This reduction in smoothness is primarily governed by the geometric representation, where sharp turns

and corners within the domain and the connection among multiple subdomains (patches) are conventionally handled by C^0 parameterizations. An alternative strategy to ensure desired continuity requirements involves constructing a basis for the corresponding C^1 isogeometric space.

We focus on the complete space of C^1-smooth isogeometric functions on any given two-patch (or multi-patch) parameterization and construct a basis for the associated C^1 continuous isogeometric space while keeping the geometric parametrization unaltered. These basis functions are formulated by means of minimal determined sets for the Bézier coefficients, ensuring that they possess a local support and are well conditioned. After then, the C^1 continuous multi-patch isogeometric space can be employed to solve 4th-order flexoelectric PDEs.

3.4.1 C^1-continuous isogeometric functions

For simplification, we restrict the cases to 2D domains, schematically shown in Fig. 3.2(a). We consider n bilinear, regular mappings

$$\mathbf{G}^{(k)} : [0,\ 1]^2 \to \mathbb{R}^2,\ k \in \{1,...,n\} \tag{3.73}$$

We assume $\mathbf{G}^{(k)}$ as a NURBS surface, and its coordinates and parametric representation is written as:

$$(\xi^{(k)}, \eta^{(k)}) \mapsto (G_1^{(k)}, G_2^{(k)}) = \sum_{i=1}^{m} \mathbf{B}_i^{(k)} R_i^{(k)}(\xi, \eta) \tag{3.74}$$

where $\mathbf{B}_i^{(k)} = [x_i^{(k)}, y_i^{(k)}]$ is the control points and $R_i^{(k)}$ is the corresponding basis. Each geometry mapping $\mathbf{G}^{(k)}$ defines a quadrilateral subdomain, i.e. patch.

$$\Omega^{(k)} = \mathbf{G}^{(k)}([0,1]^2) \tag{3.75}$$

and there is no intersection among interiors of these patches.

The physical domain $\Omega \in \mathbb{R}^2$ is defined as $\Omega = \cup\Omega^{(k)}$. The space of isogeometric function of each patch $\Omega^{(k)}$ is given as $S^{(k)} \circ (\mathbf{G}^{(k)})^{-1}$, wherein $S^{(k)}$ is a NURBS space of degree p defined on the parametric domain $[0,\ 1]^2$. The space of C^1 continuous isogeometric functions defined on the physical domain Ω can be written as:

$$Z = \{z \in C^1(\Omega) : z|_{\Omega^{(k)}} \in S^{(k)} \circ (\mathbf{G}^{(k)})^{-1} \text{ for all } k \in \{1,...,n\}\} \tag{3.76}$$

We consider an isogeometric function $w \in Z$ on each patch, and it is represented as

$$w^{(k)} = (N^{(k)} \circ (\mathbf{G}^{(k)})^{-1})(\boldsymbol{x}), \boldsymbol{x} \in \Omega^{(k)} \tag{3.77}$$

with $N^{(k)} \in S^{(k)}$. $N^{(k)}$ is a basis function defined on the local parameter domain $[0,1]^2$. $w^{(k)}$ is the associated segment of the isogeometric function defined on $\Omega^{(k)}$, and its associated graph surface $\mathbf{F}^{(k)}(\xi, \eta)$ possesses the form

$$\mathbf{F}^{(k)}(\xi, \eta) = (\mathbf{G}^{(k)}(\xi, \eta),\ N^{(k)}(\xi, \eta))^T = (G_1^{(k)}(\xi, \eta),\ G_2^{(k)}(\xi, \eta),\ N^{(k)}(\xi, \eta))^T \tag{3.78}$$

We consider two neighboring patches $\Omega^{(k_1)}$ and $\Omega^{(k_2)}$ with the common interface $\Gamma^{k_1 k_2} = \Omega^{(k_1)} \cap \Omega^{(k_2)}$. Since $w \in C^1(\Omega)$, the first derivatives of the functions $w^{(k_1)}$ and $w^{(k_2)}$ at the common interface have to satisfy:

$$\frac{\partial w^{(k_1)}(\boldsymbol{x})}{\partial \xi} = \frac{\partial w^{(k_2)}(\boldsymbol{x})}{\partial \xi},\ \frac{\partial w^{(k_1)}(\boldsymbol{x})}{\partial \eta} = \frac{\partial w^{(k_2)}(\boldsymbol{x})}{\partial \eta},\ \boldsymbol{x} \in \Gamma^{k_1 k_2} \tag{3.79}$$

where $\boldsymbol{x}$ are the global coordinates on Ω.

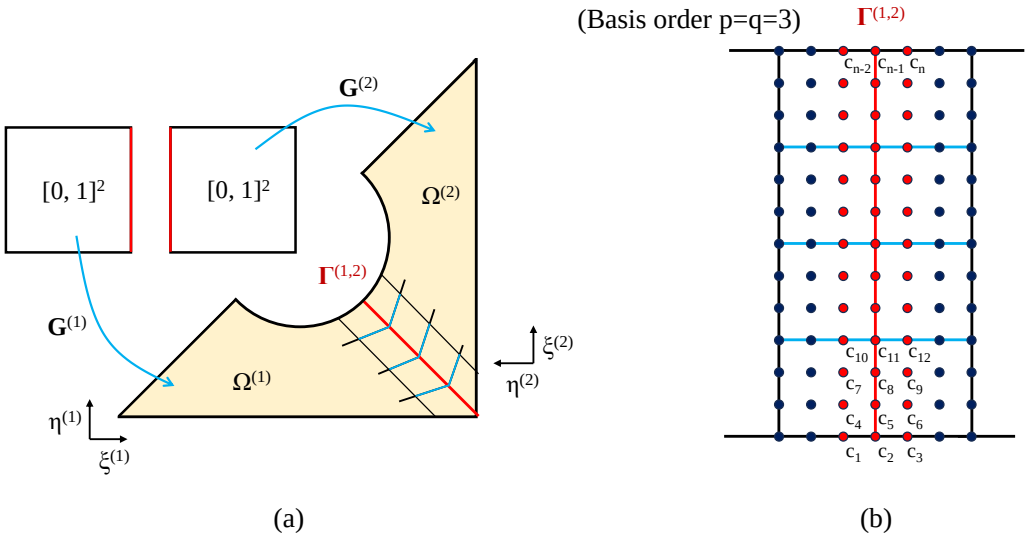

Figure 3.2: (a) The geometric mapping $\mathbf{G}^{(1)}$ and $\mathbf{G}^{(2)}$ defined on $[0,1]^2$, and elements on the common interface $\Gamma^{(1,2)}$; (b) The Bézier coefficients for four neighboring pairs of spline segments along the associated common interface $\Gamma^{(1,2)}$ of the two patches

3.4.2 C^1 continuity on two-patch geometries

We assume that both patches are bilinearly parameterized, and represented as B-spline patches of degree (p, p), as shown in Fig. 3.2(a). We first construct isogeometric basis functions on Ω, which span the space Z of all C^1 geometrically continuous isogeometric functions. Consequently, we choose the B-spline basis function $N^{(k)} \in S^{(k)}$ possessing the form of a degree p Bernstein-Bézier basis function defined on a particular element e_ℓ (i.e. each non-zero knot interval) as follows:

$$N^{(k)}|_{e_\ell}(\xi,\eta) = \sum_{i=1}^{p}\sum_{j=1}^{p} c_{ij}^{(k)} \beta_{i,p}^{(k)}(u)\beta_{j,p}^{(k)}(v) \tag{3.80}$$

where $c_{ij}^{(k)}$ are the scalar Bézier coefficients, while $\beta_{i,p}^{(k)}(u)$ and $\beta_{j,p}^{(k)}(v)$ are the Bernstein basis function. These functions are calculated on the reference interval $u,v \in [-1,1]$ as

$$\beta_{i,p}^{(k)}(u) = \frac{1}{2^p}\begin{pmatrix} p \\ i-1 \end{pmatrix}(1-u)^{p-(i-1)}(1+u)^{(i-1)},\ u \in [-1,\ 1] \tag{3.81}$$

where $\begin{pmatrix} p \\ i-1 \end{pmatrix} = \frac{p!}{(i-1)!(p+1-i)!}$, $1 \le i \le p+1$. For the particular knot-spans $[\xi_i, \xi_{i+1}]$ and $[\eta_i, \eta_{i+1}]$, the mapping is given such as $f_e : u \in [-1,1] \to \xi \in [\xi_i, \xi_{i+1}]$, i.e. $\xi = \frac{u}{2}(\xi_{i+1} - \xi_i) + \frac{1}{2}(\xi_{i+1} + \xi_i)$. The graph surface of $w^{(k)}$ can be written as

$$\mathbf{F}^{(k)}(\xi,\eta) = (G_1^{(k)}(\xi,\eta),\ G_2^{(k)}(\xi,\eta),\ N^{(k)}(\xi,\eta))^T \tag{3.82}$$

An isogeometric function w has C^0-continuity across the constructed common edge $\Gamma^{(1,2)} = \Omega^{(1)} \cap \Omega^{(2)}$ parallel to η-direction, if and only if

$$\mathbf{G}^{(1)}(1,\eta) = \mathbf{G}^{(2)}(0,\eta) \text{ and } N^{(1)}(1,\eta) = N^{(2)}(0,\eta) \text{ on } \Gamma^{(1,2)},\ \eta \in [0,1] \tag{3.83}$$

The tangent planes of the graph surfaces $\mathbf{F}^{(1)}$ and $\mathbf{F}^{(2)}$ at points along the common interface $\Gamma^{(1,2)}$ are calculated respectively by their first derivative vectors:

$$\frac{\partial \mathbf{F}^{(1)}(1,\eta)}{\partial \xi}, \frac{\partial \mathbf{F}^{(1)}(1,\eta)}{\partial \eta} \text{ and } \frac{\partial \mathbf{F}^{(2)}(0,\eta)}{\partial \xi}, \frac{\partial \mathbf{F}^{(2)}(0,\eta)}{\partial \eta} \tag{3.84}$$

The C^1-continuity of the isogeometric function w is guaranteed when their formed 3×4 matrix has rank 2 only. Due to the C^0 continuity condition (3.83) implies the identity $\frac{\partial \mathbf{F}^{(1)}(1,\eta)}{\partial \eta} = \frac{\partial \mathbf{F}^{(2)}(0,\eta)}{\partial \eta}$, thus the C^1 geometric continuous condition between two patches can be expressed as

$$\det\left(\frac{\partial \mathbf{F}^{(1)}(1,\eta)}{\partial \xi}, \frac{\partial \mathbf{F}^{(1)}(1,\eta)}{\partial \eta}, \frac{\partial \mathbf{F}^{(2)}(0,\eta)}{\partial \xi}\right) = 0, \eta \in [0,1] \tag{3.85}$$

or

$$\det\left(\frac{\partial \mathbf{F}^{(1)}(1,\eta)}{\partial \xi}, \frac{\partial \mathbf{F}^{(2)}(0,\eta)}{\partial \xi}, \frac{\partial \mathbf{F}^{(2)}(0,\eta)}{\partial \eta}\right) = 0, \eta \in [0,1] \tag{3.86}$$

Substituting (3.82) into (3.85), and expanding the determinant in (3.85) gives

$$\tilde{\alpha}(1,\eta)\frac{\partial N^{(1)}(1,\eta)}{\partial \xi} + \tilde{\beta}(1,\eta)\frac{\partial N^{(1)}(1,\eta)}{\partial \eta} + \tilde{\gamma}(0,\eta)\frac{\partial N^{(2)}(0,\eta)}{\partial \xi} = 0 \tag{3.87}$$

with

$$\begin{aligned}
\tilde{\alpha}(1,\eta) &= \frac{\partial G_1^{(1)}(1,\eta)}{\partial \eta}\frac{\partial G_2^{(2)}(0,\eta)}{\partial \xi} - \frac{\partial G_1^{(2)}(0,\eta)}{\partial \xi}\frac{\partial G_2^{(1)}(1,\eta)}{\partial \eta} \\
\tilde{\beta}(1,\eta) &= \frac{\partial G_1^{(2)}(0,\eta)}{\partial \xi}\frac{\partial G_2^{(1)}(1,\eta)}{\partial \xi} - \frac{\partial G_1^{(1)}(1,\eta)}{\partial \xi}\frac{\partial G_2^{(2)}(0,\eta)}{\partial \xi} \\
\tilde{\gamma}(0,\eta) &= \frac{\partial G_1^{(1)}(1,\eta)}{\partial \xi}\frac{\partial G_2^{(1)}(1,\eta)}{\partial \eta} - \frac{\partial G_1^{(1)}(1,\eta)}{\partial \eta}\frac{\partial G_2^{(1)}(1,\eta)}{\partial \xi}
\end{aligned}$$

When the common edge is parallel to ξ-direction, i.e. $\Gamma^{(1,2)} = \mathbf{G}^{(1)}(\xi,1) \cap \mathbf{G}^{(2)}(\xi,0)$, the C^1 continuous condition is rewritten as:

$$\det\left(\frac{\partial \mathbf{F}^{(1)}(\xi,1)}{\partial \xi}, \frac{\partial \mathbf{F}^{(1)}(\xi,1)}{\partial \eta}, \frac{\partial \mathbf{F}^{(2)}(\xi,0)}{\partial \eta}\right) = 0, \xi \in [0,1] \tag{3.88}$$

or

$$\det\left(\frac{\partial \mathbf{F}^{(1)}(\xi,1)}{\partial \eta}, \frac{\partial \mathbf{F}^{(2)}(\xi,0)}{\partial \xi}, \frac{\partial \mathbf{F}^{(2)}(\xi,0)}{\partial \eta}\right) = 0, \xi \in [0,1] \tag{3.89}$$

The expansion of (3.88) is given by:

$$\tilde{\alpha}(\xi,1)\frac{\partial N^{(1)}(\xi,1)}{\partial \xi} + \tilde{\beta}(\xi,1)\frac{\partial N^{(1)}(\xi,1)}{\partial \eta} + \tilde{\gamma}(\xi,0)\frac{\partial N^{(2)}(\xi,0)}{\partial \xi} = 0 \tag{3.90}$$

with

$$\begin{aligned}
\tilde{\alpha}(\xi,1) &= \frac{\partial G_1^{(1)}(\xi,1)}{\partial \eta}\frac{\partial G_2^{(2)}(\xi,0)}{\partial \eta} - \frac{\partial G_1^{(2)}(\xi,0)}{\partial \eta}\frac{\partial G_2^{(1)}(\xi,1)}{\partial \eta} \\
\tilde{\beta}(\xi,1) &= \frac{\partial G_1^{(2)}(\xi,0)}{\partial \eta}\frac{\partial G_2^{(1)}(\xi,1)}{\partial \xi} - \frac{\partial G_1^{(1)}(\xi,1)}{\partial \xi}\frac{\partial G_2^{(2)}(\xi,0)}{\partial \eta} \\
\tilde{\gamma}(\xi,0) &= \frac{\partial G_1^{(1)}(\xi,1)}{\partial \xi}\frac{\partial G_2^{(1)}(\xi,1)}{\partial \eta} - \frac{\partial G_1^{(1)}(\xi,1)}{\partial \eta}\frac{\partial G_2^{(1)}(\xi,1)}{\partial \xi}
\end{aligned}$$

To ensure C^1-continuity across the common boundary, we select enough collocation points along the common edge to obtain a set of continuity constraints. As the geometries are expressed by the finite-dimensional space of Bernstein-Bézier basis functions (3.80), these constraints can be equated to many linear constraints on the Bézier coefficients $c_i^{(1)}$ and $c_i^{(2)}$, which can be constructed as a homogeneous linear system

$$\mathbf{H} \cdot \boldsymbol{c} = \mathbf{0},\ \boldsymbol{c} = (c_i^{(k)})_{k=1,2} \tag{3.91}$$

Followed by the construction of the homogeneous linear matrix $\mathbf{H}$. There are two kinds of basis function in Z, i.e. the first kind only have support in one patch, while the second kind have support in both patches. Only the second kind are relevant to the common boundary, thus they are the focus here. The two bilinear patches are represented as B-spline patches of degree (p, p) in $[0,1]^2$ and $p = 3$, the knot vector in each direction is inserted t equidistant inner knots of multiplicity $p-1$. There will be $t+1$ pairs of segments (i.e. common edge of neighboring elements between two patches) along the associated common edge, shown as the red line in Fig. 3.2(a).

Since all the 2D basis functions are formed by the tensor products of 1D basis functions, we discuss the basis functions in 1D. It is straightforward to extend the conclusions to 2D cases. The B-spline basis functions of degree $p = 3$ are given in Fig. 3.3(a). We note that, the derivatives of the first two basis functions ($N_{1,3}$ and $N_{2,3}$) are non-zeros at edge $\xi = 0$. In contrast, the derivatives of the last two basis functions ($N_{7,3}$ and $N_{8,3}$) are non-zeros at $\xi = 1$. With these basis functions, the common edge between both patches is only C^0 continuity. Consequently, they are labeled as removed functions, and will be replaced by new basis. The interior knots of the knot vector have $p-1$ multiplicity, it implies that the basis functions on the edge (such as $\xi = 1/3$ and $\xi = 2/3$) of two neighboring elements within a patch have $p-(p-1)$ continuous derivatives, i.e. C^1-continuity. There are two purposes using the repeated interior knots: decreasing the support area of each basis function while preserving at least C^1-continuity, and the removed basis functions only support edge elements (i.e. elements on $\xi = 0$ and $\xi = 1$).

Here the B-spline basis functions are element-wise constructed by Bézier coefficients and Bernstein functions, i.e. equation (3.80). The modified and new B-spline basis functions are achieved by operating Bézier coefficients. The 1D cubic Bernstein functions ($\beta_{1,3}(u)$, $\beta_{2,3}(u)$, $\beta_{3,3}(u)$, $\beta_{4,3}(u)$) are shown in Fig. 3.3(b). We can see that at $u = -1$, the derivatives of $\beta_{1,3}(u)$ and $\beta_{2,3}(u)$ are non-zero. Therefore, the coefficients associated with these functions will influence the derivatives at the edge $u = -1$. Analogously, $\beta_{3,3}(u)$ and $\beta_{4,3}(u)$ will impact the derivatives at edges $u = 1$. Since we consider functions of the second kind, only the Bézier coefficients along the common edge and in the neighboring columns are relevant. The coefficients influencing the common edge continuity are marked by red dots in Fig. 3.2(b), and numbered from bottom to top along the common interface. In total we obtain $n_c = 3p(t+1)+3$ coefficients c_i.

Another important issue is to select suitable number of constraint conditions for the homogeneous linear system $\mathbf{H}$ where the nullspace determines the values of the relevant Bézier coefficients. It can be obtained by calculating the constraint equations (3.87) or (3.90) at the uniformly distributed collocation points on each segments (the red and blue lines shown in Fig. 3.2). To construct a determined system, the number of distributed collocation points should be larger than n_c (the number of undetermined Bézier coefficients), and they are uniformly selected on each segment.

When solving a homogeneous linear system $\mathbf{H} \cdot \boldsymbol{c} = 0$, the null space is not uniquely defined. If not select the nullspace carefully, it would result in basis functions with support over all the boundary elements associated with the common interface, and possibly lead to ill-conditioning and non-banded stiffness matrices with a large number of non-zero entries. We thus construct a sparse basis of the nullspace of $\mathbf{H}$ by finding a minimal determined set of the coefficients. Minimal determined set is a set of coefficients, where the Bézier coefficients can be chosen

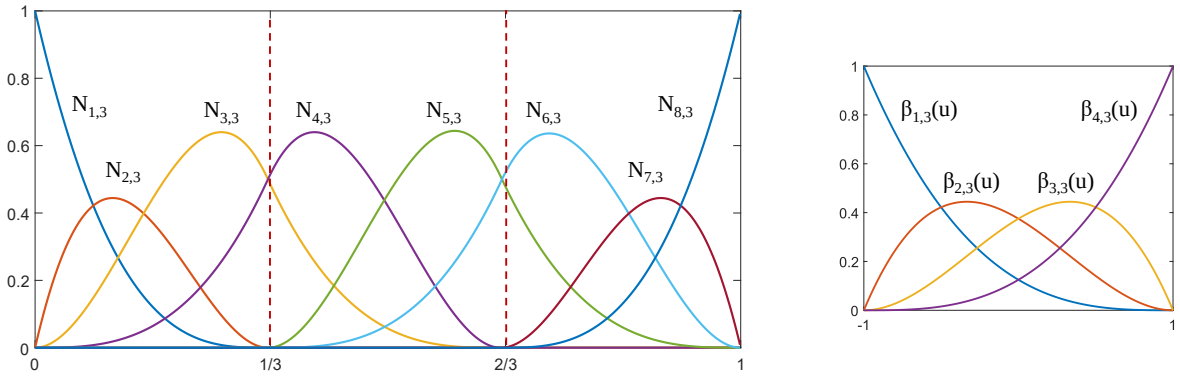

(a) (b)

Figure 3.3: (a) 1D B-spline basis, degree $p = 3$ and knots ξ=[0, 0, 0, 0, 1/3, 1/3, 2/3, 2/3, 1, 1, 1, 1]; (b) 1D Bernstein basis of degree $p = 3$;

arbitrarily while preserving C^1-continuity. To understand minimal determined set, we begin by using Gaussian elimination to transform $\mathbf{H}$ into a block matrix

$$\mathbf{H} = \begin{bmatrix} \mathbf{D}_{r\times r}, \mathbf{A}_{r\times m} \\ \mathbf{0}_{n\times r}, \mathbf{0}_{n\times m} \end{bmatrix} \tag{3.92}$$

where $\mathbf{D}_{r\times r}$ is $r \times r$ nonsingular diagonal matrix and $\mathbf{A}_{r\times m}$ is an $r \times m$ matrix. r is the rank of $\mathbf{A}$ and m is the number of active points in a minimal determining set, i.e. the number of new second kind basis. Thus, we obtain an initial minimal determining set containing all the points corresponding to the columns of $\mathbf{A}$, which form a basis of the null space $\boldsymbol{c}$. Minimal determined set is in general not uniquely defined. Here, we use the approach shown in Algorithm 1 [205] to obtain the minimal determining set. This procedure also performs some kind of normalization for the spline coefficients, which ensures that the resulting basis functions are well conditioned.

Algorithm 1 Computation of minimal determined set of homogeneous matrix

Input: $\mathbf{H}$ - homogeneous system
Output: MDS - minimal determined set of Bézier coefficients c_i

Initialize MDS column index I_{MDS}=[];
Bézier coefficients index $\bar{I} = [1, 2, ..., n_c]$;
for $i = 1$ to n_c **do**
  solve $\mathbf{H} \cdot \boldsymbol{c} = \mathbf{0}$ with condition $c_i = 1$ and $c_j = 0$ for $j \in I_{MDS} \cup (\bar{I} \backslash [i])$
  if a solution $\boldsymbol{c}^*$ exists **then**
    find k such that $|c_k^*|$=max($|\boldsymbol{c}^*|$)
    $I_{MDS} = I_{MDS} \cup [k]$
  end if
  $\bar{I} = \bar{I} \backslash [i]$
end for
return MDS=$[c_i]_{i \in I_{MDS}}$

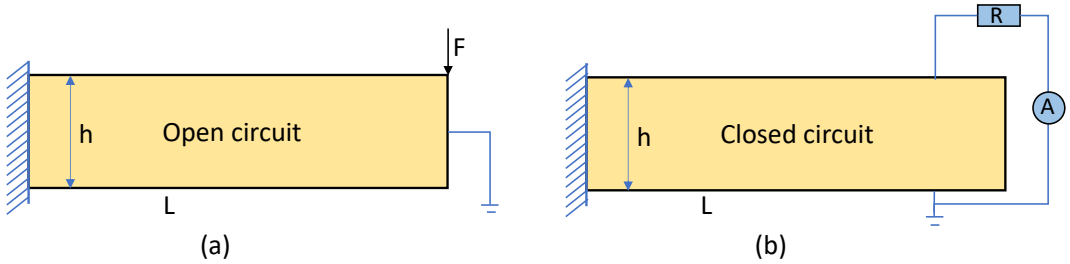

Figure 3.4: Electromechanical coupling cantilever beam with (a) open circuit boundary conditions; (b) close-circuit boundary conditions.

3.5 Numerical examples

In this section, we first validate the present IGA formulation for dynamic flexoelectric calculations. Then, we use the present numerical model to discuss the influence of parameters in vibrating flexoelectric systems. Finally, we construct a multi-patch C^1-continuous complex geometry and analysis its dynamic effects.

3.5.1 Validation of the IGA flexoelectric model

3.5.1.1 Static flexoelectric benchmark

First, we validate the present IGA framework on a static flexoelectric benchmark. A beam made of a flexoelectric material is considered, as shown in Fig. 3.4 (a). Displacements are fixed on the left-end, and a static force $F = 1$ N is prescribed on the top-right corner along the $y-$direction. On the right end, zero electric potential is prescribed to mimic an open circuit. The beam has dimensions $h \times L$. The length of the beam is $L = 20h$ and the thickness h varies. It is assumed that only the stress component σ_{11} and electric field component E_2 are non-zero. The analytical solution of the energy conversion d_{eff} for a 1-D flexoelectric beam model was provided in Majoub et al. [206] as:

$$d_{eff} = \frac{\chi}{1+\chi}\sqrt{\frac{\alpha}{\mathrm{E}}(e^2 + 12(\frac{\mu}{h}))} \tag{3.93}$$

where χ is electric susceptibility, $\alpha = \alpha_{33}$ is dielectric coefficient, E is the Young's modulus, $e = e_{31}$ is the transversal piezoelectric coefficient, and $\mu = \mu_{12}$ is the transversal flexoelectric coefficient. Then the analytical expression of the normalized effective piezoelectric constant (NEPC) d^* for this problem was provided as [206]

$$d^* = \frac{d_{eff}}{d_{piez}} = \sqrt{\left(1 + 12\left(\frac{\mu_{12}}{eh}\right)^2\right)} \tag{3.94}$$

To simulate the one-dimensional analytical model in [206], we simplify our model by neglecting the Poisson's ratio (i.e. $\nu = 0$) and considering only the transversal piezoelectric and flexoelectric constants e_{13} and μ_{12} to be non-zero. The numerical values of the coefficients are provided in Table 3.1. For numerical calculations, the rectangular domain corresponding to the beam is discretized with $N_x \times N_y$ B-spline elements of order 2. Considering plane strains, the matrices $\mathbf{K}_{\phi\phi}$ and $\mathbf{K}_{uu}$ in (3.52) are assembled using the values of $\mathbb{C}$, $\boldsymbol{\alpha}$, $\mathbf{e}$ in (3.58) as:

$$\mathbb{C} = \frac{\mathrm{E}}{(1+\nu)(1-2\nu)}\begin{bmatrix} 1-\nu & \nu & 0 \\ \nu & 1-\nu & 0 \\ 0 & 0 & \frac{1}{2}-\nu \end{bmatrix}, \quad \boldsymbol{\alpha} = \begin{bmatrix} \alpha_{33} & 0 \\ 0 & \alpha_{33} \end{bmatrix} \tag{3.95}$$

Table 3.1: Material parameters.

E	ν	μ_{12}	α_{33}	e_{31}
100 GPa	0	10 nC/m	1nC/Vm	-4.4 C/m^2

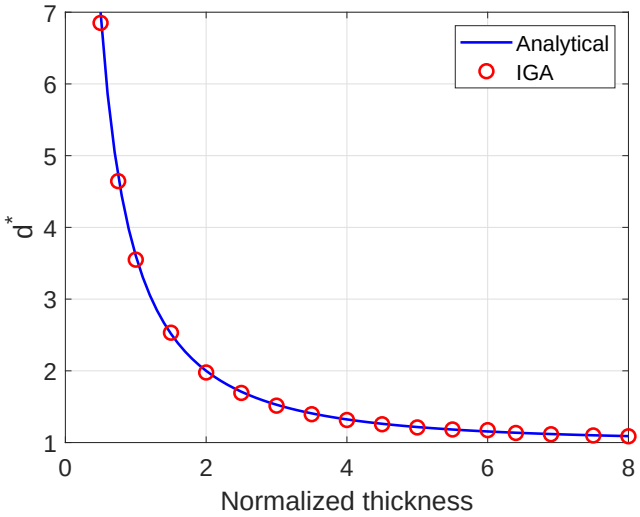

Figure 3.5: Normalized effective piezoelectric coefficient (NEPC) with respect to nomalized thickness h'.

$$\boldsymbol{\mu} = \begin{bmatrix} 0 & \mu_{12} & 0 & 0 & 0 & 0 \\ 0 & 0 & 0 & 0 & \mu_{12} & 0 \end{bmatrix} \quad \boldsymbol{e} = \begin{bmatrix} 0 & 0 & 0 \\ e_{31} & 0 & 0 \end{bmatrix} \tag{3.96}$$

and $\mathbb{G} = 0$ in (3.60). The NEPC is evaluated from the numerical IGA calculations by:

$$\tilde{d}^* = \frac{\sqrt{\frac{\frac{1}{2}\phi_1 \cdot \mathbf{K}_{\phi\phi} \cdot \phi_1}{\frac{1}{2}\mathbf{u}_1 \cdot \mathbf{K}_{uu} \cdot \mathbf{u}_1}}}{\sqrt{\frac{\frac{1}{2}\phi_2 \cdot \mathbf{K}_{\phi\phi} \cdot \phi_2}{\frac{1}{2}\mathbf{u}_2 \cdot \mathbf{K}_{uu} \cdot \mathbf{u}_2}}} \tag{3.97}$$

where ϕ and $\mathbf{u}$ are the vector solutions of the linear system (3.52), and the subscript 1 and 2 correspond to piezo-flexoelectric effects and only piezoelectric effects, respectively. A comparison between the analytical and the numerical NEPC solutions are provided in Fig. 3.5 for a fixed 240×24 B-Spline elements of order 2 and varying values of the normalized thickness $h' = -eh/\mu$. A very good agreement between both solutions can be appreciated.

3.5.1.2 Dynamic benchmark

In this next example, we consider the free vibration of a cantilever beam with square section where the left end is fixed and the other boundaries are free. The objective is to validate the IGA scheme in the dynamic case. Here, the electromechanical coupling is not taken into account. The analytical expression of the natural frequencies f_r are given by [207]:

$$f_r = \frac{\lambda_r^2}{2\pi L^2}\sqrt{\frac{Eh^2}{12\rho}} \quad (Hz) \tag{3.98}$$

where r is the frequency number, $I = bh^3/12$ ($b = h$ is width) is the moment of inertia for a square section, ρ is the density, and λ_r are the roots of the characteristic equation:

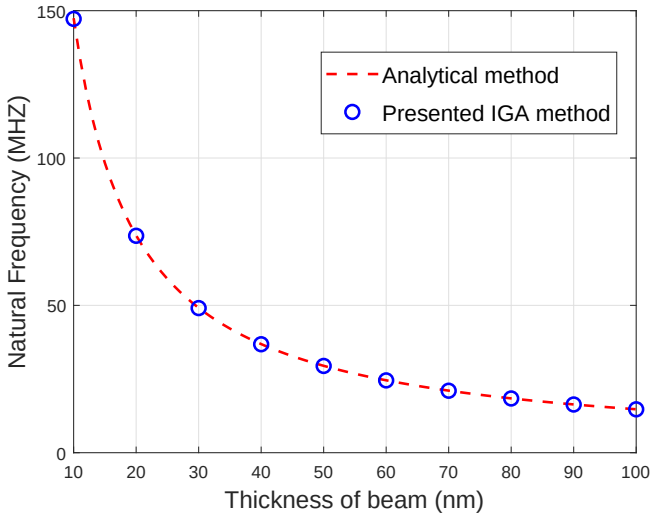

Figure 3.6: Natural frequency of an elastic beam: comparison between exact and present IGA solutions.

$$1+\cos\lambda_r\cosh\lambda_r=0 \tag{3.99}$$

Here, λ_1 is found numerically as $\lambda_1 = 1.875$. The other parameters are the same as in the previous example. The first natural frequency is computed from the IGA calculation by solving the eigenvalue problem

$$\mathbf{K}_{uu}-\omega_r^2\mathbf{M}=0,\quad f_1=\frac{\omega_1}{2\pi}. \tag{3.100}$$

A comparison between the present IGA and the exact solution is provided in Fig. 3.6, showing a very good agreement.

3.5.2 Frequency response of a flexoelectric beam

In this example, the effects of flexoelectricity on dynamic voltage, power and displacement responses of a beam are investigated. The voltage and displacement responses are defined as the absolute value of voltage and and displacement at the top right corner of the structure. The power is obtained as $P=\frac{\bar{\Phi}^2}{R}$, where $\bar{\Phi}$ is the potential at the top right corner of the structure. Both open and close-circuit boundary conditions, as depicted in Fig. 3.4 (a) and (b), are considered. The dimensions of the beam are $h = 200$ nm and $L = 2000$ nm. The left end is clamped and an excitation force $F(\omega)=F_y e^{j\omega t}$ is prescribed on the top right corner in the y-direction with F_y = 1 N. The effect of the resistor R is taken into account through Eq. (3.72). The material parameters of the material composing the beam are taken from [167] and correspond to a PZT/PZT composite. The corresponding coefficients are provided in (3.101)-(3.105). The density is taken as $\rho = 7500\ \mathrm{kg}\cdot\mathrm{m}^{-3}$.

To define the matrix $\mathbf{G}$, we follow [208], and use the definition $G_{ijmkln}=C_{ijkl}L_{mn}$, where we use $L_{mn}=\ell\delta_{mn}$. There is no general agreement on the choice of the length scale ℓ. In [200], it is recommended that ℓ should be of the order of L, L being the typical characteristic length of heterogeneities. Then, we have chosen here $\ell = 10^{-8}$ m. Other authors have used such values, see e.g. [60]. In [200], Askes et al. suggested the heuristic rule for the dynamic length parameter $\ell_d > \ell$. In their work, they employed a gradient elasticity model to fit wave dispersion results of carbon nanotubes based on molecular dynamics (MD) obtained by Wang

et al. [209], and found a good agreement with the MD results when ℓ_d is in the range 3ℓ - 35ℓ. Then, in this work, ℓ_d was chosen as $\ell_d = 10\ell$. The modal damping ratios in (3.66) are found as $\xi_1 = \xi_2 = 0.01$. For the close-circuit of Fig. 3.4 (b), the potential on the top and bottom surfaces is enforced to be equal using a penalty method and the penalty parameter is taken as 10^2 (see e.g. [210]).

The evolution of the voltage, $y-$displacement and power frequency responses is shown in Fig. 3.7, when the value of the resistor R varies. First, we can notice that the use of a flexoelectric material instead of a purely piezoelectric creates a voltage response while the purely piezoelectric material creates zero voltage (see Fig. 3.7). On the contrary, the displacement response is significantly larger when considering non-flexoelectric material, and a small difference in the resonance frequency can be noticed. In Fig. 3.7(c), the amplitude of the output power decreases with respect to the increasing resistors, while the increase of output voltage is not significant.

$$\mathbf{C}_1 = \begin{bmatrix} 132.1 & 84 & 0 \\ 84 & 155.6 & 0 \\ 0 & 0 & 35.8 \end{bmatrix} (\text{GPa}) \tag{3.101}$$

$$\boldsymbol{\mu} = \begin{bmatrix} 1.365 & 1.365 & 0 & 0 & 0 & 0 \\ 0 & 0 & 0 & 2.641 & 2.641 & 0 \end{bmatrix} (\times 10^{-4} \text{C} \cdot \text{m}^{-1}) \tag{3.102}$$

$$\boldsymbol{e} = \begin{bmatrix} -0.5217 & -0.5217 & 0 \\ 0 & 0 & 0 \end{bmatrix} (\text{C} \cdot \text{m}^{-2}) \tag{3.103}$$

$$\boldsymbol{\alpha}_1 = \begin{bmatrix} 2.102 & 0 \\ 0 & 4.065 \end{bmatrix} (\text{nC}^2 \cdot \text{N}^{-1} \cdot \text{m}^{-2}) \tag{3.104}$$

$$\mathbf{g} = \ell^2 \begin{bmatrix} 132.1 & 0 & 0 & 84 & 0 & 0 \\ 0 & 132.1 & 84 & 0 & 0 & 0 \\ 0 & 84 & 132.1 & 0 & 0 & 0 \\ 84 & 0 & 0 & 132.1 & 0 & 0 \\ 0 & 0 & 0 & 0 & 35.8 & 0 \\ 0 & 0 & 0 & 0 & 0 & 35.8 \end{bmatrix} \times 10^9 \tag{3.105}$$

In this last test, we evaluate the variation of the dynamic response of the system with respect to the dynamic length scale parameter ℓ_d, which is varied from 5ℓ to 30ℓ ($\ell = 10^{-8}$ m). Results are presented in Fig. 3.8. We can note that changing ℓ_d has no influence on the amplitude of voltage and displacement responses, and only small influence on the resonance frequency.

3.5.3 Dynamic behavior of a flexoelectric beam with periodic wavy shape

In this example, the dynamic response of a flexoelectric beam with periodic wavy shape is investigated, to illustrate the present numerical framework for more complex structural geometries. The geometry of the beam is described in Fig. 3.9. The beam geometry is defined by 4×1 patterns of dimensions $H_1 \times H_2$ as described in Fig. 3.9 (b) and parameterized by a parameter h. The dimensions of the rectangular domain containing the patch are $H_1 = 200$ nm and $H_2 = 300$ nm. The geometric data, i.e. the coordinates of the control points defining the different NURBS curves of one cell, are provided in Table 3.2. Both open and closed circuit

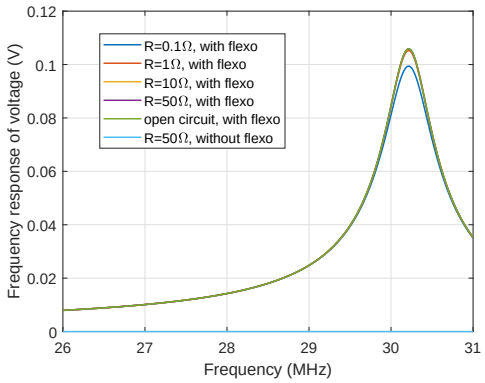

(a) Voltage frequency response

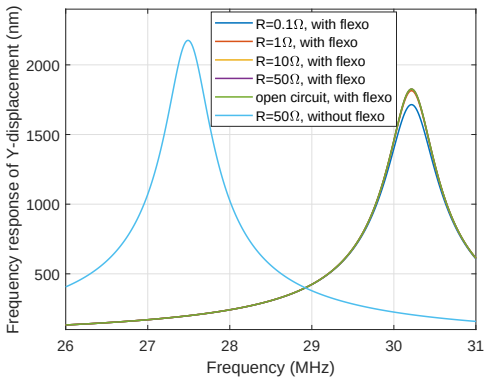

(b) y-displacement frequency response

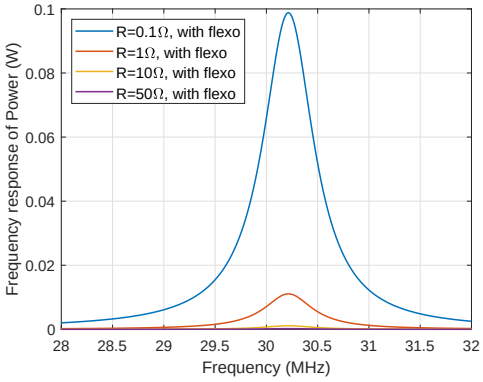

(c) Power frequency response

Figure 3.7: (a) Voltage, (b) displacement and(c) power frequency responses for varying values of the resistor R in the open and close-circuit conditions.

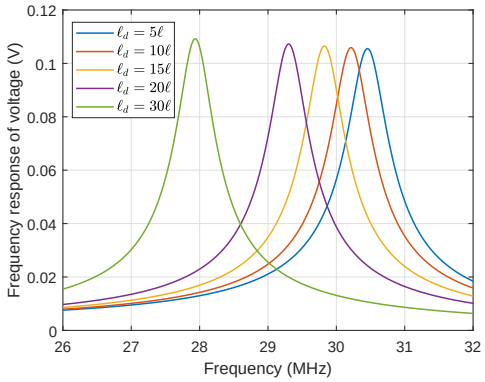

(a) Voltage frequency response

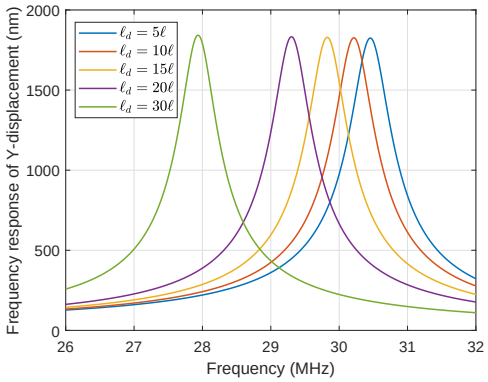

(b) y-displacement frequency response

Figure 3.8: (a) Voltage and (b) displacement frequency responses for varying values of the micro inertial ℓ_d in the open circuit conditions.

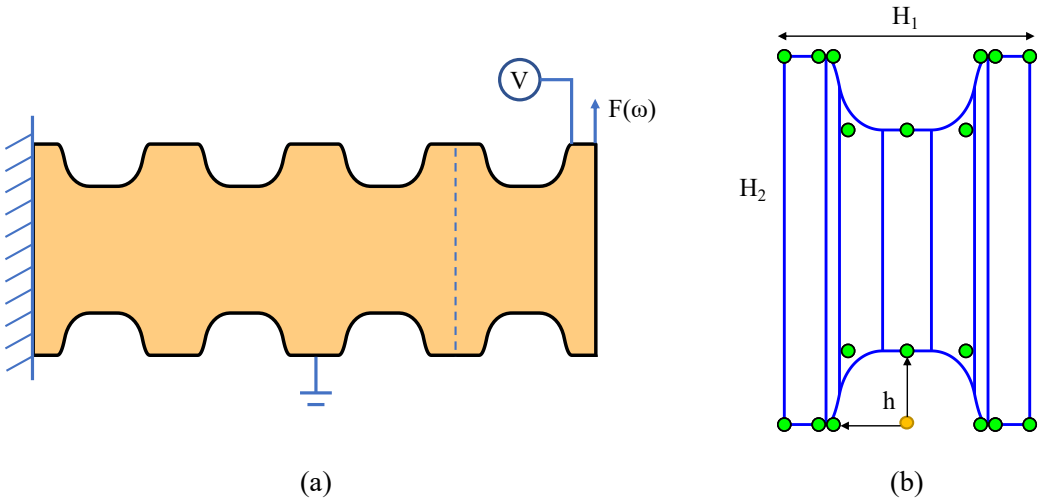

Figure 3.9: Flexoelectric beam with periodic wavy shape: (a) geometry and boundary conditions; (b) initial IGA discretization of a periodic pattern.

Table 3.2: Control points $B_{i,j}$ and weights $w_{i,j}$ for the geometry shown in Fig. 3.9.

i	$B_{i,1}$ (nm)	$w_{i,1}$	$B_{i,2}$ (nm)	$w_{i,2}$
1	(0,0)	1	(0 300)	1
2	(100-6h/5,0)	1	(100-6h/5,300)	1
3	(100-h,0)	1	(100-h,300)	1
4	(100-4h/5,h)	$\sqrt{2}/2$	(100-4h/5,300-h)	$\sqrt{2}/2$
5	(100,h)	1	(100,300-h)	1
6	(100+4h/5,h)	$\sqrt{2}/2$	(100+4h/5,300-h)	$\sqrt{2}/2$
7	(100+h,0)	1	(100+h,300)	1
8	(100+6h/5h,0)	1	(100+6h/5,300)	1
9	(200,0)	1	(200,300)	1

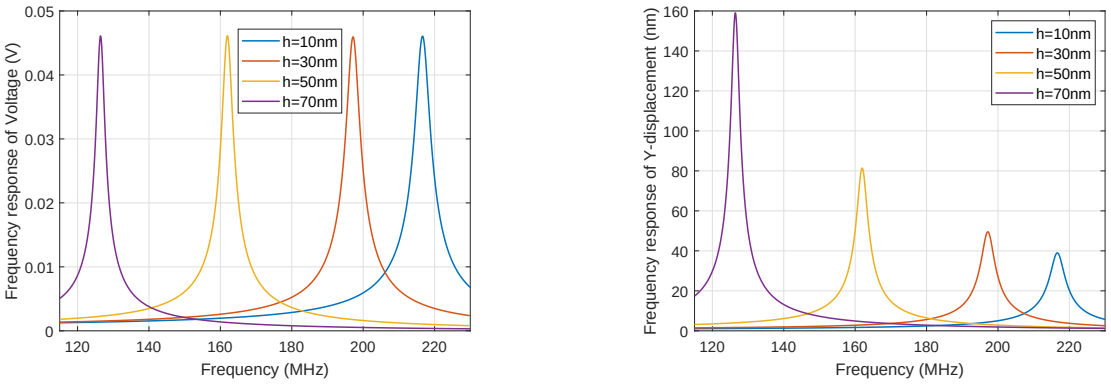

(a) Voltage frequency response

(b) y-displacement frequency response

Figure 3.10: (a) Voltage and (b) displacement frequency responses with respect to the geometrical h parameter in the open-circuit conditions.

conditions are considered, but only the open circuit boundary conditions are depicted in Fig. 3.9. The closed circuit conditions are the same than in Fig. 3.4(b). The material parameters are the same than in the previous example and are provided in (3.101)-(3.105) while the dynamic length parameter is chosen as $\ell_d = 20\ell$.

First, the variations of voltage and y-displacements frequency responses are studied for a variation of h in the open-circuit conditions. Results are shown in Fig. 3.10. It can be seen that a larger h increases displacement response while a small increase on voltage response, and with a significant decrease of the resonance frequency.

In Fig. 3.11, voltage, $y-$displacement and power frequency responses are presented for the close-circuit, for different values of resistor R and fixed value of the parameter $h = 50$ nm. We can note that in this configuration, the voltage and displacement responses monotonically increase while increasing resistors decreases the power response. This suggests that an optimal resistor value must be chosen to maximize the effects in the application of flexoelectricity to energy harvesters.

The results associated with the same configuration but for the close-circuit with $R = 0.01$ Ω are shown in Fig. 3.12. In that case, increasing the parameter h increases the voltage and power responses, but still increases the displacement response. In all cases, increasing h slightly decreases the resonance frequency. It is worth noting that in this example, varying h was done easily by simply moving the control points in the present IGA framework.

3.5.4 h-p refinement effects on flexoelectric beam with complex geometry

In this example, we investigate the effects of mesh refinement ($h-$refinement) and high-order approximation ($p-$refinement) of IGA to the dynamic analysis of flexoelectric structures with complex geometry, which could arise e.g. from CAD (Computer Aided Design). The geometry and boundary conditions of the beam are shown in Fig. 3.13. The geometric data, i.e. the control points defining the different NURBS curves, are provided in Table 3.3. The material parameters are listed in (3.101)-(3.105).

The maximum voltage frequency response is defined as the absolute value of voltage on the first resonance frequency at the top right corner of the structure. The convergence of the maximum voltage frequency response with respect to $h-$ and $p-$refinements is presented in Fig. 3.14. We can appreciate the convergence of the solution using either $h-$ or $p-$refinement. We can also observe from Fig. 3.14(a) that increasing the order of approximation p may be advantageous to quickly reach convergence, as compared to mesh refinement, which converges more slowly (see Fig. 3.14(b)). This constitutes an advantage over classical FEM, as increasing

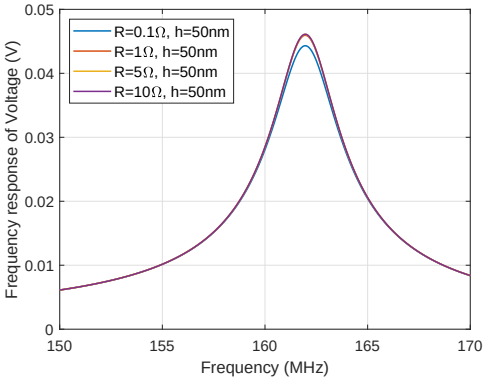

(a) Voltage frequency response

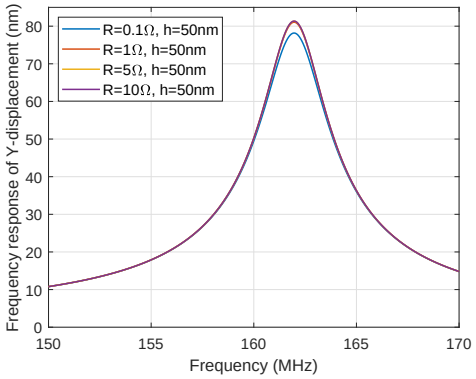

(b) y-displacement frequency response

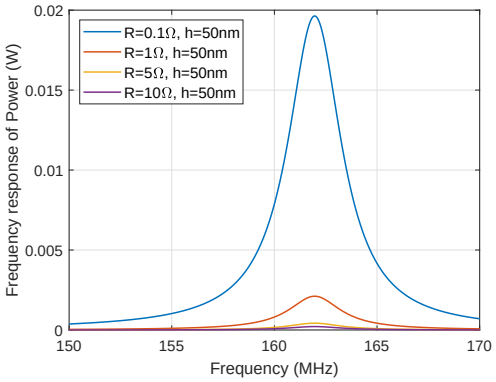

(c) Power frequency response

Figure 3.11: (a) Voltage, (b) displacement and (c) power frequency responses with respect to resistor R for a fixed radius $h = 50$ nm in the close-circuit conditions.

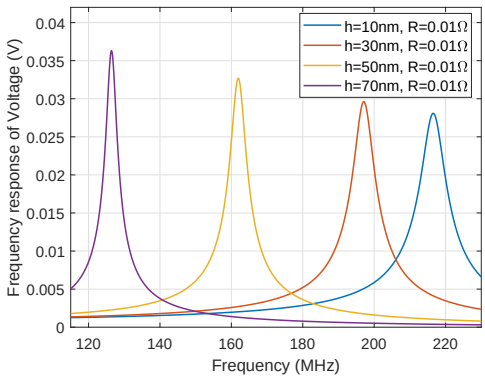

(a) Voltage frequency response

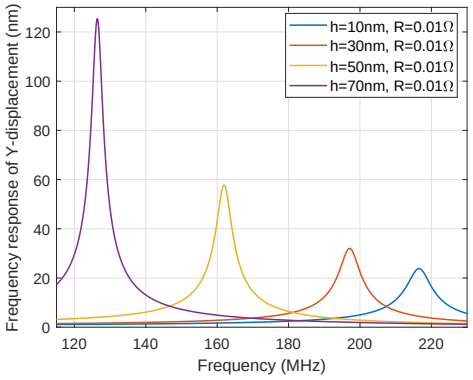

(b) y-displacement frequency response

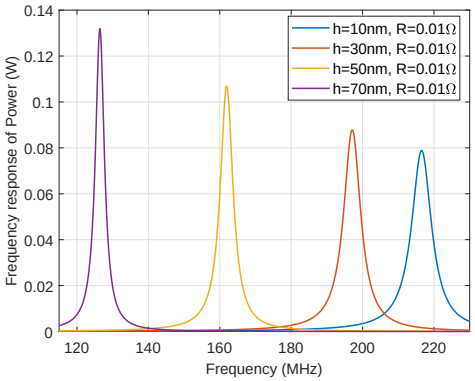

(c) Power frequency response

Figure 3.12: Voltage and displacement and power frequency responses with respect to geometrical parameter h for resistor $R = 0.01\ \Omega$ in the close-circuit conditions

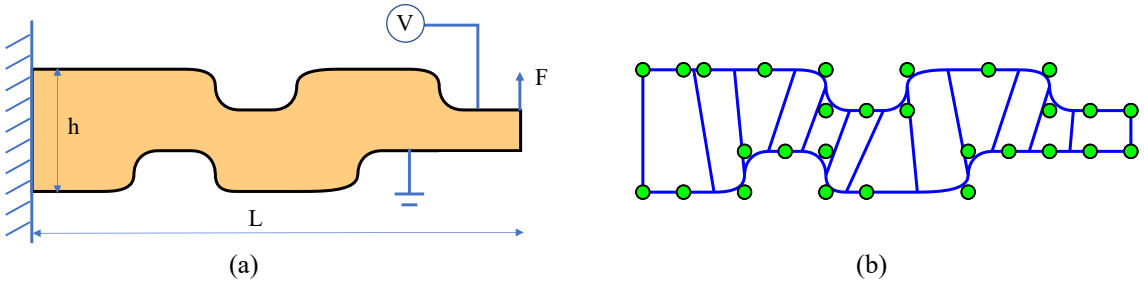

Figure 3.13: Flexoelectric beam with complex geometry: (a) geometry and boundary conditions; (b) initial IGA discretization.

Table 3.3: Control points $B_{i,j}$ and weights $w_{i,j}$ for the geometry shown in Fig. 3.13

i	$B_{i,1}(\times 10$ nm$)$	$w_{i,1}$	$B_{i,2}(\times 10$ nm$)$	$w_{i,2}$
1	(0,0)	1	(0,6)	1
2	(2,0)	1	(2,6)	1
3	(5,0)	1	(3,6)	1
4	(5,2)	$1/\sqrt{2}$	(6,6)	1
5	(7,2)	1	(9,6)	1
6	(9,2)	$1/\sqrt{2}$	(9,4)	$1/\sqrt{2}$
7	(9,0)	1	(11,4)	1
8	(11,0)	1	(13,4)	$1/\sqrt{2}$
9	(16,0)	1	(13,6)	1
10	(16,2)	$1/\sqrt{2}$	(17,6)	1
11	(18,2)	1	(20,6)	1
12	(20,2)	1	(20,4)	$1/\sqrt{2}$
13	(22,2)	1	(22,4)	1
14	(24,2)	1	(24,4)	1

the order in FEM, especially considering C^1 continuity, introduces an intractable complexity.

As is shown in Fig. 3.14(a), the maximum voltage frequency response converge to a constant value for each mesh when order $p \geq 3$. It is due to C^1 continuity requirement for flexoelectricity, where the strain gradient is calculated by second derivative of displacement basis functions. For $p = 2$, the IGA elements are exactly 'constant strain gradient states', and it is possible to be discontinuous strain gradient values among elements, especially for coarse mesh. While for order $p \geq 3$, it guarantees the smooth strain gradient variation among elements, and the influence of higher order elevation won't be as pronounced as the first one. It is worth to mention that, the knot insertion on knot vector $\boldsymbol{\xi}$ is done when construct the initial IGA geometry, although p-refinement is performed, the continuity of the basis function at internal knots remains unchanged, as is said in [103]. In addition, different number of degree of freedom for each mesh will lead to different converging maximum voltage frequency responses.

3.5.5 C^1 continuous multi-patch beam with circular voids

In this example, we consider a beam with four circular voids, where the beam geometry is constructed by 18 NURBS patches, as shown in Fig. 3.15. There are 21 common edges marked in blue and 30 vertices. We also note 10 extraordinary vertices [v_3, v_4, v_5, v_8, v_{13}, v_{15}, v_{17}, v_{20}, v_{25}, v_{27}], and each is contained in 3 or 4 patches. For multiple patches (more than 2) coupling, the main idea is similar to the two-patch case. We then construct C^1-smooth geometrically

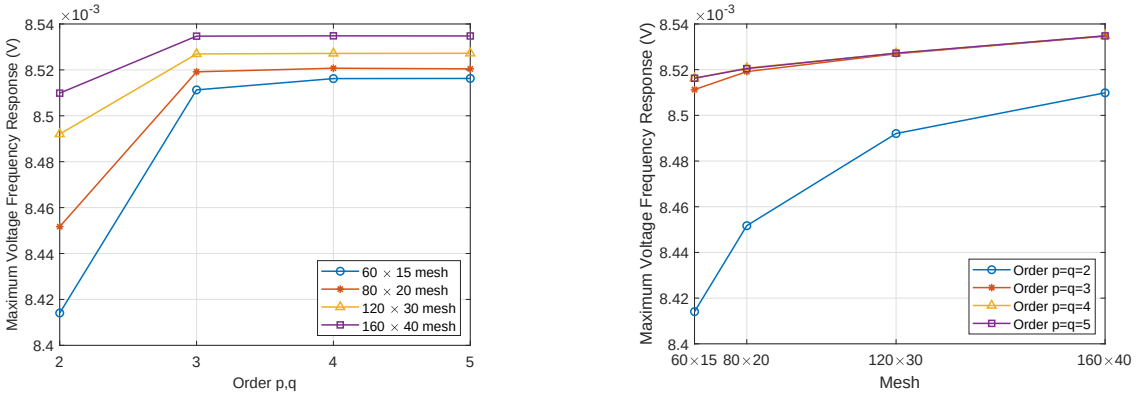

Figure 3.14: Voltage frequency response on the first resonance with respect to (a) h-refinements and (b) $p-$refinement for open-circuit conditions.

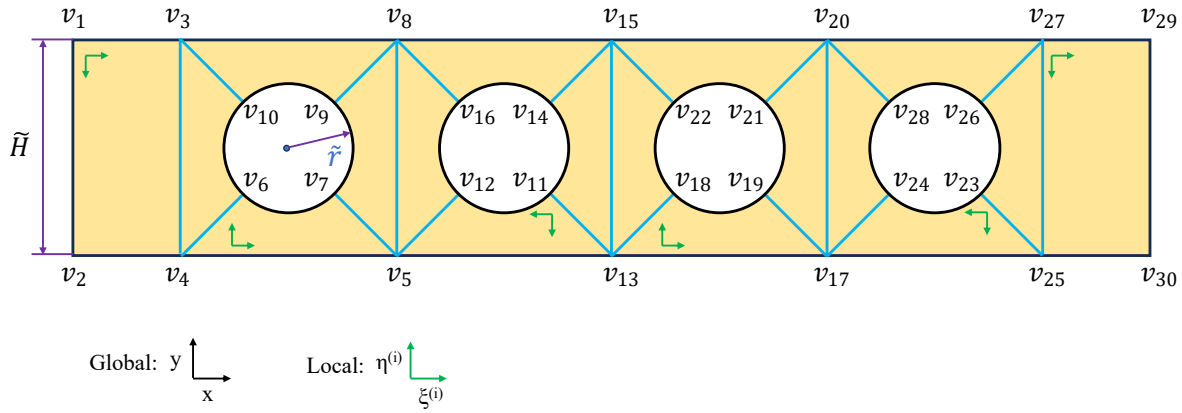

Figure 3.15: Beam with 4 circular voids, constructed by 18 patches

continuous isogeometric functions as described in section 3.4. The derivatives of several new basis across the common edges among patches are shown in Fig. 3.16. In Fig. 3.16, (a) and (b) present a typical derivatives of new basis across patch interface parallel to ξ-direction, while in (c) and (d), (e) and (f), however there are extraordinary new basis supporting the multiple interconnected interfaces among patches. All of them are local support.

With C^1 continuous isogeometric functions constructed on multi-patch domain, we then investigate the dynamic effects of this flexoelectric beam with circular voids. The height of beam is $\tilde{H} = 0.1\mu$m and length 0.5μm. The beam is made of centrosymmetric flexoelectric (non-piezoelectric) material $SrTiO_3$ (STO), whose parameters are given in (3.106)-(3.109). The density is $\rho = 5120$ kg $\cdot$ m^{-3}. The length scales are $\ell = 1 \times 10^{-8}$ m and $\ell_d = 10\ell$. The open circuit conditions are considered where the left edge $(v_1 - v_2)$ is fixed and grounded, while the excitation force $F(\omega) = F_y e^{j\omega t}$ is imposed on the down right corner (v_{30}) in the y-direction with F_y = -1 N. The degree of isogeometric function is set as $p = q = 3$ and the beam is discretized by 17608 control points, wherein the number of new basis of second kind is 680 which construct the C^1 continuous isogeometric functions across the common interfaces of 18 patches.

The evolution of the maximum voltage and $y-$displacement frequency responses are shown in Fig. 3.17, when the value of the radius $\tilde{r}$ varies. We can see from Fig. 3.17 that both the first resonant displacements and voltages increase with the radius of voids increasing, since

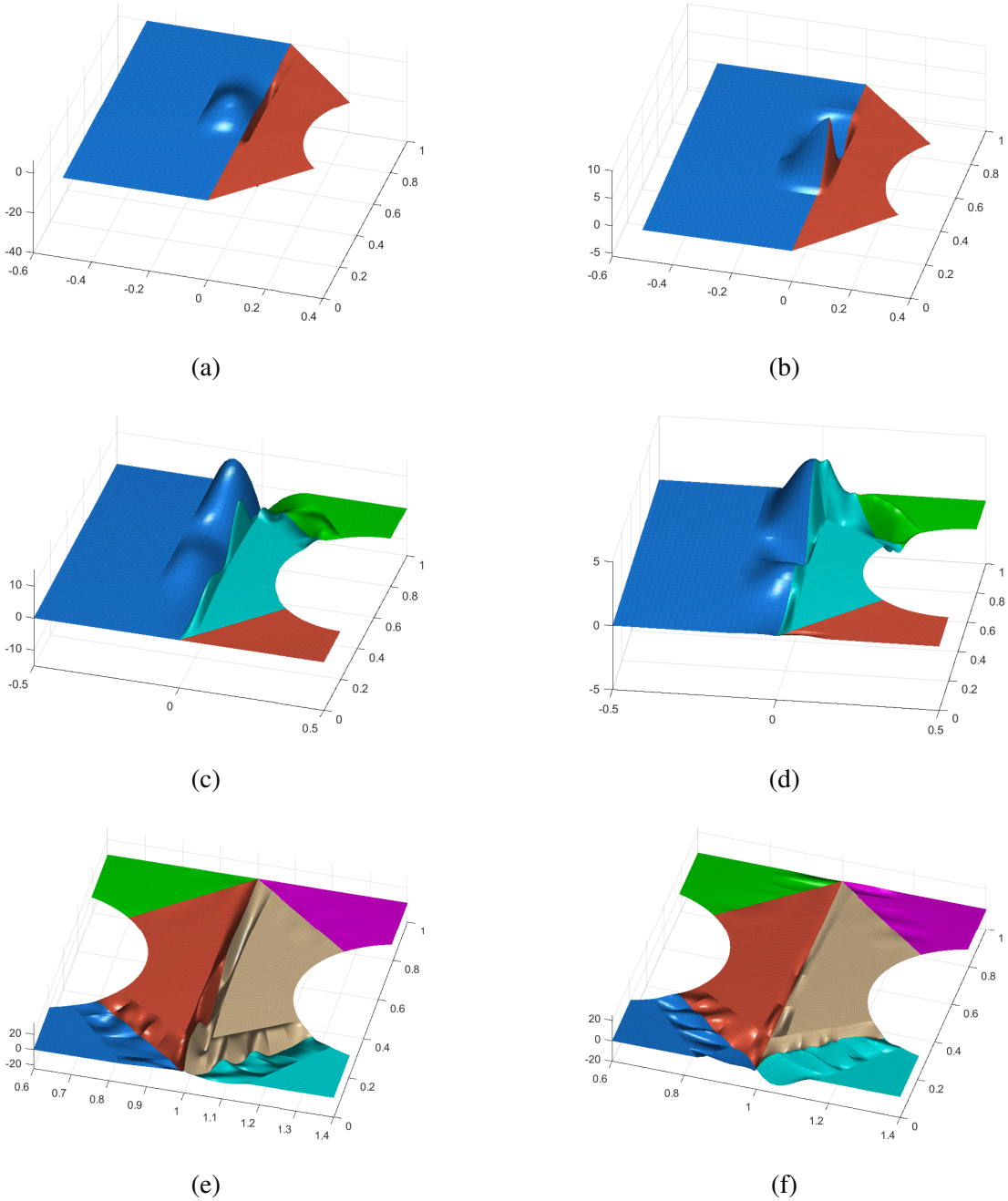

(a) (b)

(c) (d)

(e) (f)

Figure 3.16: The new basis of the second kind, x and y derivatives across the patches' common edges, wherein first row $v_3 - v_4$, second row ($v_3 - v_4$, $v_3 - v_{10}$, $v_4 - v_6$), third row ($v_5 - v_7$, $v_5 - v_8$, $v_5 - v_{12}$, $v_8 - v_9$, $v_8 - v_{16}$): (a) (c) (e) $\frac{dR}{dx}$; (b) (d) (f) $\frac{dR}{dy}$

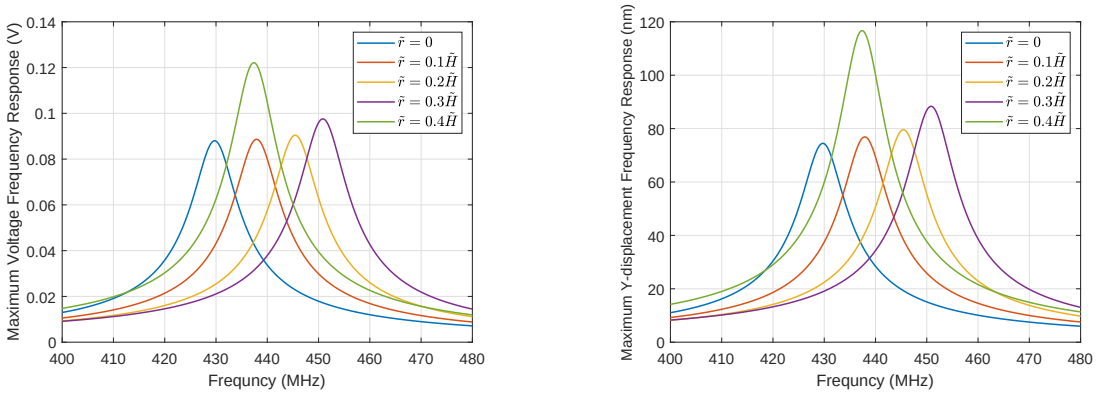

(a) (b)

Figure 3.17: (a) Voltage and (b) y-displacement frequency responses with respect to radius $\tilde{r}$ of circular void in the open-circuit conditions

the larger voids induce greater areas of heterogeneity, resulting in the improvement of resonant voltages. However, the first resonance frequency increase then decrease as the radius of voids changes from 0 to $0.4\tilde{H}$. It should be note that the case of $\tilde{r}=0$ is calculated by one-patch NURBS surface. It indicates that the constructed C^1 continuous multi-patch beam is consistent to the computation of one-patch cases. We can also observe from Fig. 3.18 that the maximum voltages of the first resonance converge with mesh refinement.

$$\mathbf{C}_1 = \begin{bmatrix} 319 & 100 & 0 \\ 100 & 319 & 0 \\ 0 & 0 & 110 \end{bmatrix} (\text{GPa}) \tag{3.106}$$

$$\boldsymbol{\mu} = \begin{bmatrix} 0.2 & 0 & 7 & 0 & 0 & 5.8 \\ 0 & 7 & 0 & 0.2 & 5.8 & 0 \end{bmatrix} (\text{nC}\cdot\text{m}^{-1}) \tag{3.107}$$

$$\boldsymbol{\alpha}_1 = \begin{bmatrix} 2.656 & 0 \\ 0 & 2.656 \end{bmatrix} (\text{nC}^2\cdot\text{N}^{-1}\cdot\text{m}^{-2}) \tag{3.108}$$

$$\mathbf{g} = \ell^2 \begin{bmatrix} 319 & 0 & 0 & 100 & 0 & 0 \\ 0 & 319 & 100 & 0 & 0 & 0 \\ 0 & 100 & 319 & 0 & 0 & 0 \\ 100 & 0 & 0 & 319 & 0 & 0 \\ 0 & 0 & 0 & 0 & 110 & 0 \\ 0 & 0 & 0 & 0 & 0 & 110 \end{bmatrix} \times 10^9 \tag{3.109}$$

3.6 Conclusion

In this work, we developed an isogeometric analysis (IGA) framework to solve the dynamic response of flexoelectric energy harvesters for arbitrary geometries, in the frequency domain, including the inertial effect of deformation gradients. As compared to the previous related works available in the literature, the IGA discretization was proposed here for the first time to solve dynamic flexoelectric problems in the frequency domain. The conditions of both open and close-circuits were formulated. The potential of the present formulation has been applied to

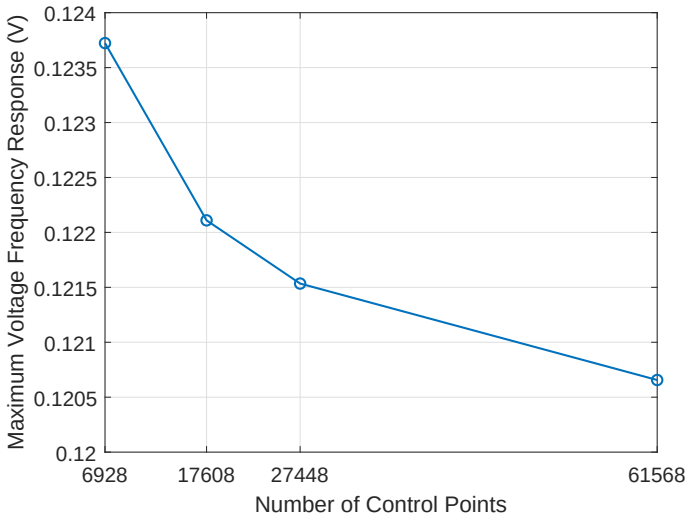

Figure 3.18: Voltage frequency responses on the first resonance with respect to h-refinements for open-circuit conditions.

evaluate the sensitivity of different parameters such as load resistors, flexoelectricity, dynamic scale parameter and geometric features on the frequency response of output voltage, power and displacements of beam-like dynamic energy harvesters, possibly including structural geometrical features. It was shown that using a flexoelectric material instead of a piezoelectric material has a critical influence on the voltage response of the energy harvester in open circuit conditions, showing the optimal resistive loads in the close-circuits. We also observe that the dynamic length parameter related to the gradient inertial term has only a small influence on the numerical results. Then, we could conclude that creating large holes in a beam-like structure made of a flexoelectric material can significantly increase voltage, power and displacement responses in a dynamic energy harvester. Finally, the advantages of IGA for $h-$ and $p-$refinement in the present flexoelectric context with applications to dynamic loads have been demonstrated for complex geometries.

As another contribution, we proposed the construction of C^1 continuous isogeometric functions for multi-patch domains. The C^1-continuity across the common interfaces of multi-patch domains is constructed by considering geometric continuity of surfaces where the C^1-continuity of isogeometric functions is achieved by ensuring that their geometric smoothness are of the same order as that of their graph surfaces. Finally, a beam with 4 circular voids, comprised of 18 patches, was constructed to ensure C^1 continuity. The numerical results showed that the constructed C^1 continuous multi-patch beam is consistent to the one of one-patch cases. The first resonant displacements and voltages of the flexoelectric beam with circular voids increase with the radius of voids increasing, while the solution of the multi-patch beam converges with mesh refinement.

Chapter 4

Topology optimization of direct and converse flexoelectric composites using computational homogenization

As concluded in previous chapter, the effective direct and converse flexoelectric properties of periodic piezoelectric composites can be tuned to be much higher than the constituents, by creating a heterogeneity through asymmetric geometric inclusions and multiple constitutive materials. This serves as a motivation for our research in optimization designs of flexoelectric properties in piezoelectric microstructures.

In this chapter, we present a topology optimization framework to design periodic composites comprised of piezoelectric constituents that exhibit large direct and converse flexoelectric constants, respectively. This methodology leverages a representative volume element (RVE)-based computational homogenization approach that enables the analysis of periodic composites where the characteristic dimensions of the microstructure are significantly smaller than those of the structure, and as such requires only the optimization of a single RVE rather than that of the entire structure. We utilize this approach to formulate two topology optimization problems to enhance respectively direct and converse flexoelectric constants of micro structure for piezoelectric composites, and then analyze the enhancement in direct and converse flexoelectric constants that can be achieved in different types of PZT-based composites, including hard-hard (PZT-PZT), and hard-soft (PZT-polymer composite, and porous PZT) structures. We show that it is theoretically possible to obtain optimized designs of composites with apparent direct and converse flexoelectric properties 1-2 orders of magnitude larger than ones obtained with naive guess designs. We also identify different mechanisms governing the enhanced electromechanical couplings, which can arise either from an enhancement of effective piezoelectricity in the RVE for PZT-PZT composites, or from a more subtle interplay involving the enhancement of effective piezoelectric and dielectric properties coupled with a reduction in mechanical compliance for PZT-polymer and porous PZT RVEs.

This chapter is adapted from the published articles [167, 168].

4.1 SIMP topology optimization for direct flexoelectric composites

In this section, we propose a topology optimization framework to design periodic composites comprising piezoelectric constituents that exhibit large direct flexoelectric constants. The approach leverages the computational homogenization framework for effective flexoelectric materials developed in Chapter 2 of this thesis that enables the estimation of the (apparent) effective flexoelectric properties of a periodic composite made of piezoelectric phases. The adjoint

sensitivity expressions are derived in this context and a SIMP (Solid Isotropic Material with Penalization) topology optimization framework is developed. This approach allows us to restrict the analysis to a single representative volume element (RVE) that describes the microstructure, and importantly does not require the optimization of the fully detailed structure. This presents significant advantages when there is scale separation, i.e. when the characteristic dimensions of the heterogeneities are negligible as compared to those of the structure.

4.1.1 Topology optimization problem formulation

Here we formulate the topology optimization problem to maximize the absolute values of the flexoelectric tensor components in (2.89) and (2.110) in Chapter 2. First, the periodic unit cell is discretized into N_e finite elements which match the mesh used for solving the electromechanical problem defined in the previous section. We define the material density ρ_e in each element e, $e = 1,2,...,N_e$ such that $\rho_e = 0$ is associated with the inclusion/void phase and $\rho = 1$ is associated with the matrix phase. The topology optimization is formulated as follows:

$$\begin{aligned} \text{Maximize}: \quad & |\bar{\mathbb{F}}_{ijkl}(\boldsymbol{\rho})| \\ \text{subject}: \quad & \mathbf{KU} = \mathbf{F} \\ : \quad & \textstyle\sum_{e=1}^{N_e} \rho_e v_e / (\sum_{e=1}^{N_e} v_e) = f \\ & 0 \leq \rho_e \leq 1, \;\; e = 1,2,...,N_e \end{aligned} \tag{4.1}$$

The discrete system $\mathbf{KU} = \mathbf{F}$ is defined in Eqs. (2.65)-(2.70) in Chapter 2. Above, v_e is the volume of an element e and f is the inclusion volume fraction.

We use the SIMP method [21, 22, 23] to solve the problem. In this framework, the local material properties are interpolated with respect to the local densities in a continuous manner, using penalty exponents to enforce local densities to converge to values close to 0 or 1. Selection of exponents has been investigated in [211]. For composites made of two phases, we use the following expression:

$$\begin{aligned} [C_{ijkl}(\rho)] &= \rho^{pc}[C^1_{ijkl}] + (1-\rho^{pc})[C^2_{ijkl}] \\ [\alpha_{ij}(\rho)] &= \rho^{pa}[\alpha^1_{ij}] + (1-\rho^{pa})[\alpha^2_{ij}] \\ [\mathcal{E}_{kij}(\rho)] &= \rho^{pe}[\mathcal{E}^1_{kij}] + (1-\rho^{pe})[\mathcal{E}^2_{kij}] \end{aligned} \tag{4.2}$$

where the superscript 1 and 2 are associated with phase 1 and phase 2, respectively and pc, pa and pe are penalty exponents. In most of the numerical examples, these values are chosen as $pc = pa = pe = 3$, except in a few cases where $pe = 4$ is sometimes used to improve the convergence. For the optimization of porous materials, a fictitious material with small values of the (stiffness, dielectric, piezoelectric) properties is used to mimic the void phase.

The above problem (4.1) requires evaluating the gradient of the objective function with respect to the local densities (subsequently referred to as sensitivities). The objective function, i.e. the effective flexoelectric tensor, is written in matrix form as (see section 2.3.2):

$$[\bar{\mathbb{F}}(\rho)] = \langle (\mathbf{B}^0)^T : \mathbb{C} : \tilde{\mathbf{A}}^1 - (\mathbf{h}^0)^T \cdot \mathcal{E} : \tilde{\mathbf{A}}^1 - (\mathbf{B}^0)^T : \mathcal{E}^T \cdot \tilde{\mathbf{D}}^1 - (\mathbf{h}^0)^T \cdot \boldsymbol{\alpha} \cdot \tilde{\mathbf{D}}^1 \rangle \tag{4.3}$$

where we have omitted the dependence to the coordinates $\mathbf{x}$ and design variable ρ to alleviate the notations. The developed expressions for the sensitivities are given the next section. The optimization problem (4.1) is solved by the Conservative Convex Separable Approximations (CCSA) optimizer [144].

A useful parameter to compare different piezoelectric and flexoelectric materials is the electromechanical coupling coefficient denoted as $\mathcal{K}$. The coupling coefficient is a measure of the

conversion efficiency between mechanical and electrical energy using the piezoelectric material. It takes the same indices as the piezoelectric coefficient $\mathcal{E}$ and is formulated as [212]

$$\bar{\mathcal{K}}_{iJ} = \frac{\bar{\mathcal{D}}_{iJ}}{\sqrt{\bar{e}_{ii}\bar{\mathbb{S}}_{JJ}}} \tag{4.4}$$

with

$$[\bar{\mathcal{D}}] = [\bar{\mathcal{E}}] : [\bar{\mathbb{C}}]^{-1},\ [\bar{\mathbf{e}}] = ([\bar{\mathcal{E}}] : [\bar{\mathbb{C}}]^{-1} : [\bar{\mathcal{E}}]^T + [\bar{\alpha}]) : [\bar{\mathbb{C}}]^{-1},\ [\bar{\mathbb{S}}] = [\bar{\mathbb{C}}]^{-1}, \tag{4.5}$$

where $\bar{\mathcal{D}}$, $\bar{\mathbf{e}}$ and $\bar{\mathbb{S}}$ denote the piezoelectric coefficient, dielectric constant and compliance matrix, respectively.

4.1.2 Numerical analysis of sensitivity

The gradient of flexoelectric tensor $[\bar{\mathbb{F}}]$ with respect to ρ, is expressed as:

$$\begin{aligned}
\frac{\partial[\bar{\mathbb{F}}]}{\partial\rho} =& \langle \frac{\partial((\mathbf{B}^0)^T[\mathbb{C}(\rho)]\tilde{\mathbf{A}}^1)}{\partial\rho} - \frac{\partial((\mathbf{h}^0)^T[\mathcal{E}(\rho)]\tilde{\mathbf{A}}^1)}{\partial\rho} - \frac{\partial((\mathbf{B}^0)^T[\mathcal{E}(\rho)]^T\tilde{\mathbf{D}}^1)}{\partial\rho} - \frac{\partial((\mathbf{h}^0)^T[\boldsymbol{\alpha}(\rho)]\tilde{\mathbf{D}}^1)}{\partial\rho} \rangle \\
=& \langle \frac{\partial\{(\mathbf{V}_u^T)\mathbf{B}_u^T[\mathbb{C}(\rho)]\mathbf{B}_u(\mathbf{W}_u - \mathbf{W}_u{}^x)\}}{\partial\rho} + \frac{\partial\{(\mathbf{V}_\phi{}^T)\mathbf{B}_\phi^T[\mathcal{E}(\rho)]\mathbf{B}_u(\mathbf{W}_u - \mathbf{W}_u{}^x)\}}{\partial\rho} \\
&+ \frac{\partial\{(\mathbf{V}_u^T)\mathbf{B}_u^T[\mathcal{E}(\rho)]^T\mathbf{B}_\phi(\mathbf{W}_\phi - \mathbf{W}_\phi{}^x)\}}{\partial\rho} - \frac{\partial\{(\mathbf{V}_\phi{}^T)\mathbf{B}_\phi^T[\boldsymbol{\alpha}(\rho)]\mathbf{B}_\phi(\mathbf{W}_\phi - \mathbf{W}_\phi{}^x)\}}{\partial\rho} \rangle
\end{aligned} \tag{4.6}$$

Expanding Eq. (4.6), we have

$$\begin{aligned}
\frac{\partial[\bar{\mathbb{F}}]}{\partial\rho} =& \langle \frac{\partial(\mathbf{V}_u^T)}{\partial\rho}\mathbf{B}_u^T[\mathbb{C}(\rho)]\mathbf{B}_u(\mathbf{W}_u - \mathbf{W}_u{}^x) + (\mathbf{V}_u)^T\frac{\partial(\mathbf{B}_u^T[\mathbb{C}(\rho)]\mathbf{B}_u)}{\partial\rho}(\mathbf{W}_u - \mathbf{W}_u{}^x) \\
&+ (\mathbf{V}_u^T)\mathbf{B}_u^T[\mathbb{C}(\rho)]\mathbf{B}_u\frac{\partial(\mathbf{W}_u - \mathbf{W}_u{}^x)}{\partial\rho} + \{\frac{\partial(\mathbf{V}_\phi{}^T)}{\partial\rho}\mathbf{B}_\phi^T[\mathcal{E}(\rho)]\mathbf{B}_u(\mathbf{W}_u - \mathbf{W}_u{}^x) \\
&+ (\mathbf{V}_\phi)^T\frac{\partial(\mathbf{B}_\phi^T[\mathcal{E}(\rho)]\mathbf{B}_u)}{\partial\rho}(\mathbf{W}_u - \mathbf{W}_u{}^x) + (\mathbf{V}_\phi{}^T)\mathbf{B}_\phi^T[\mathcal{E}(\rho)]\mathbf{B}_u\frac{\partial(\mathbf{W}_u - \mathbf{W}_u{}^x)}{\partial\rho}\} \\
&+ \{\frac{\partial(\mathbf{V}_u^T)}{\partial\rho}\mathbf{B}_u^T[\mathcal{E}(\rho)]^T\mathbf{B}_\phi(\mathbf{W}_\phi - \mathbf{W}_\phi{}^x) + (\mathbf{V}_u)^T\frac{\partial(\mathbf{B}_u^T[\mathcal{E}(\rho)]^T\mathbf{B}_\phi)}{\partial\rho}(\mathbf{W}_\phi - \mathbf{W}_\phi{}^x) \\
&+ (\mathbf{V}_u^T)\mathbf{B}_u^T[\mathcal{E}(\rho)]^T\mathbf{B}_\phi\frac{\partial(\mathbf{W}_\phi - \mathbf{W}_\phi{}^x)}{\partial\rho}\} - \{\frac{\partial(\mathbf{V}_\phi{}^T)}{\partial\rho}\mathbf{B}_\phi^T[\boldsymbol{\alpha}(\rho)]\mathbf{B}_\phi(\mathbf{W}_\phi - \mathbf{W}_\phi{}^x) \\
&+ (\mathbf{V}_\phi)^T\frac{\partial(\mathbf{B}_\phi^T[\boldsymbol{\alpha}(\rho)]\mathbf{B}_\phi)}{\partial\rho}(\mathbf{W}_\phi - \mathbf{W}_\phi{}^x) + (\mathbf{V}_\phi{}^T)\mathbf{B}_\phi^T[\boldsymbol{\alpha}(\rho)]\mathbf{B}_\phi\frac{\partial(\mathbf{W}_\phi - \mathbf{W}_\phi{}^x)}{\partial\rho}\}\rangle
\end{aligned} \tag{4.7}$$

After rearranging Eq. (4.7), we obtain

$$\begin{aligned}\frac{\partial[\bar{\mathbb{F}}]}{\partial\rho} =& \frac{\partial(\mathbf{V}_u^T)}{\partial\rho}\left\langle \mathbf{B}_u^T[\mathbb{C}(\rho)]\mathbf{B}_u(\mathbf{W}_u-\mathbf{W}_u{}^x)+\mathbf{B}_u^T[\mathcal{E}(\rho)]^T\mathbf{B}_\phi(W_\phi-\mathbf{W}_\phi{}^x)\right\rangle \\ &+\frac{\partial(\mathbf{V}_\phi{}^T)}{\partial\rho}\left\langle \mathbf{B}_\phi^T[\mathcal{E}(\rho)]\mathbf{B}_u(\mathbf{W}_u-\mathbf{W}_u{}^x)-\mathbf{B}_\phi^T[\boldsymbol{\alpha}(\rho)]\mathbf{B}_\phi(\mathbf{W}_\phi-\mathbf{W}_\phi{}^x)\right\rangle \\ &+\left\langle (\mathbf{V}_u^T)\mathbf{B}_u^T[\mathbb{C}(\rho)]\mathbf{B}_u+(\mathbf{V}_\phi{}^T)\mathbf{B}_\phi^T[\mathcal{E}(\rho)]\mathbf{B}_u\right\rangle\frac{\partial(\mathbf{W}_u-\mathbf{W}_u{}^x)}{\partial\rho} \\ &+\left\langle (\mathbf{V}_u^T)\mathbf{B}_u^T[\mathcal{E}(\rho)]^T\mathbf{B}_\phi-(\mathbf{V}_\phi{}^T)\mathbf{B}_\phi^T[\boldsymbol{\alpha}(\rho)]\mathbf{B}_\phi\right\rangle\frac{\partial(\mathbf{W}_\phi-\mathbf{W}_\phi{}^x)}{\partial\rho} \\ &+(\mathbf{V}_u)^T\left\langle\frac{\partial(\mathbf{B}_u^T[\mathbb{C}(\rho)]\mathbf{B}_u)}{\partial x}\right\rangle(\mathbf{W}_u-\mathbf{W}_u{}^x)+(\mathbf{V}_\phi)^T\left\langle\frac{\partial(\mathbf{B}_\phi^T[\mathcal{E}(\rho)]\mathbf{B}_u)}{\partial x}\right\rangle(\mathbf{W}_u-\mathbf{W}_u{}^x) \\ &+(\mathbf{V}_u)^T\left\langle\frac{\partial(\mathbf{B}_u^T[\mathcal{E}(\rho)]^T\mathbf{B}_\phi)}{\partial\rho}\right\rangle(\mathbf{W}_\phi-\mathbf{W}_\phi{}^x)-(\mathbf{V}_\phi)^T\left\langle\frac{\partial(\mathbf{B}_\phi^T[\boldsymbol{\alpha}(\rho)]\mathbf{B}_\phi)}{\partial\rho}\right\rangle(\mathbf{W}_\phi-\mathbf{W}_\phi{}^x)\end{aligned} \tag{4.8}$$

The adjoint method has been widely used for sensitivity analysis of gradient-based optimization algorithm [213], also employed here. The corresponding Lagrangian function of optimization problem (4.1) is formed by introducing an adjoint vector λ as:

$$L=\overline{\mathbb{F}}+\lambda(\mathbf{KU}-\mathbf{F}) \tag{4.9}$$

Due to $\mathbf{KU}-\mathbf{F}=\mathbf{0}$, then $\lambda=[\lambda_i,\mu_i](i=1,2,3)$ can take arbitrary values. Differentiating the Lagrangian function L with respect to the design variable ρ, it gives,

$$\frac{\partial L}{\partial\rho}=\frac{\partial\overline{\mathbb{F}}}{\partial\rho}+\lambda\frac{\partial(\mathbf{KU}-\mathbf{F})}{\partial\rho} \tag{4.10}$$

The $\mathbf{KU}=\mathbf{F}$ is defined in Eqs. (2.65)-(2.70) in Chapter 2. Substituting these equations into (4.10), then dividing the expression (4.8) as 4 parts, denoted by I,II,III,IV, we have:

$$\begin{aligned}\frac{\partial[\overline{\mathbb{F}}^I]}{\partial\rho} =& \frac{\partial(\mathbf{V}_u^T)}{\partial\rho}\left\langle \mathbf{B}_u^T[\mathbb{C}(\rho)]\mathbf{B}_u(\mathbf{W}_u-\mathbf{W}_u{}^x)+\mathbf{B}_u^T[\mathcal{E}(\rho)]^T\mathbf{B}_\phi(W_\phi-\mathbf{W}_\phi{}^x)\right\rangle \\ &+\frac{\partial(\mathbf{V}_\phi{}^T)}{\partial\rho}\left\langle \mathbf{B}_\phi^T[\mathcal{E}(\rho)]\mathbf{B}_u(\mathbf{W}_u-\mathbf{W}_u{}^x)-\mathbf{B}_\phi^T[\boldsymbol{\alpha}(\rho)]\mathbf{B}_\phi(\mathbf{W}_\phi-\mathbf{W}_\phi{}^x)\right\rangle \\ &+\left\{\frac{\partial(\mathbf{V}_\phi{}^T)}{\partial\rho}\mathbf{K}_{\phi\phi}+(\mathbf{V}_\phi{}^T)\frac{\partial\mathbf{K}_{\phi\phi}}{\partial\rho}+\frac{\partial(\mathbf{V}_u^T)}{\partial\rho}\mathbf{K}_{\phi u}^T+(\mathbf{V}_u^T)\frac{\partial\mathbf{K}_{\phi u}^T}{\partial\rho}\right\}\boldsymbol{\lambda}_1 \\ &+\left\{-\frac{\partial(\mathbf{V}_\phi{}^T)}{\partial\rho}\mathbf{K}_{\phi u}-(\mathbf{V}_\phi{}^T)\frac{\partial\mathbf{K}_{\phi u}}{\partial\rho}+\frac{\partial(\mathbf{V}_u^T)}{\partial\rho}\mathbf{K}_{uu}+(\mathbf{V}_u^T)\frac{\partial\mathbf{K}_{uu}}{\partial\rho}\right\}\boldsymbol{\mu}_1 \\ =& \frac{\partial(\mathbf{V}_u^T)}{\partial\rho}\left\{\langle\mathbf{B}_u^T[\mathbb{C}(\rho)]\mathbf{B}_u\rangle(\mathbf{W}_u-\mathbf{W}_u{}^x)+\langle\mathbf{B}_u^T[\mathcal{E}(\rho)]^T\mathbf{B}_\phi\rangle(W_\phi-\mathbf{W}_\phi{}^x)+\mathbf{K}_{\phi u}^T\boldsymbol{\lambda}_1+\mathbf{K}_{uu}\boldsymbol{\mu}_1\right\} \\ &+\frac{\partial(\mathbf{V}_\phi{}^T)}{\partial\rho}\left\{\langle\mathbf{B}_\phi^T[\mathcal{E}(\rho)]\mathbf{B}_u\rangle(\mathbf{W}_u-\mathbf{W}_u{}^x)-\langle\mathbf{B}_\phi^T[\boldsymbol{\alpha}(\rho)]\mathbf{B}_\phi\rangle(\mathbf{W}_\phi-\mathbf{W}_\phi{}^x)+\mathbf{K}_{\phi\phi}\boldsymbol{\lambda}_1-\mathbf{K}_{\phi u}\boldsymbol{\mu}_1\right\} \\ &+\left\{(\mathbf{V}_\phi{}^T)\frac{\partial\mathbf{K}_{\phi\phi}}{\partial\rho}+(\mathbf{V}_u^T)\frac{\partial\mathbf{K}_{\phi u}^T}{\partial\rho}\right\}\boldsymbol{\lambda}_1+\left\{-(\mathbf{V}_\phi{}^T)\frac{\partial\mathbf{K}_{\phi u}}{\partial\rho}+(\mathbf{V}_u^T)\frac{\partial\mathbf{K}_{uu}}{\partial\rho}\right\}\boldsymbol{\mu}_1\end{aligned} \tag{4.11}$$

As Eq. (4.11) holds for arbitrary vectors $\boldsymbol{\lambda}_1$ and $\boldsymbol{\mu}_1$, the adjoint vectors $\boldsymbol{\lambda}_1$ and $\boldsymbol{\mu}_1$ can be chosen as the solution of the following adjoint equation to eliminate the implicit terms $\frac{\partial(\mathbf{V}_u{}^T)}{\partial\rho}$ and $\frac{\partial(\mathbf{V}_\phi{}^T)}{\partial\rho}$. Then the corresponding adjoint problem is defined as,

$$\begin{aligned}
&\frac{\partial(\mathbf{V}_u^T)}{\partial\rho}\left\{\langle\mathbf{B}_u^T[\mathbb{C}(\rho)]\mathbf{B}_u\rangle(\mathbf{W}_u-\mathbf{W}_u{}^x)+\langle\mathbf{B}_u^T[\mathcal{E}(\rho)]^T\mathbf{B}_\phi\rangle(\mathbf{W}_\phi-\mathbf{W}_\phi{}^x)+\mathbf{K}_{\phi u}^T\boldsymbol{\lambda}_1+\mathbf{K}_{uu}\boldsymbol{\mu}_1\right\}=0\\
&\frac{\partial(\mathbf{V}_\phi{}^T)}{\partial\rho}\left\{\langle\mathbf{B}_\phi^T[\mathcal{E}(\rho)]\mathbf{B}_u\rangle(\mathbf{W}_u-\mathbf{W}_u{}^x)-\langle\mathbf{B}_\phi^T[\boldsymbol{\alpha}(\rho)]\mathbf{B}_\phi\rangle(\mathbf{W}_\phi-\mathbf{W}_\phi{}^x)+\mathbf{K}_{\phi\phi}\boldsymbol{\lambda}_1-\mathbf{K}_{\phi u}\boldsymbol{\mu}_1\right\}=0
\end{aligned}\tag{4.12}$$

and written in matrix form, gives

$$\begin{bmatrix}\mathbf{K}_{\phi\phi} & -\mathbf{K}_{\phi u}\\ \mathbf{K}_{\phi u}^T & \mathbf{K}_{uu}\end{bmatrix}\begin{bmatrix}\boldsymbol{\lambda}_1\\ \boldsymbol{\mu}_1\end{bmatrix}=-\begin{bmatrix}\langle\mathbf{B}_\phi^T[\mathcal{E}(\rho)]\mathbf{B}_u\rangle(\mathbf{W}_u-\mathbf{W}_u{}^x)-\langle\mathbf{B}_\phi^T[\alpha(\rho)]\mathbf{B}_\phi\rangle(\mathbf{W}_\phi-\mathbf{W}_\phi{}^x)\\ \langle\mathbf{B}_u^T[\mathbb{C}(\rho)]\mathbf{B}_u\rangle(\mathbf{W}_u-\mathbf{W}_u{}^x)+\langle\mathbf{B}_u^T[\xi(\rho)]^T\mathbf{B}_\phi\rangle(W_\phi-\mathbf{W}_\phi{}^x)\end{bmatrix}\tag{4.13}$$

Part *II* of (4.11) is given by

$$\begin{aligned}
\frac{\partial[\overline{\mathbb{F}}^{II}]}{\partial\rho}=&\left\langle\mathbf{V}_u^T\mathbf{B}_u^T[\mathbb{C}(\rho)]\mathbf{B}_u+\mathbf{V}_\phi^T\mathbf{B}_\phi^T[\mathcal{E}(\rho)]\mathbf{B}_u\right\rangle\frac{\partial\mathbf{W}_u}{\partial\rho}\\
&+\left\langle\mathbf{V}_u^T\mathbf{B}_u^T[\mathcal{E}(\rho)]^T\mathbf{B}_\phi-\mathbf{V}_\phi^T\mathbf{B}_\phi^T[\boldsymbol{\alpha}(\rho)]\mathbf{B}_\phi\right\rangle\frac{\partial\mathbf{W}_\phi}{\partial\rho}\\
&+\boldsymbol{\lambda}_2^T\left\{\frac{\partial\mathbf{K}_{\phi\phi}}{\partial\rho}\mathbf{W}_\phi+\mathbf{K}_{\phi\phi}\frac{\partial\mathbf{W}_\phi}{\partial\rho}+\frac{\partial\mathbf{K}_{\phi u}}{\partial\rho}\mathbf{W}_u+\mathbf{K}_{\phi u}\frac{\partial\mathbf{W}_u}{\partial\rho}-\frac{\partial\mathbf{F}_\phi}{\partial\rho}\right\}\\
&+\boldsymbol{\mu}_2^T\left\{-\frac{\partial\mathbf{K}_{\phi u}^T}{\partial\rho}\mathbf{W}_\phi-\mathbf{K}_{\phi u}^T\frac{\partial\mathbf{W}_\phi}{\partial\rho}+\frac{\partial\mathbf{K}_{uu}}{\partial\rho}\mathbf{W}_u+\mathbf{K}_{uu}\frac{\partial\mathbf{W}_u}{\partial\rho}-\frac{\partial\mathbf{F}_u}{\partial\rho}\right\}\\
=&\left\{\mathbf{V}_u^T\langle\mathbf{B}_u^T[\mathbb{C}(\rho)]\mathbf{B}_u\rangle+\mathbf{V}_\phi{}^T\langle\mathbf{B}_\phi^T[\mathcal{E}(\rho)]\mathbf{B}_u\rangle+\boldsymbol{\lambda}_2^T\mathbf{K}_{\phi u}+\boldsymbol{\mu}_2^T\mathbf{K}_{uu}\right\}\frac{\partial\mathbf{W}_u}{\partial\rho}\\
&+\left\{\mathbf{V}_u^T\langle\mathbf{B}_u^T[\mathcal{E}(\rho)]^T\mathbf{B}_\phi\rangle-\mathbf{V}_\phi^T\langle\mathbf{B}_\phi^T[\boldsymbol{\alpha}(\rho)]\mathbf{B}_\phi\rangle+\boldsymbol{\lambda}_2^T\mathbf{K}_{\phi,\phi}-\boldsymbol{\mu}_2^T\mathbf{K}_{\phi u}^T\right\}\frac{\partial\mathbf{W}_\phi}{\partial\rho}\\
&+\boldsymbol{\lambda}_2^T\left\{\frac{\partial\mathbf{K}_{\phi\phi}}{\partial\rho}\mathbf{W}_\phi+\frac{\partial\mathbf{K}_{\phi u}}{\partial\rho}\mathbf{W}_u-\frac{\partial\mathbf{F}_\phi}{\partial\rho}\right\}+\boldsymbol{\mu}_2^T\left\{-\frac{\partial\mathbf{K}_{\phi u}^T}{\partial\rho}\mathbf{W}_\phi+\frac{\partial\mathbf{K}_{uu}}{\partial\rho}\mathbf{W}_u-\frac{\partial\mathbf{F}_u}{\partial\rho}\right\}
\end{aligned}\tag{4.14}$$

The derivatives of body forces with respect to ρ must also be evaluated. Using the same method as for Part *I*, after eliminating the displacement derivatives, the adjoint problem for Eq. (4.14) reads:

$$\begin{bmatrix}\mathbf{K}_{\phi\phi} & -\mathbf{K}_{\phi u}\\ \mathbf{K}_{\phi u}^T & \mathbf{K}_{uu}\end{bmatrix}\begin{bmatrix}\boldsymbol{\lambda}_2\\ \boldsymbol{\mu}_2\end{bmatrix}=-\begin{bmatrix}\langle\mathbf{B}_\phi^T[\mathcal{E}(\rho)]\mathbf{B}_u\rangle\mathbf{V}_u-\langle\mathbf{B}_\phi^T[\boldsymbol{\alpha}(\rho)]\mathbf{B}_\phi\rangle\mathbf{V}_\phi\\ \langle\mathbf{B}_u^T[\mathbb{C}(\rho)]\mathbf{B}_u\rangle\mathbf{V}_u+\langle\mathbf{B}_u^T[\mathcal{E}(\rho)]^T\mathbf{B}_\phi\rangle\mathbf{V}_\phi\end{bmatrix}\tag{4.15}$$

Similarly:

$$
\begin{aligned}
\frac{\partial[\overline{\mathbb{F}}^{III}]}{\partial\rho} =& \left\langle (\mathbf{V}_u^T)\mathbf{B}_u^T[\mathbb{C}(\rho)]\mathbf{B}_u + (\mathbf{V}_\phi{}^T)\mathbf{B}_\phi^T[\mathcal{E}(\rho)]\mathbf{B}_u \right\rangle \left(-\frac{\partial \mathbf{W}_u^x}{\partial\rho}\right) \\
&+ \left\langle (\mathbf{V}_u^T)\mathbf{B}_u^T[\mathcal{E}(\rho)]^T\mathbf{B}_\phi - (\mathbf{V}_\phi{}^T)\mathbf{B}_\phi^T[\boldsymbol{\alpha}(\rho)]\mathbf{B}_\phi \right\rangle \left(-\frac{\partial \mathbf{W}_\phi{}^x}{\partial\rho}\right) \\
&+ \boldsymbol{\lambda}_3^T \left\{ \frac{\partial \mathbf{K}_{\phi\phi}}{\partial\rho}\mathbf{U}_\phi + \mathbf{K}_{\phi\phi}\frac{\partial \mathbf{U}_\phi}{\partial\rho} + \frac{\partial \mathbf{K}_{\phi u}}{\partial\rho}\mathbf{U}_u + \mathbf{K}_{\phi u}\frac{\partial \mathbf{U}_u}{\partial\rho} \right\} \\
&+ \boldsymbol{\mu}_3^T \left\{ -\frac{\partial \mathbf{K}_{\phi u}^T}{\partial\rho}\mathbf{U}_\phi - \mathbf{K}_{\phi u}^T\frac{\partial \mathbf{U}_\phi}{\partial\rho} + \frac{\partial \mathbf{K}_{uu}}{\partial\rho}\mathbf{U}_u + \mathbf{K}_{uu}\frac{\partial \mathbf{U}_u}{\partial\rho} \right\} \\
=& \left\{ -\mathbf{V}_u^T\langle \mathbf{B}_u^T[\mathbb{C}(\rho)]\mathbf{B}_u x\rangle - \mathbf{V}_\phi{}^T\langle \mathbf{B}_\phi^T[\mathcal{E}(\rho)]\mathbf{B}_u x\rangle + \boldsymbol{\lambda}_3^T\mathbf{K}_{\phi u} + \boldsymbol{\mu}_3\mathbf{K}_{uu} \right\} \frac{\partial \mathbf{U}_u}{\partial\rho} \\
&+ \left\{ -\mathbf{V}_u^T\langle \mathbf{B}^T[\mathcal{E}(\rho)]^T\mathbf{B}_\phi x\rangle + (\mathbf{V}_\phi{}^T)\langle \mathbf{B}_\phi^T[\boldsymbol{\alpha}(\rho)]\mathbf{B}_\phi x\rangle + \boldsymbol{\lambda}_3^T\mathbf{K}_{\phi\phi} - \mu_3^T\mathbf{K}_{\phi u}^T \right\} \frac{\partial \mathbf{U}_\phi}{\partial\rho} \\
&+ \boldsymbol{\lambda}_3^T \left\{ \frac{\partial \mathbf{K}_{\phi\phi}}{\partial\rho}\mathbf{U}_\phi + \frac{\partial \mathbf{K}_{\phi u}}{\partial\rho}\mathbf{U}_u \right\} + \boldsymbol{\mu}_3^T \left\{ -\frac{\partial \mathbf{K}_{\phi u}^T}{\partial\rho}\mathbf{U}_\phi + \frac{\partial \mathbf{K}_{uu}}{\partial\rho}\mathbf{U}_u \right\}
\end{aligned}
\tag{4.16}
$$

The adjoint problem for Part *III* is written as:

$$
\begin{bmatrix} \mathbf{K}_{\phi\phi} & -\mathbf{K}_{\phi u} \\ \mathbf{K}_{\phi u}^T & \mathbf{K}_{uu} \end{bmatrix} \begin{bmatrix} \boldsymbol{\lambda}_3 \\ \boldsymbol{\mu}_3 \end{bmatrix} = - \begin{bmatrix} -\langle \mathbf{B}_\phi^T[\mathcal{E}(\rho)]\mathbf{B}_u x\rangle\mathbf{V}_u + \langle \mathbf{B}_\phi^T[\alpha(\rho)]\mathbf{B}_\phi x\rangle\mathbf{V}_\phi \\ -\langle \mathbf{B}_u^T[\mathbb{C}(\rho)]\mathbf{B}_u x\rangle\mathbf{V}_u - \langle \mathbf{B}_u^T[\mathcal{E}(\rho)]^T\mathbf{B}_\phi x\rangle\mathbf{V}_\phi \end{bmatrix} \tag{4.17}
$$

From Eq. (4.8), we can obtain Part *IV*, which is explicit and can be easily calculated in terms the interpolation function Eq. (4.2).

$$
\begin{aligned}
\frac{\partial[\overline{\mathbb{F}}^{IV}]}{\partial\rho} =& (\mathbf{V}_u)^T \left\langle \mathbf{B}_u^T \frac{\partial([\mathbb{C}(\rho)])}{\partial x}\mathbf{B}_u \right\rangle (\mathbf{W}_u - \mathbf{W}_u{}^x) + (\mathbf{V}_\phi)^T \left\langle \mathbf{B}_\phi^T \frac{\partial([\mathcal{E}(\rho)])}{\partial x}\mathbf{B}_u \right\rangle (\mathbf{W}_u - \mathbf{W}_u{}^x) \\
&+ (\mathbf{V}_u)^T \left\langle \mathbf{B}_u^T \frac{\partial([\mathcal{E}(\rho)])}{\partial\rho}\mathbf{B}_\phi \right\rangle (\mathbf{W}_\phi - \mathbf{W}_\phi{}^x) - (\mathbf{V}_\phi)^T \left\langle \mathbf{B}_\phi^T \frac{\partial([\boldsymbol{\alpha}(\rho)])}{\partial\rho}\mathbf{B}_\phi \right\rangle (\mathbf{W}_\phi - \mathbf{W}_\phi{}^x)
\end{aligned}
\tag{4.18}
$$

After solving all the above adjoint problems, we can get the whole explicit sensitivity of flexoelectric tensor with respect to density ρ as:

$$
\begin{aligned}
\frac{\partial[\overline{\mathbb{F}}]}{\partial\rho} =& \left\{ (\mathbf{V}_\phi{}^T)\frac{\partial \mathbf{K}_{\phi\phi}}{\partial\rho} + (\mathbf{V}_u^T)\frac{\partial \mathbf{K}_{\phi u}^T}{\partial\rho} \right\} \boldsymbol{\lambda}_1 + \left\{ -(\mathbf{V}_\phi{}^T)\frac{\partial \mathbf{K}_{\phi u}}{\partial\rho} + (\mathbf{V}_u^T)\frac{\partial \mathbf{K}_{uu}}{\partial\rho} \right\} \boldsymbol{\mu}_1 \\
&+ \boldsymbol{\lambda}_2^T \left\{ \frac{\partial \mathbf{K}_{\phi\phi}}{\partial\rho}\mathbf{W}_\phi + \frac{\partial \mathbf{K}_{\phi u}}{\partial\rho}\mathbf{W}_u - \frac{\partial \mathbf{F}_\phi}{\partial\rho} \right\} + \boldsymbol{\mu}_2^T \left\{ -\frac{\partial \mathbf{K}_{\phi u}^T}{\partial\rho}\mathbf{W}_\phi + \frac{\partial \mathbf{K}_{uu}}{\partial\rho}\mathbf{W}_u - \frac{\partial \mathbf{F}_u}{\partial\rho} \right\} \\
&+ \boldsymbol{\lambda}_3^T \left\{ \frac{\partial \mathbf{K}_{\phi\phi}}{\partial\rho}\mathbf{W}_\phi{}^x + \frac{\partial \mathbf{K}_{\phi u}}{\partial\rho}\mathbf{W}_u{}^x \right\} + \boldsymbol{\mu}_3^T \left\{ -\frac{\partial \mathbf{K}_{\phi u}^T}{\partial\rho}\mathbf{W}_\phi{}^x + \frac{\partial \mathbf{K}_{uu}}{\partial\rho}\mathbf{W}_u{}^x \right\} \\
&+ (\mathbf{V}_u)^T \left\langle \frac{\partial(\mathbf{B}_u^T[\mathbb{C}(\rho)]\mathbf{B}_u)}{\partial\rho} \right\rangle (\mathbf{W}_u - \mathbf{W}_u{}^x) + (\mathbf{V}_\phi)^T \left\langle \frac{\partial(\mathbf{B}_\phi^T[\mathcal{E}(\rho)]\mathbf{B}_u)}{\partial\rho} \right\rangle (\mathbf{W}_u - \mathbf{W}_u{}^x) \\
&+ (\mathbf{V}_u)^T \left\langle \frac{\partial(\mathbf{B}_u^T[\xi(\rho)]^T\mathbf{B}_\phi)}{\partial\rho} \right\rangle (\mathbf{W}_\phi - \mathbf{W}_\phi{}^x) - (\mathbf{V}_\phi)^T \left\langle \frac{\partial(\mathbf{B}_\phi^T[\alpha(\rho)]\mathbf{B}_\phi)}{\partial\rho} \right\rangle (\mathbf{W}_\phi - \mathbf{W}_\phi{}^x)
\end{aligned}
\tag{4.19}
$$

4.1.3 Numerical investigation

In this section, the proposed computational homogenization framework is applied to optimize the components of the effective flexoelectric tensor of a two-phase composite. More specifically, we investigate the optimization of the $\bar{F}_{1221}$, $\bar{F}_{2221}$, $\bar{F}_{1112}$ and $\bar{F}_{2112}$ coefficients, as these coefficients characterize polarization under the action of bending. The other coefficients of the flexoelectric tensor, i.e. $\bar{F}_{1111}$, $\bar{F}_{2111}$, $\bar{F}_{1222}$, $\bar{F}_{2222}$ are not investigated here, as they correspond to polarization under more complex strain gradient modes. The homogenization and optimization is performed on a periodic heterogeneous material composed of piezoelectric phases. We consider three cases: (1) a composite made of two stiff piezoelectric phases; (2) a composite made of a stiff piezoelectric matrix and soft polymer inclusion; (3) a porous piezoelectric material. In all numerical examples, the RVEs are discretized by 60×60 8-node quadratic finite elements.

4.1.3.1 Ceramic/ceramic piezoelectric composite

We first consider a two-phase composite made of piezoelectric phases. Each phase is made with PZT (lead zirconium titanate ceramics). To induce a heterogeneity, the crystal lattice is oriented by a mismatch angle of $\theta = \pi$ in the inclusion phase. The related properties of the matrix and inclusion are indicated in matrix form in (4.20)-(4.23), in which the subscripts m and i refer to the matrix and inclusion, respectively [214].

$$[\mathbf{C}^m] = [\mathbf{C}^i] = \begin{bmatrix} 131.39 & 83.237 & 0 \\ 83.237 & 154.837 & 0 \\ 0 & 0 & 35.8 \end{bmatrix} (\text{GPa}), \tag{4.20}$$

$$[\boldsymbol{\alpha}^m] = [\boldsymbol{\alpha}^i] = \begin{bmatrix} 2.079 & 0 \\ 0 & 4.065 \end{bmatrix} (\text{nC} \cdot \text{m}^{-1} \cdot \text{V}^{-1}), \tag{4.21}$$

$$[\mathcal{E}^m] = \begin{bmatrix} -2.120582 & -2.120582 & 0 \\ 0 & 0 & 0 \end{bmatrix} (\text{C} \cdot \text{m}^{-2}). \tag{4.22}$$

$$[\mathcal{E}^i] = \begin{bmatrix} 2.120582 & 2.120582 & 0 \\ 0 & 0 & 0 \end{bmatrix} (\text{C} \cdot \text{m}^{-2}). \tag{4.23}$$

We perform the topology optimization of the inclusion shape with respect to the flexoelectric coefficients $\bar{F}_{1221}$ and $\bar{F}_{2112}$, and set the inclusion volume fraction to $f = 0.4$. As a first guess, the design variables are uniformly set to $\rho_e = 0.4$ (e = 1,..., N_e = 3600). The guess design with triangular shape which is illustrated in Fig. 4.1a has been investigated in [179] and will serve as a comparison solution with respect to optimized topological designs.

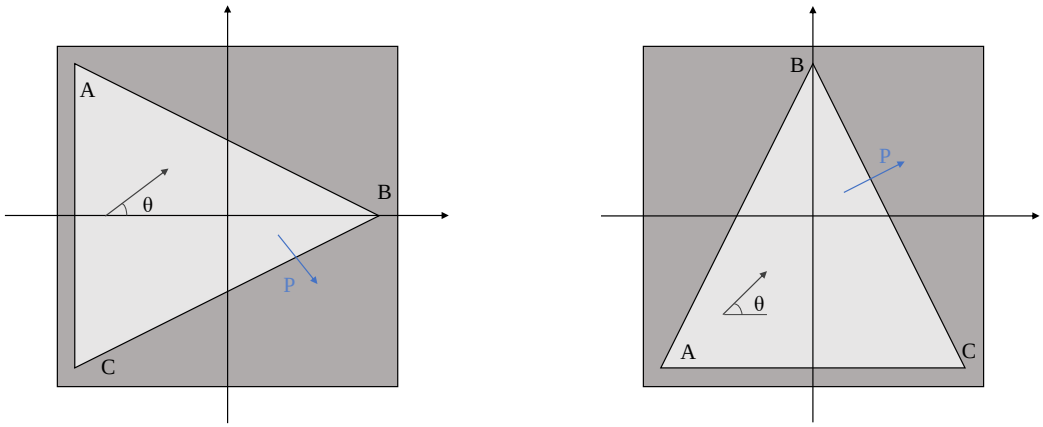

(a) (b)

Figure 4.1: Unit cells with triangular inclusions with inclusion volume fraction of $f = 0.4$, polarization P and the mismatch angle θ between matrix and inclusion phases; (a) guess design used for computing $\overline{F}_{1221}$ and $\overline{F}_{2112}$; (b) guess design used for computing $\overline{F}_{1112}$ and $\overline{F}_{2221}$.

The final optimized unit cell topologies are shown in Figs. 4.3a and 4.6a, where the optimization process converges in about 60 iterations for $\bar{F}_{1221}$ and $\bar{F}_{2112}$. In all figures, the copper and black colors refer to the inclusion and matrix phases, respectively. Iteration histories are shown in Fig. 4.2. In current paper, the words 'Normalized Flexoelectric F' showed in all the iteration figures is defined as '$\overline{F}_{ijkl}/\overline{F}^{Ref}_{ijkl}$', the $\overline{F}^{Ref}_{ijkl}$ means the reference solution obtained by unit cell with triangular shape inclusion.

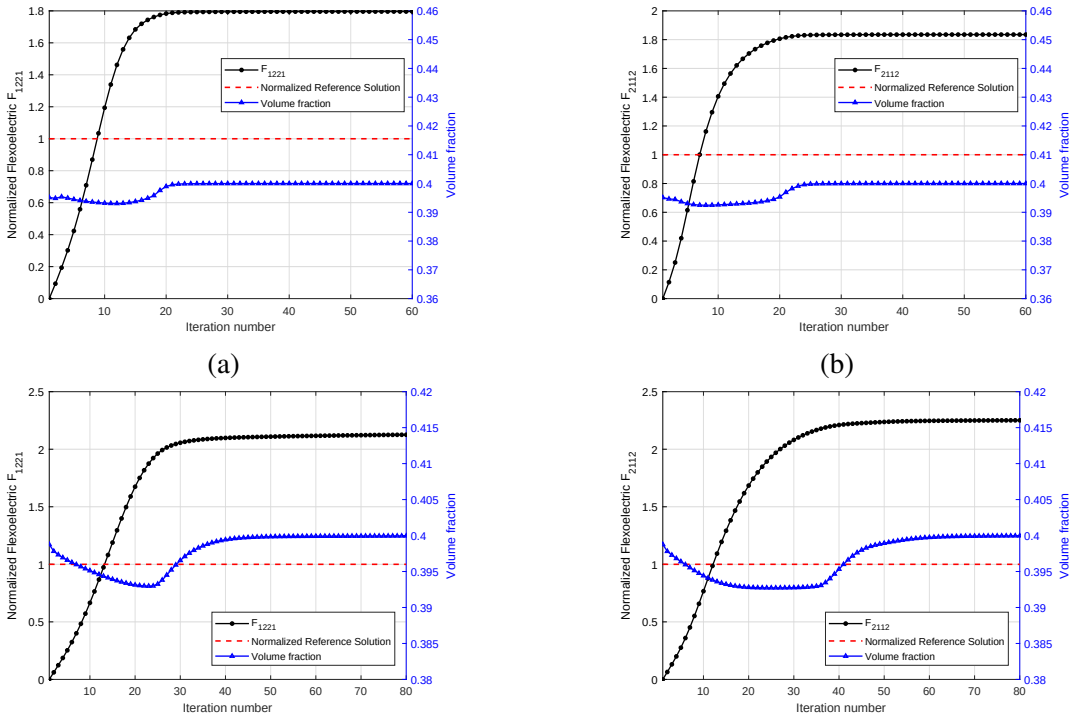

Figure 4.2: Topology optimization process with respect to normalized flexoelectric components and volume fractions for the PZT/PZT: (a) $\bar{F}_{1221}$, 1×1 cells; (b) $\bar{F}_{2112}$, 1×1 cells; (c) $\bar{F}_{1221}$, 2×2 cells; (d) $\bar{F}_{2112}$, 2×2 cells.

The final values for the optimized microstructures are $\bar{F}_{1221} = 1.365 \times 10^{-4}$ C·m^{-1} and $\bar{F}_{2112} = 2.689 \times 10^{-4}$ C·m^{-1}, which represents a significant improvement of the values as compared to the reference triangular solutions of 79.61% and 83.55% for $\bar{F}_{1221}$ and $\bar{F}_{2112}$, respec-

tively. It should be noticed that the obtained values are higher than naturally flexoelectric materials, such as $BaTiO_3$ and PMN-PT [215] whose flexoelectricity is reported as of the order of 10^{-5} C·m^{-1}. It is worth noting that in the present procedure, the initial design is homogeneous, which explains that the flexoelectric coefficients are initially zero.

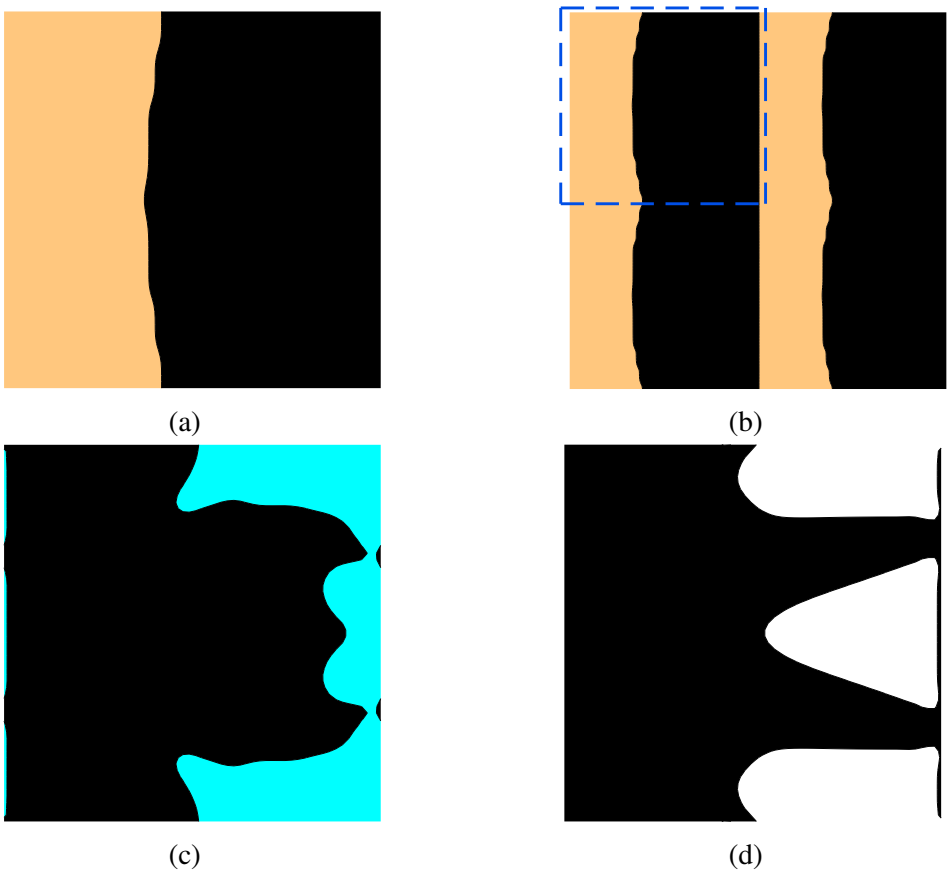

Figure 4.3: Optimal topology for $\bar{F}_{1221}$: (a) PZT/PZT, 1×1 cells; (b)PZT/PZT, 2×2 cells; (c) PZT/polymer, 1×1 cells; (d) PZT/void, 1×1 cells.

We consider the optimized RVE of Fig. 4.3a and we use the same material parameters as in (4.20)-(4.23). Here again, the RVE is composed of 1×1 unit cell. The dimensions of the RVE are varied according to $\varepsilon_0 = \ell/\ell_0$, where $\ell_0 = 1$ mm and ℓ is the length of the RVE. It appears clearly from Fig. 4.4 that $\overline{\mathbb{F}}$ varies according to ε_0.

The electromechanical coefficients for the reference RVE with triangular inclusion are $\bar{\mathcal{K}}_{31}^{ref} = 0.0929$ and $\bar{\mathcal{K}}_{32}^{ref} = 0.0736$. For the optimized $\bar{F}_{1221}$, the coupling coefficients are found as $\bar{\mathcal{K}}_{31} = 0.1141$ and $\bar{\mathcal{K}}_{32} = 0.0903$, increasing respectively by 22.8% and 22.7%. Similarly, for the optimized $\bar{F}_{2112}$, the coupling coefficients are found as $\bar{\mathcal{K}}_{31} = 0.1183$ and $\bar{\mathcal{K}}_{32} = 0.0937$, with each increasing by 27.3%.

To gain more insight into the mechanisms driving the increase in the flexoelectric constants, we plot in Fig. 4.5 the local electric field component E_2 and local strain gradient component $\nabla\varepsilon_{112}$ within the optimized F_{2112} unit cell shown in Fig. 4.6(a) for a prescribed strain gradient $\bar{\nabla}\bar{\varepsilon}_{112} = 1$ m^{-1}. This is done as the value of the flexoelectric constant F_{ajkl} depends on the polarization direction a, and the strain gradient $\nabla\bar{\varepsilon}_{jkl}$. We can observe that both the electric field and strain gradient are localized within the microstructure, roughly at the interface between the PZT matrix and PZT inclusion. Furthermore, the electric field is asymmetric with respect to the polarization direction, which is required to obtain non-zero flexoelectric constants. While the strain gradient and electric field are both localized at the interface, the enhancements are not as large as for later examples using a hard/soft interface, and thus the enhancement in the optimized $\bar{F}_{2112}$, while excellent at 83.5%, is smaller than the later optimized hard/soft structures.

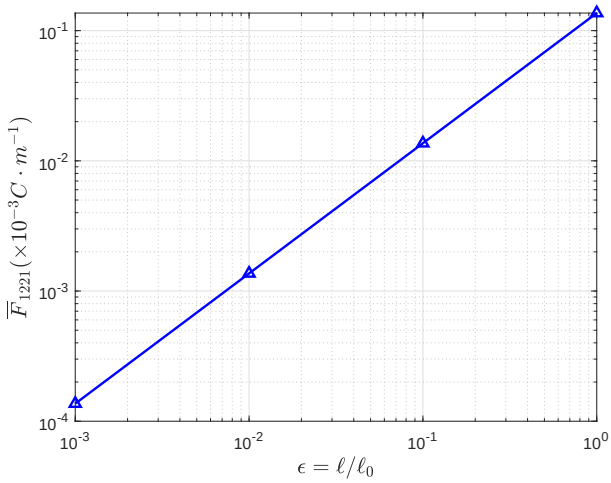

Figure 4.4: Size-dependent effective strain-gradient properties $\overline{F}_{1221}$ for RVE with topology of Fig.4.3a

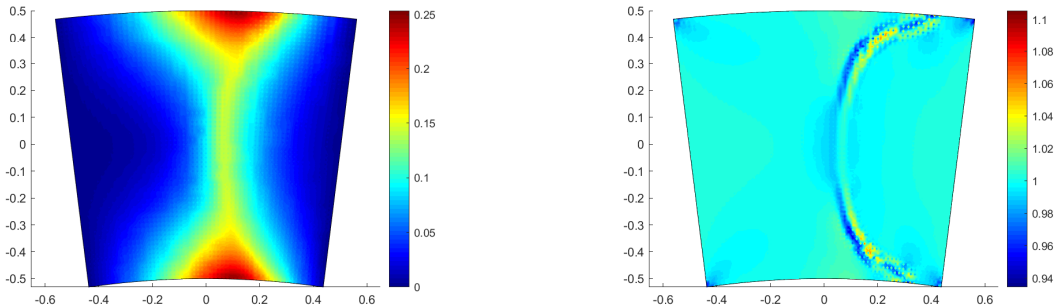

(a) $E_2(\mathbf{x})$ (b) $\nabla\varepsilon_{112}(\mathbf{x})$

Figure 4.5: Electric field (E_2-component) and strain gradient ($\nabla\varepsilon_{112}$-component within the PZT-PZT-optimized microstructure corresponding to the optimized $\bar{F}_{2112}$ in Fig. 4.6(a).

To understand the enhancement in electromechanical coupling coefficient $\bar{\mathcal{K}}$, we examine the different terms contributing to it in Table 4.1. There, we find that for the PZT/PZT case, because the matrix and inclusion are comprised of the same material, the compliance $\bar{\mathbb{S}}$ and dielectric matrices $\bar{\mathbf{e}}$ have the same values. Therefore, the increase in electromechanical coupling $\bar{\mathcal{K}}$ for the hard/hard composite is entirely driven by the enhancement in effective RVE piezoelectric constants $\bar{\mathcal{D}}$.

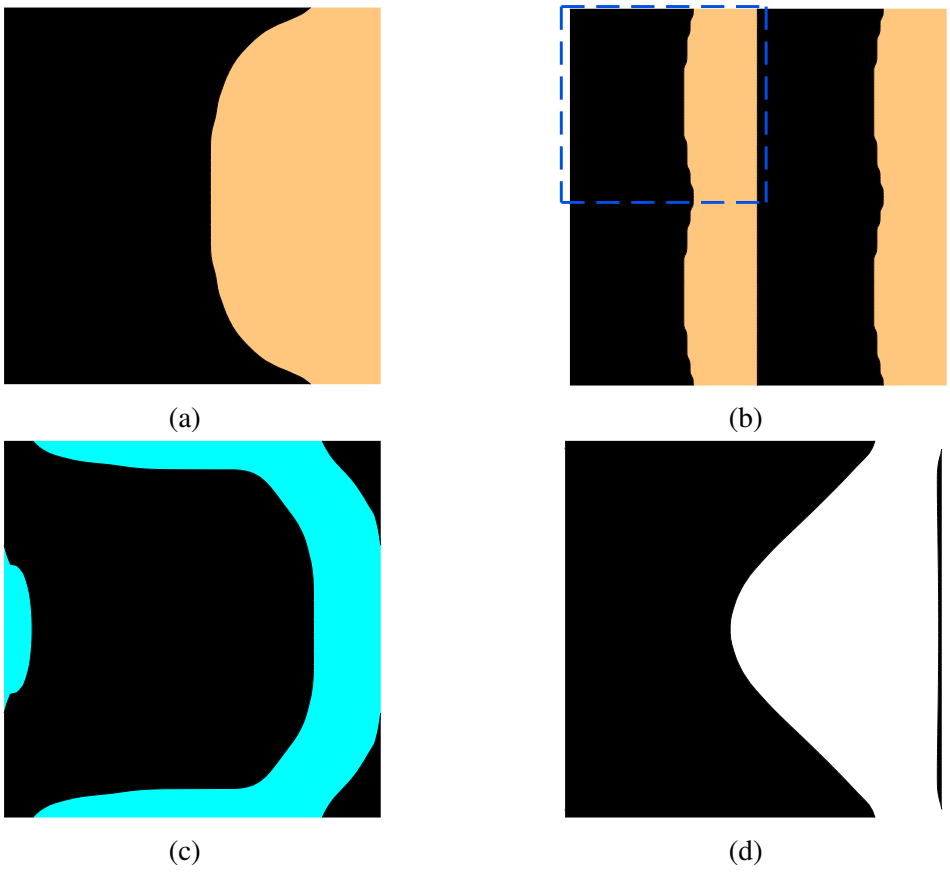

Figure 4.6: Optimal topology for $\bar{F}_{2112}$: (a) PZT/PZT, 1×1 cells; (b)PZT/PZT, 2×2 cells; (c) PZT/polymer, 1×1 cells; (d) PZT/void, 1×1 cells.

Next, we investigate the influence of the volume fraction f on the obtained geometries obtained by optimizing $\bar{F}_{1221}$ and $\bar{F}_{2112}$ in Figs. 4.7 and 4.8, respectively. We first note that the volume fraction has a direct influence on the obtained geometry. When f is around 0.5, a simple layered structure is obtained. However, more asymmetric geometries with respect to the $y-$axis are induced for other volume fractions. In addition, the corresponding values of the optimized coefficients do not increase monotonically with the volume fraction, but reach the largest value around $f = 0.5$, leading to $\bar{F}_{1221} = 1.43$ ($\times 10^{-4}$ C $\cdot$ m^{-1}) and $\bar{F}_{2112} = 2.767$ ($\times 10^{-4}$ C $\cdot$ m^{-1}). When the unit cell is homogeneous ($f = 0$ and $f = 1$), the flexoelectric coefficients vanish.

It has been in shown in [179, 195] that in the present computational framework, the effective flexoelectric properties quickly converge with respect to the number of unit cells. Next, a 2×2 periodic repetition of unit cells is investigated to determine the influence of using more cells within the RVE for the calculations. Each unit cell is composed of 60×60 elements, thus $4 \times 60 \times 60$ elements are used in the 2×2 unit cells.

The optimized structures of the 2×2 periodic unit cell are obtained in Fig. 4.3b and Fig. 4.6b for $f = 0.4$. In that case, the maximum values of the flexoelectric coefficients are $\bar{F}_{1221} = 1.616$ ($\times 10^{-4}$ C $\cdot$ m^{-1}) and $\bar{F}_{2112} = 3.298$ ($\times 10^{-4}$ C $\cdot$ m^{-1}). The coupling coefficients are obtained as $\bar{\mathcal{K}}_{31} = 0.1449$ and $\bar{\mathcal{K}}_{32} = 0.1147$ for optimized $\bar{F}_{1221}$, and $\bar{\mathcal{K}}_{31} = 0.1169$ and $\bar{\mathcal{K}}_{32} = 0.0925$ for optimized $\bar{F}_{2112}$. Then, a notable change is obtained as compared to the 1×1

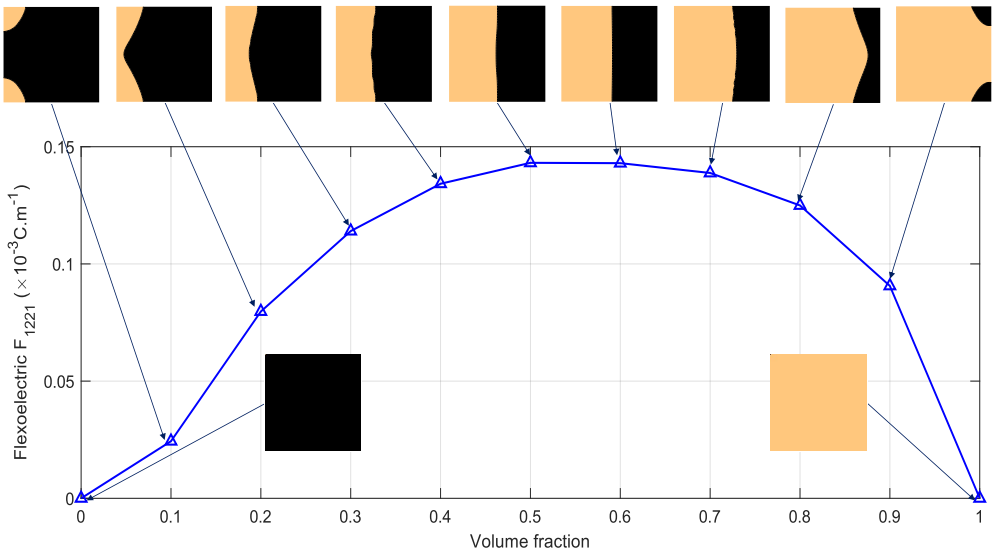

Figure 4.7: Optimal values of flexoelectric coefficient $\bar{F}_{1221}$ and corresponding topologies with respect to volume fraction of inclusion.

unit cell. However, the obtained topologies are very similar, which suggest that the topology optimization can be conducted on a single unit cell, while the effective properties can be estimated using more repeated unit cells.

4.1.3.2 Ceramic/doped piezoelectric polymer composite

In our second example, we replace the misoriented and mechanically stiff PZT inclusion with a soft, dielectric, polymer inclusion (polyvinylidene fluoride, PVDF). The elastic, piezoelectric and dielectric properties for the polymer are given below. In comparison to the PZT properties in Eqs. (4.20)-(4.23), all of the polymer properties are 1-2 orders in magnitude lower than for PZT. Despite this, we shall demonstrate in this example that the potential of increased strain gradients that may be possible by using hard/soft composites can lead to effective flexoelectric constants and electromechanical coupling constants that can exceed those of the PZT/PZT composite in the previous example. The material parameters of matrix PZT are expressed in (4.20)-(4.22), while the material properties of PVDF are described in (4.24)-(4.26) [216].

$$[\mathbf{C}^i] = \begin{bmatrix} 6.066 & 3.911 & 0 \\ 3.911 & 6.066 & 0 \\ 0 & 0 & 1.078 \end{bmatrix} (\text{GPa}) \tag{4.24}$$

$$[\boldsymbol{\alpha}^i] = \begin{bmatrix} 0.025 & 0 \\ 0 & 0.084 \end{bmatrix} (\text{nC} \cdot \text{m}^{-1} \cdot \text{V}^{-1}) \tag{4.25}$$

$$[\mathcal{E}^i] = \begin{bmatrix} 0.1272 & 0.0873 & 0 \\ 0 & 0 & 0 \end{bmatrix} (\text{C} \cdot \text{m}^{-2}). \tag{4.26}$$

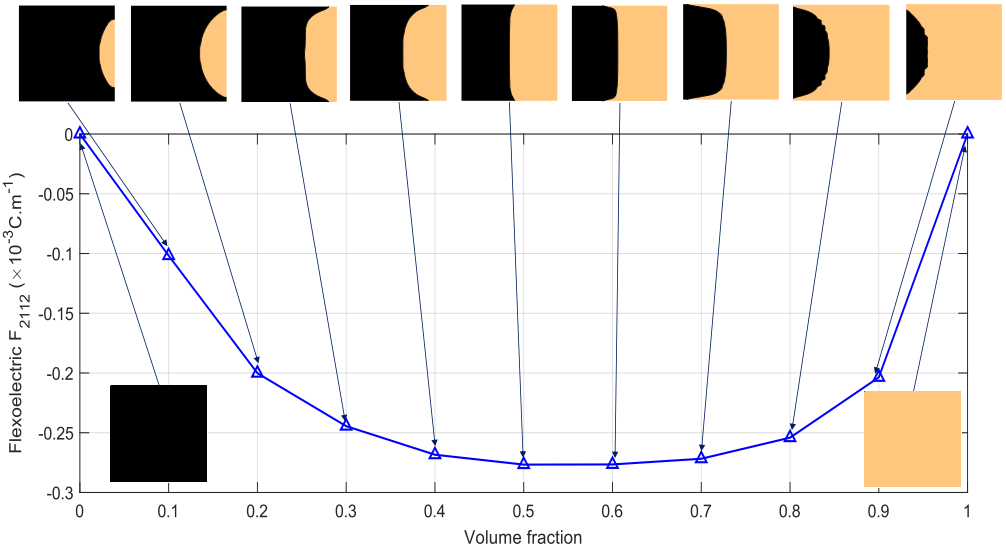

Figure 4.8: Optimal values of flexoelectric coefficient $\bar{F}_{2112}$ and corresponding topologies with respect to volume fraction of inclusion.

(a) (b)

Figure 4.9: Optimal topology for $\bar{F}_{2221}$: (a) PZT/polymer; (b) PZT/void.

(a) (b)

Figure 4.10: Optimal topology for $\bar{F}_{1112}$: (a) PZT/polymer; (b) PZT/void.

We perform topology optimization of the PVDF inclusion with respect to the flexoelectric coefficients $\bar{F}_{1221}$, $\bar{F}_{2221}$, $\bar{F}_{1112}$ and $\bar{F}_{2112}$. To ensure that these results can be compared against the previous PZT/PZT results, we set the volume fraction of the PVDF inclusion to be $f = 0.4$ for all cases. Similarly, the initial guess is set by $\rho_e = 0.4$, $e = 1,2,...,N_e = 3600$. The periodic density conditions are considered here. The final optimal unit cells of the flexoelectric coefficients $\bar{F}_{1221}$, $\bar{F}_{2221}$, $\bar{F}_{1112}$ and $\bar{F}_{2112}$ are obtained in Figs. 4.3c, 4.9a, 4.10a and 4.6c. In these

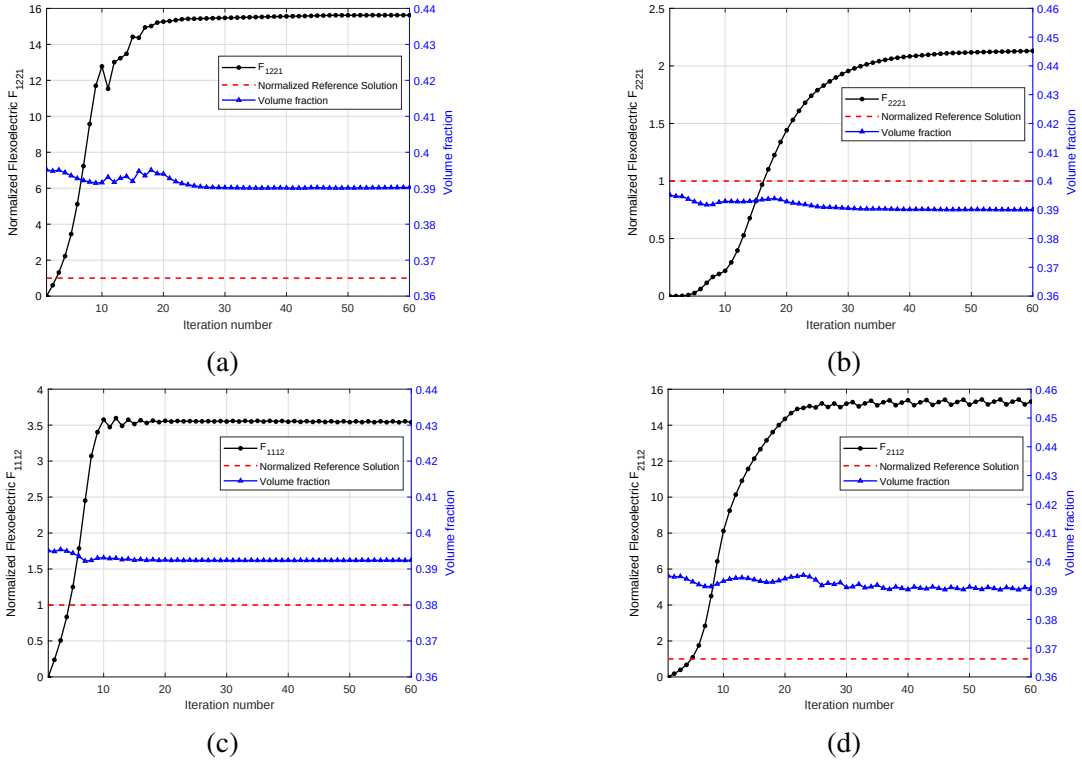

Figure 4.11: Topology optimization process with respect to normalized flexoelectric components and volume fractions for the PVDF/PZT: (a) $\bar{F}_{1221}$; (b) $\bar{F}_{2221}$; (c) $\bar{F}_{1112}$; (d) $\bar{F}_{2112}$.

figures, the cyan and black colors refer to the inclusion PVDF and matrix PZT, respectively. Iteration histories are shown in Fig. 4.11. The reference solutions calculated by a triangular PVDF inclusion as in Fig. 4.1 are shown in all cases.

We obtained four different optimized unit cells, and a significant improvement can be found compared to the reference triangular solutions. The optimal absolute values are $\bar{F}_{1221} = 1.484 \times 10^{-4}$ C·m^{-1}, $\bar{F}_{2221} = 3.49 \times 10^{-5}$ C·m^{-1}, $\bar{F}_{1112} = 7.33 \times 10^{-5}$ C·m^{-1} and $\bar{F}_{2112} = 2.006 \times 10^{-4}$ C·m^{-1}, which imply increases by 1462%, 113%, 254% and 1431%, respectively. Interestingly, despite being comprised of a polymer inclusion whose (elastic, piezoelectric, and dielectric) properties are all about two orders of magnitude smaller than the PZT matrix, the flexoelectric constants are quite similar to those obtained for the optimized PZT/PZT composites discussed previously, with significantly larger percentage enhancements. We compare the optimal topology configurations of the PZT/PVDF composites by $\overline{F}_{2221}$ with regular and irregular meshing in Fig. 4.12. The two similar topologies with regular and irregular meshing present that the obtained optimal topology doesn't depend on the meshing. In Fig. 4.13, we present the bending deformation of unit cell optimized by $\bar{F}_{2112}$, induced by electric fields.

The mechanism for this can be seen in Fig. 4.14, where the electric field and strain gradient of the optimized unit cell for $\bar{F}_{2112}$ previously shown in Fig. 4.6(c) are shown. In comparing the magnitudes of the electric field and strain gradient for the PZT/polymer RVE in Fig. 4.14 and the PZT/PZT RVE in Fig. 4.5, both the electric field and strain gradient for the hard/soft PZT/polymer case are 1-2 orders of magnitude larger than in the PZT/PZT case, which is reasonable given the curved hard/soft material boundary that exists within the RVE. Because the flexoelectric constants are dependent on the product of the electric field and strain gradient, this explains how the flexoelectric constants of the PZT/polymer case can rival and/or exceed those of the PZT/PZT case, as summarized in Table 4.2, despite being comprised of constituents with smaller physical properties.

The electromechanical coupling coefficients are also improved in the optimized designs. We obtain $\bar{\mathcal{K}}_{31} = 0.409$ and $\bar{\mathcal{K}}_{32} = 0.2694$ for optimized $\bar{F}_{1221}$, $\bar{\mathcal{K}}_{31} = 0.1059$ $\bar{\mathcal{K}}_{32} = 0.2444$

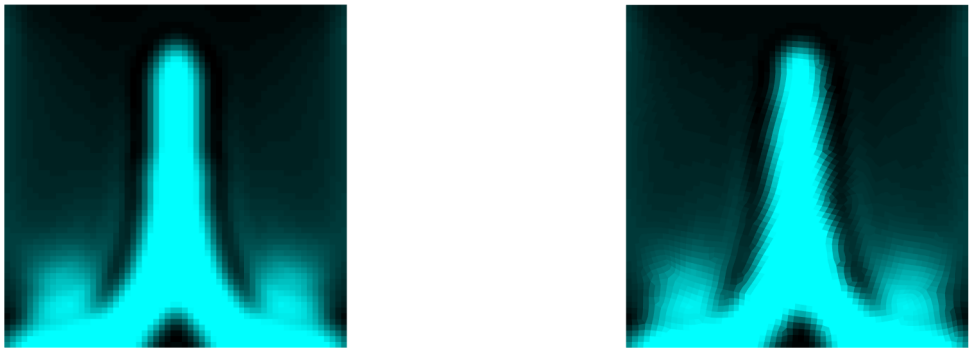

(a) (b)

Figure 4.12: Optimal topology for $\overline{F}_{2221}$ on PZT/polymer: (a) with regular meshing; (b) with irregular meshing

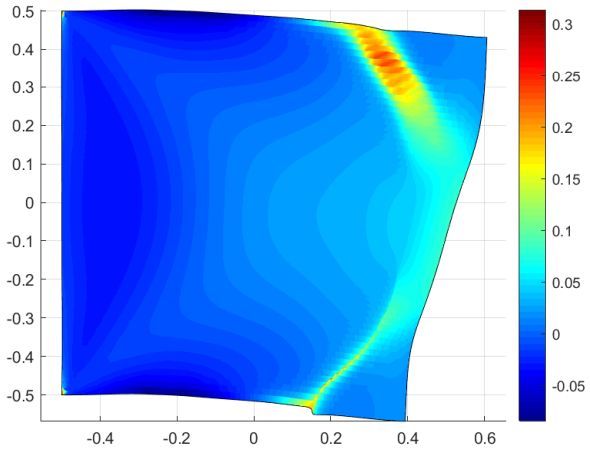

Figure 4.13: Deformation and strain ε_{22} of optimized unit cell in Fig. 4.6c induced by electric filed E_2

for optimized $\bar{F}_{2221}$, $\bar{\mathcal{K}}_{31} = 0.4981$ and $\bar{\mathcal{K}}_{32} = 0.3226$ for optimized $\bar{F}_{1112}$, while $\bar{\mathcal{K}}_{31} = 0.0337$ and $\bar{\mathcal{K}}_{32} = 0.3136$ for optimized $\bar{F}_{2112}$. In contrast with $\bar{\mathcal{K}}_{31} = 0.3151$ and $\bar{\mathcal{K}}_{32} = 0.067$ for triangular PVDF, the values of $\bar{\mathcal{K}}_{32}$ for the optimal unit cells are improved by 302.1%, 264.8%, 381.5%, 368.1%, respectively, while $\bar{\mathcal{K}}_{31}$ for the optimal unit cells increases by 29.8%, -66.4%, 58.1% and -89.3%. We can note that the value of $\bar{\mathcal{K}}_{31}$ for optimized $\bar{F}_{2221}$ and $\bar{F}_{2112}$ decrease. However $\bar{\mathcal{K}}_{32}$ for all other optimized unit cells increase. For optimized $\bar{F}_{1221}$ and $\bar{F}_{1112}$, both electromechanical coefficients can be improved.

The mechanisms underlying the enhancement in electromechanical coupling coefficients corresponding to the PZT/polymer composites that maximize $\bar{F}_{2112}$ differ from those previously discussed for the PZT/PZT composites. In examining the contributions to the coupling coefficient $\bar{\mathcal{K}}$ in Table 4.1, we see that due to the multiple materials that comprise the RVE, all of the effective properties, i.e. compliance $\bar{\mathbb{S}}$, dielectric $\bar{\mathbf{e}}$ and piezoelectric $\bar{\mathcal{D}}$ change during the RVE optimization. For the $\bar{\mathcal{K}}_{31}$ constant, a significant decrease during optimization is found, which is driven by the significant decrease in the corresponding piezoelectric $\bar{\mathcal{D}}_{31}$ constant.

For the $\bar{\mathcal{K}}_{32}$ constant, a nearly four-fold increase is observed during optimization. Some of this is due to the doubling of the $\bar{\mathcal{D}}_{32}$ piezoelectric constant. However, the optimization also leads to an increase in the dielectric properties $\bar{\mathbf{e}}$, and a decrease in the compliance $\bar{\mathbb{S}}$, as shown in Table 4.1. The increase in effective piezoelectric and dielectric properties are related to the enhanced localized electric field shown in Fig. 4.14, while the enhanced strain gradient shown in Fig. 4.14 is connected to the reduction in compliance. Thus, for the PZT/polymer RVE, it is

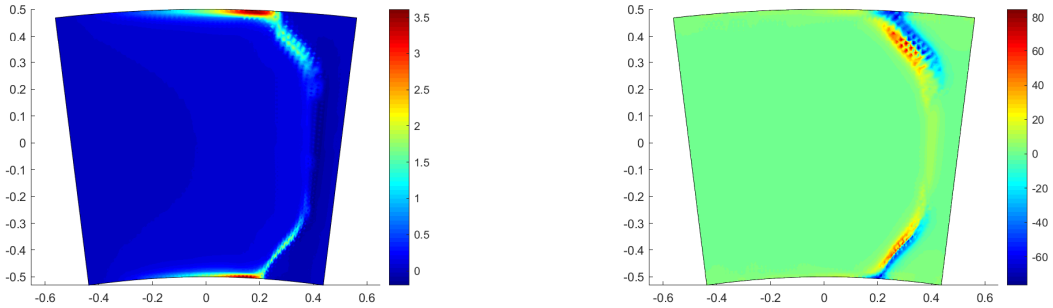

(a) $E_2(\mathbf{x})$ (b) $\nabla\varepsilon_{112}(\mathbf{x})$

Figure 4.14: Electric field (E_2-component) and strain gradient ($\nabla\varepsilon_{112}$-component) within the PZT-PVDF-optimized microstructure shown in Fig. 4.6(c).

this subtle interplay between the electrical, mechanical, and electromechanical properties that leads to the increase in electromechanical coupling.

Table 4.1: Electromechanical coupling and effective tensors for initial (guess) designs and optimized geometries, all corresponding to the $\bar{F}_{2112}$ flexoelectric constant.

	$\bar{\mathcal{K}}$	$\bar{\mathcal{D}}$	$\bar{\mathbf{e}}$	$\bar{\mathbb{S}}$
PZT/PZT				
Guess design	$\begin{bmatrix} -0.0929 & -0.0736 & 0 \\ 0 & 0 & 0 \end{bmatrix}$	$\begin{bmatrix} -0.0023 & -0.0015 & 0 \\ 0 & 0 & 0 \end{bmatrix}$	$\begin{bmatrix} 2.1083 & 0 \\ 0 & 4.0650 \end{bmatrix}$	$\begin{bmatrix} 0.0115 & -0.0062 & 0 \\ -0.0062 & 0.0098 & 0 \\ 0 & 0 & 0.0279 \end{bmatrix}$
Optimized	$\begin{bmatrix} -0.1183 & -0.0937 & 0 \\ 0 & 0 & 0 \end{bmatrix}$	$\begin{bmatrix} -0.0029 & -0.0019 & 0 \\ 0 & 0 & 0 \end{bmatrix}$	$\begin{bmatrix} 2.1053 & 0 \\ 0 & 4.065 \end{bmatrix}$	$\begin{bmatrix} 0.0115 & -0.0062 & 0 \\ -0.0062 & 0.0098 & 0 \\ 0 & 0 & 0.0279 \end{bmatrix}$
PZT/PVDF				
Guess design	$\begin{bmatrix} -0.3151 & -0.0670 & 0 \\ 0 & 0 & -0.0723 \end{bmatrix}$	$\begin{bmatrix} -0.0085 & -0.0023 & 0 \\ 0 & 0 & -0.0060 \end{bmatrix}$	$\begin{bmatrix} 1.0951 & 0 \\ 0 & 1.1765 \end{bmatrix}$	$\begin{bmatrix} 0.0245 & -0.0109 & 0 \\ -0.0109 & 0.0316 & 0 \\ 0 & 0 & 0.0705 \end{bmatrix}$
Optimized	$\begin{bmatrix} 0.0337 & -0.3136 & 0 \\ 0 & 0 & 0.0107 \end{bmatrix}$	$\begin{bmatrix} 0.0007 & -0.0047 & 0 \\ 0 & 0 & 0.0013 \end{bmatrix}$	$\begin{bmatrix} 1.064 & 0 \\ 0 & 2.6898 \end{bmatrix}$	$\begin{bmatrix} 0.0204 & -0.0082 & 0 \\ -0.0082 & 0.0141 & 0 \\ 0 & 0 & 0.0467 \end{bmatrix}$
PZT/Void				
Guess design	$\begin{bmatrix} -0.378 & -0.1034 & 0 \\ 0 & 0 & -0.0987 \end{bmatrix}$	$\begin{bmatrix} -0.0110 & -0.0049 & 0 \\ 0 & 0 & -0.0079 \end{bmatrix}$	$\begin{bmatrix} 1.0808 & 0 \\ 0 & 1.0365 \end{bmatrix}$	$\begin{bmatrix} 0.0270 & -0.0099 & 0 \\ -0.0099 & 0.0435 & 0 \\ 0 & 0 & 0.0775 \end{bmatrix}$
Optimized	$\begin{bmatrix} -0.2940 & -0.2833 & 0 \\ 0 & 0 & -0.0226 \end{bmatrix}$	$\begin{bmatrix} -0.0105 & -0.0057 & 0 \\ 0 & 0 & -0.0028 \end{bmatrix}$	$\begin{bmatrix} 0.928 & 0 \\ 0 & 1.8637 \end{bmatrix}$	$\begin{bmatrix} 0.0383 & -0.0126 & 0 \\ -0.0126 & 0.0216 & 0 \\ 0 & 0 & 0.0658 \end{bmatrix}$

4.1.3.3 Heterogeneous porous microstructure

In our final example, we consider a unit cell composed of a piezoelectric material with properties described by Eqs. (4.20)-(4.22), while the second phase is void. The flexoelectric coefficients $\bar{F}_{1221}$, $\bar{F}_{2221}$, $\bar{F}_{1112}$ and $\bar{F}_{2112}$ are considered. To model the void phase, soft properties are chosen for the void as $[C^{void}] = 10^{-9} \times [C^m]$, $[\mathcal{E}^{void}] = 10^{-9} \times [\mathcal{E}^m]$ and $[\alpha^{void}] = 10^{-9} \times [\alpha^m]$.

The optimization is performed with respect to the different flexoelectric coefficients independently. In each case, the optimization process converges in roughly 80 iterations. Here, the volume fraction of the solid phase is constrained to $f = 0.6$, such that the void (inclusion) volume fraction is 0.4, the same as for the PZT/PZT and PZT/polymer composites. The initial design is a homogeneous unit cell with densities $\rho_e = 0.6$ (e = 1,..., N_e = 3600). Periodic density conditions are used here. The final optimal design for the coefficients $\bar{F}_{1221}$, $\bar{F}_{2221}$, $\bar{F}_{1112}$ and $\bar{F}_{2112}$ are summarized in Figs. 4.3d, 4.6d, 4.10b and 4.9b, while their iteration histories are shown in Fig. 4.15. The reference solutions obtained by a triangular void as in Fig. 4.1 are reported in each case. We can see that four different optimized design are obtained for the different coefficients. It is interesting to note that the obtained geometries obtained by optimizing $\bar{F}_{1221}$ and $\bar{F}_{2112}$ have the same symmetry, as well as $\bar{F}_{2221}$ and $\bar{F}_{1112}$. In addition, we can note that even though the materials are different, the topologies obtained for the same optimized component can show significant similarities (see e.g. Figs. 4.9a and 4.9b).

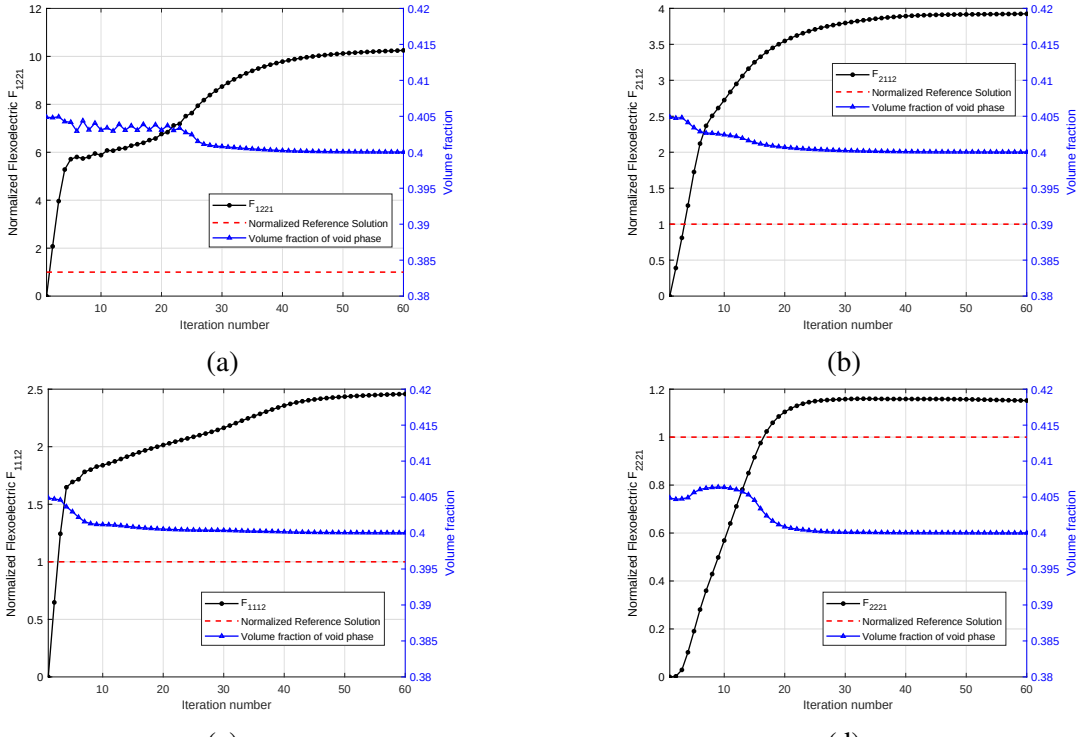

Figure 4.15: Topology optimization process with respect to normalized flexoelectric components and volume fractions for the PZT/void: (a) $\bar{F}_{1221}$; (b) $\bar{F}_{2112}$; (c) $\bar{F}_{1112}$; (d) $\bar{F}_{2221}$.

The obtained absolute values are $\bar{F}_{1221} = 7.99 \times 10^{-5}$ C·m^{-1}, $\bar{F}_{2112} = 3.85 \times 10^{-5}$ C·m^{-1}, $\bar{F}_{1112} = 2.36 \times 10^{-5}$ C·m^{-1} and $\bar{F}_{2221} = 1.15 \times 10^{-5}$ C·m^{-1}. In contrast with the flexoelectric properties of the unit cell with triangular void, we get a very large gain in the optimized structures for the components of $\bar{F}_{1221}$, $\bar{F}_{2112}$ and $\bar{F}_{1112}$, which are improved by 924%, 293% and 145%, respectively. However, only an increase by 15% for $\bar{F}_{2221}$ is obtained, and it has the similar topology as the reference triangular unit cells. We obtain $\bar{\mathcal{K}}_{31} = 0.4175$ and $\bar{\mathcal{K}}_{32} = 0.2226$ for optimized $\bar{F}_{1221}$, $\bar{\mathcal{K}}_{31} = 0.2086$ and $\bar{\mathcal{K}}_{32} = 0.2064$ for optimized $\bar{F}_{2221}$, $\bar{\mathcal{K}}_{31} = 0.3038$ and $\bar{\mathcal{K}}_{32} = 0.1657$ for optimized $\bar{F}_{1112}$, while we have $\bar{\mathcal{K}}_{31} = 0.2940$ and $\bar{\mathcal{K}}_{32} = 0.2833$ for optimized $\bar{F}_{2112}$.

We show in Fig. 4.16 the electric field and strain gradient for corresponding to the optimized PZT/void microstructure in Fig. 4.6 that maximizes $\bar{F}_{2112}$. Similar to the PZT/polymer case in Fig. 4.14, the electric field and strain gradient are largest around the PZT/void interface, though the magnitude of each is smaller than in the PZT/polymer case. For that reason, the resulting flexoelectric constants for the PZT/void RVEs are smaller than the PZT/polymer and PZT/PZT RVEs, as summarized in Table 4.2. The mechanism for the changes in electromechanical coupling are also similar to the PZT/polymer case. Specifically, localized electric field-driven increases along the PZT/void boundary lead to enhancements in the effective piezoelectric and dielectric properties, while the enhanced strain gradient is related to the reduction in compliance, with the interplay resulting in an increase in $\bar{\mathcal{K}}_{31}$ and an increase in $\bar{\mathcal{K}}_{32}$.

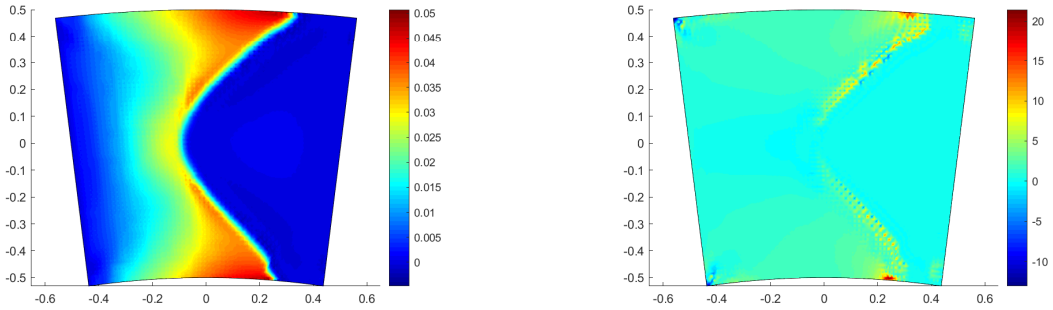

(a) $E_2(\mathbf{x})$ (b) $\nabla\varepsilon_{112}(\mathbf{x})$

Figure 4.16: Electric field (E_2-component) and strain gradient ($\nabla\varepsilon_{112}$)-component within the PZT-void-optimized microstructure in Fig. 4.6(d).

We summarize in Table 4.2 the optimal values for flexoelectric coefficients found in the different composites. For reference, the values are compared with the flexoelectric coefficient of $BaTiO_3$ [39]. As can be seen, the RVE-based topology optimization approach leads to unit cells whose effective flexoelectric constants can exceed, by significant amounts, the flexoelectric properties of $BaTiO_3$, as driven by the different electromechanical mechanisms discussed previously.

Table 4.2: Optimized flexoelectric coefficients for PZT/PZT, PZT/PVDF and porous PZT composites.

	$\bar{F}_{1221}$	$\bar{F}_{2112}$	$\bar{F}_{2221}$	$\bar{F}_{1112}$
PZT/PZT	136 μC/m	268 μC/m		
PZT/PVDF	148 μC/m	200 μC/m	35 μC/m	73 μC/m
Porous PZT	80 μC/m	38 μC/m	11 μC/m	23 μC/m
$BaTiO_3$ [39]	10-50 μC/m			

4.2 SIMP topology optimization for converse flexoelectric composites

In this section, we combine the homogenization approach with topology optimization to obtain tailored microstructures with converse flexoelectric properties, aiming to enhance the converse flexoelectric constants of periodic piezoelectric composites. The sensitivity expressions of the converse flexoelectric tensor with respect to design variables are derived based on a SIMP (Solid

Isotropic Material with Penalization) model. We show in the numerical examples that it is theoretically possible to obtain optimized designs of composites with apparent converse flexoelectric properties 1-2 orders of magnitude larger than ones obtained with naive guess designs.

4.2.1 Topology optimization problem formulation

In this section, we formulate the topology optimization problem to maximize the absolute values of the converse flexoelectric tensor components in (2.93) in Chapter 2. First, the periodic unit cell is discretized with a regular mesh of N_e 4-node quadrilateral finite elements. We define the inclusion material density ρ_e in each element e, $e = 1,2,...,N_e$ such that $\rho_e = 1$ is associated with the inclusion phase and $\rho_e = 0$ is associated with the matrix phase. The topology optimization is formulated as follows:

$$\begin{aligned} \text{Maximize}: \quad & |\overline{K}_{ijkl}(\boldsymbol{\rho})| \\ \text{subject}: \quad & \mathbf{KU} = \mathbf{F} \\ : \quad & \textstyle\sum_{e=1}^{N_e} \rho_e v_e / (\sum_{e=1}^{N_e} v_e) = f \\ & 0 \le \rho_e \le 1, \;\; e = 1,2,...,N_e \end{aligned} \tag{4.27}$$

We still use the SIMP method to solve the problem. The local material interpolation scheme is same as those in (4.1). In the numerical examples, the penalty exponents are chosen as $pc = pa = pe = 3$.

4.2.2 Adjoint sensitivity

The above problem (4.1) requires evaluating the gradient of the objective function with respect to the local densities (subsequently referred to as sensitivities). The adjoint method is also employed here to obtain the numerical sensitivity. The objective function, i.e. the effective converse flexoelectric tensor, is written in matrix form as:

$$[\overline{\mathbb{K}}] = \langle -(\mathbf{A}^0)^T[\mathbb{C}]\tilde{\mathbf{B}}^1 + (\mathbf{D}^0)^T[\mathcal{E}]\tilde{\mathbf{B}}^1 + (\mathbf{A}^0)^T[\mathcal{E}]\tilde{\mathbf{h}}^1 + (\mathbf{D}^0)^T[\boldsymbol{\alpha}]\tilde{\mathbf{h}}^1 \rangle \tag{4.28}$$

The corresponding Lagrangian function for the optimization problem (4.27) is formed by introducing 3 adjoint vectors $\boldsymbol{\lambda}_1$, $\boldsymbol{\lambda}_2$ and $\boldsymbol{\lambda}_3$ as:

$$L = \overline{\mathbb{K}} + \cdot(\mathbf{KU} - \mathbf{F})^T \cdot \boldsymbol{\lambda}_1 + \boldsymbol{\lambda}_2^T \cdot (\mathbf{KZ} - \mathbf{F}) + \boldsymbol{\lambda}_3^T \cdot (\mathbf{KV} - \mathbf{F}) \tag{4.29}$$

where $\mathbf{KU} - \mathbf{F} = \mathbf{0}$, $\mathbf{KU} - \mathbf{F} = \mathbf{0}$ and $\mathbf{KV} - \mathbf{F} = \mathbf{0}$ holds respectively for arbitrary adjoint vectors $\boldsymbol{\lambda}_1$, $\boldsymbol{\lambda}_2$ and $\boldsymbol{\lambda}_3$. Differentiating the Lagrangian function L with respect to the design variable ρ, we have:

$$\frac{\partial L}{\partial \rho} = \frac{\partial \overline{\mathbb{K}}}{\partial \rho} + \frac{\partial (\mathbf{KU} - \mathbf{F})^T}{\partial \rho} \cdot \boldsymbol{\lambda}_1 + \boldsymbol{\lambda}_2^T \cdot \frac{\partial (\mathbf{KZ} - \mathbf{F})}{\partial \rho} + \boldsymbol{\lambda}_3^T \cdot \frac{\partial (\mathbf{KV} - \mathbf{F})}{\partial \rho} \tag{4.30}$$

The detailed expression is presented in the following:

$$\begin{aligned} \frac{\partial [\bar{\mathbb{K}}]}{\partial \rho} =& \langle \frac{\partial (-(\mathbf{A}^0)^T[\mathbb{C}]\tilde{\mathbf{B}}^1)}{\partial \rho} + \frac{\partial ((\mathbf{D}^0)^T[\mathcal{E}]\tilde{\mathbf{B}}^1)}{\partial \rho} + \frac{\partial ((\mathbf{A}^0)^T[\mathcal{E}]\tilde{\mathbf{h}}^1)}{\partial \rho} + \frac{\partial ((\mathbf{D}^0)^T[\boldsymbol{\alpha}]\tilde{\mathbf{h}}^1)}{\partial \rho} \rangle \\ =& \langle \frac{\partial \{-(\mathbf{U}_u^T)\mathbf{B}_u^T[\mathbb{C}(\rho)]\mathbf{B}_u(\mathbf{Z}_u - \mathbf{Z}_u^x)\}}{\partial \rho} + \frac{\partial \{-(\mathbf{U}_\phi{}^T)\mathbf{B}_\phi^T[\mathcal{E}(\rho)]\mathbf{B}_u(\mathbf{Z}_u - \mathbf{Z}_u^x)\}}{\partial \rho} \\ & + \frac{\partial \{-(\mathbf{U}_u^T)\mathbf{B}_u^T[\mathcal{E}(\rho)]^T\mathbf{B}_\phi(\mathbf{Z}_\phi - \mathbf{Z}_\phi^x)\}}{\partial \rho} + \frac{\partial \{(\mathbf{U}_\phi{}^T)\mathbf{B}_\phi^T[\boldsymbol{\alpha}(\rho)]\mathbf{B}_\phi(\mathbf{Z}_\phi - \mathbf{Z}_\phi^x)\}}{\partial \rho} \rangle \\ & + \frac{\partial \{\mathbf{K}(\rho)\cdot\mathbf{U}(\rho)\}^T}{\partial \rho} \cdot \boldsymbol{\lambda}_1 + \boldsymbol{\lambda}_2^T \cdot \frac{\partial \{\mathbf{K}(\rho)\cdot\mathbf{Z}(\rho)\}}{\partial \rho} + \boldsymbol{\lambda}_3^T \cdot \frac{\partial \{\mathbf{K}(\rho)\cdot\mathbf{V}(\rho)\}}{\partial \rho} \end{aligned} \tag{4.31}$$

After some algebraic manipulations, we finally obtain the explicit sensitivity as:

$$\begin{aligned}\frac{\partial[\overline{\mathbb{K}}]}{\partial\rho} &= \left\{(\mathbf{U}_\phi{}^T)\frac{\partial\mathbf{K}_{\phi\phi}}{\partial\rho}+(\mathbf{U}_u^T)\frac{\partial\mathbf{K}_{\phi u}^T}{\partial\rho}\right\}\boldsymbol{\lambda}_{1\phi}+\left\{-(\mathbf{U}_\phi{}^T)\frac{\partial\mathbf{K}_{\phi u}}{\partial\rho}+(\mathbf{U}_u^T)\frac{\partial\mathbf{K}_{uu}}{\partial\rho}\right\}\boldsymbol{\lambda}_{1u}\\ &+\boldsymbol{\lambda}_{2\phi}^T\left\{\frac{\partial\mathbf{K}_{\phi\phi}}{\partial\rho}\mathbf{Z}_\phi+\frac{\partial\mathbf{K}_{\phi u}}{\partial\rho}\mathbf{Z}_u-\frac{\partial\mathbf{F}_\phi}{\partial\rho}\right\}+\boldsymbol{\lambda}_{2u}^T\left\{-\frac{\partial\mathbf{K}_{\phi u}^T}{\partial\rho}\mathbf{Z}_\phi+\frac{\partial\mathbf{K}_{uu}}{\partial\rho}\mathbf{Z}_u-\frac{\partial\mathbf{F}_u}{\partial\rho}\right\}\\ &+\boldsymbol{\lambda}_{3\phi}^T\left\{\frac{\partial\mathbf{K}_{\phi\phi}}{\partial\rho}\mathbf{V}_\phi+\frac{\partial\mathbf{K}_{\phi u}}{\partial\rho}\mathbf{V}_u\right\}+\boldsymbol{\lambda}_{3u}^T\left\{-\frac{\partial\mathbf{K}_{\phi u}^T}{\partial\rho}\mathbf{V}_\phi+\frac{\partial\mathbf{K}_{uu}}{\partial\rho}\mathbf{V}_u\right\}\\ &+(\mathbf{U}_u)^T\left\langle\mathbf{B}_u^T\frac{\partial[\mathbb{C}(\rho)]}{\partial\rho}\mathbf{B}_u\right\rangle(\mathbf{Z}_u-\mathbf{Z}_u{}^x)+(\mathbf{U}_\phi)^T\left\langle\mathbf{B}_\phi^T\frac{\partial[\mathcal{E}(\rho)]}{\partial\rho}\mathbf{B}_u\right\rangle(\mathbf{Z}_u-\mathbf{Z}_u{}^x)\\ &+(\mathbf{U}_u)^T\left\langle\mathbf{B}_u^T\frac{\partial[\mathcal{E}(\rho)]^T}{\partial\rho}\mathbf{B}_\phi\right\rangle(\mathbf{Z}_\phi-\mathbf{Z}_\phi{}^x)-(\mathbf{U}_\phi)^T\left\langle\mathbf{B}_\phi^T\frac{\partial[\alpha(\rho)]}{\partial\rho}\mathbf{B}_\phi\right\rangle(\mathbf{Z}_\phi-\mathbf{Z}_\phi{}^x)\end{aligned} \tag{4.32}$$

where the adjoint vectors $[\boldsymbol{\lambda}_{1\phi};\ \boldsymbol{\lambda}_{1u}]$, $[\boldsymbol{\lambda}_{2\phi};\ \boldsymbol{\lambda}_{2u}]$ and $[\boldsymbol{\lambda}_{3\phi};\ \boldsymbol{\lambda}_{3u}]$ can be calculated by solving the following adjoint equations:

$$\begin{bmatrix}\mathbf{K}_{\phi\phi} & -\mathbf{K}_{\phi u}\\ \mathbf{K}_{\phi u}^T & \mathbf{K}_{uu}\end{bmatrix}\begin{bmatrix}\boldsymbol{\lambda}_{1\phi}\\ \boldsymbol{\lambda}_{1u}\end{bmatrix}=-\begin{bmatrix}\langle\mathbf{B}_\phi^T[\alpha(\rho)]\mathbf{B}_\phi\rangle(\mathbf{Z}_\phi-\mathbf{Z}_\phi{}^x)-\langle\mathbf{B}_\phi^T[\mathcal{E}(\rho)]\mathbf{B}_u\rangle(\mathbf{Z}_u-\mathbf{Z}_u{}^x)\\ -\langle\mathbf{B}_u^T[\mathbb{C}(\rho)]\mathbf{B}_u\rangle(\mathbf{Z}_u-\mathbf{Z}_u{}^x)-\langle\mathbf{B}_u^T[\mathcal{E}(\rho)]^T\mathbf{B}_\phi\rangle(Z_\phi-\mathbf{Z}_\phi{}^x)\end{bmatrix} \tag{4.33}$$

and

$$\begin{bmatrix}\mathbf{K}_{\phi\phi} & -\mathbf{K}_{\phi u}\\ \mathbf{K}_{\phi u}^T & \mathbf{K}_{uu}\end{bmatrix}\begin{bmatrix}\boldsymbol{\lambda}_{2\phi}\\ \boldsymbol{\lambda}_{2u}\end{bmatrix}=-\begin{bmatrix}\langle\mathbf{B}_\phi^T[\alpha(\rho)]\mathbf{B}_\phi\rangle\mathbf{U}_\phi-\langle\mathbf{B}_\phi^T[\mathcal{E}(\rho)]\mathbf{B}_u\rangle\mathbf{U}_u\\ -\langle\mathbf{B}_u^T[\mathbb{C}(\rho)]\mathbf{B}_u\rangle\mathbf{U}_u-\langle\mathbf{B}_u^T[\mathcal{E}(\rho)]^T\mathbf{B}_\phi\rangle\mathbf{U}_\phi\end{bmatrix} \tag{4.34}$$

and

$$\begin{bmatrix}\mathbf{K}_{\phi\phi} & -\mathbf{K}_{\phi u}\\ \mathbf{K}_{\phi u}^T & \mathbf{K}_{uu}\end{bmatrix}\begin{bmatrix}\boldsymbol{\lambda}_{3\phi}\\ \boldsymbol{\lambda}_{3u}\end{bmatrix}=-\begin{bmatrix}-\langle\mathbf{B}_\phi^T[\alpha(\rho)]\mathbf{B}_\phi x\rangle\mathbf{U}_\phi+\langle\mathbf{B}_\phi^T[\mathcal{E}(\rho)]\mathbf{B}_u x\rangle\mathbf{U}_u\\ \langle\mathbf{B}_u^T[\mathbb{C}(\rho)]\mathbf{B}_u x\rangle\mathbf{U}_u+\langle\mathbf{B}_u^T[\mathcal{E}(\rho)]^T\mathbf{B}_\phi x\rangle\mathbf{U}_\phi\end{bmatrix} \tag{4.35}$$

The optimization problem (4.27) is solved by the Conservative Convex Separable Approximations (CCSA) optimizer [144] based on the adjoint sensitivity.

4.2.3 Numerical examples

4.2.3.1 Topology optimization of the ceramic/ceramic piezoelectric composite

In the previous chapter, having established that the converse flexoelectric effect makes a significant contribution to the overall flexoelectric response of the PZT/PZT composites, we now perform topology optimization to determine topologies that maximize the converse flexoelectric contributions. We thus consider the topology optimization of a two-phase composite made of piezoelectric phases. Each phase is made with PZT (lead zirconium titanate ceramics) as in the previous example. Here, the crystal lattice is oriented by a mismatch angle of $\theta=\pi$ in the inclusion phase. Then via (2.141)-(2.143) in Chapter 2, the properties of the inclusion phase can be obtained as $[\mathbb{C}^2]=[\mathbb{C}^1]$ given by (4.20), $[\alpha^2]=[\alpha^1]$ given by (4.21) and $[\mathcal{E}^1]$ given in (4.22).

We perform the topology optimization of the inclusion shape with respect to the converse flexoelectric coefficients $\overline{K}_{1111}$, $\overline{K}_{2211}$ and $\overline{K}_{1212}$ and set the inclusion volume fraction to $f=0.4$. As a first guess, the design variables are uniformly set to $\rho_e=0.4$ (e = 1,..., N_e = 6400). The guess design with triangular shape which is illustrated in Fig. 2.3 has been investigated in

(a) (b) (c)

Figure 4.17: Optimal topology for $\overline{K}$ for the PZT/PZT composite: (a) $\overline{K}_{1111}$; (b) $\overline{K}_{2211}$; (c) $\overline{K}_{1212}$.

section 2.4.2, recalling that the reference solutions are taken as the extremum values of $\overline{K}_{1111}$, $\overline{K}_{2211}$ and $\overline{K}_{1212}$ for the triangular microstructure at $\theta = \pi$ in Fig. 2.7 (a), and will serve as a comparison solution with respect to optimized topological designs, i.e. $\overline{K}^{ref}_{1111} = 0.1860 \times 10^{-3}$ C $\cdot$ m^{-1} $\overline{K}^{ref}_{2211} = 0.1181 \times 10^{-3}$ C $\cdot$ m^{-1} and $\overline{K}^{ref}_{1212} = 0.0504 \times 10^{-3}$ C $\cdot$ m^{-1}. However, for the components $\overline{K}_{1112}$, $\overline{K}_{2222}$ and $\overline{K}_{1222}$, the reference solution obtained by microstructure with triangular inclusion are all zero at $\theta = \pi$, as shown in Fig. 2.7(a). Therefore, we do not consider topology optimization for those components in the present case of PZT/PZT composites.

The final optimized unit cell topologies are shown in Figs. 4.17, where the copper and black colors refer to the inclusion and matrix phases, respectively. The iteration histories for $\overline{K}_{1111}$, $\overline{K}_{2211}$ and $\overline{K}_{1212}$ are shown in Fig. 4.18. It is noted that the present optimization procedure leads to stable and convergent optimal solutions. The final values for the optimized microstructures are $\overline{K}_{1111} = 0.3525 \times 10^{-3}$ C $\cdot$ m^{-1}, $\overline{K}_{2211} = 0.2241 \times 10^{-3}$ C $\cdot$ m^{-1} and $\overline{K}_{2112} = 0.0955 \times 10^{-3}$ C $\cdot$ m^{-1}, which represents a significant improvement as compared to the reference triangular solutions by a factor of 1.89 for the components $\overline{K}_{1111}$, $\overline{K}_{2211}$ and $\overline{K}_{1212}$. From Fig. 4.17, we can see that the three optimized unit cells obtained by $\overline{K}_{1111}$, $\overline{K}_{2211}$ and $\overline{K}_{1212}$ have similar topologies. Finally, we note that the optimized microstructures are similar to the ones obtained by optimizing the direct flexoelectric constants $\overline{F}_{1221}$ and $\overline{F}_{2112}$ for the PZT/PZT case [168].

4.2.3.2 Topology optimization of the ceramic/doped piezoelectric polymer composite

In this example, we replace the stiff PZT inclusion with a soft, dielectric, polymer inclusion (polyvinylidene fluoride, PVDF). The elastic, piezoelectric and dielectric properties for the polymer are given below. In comparison to the PZT properties, all of the polymer properties are 1-2 orders in magnitude lower than for PZT. The material parameters of matrix PZT are expressed in (4.20)-(4.22) [214], while the material properties of PVDF are described in (4.36)-(4.38) [216].

$$[C^2] = \begin{bmatrix} 6.066 & 3.911 & 0 \\ 3.911 & 6.066 & 0 \\ 0 & 0 & 1.078 \end{bmatrix} (\text{GPa}) \tag{4.36}$$

$$[\alpha^2] = \begin{bmatrix} 0.025 & 0 \\ 0 & 0.084 \end{bmatrix} (\text{nC} \cdot \text{m}^{-1} \cdot \text{V}^{-1}) \tag{4.37}$$

$$[e^2] = \begin{bmatrix} 0.1272 & 0.0873 & 0 \\ 0 & 0 & 0 \end{bmatrix} (\text{C} \cdot \text{m}^{-2}) \tag{4.38}$$

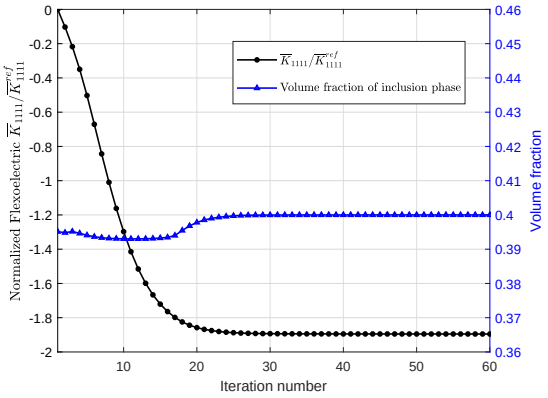

(a)

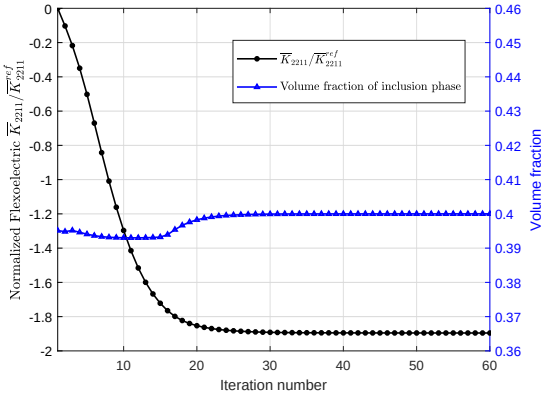

(b)

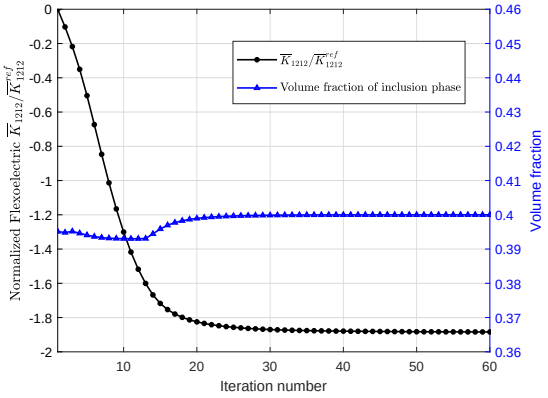

(c)

Figure 4.18: Topology optimization process with respect to normalized flexoelectric components and volume fractions for the PZT/PZT composite: (a) $\overline{K}_{1111}$; (b) $\overline{K}_{2211}$; (c) $\overline{K}_{1212}$.

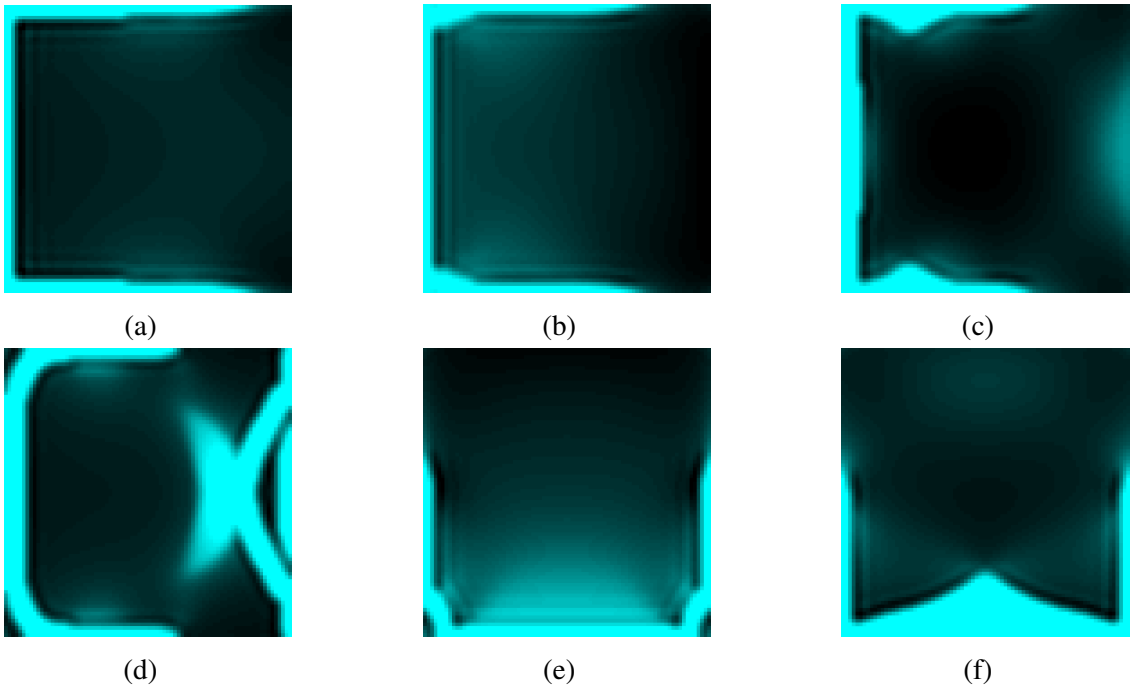

Figure 4.19: Optimal topology for $\overline{K}$ for the PZT/PVDF composite: (a) $\overline{K}_{1111}$; (b) $\overline{K}_{2211}$; (c) $\overline{K}_{1212}$; (d) $\overline{K}_{2222}$; (e) $\overline{K}_{2212}$; (f) $\overline{K}_{1211}$.

We perform topology optimization of the PVDF inclusion with respect to the converse flexoelectric coefficients $\overline{K}_{1111}$, $\overline{K}_{2211}$, $\overline{K}_{1212}$, $\overline{K}_{2222}$, $\overline{K}_{2212}$ and $\overline{K}_{1211}$. To ensure that these results can be compared against the previous PZT/PZT results, we set the volume fraction of the PVDF inclusion to be $f = 0.4$ for all cases. Similarly, the initial guess is set by $\rho_e = 0.4$, $e = 1,2,...,N_e = 6400$. The final optimal unit cells of the converse flexoelectric coefficients $\overline{K}_{1111}$, $\overline{K}_{2211}$, $\overline{K}_{1212}$, $\overline{K}_{2222}$, $\overline{K}_{2212}$ and $\overline{K}_{1211}$ are shown in Fig. 4.19. In these figures, the cyan and black colors refer to the inclusion PVDF and matrix PZT, respectively. The reference solutions calculated by a triangular PVDF inclusion as in Fig. 2.2(b) of Chapter 2 are shown for each case. The reference values obtained are $\overline{K}_{1111} = 0.0432 \times 10^{-3}$ C$\cdot$m^{-1}, $\overline{K}_{2211} = 0.0139 \times 10^{-3}$ C$\cdot$m^{-1}, $\overline{K}_{1212} = 0.0073 \times 10^{-3}$ C$\cdot$m^{-1}, $\overline{K}_{2222} = 0.0262 \times 10^{-3}$ C$\cdot$m^{-1}, $\overline{K}_{2212} = 0.0033 \times 10^{-3}$ C$\cdot$m^{-1} and $\overline{K}_{1211} = 0.0004 \times 10^{-3}$ C$\cdot$m^{-1} for the PZT/polymer composites with triangular inclusion.

We obtained six different optimized unit cells, and a significant improvement can be found as compared to the reference triangular solutions. The optimal absolute values are $\overline{K}_{1111} = 0.3420 \times 10^{-3}$ C$\cdot$m^{-1}, $\overline{K}_{2211} = 0.2054 \times 10^{-3}$ C$\cdot$m^{-1}, $\overline{K}_{1212} = 0.0923 \times 10^{-3}$ C$\cdot$m^{-1}, $\overline{K}_{2222} = 0.1218 \times 10^{-3}$ C$\cdot$m^{-1}, $\overline{K}_{2212} = 0.3267 \times 10^{-3}$ C$\cdot$m^{-1} and $\overline{K}_{1211} = 0.0821 \times 10^{-3}$ C$\cdot$m^{-1}, which represents increases by factors of 7.92, 14.78, 12.64, 4.65, 99 and 205.25 times, respectively. Interestingly, despite being comprised of a polymer inclusion whose (elastic, piezoelectric, and dielectric) properties are all about two orders of magnitude smaller than the PZT matrix, the flexoelectric constants are quite similar to those obtained for the optimized PZT/PZT composites discussed previously, with significantly larger percentage enhancements.

In Figs. 4.20 and 4.21, we depict the local electric gradient and strain components of the optimized microstructures that are associated with the converse flexoelectric coefficients $\overline{K}_{2222}$ and $\overline{K}_{1211}$, respectively. In the different cases, we can note that the optimized geometry favors the localization of these fields near the interfaces, which may be expected due to the problem being one of a soft inclusion within a stiff matrix.

The numerical investigations revealed that the apparent converse flexoelectric coefficients in a composite made of periodic triangular inclusions have the same order of magnitude as the direct flexoelectric properties of the local constituents. We show that optimized designs can lead to effective converse flexoelectric properties which can be improved by 1-2 orders of magnitude

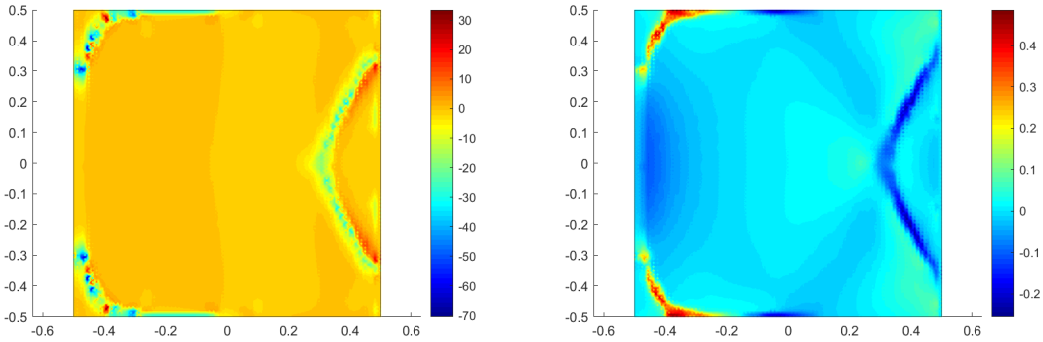

(a) Electric gradient ∇E_{22}-component (b) Strain ε_{22}-component

Figure 4.20: Electric field gradient component ∇E_{22} and strain component ε_{22} within the PZT-PVDF microstructure corresponding to the optimized coefficient $\overline{K}_{2222}$.

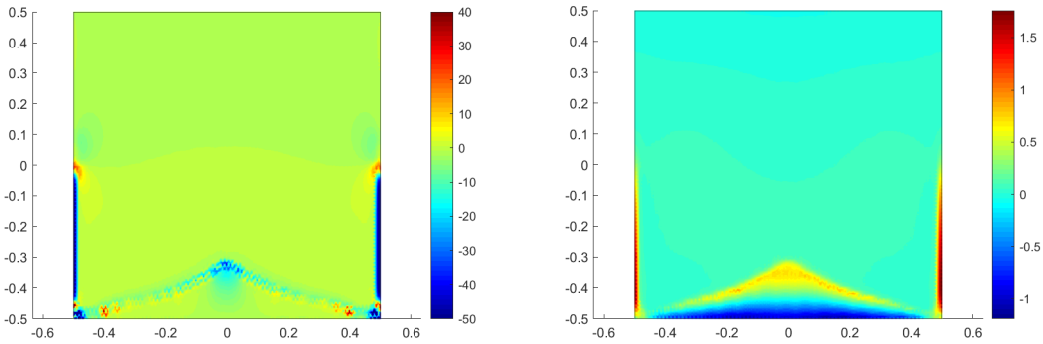

(a) Electric gradient ∇E_{11}-component (b) Strain ε_{12}-component

Figure 4.21: Electric field gradient component ∇E_{11} and strain component ε_{12} within the PZT-PVDF microstructure corresponding to the optimized coefficient $\overline{K}_{1211}$.

as compared to guess designs for ceramics/ceramics or polymer/ceramics composites.

4.3 Conclusion

In this chapter, a topology optimization framework has been proposed to maximize the effective direct flexoelectric properties of composites made of piezoelectric phases, then extended to enhance the converse flexoelectric properties. The original contribution here is to combine computational homogenization for flexoelectric materials with Toplogy Optimization of microstructures. We use a homogenization method to estimate the direct and converse flexoelectric properties from the distribution of local phases in a Representative Volume Element (RVE), which precludes the necessity of optimizing the entire structure. The electromechanical coupling computational homogenization framework to estimate the effective direct and converse flexoelectric tensors of periodic piezoelectric composites was already formulated in Chapter 2. A SIMP (Solid Isotropic Material with Penalization) method was used to interpolate the material constitutive properties of phases with spatially varying densities. The adjoint numerical sensitivities of direct and converse flexoelectric coefficients were respectively derived. The topology optimization problems were performed to maximize the absolute values of the flexoelectric tensor under the constraint of a constant volume fraction of inclusion. Results show that on several cases (piezo-piezo, piezo-polymer and porous piezo-composites), the present scheme allows increasing the effective direct and converse flexoelectric properties up to 1-2 orders of magnitude as compared to a naive "guess" design.

We found different mechanisms to enhance the flexoelectric properties, and the electromechanical coupling. Specifically, piezo-piezo (hard/hard) composites generated an enhanced electromechanical response through enhancement of their effective piezoelectric properties. In contrast, piezo-polymer (hard/soft) composites generated an enhanced electromechanical response through an interplay of enhanced electromechanical (piezoelectric) and electrical (dielectric) properties, and reduced mechanical compliance, which result from significantly enhanced local electric fields and strain gradients along the hard/soft interface. We believe that the present framework has the potential to design high-performance flexoelectric components for use e.g. in energy harvesting systems, sensors or actuators without the need for materials exhibiting intrinsically high flexoelectricity, that will be further discussed in the next chapters.

Chapter 5

Multiscale topology optimization of an electromechanical dynamic energy harvester made of non-piezoelectric material

In the realm of flexoelectric composites, research has concentrated on developing piezoelectric composites using non-piezoelectric materials, driven by earlier work [24, 25]. Traditional piezoelectric composites usually include lead-containing PZT for higher permittivity. Piezoelectric responses, achieved in these composites made of purely flexoelectric materials, can be comparable to common single-phase piezoelectrics. Non-piezoelectric flexoelectric materials can serve as low-cost, lead-free alternatives to traditional piezoelectric materials, thereby promoting the sustainability of electromechanical applications.

In this chapter, a multiscale topology optimization method has been proposed for the design of electromechanical energy harvesting systems converting mechanical vibrations into electric currents made of non-piezoelectric materials. At the microscopic scale, the material is assumed to be periodic, porous and flexoelectric, although not piezoelectric. A first step of topology optimization is performed, in order to maximize the effective (homogenized) flexoelectric properties of the material. As a result, the effective material, although made of a non-piezoelectric material, has apparent piezoelectric properties. In a second step, these properties are used to model the behaviour of a dynamic electromechanical energy harvesting system structure. A second topology optimisation step, this time performed at the structural scale, aims to maximize the system Electromechanical Coupling Factor (ECF) for a given forced vibration frequency. At both scales, an Isogeometric Analysis (IGA) method is employed to solve the strain-gradient problems numerically. We show that the optimized structure obtained offers significant gains in terms of ECF compared with non-optimized structures of the same volume, over a wide range of excitation frequencies. The procedure could open up new possibilities in the design of energy recovery systems without the use of piezoelectric materials.

This chapter is adapted from the published articles [217].

5.1 Homogenization of heterogeneous flexoelectric materials

5.1.1 Micro RVE problem

We first present a framework to perform the homogenization of microstructures made of flexoelectric materials. We consider a periodic composite (see Fig. 5.1(a)) characterized by a Representative Volume Element (RVE) defined in a domain $\Omega_m \in \mathbb{R}^2$ whose boundary is denoted by $\partial\Omega_m$, as shown schematically in Fig. 5.1(b). The phases within the RVE are assumed

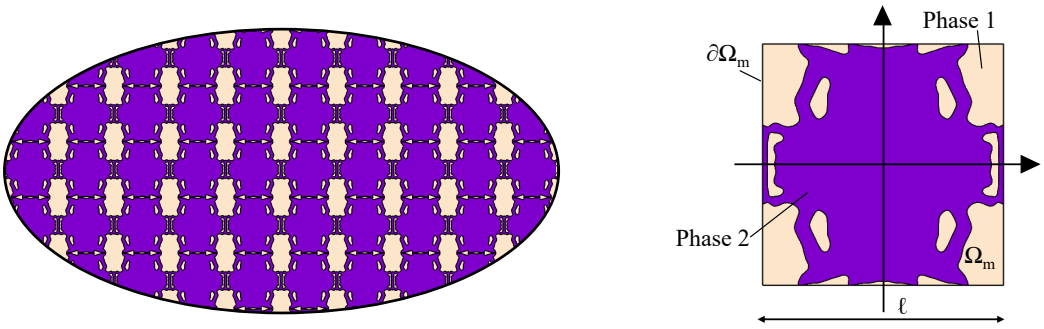

(a) (b)

Figure 5.1: (a) Periodic flexoelectric structure and (b) Representative Volume Element (RVE) made of two phases.

to be linearly flexoelectric and characterized by an elastic tensor C, a dielectric tensor α and a flexoeletric tensor μ. The energy density function of a purely flexoelectric material (non-piezoelectric) at the microscale is defined by:

$$W_1 = \frac{1}{2}C_{ijkl}\varepsilon_{ij}\varepsilon_{kl} - \frac{1}{2}\alpha_{ij}E_iE_j - \mu_{ijkl}E_i\nabla\varepsilon_{jkl} \tag{5.1}$$

where ε denotes strain tensor, E denotes electric field vector, related to the electric potential ϕ by $E_i = -\phi_{,i}$, and $\nabla\varepsilon$ denotes the third-order strain gradient tensor.

The local equilibrium equations are given by

$$\sigma_{ij,j} - \tau_{ijk,jk} - f_i = R_{1i} = 0, \text{ in } \Omega_m \tag{5.2}$$
$$d_{i,i} = R_2 = 0, \text{ in } \Omega_m \tag{5.3}$$

with:

$$\sigma_{ij} = C_{ijkl}\varepsilon_{kl} \tag{5.4}$$
$$d_i = \alpha_{ij}E_j + \mu_{ijkl}\nabla\varepsilon_{jkl} \tag{5.5}$$
$$\tau_{jkl} = -\mu_{ijkl}E_i \tag{5.6}$$

where σ denotes the stress tensor, f is body forces vector, $\boldsymbol{d}$ is the electric displacement, and τ denotes the couple stress. The RVE is assumed to be subjected to macroscopic loads, i.e. a macroscopic strain $\overline{\varepsilon}$, a macroscopic electric field $\overline{E}$ and a macroscopic strain gradient $\overline{\nabla\varepsilon}$ which are defined at the scale of the structure. They are transferred to the RVE through the quadratic boundary conditions:

$$u_i = \overline{\varepsilon}_{ij}x_j + \frac{1}{2}\overline{g}_{ijk}x_jx_k + \tilde{u}_i \text{ on } \partial\Omega_m \tag{5.7}$$

with

$$\overline{g}_{ijk} = \overline{\nabla\varepsilon}_{ijk} + \overline{\nabla\varepsilon}_{ikj} - \overline{\nabla\varepsilon}_{jki} \tag{5.8}$$

and

$$\phi = -\overline{E}_ix_i \text{ on } \partial\Omega_m \tag{5.9}$$

The forces f in (5.2) have been introduced to induce purely uniform fields of derivatives when the RVE is homogeneous. Their expression is given by:

$$f_i = \overline{C}_{ijkl}\overline{\nabla\varepsilon}_{klj} \tag{5.10}$$

Using superposition, the local strain field $\varepsilon(x)$, local electric field $E(x)$ and local strain gradient field $\nabla\varepsilon(x)$ at a point $x \in \Omega_m$ can be expressed in the form:

$$\varepsilon_{ij}(x) = A^0_{ijpq}(x)\overline{\varepsilon}_{pq} - B^0_{ijp}(x)\overline{E}_p - A^1_{ijpqr}(x)\overline{\nabla\varepsilon}_{pqr} \tag{5.11}$$

$$E_i(x) = D^0_{ipq}(x)\overline{\varepsilon}_{pq} - h^0_{ip}(x)\overline{E}_p - D^1_{ipqr}(x)\overline{\nabla\varepsilon}_{pqr} \tag{5.12}$$

$$\nabla\varepsilon_{ijk}(x) = J^0_{ijkpq}(x)\overline{\varepsilon}_{pq} - Q^0_{ijkp}(x)\overline{E}_p - J^1_{ijkpqr}(x)\overline{\nabla\varepsilon}_{pqr} \tag{5.13}$$

where the local fields A^0, B^0, A^1, D^0, h^0, D^1, J^0, Q^0 and J^1 are obtained by solving Eqs. (5.2) and (5.3) on the RVE by the Isogeometric Analysis method (IGA). More details are provided in Section.5.1.2). Substituting (5.11)-(5.13) into (5.1), the effective (homogenized) flexoelectric tensor is obtained as:

$$\overline{\mu}_{ijkl} = \left\langle -B^0_{pqi}C_{pqrs}A^1_{rsjkl} + h^0_{pi}\alpha_{pq}D^1_{qjkl} + Q^0_{pqri}\mu_{pqrs}D^1_{sjkl} + h^0_{pi}\mu_{pqrs}J^1_{qrsjkl} \right\rangle \tag{5.14}$$

where $\langle\cdot\rangle = \frac{1}{V}\int(\cdot)dV$. In the above, the dependence to x has been ommitted to alleviate the notations. The 2D matrix form of the effective flexoelectric tensor can be written as:

$$\overline{\boldsymbol{\mu}} = \begin{bmatrix} \overline{\mu}_{1111} & \overline{\mu}_{1112} & \overline{\mu}_{1221} & \overline{\mu}_{1222} & \overline{\mu}_{1121} & \overline{\mu}_{1122} \\ \overline{\mu}_{2111} & \overline{\mu}_{2112} & \overline{\mu}_{2221} & \overline{\mu}_{2222} & \overline{\mu}_{2121} & \overline{\mu}_{2122} \end{bmatrix} \tag{5.15}$$

5.1.2 Calculation of effective flexoelectric tensor

The strain and electric fields solutions, strain gradient fields solutions of the problem (5.3) can be expressed as the functions of the effective strain, electric and strain gradient fields as

$$\varepsilon_{ij} = A^0_{ijpq}\overline{\varepsilon}_{pq} - B^0_{ijp}\overline{E}_p - A^1_{ijpqr}\overline{\nabla\varepsilon}_{pqr} \tag{5.16}$$

$$E_i = D^0_{ipq}\overline{\varepsilon}_{pq} - h^0_{ip}\overline{E}_p - D^1_{ipqr}\overline{\nabla\varepsilon}_{pqr} \tag{5.17}$$

$$\nabla\varepsilon_{ijk} = J^0_{ijkpq}\overline{\varepsilon}_{pq} - Q^0_{ijkp}\overline{E}_p - J^1_{ijkpqr}\overline{\nabla\varepsilon}_{pqr} \tag{5.18}$$

We define the displacement and electric fields matrices:

$$\mathbf{U} = \{\mathbf{U}_\phi; \mathbf{U}_u\},\ \mathbf{V} = \{\mathbf{V}_\phi; \mathbf{V}_u\},\ \mathbf{W} = \{\mathbf{W}_\phi; \mathbf{W}_u\} \tag{5.19}$$

$$\mathbf{U}_u = [\mathbf{u}^1, \mathbf{u}^2, \mathbf{u}^3],\ \mathbf{V}_u = [\mathbf{u}^4, \mathbf{u}^5],\ \mathbf{W}_u = [\mathbf{u}^6, \mathbf{u}^7, \mathbf{u}^8, \mathbf{u}^9, \mathbf{u}^{10}, \mathbf{u}^{11}] \tag{5.20}$$

$$\mathbf{U}_\phi = [\phi^1, \phi^2, \phi^3],\ \mathbf{V}_\phi = [\phi^4, \phi^5],\ \mathbf{W}_\phi = [\phi^6, \phi^7, \phi^8, \phi^9, \phi^{10}, \phi^{11}] \tag{5.21}$$

The displacement fields $\mathbf{u}^i$ and the electric fields ϕ^i are the vector columns containing respectively the nodal displacement and electric potentials solution of the localization problems Eqs. (5.3) with the boundary conditions described in Table 5.1.

The matrices associated with the tensors A^0, B^0, A^1, D^0, A^0, h^0, D^1, J^0, Q^0 and J^1 in (5.16)-(5.18) can be computed according to

$$\mathbf{A}^0(x) = \mathbf{B}_u(x)\mathbf{U}_u, \quad \mathbf{B}^0(\mathbf{x}) = \mathbf{B}_u(x)\mathbf{V}_u, \quad \mathbf{A}^1(\mathbf{x}) = \mathbf{B}_u(\mathbf{x})\mathbf{W}_u; \tag{5.22}$$

$$\mathbf{D}^0(x) = -\mathbf{B}_\phi(x)\mathbf{U}_\phi, \quad \mathbf{h}^0(x) = -\mathbf{B}_\phi(x)\mathbf{V}_\phi, \quad \mathbf{D}^1(x) = -\mathbf{B}_\phi(x)\mathbf{W}_\phi \tag{5.23}$$

$$\mathbf{J}^0(x) = \mathbf{H}_u(x)\mathbf{U}_u, \quad \mathbf{Q}^0(x) = \mathbf{H}_u(x)\mathbf{V}_u, \quad \mathbf{J}^1(x) = \mathbf{H}_u(x)\mathbf{W}_u \tag{5.24}$$

Substituting (5.22)-(5.24) into (5.14), we have the effective flexoelectric tensor in matrix form as

$$\overline{\boldsymbol{\mu}} = -\left\langle \mathbf{V}_u^T\mathbf{B}_u^T\mathbf{C}\mathbf{B}_u\mathbf{W}_u - \mathbf{V}_\phi^T\mathbf{B}_\phi^T\boldsymbol{\alpha}\mathbf{B}_\phi\mathbf{W}_\phi + \mathbf{V}_u^T\mathbf{H}_u^T\boldsymbol{\mu}\mathbf{B}_\phi\mathbf{W}_\phi + \mathbf{V}_\phi^T\mathbf{B}_\phi^T\boldsymbol{\mu}\mathbf{H}_u\mathbf{W}_u \right\rangle \tag{5.25}$$

Table 5.1: Elementary solution corresponding to the prescribed macroscopic strain, electric potential and strain gradient components

Field	$(\overline{\varepsilon}_{11},\overline{\varepsilon}_{22},\overline{\varepsilon}_{12})$	$(\overline{E_1},\overline{E_2})$	$(\overline{\nabla\varepsilon}_{111},\overline{\nabla\varepsilon}_{221},\overline{\nabla\varepsilon}_{122},\overline{\nabla\varepsilon}_{222},\overline{\nabla\varepsilon}_{112},\overline{\nabla\varepsilon}_{121})$
$\mathbf{u}^1,\phi^1$	(1,0,0)	(0,0)	(0,0,0,0,0,0)
$\mathbf{u}^2,\phi^2$	(0,1,0)	(0,0)	(0,0,0,0,0,0)
$\mathbf{u}^3,\phi^3$	$(0,0,\frac{1}{2})$	(0,0)	(0,0,0,0,0,0)
$\mathbf{u}^4,\phi^4$	(0,0,0)	(1,0)	(0,0,0,0,0,0)
$\mathbf{u}^5,\phi^5$	(0,0,0)	(0,1)	(0,0,0,0,0,0)
$\mathbf{u}^6,\phi^6$	(0,0,0)	(0,0)	(1,0,0,0,0,0)
$\mathbf{u}^7,\phi^7$	(0,0,0)	(0,0)	(0,1,0,0,0,0)
$\mathbf{u}^8,\phi^8$	(0,0,0)	(0,0)	(0,0,1,0,0,0)
$\mathbf{u}^9,\phi^9$	(0,0,0)	(0,0)	(0,0,0,1,0,0)
$\mathbf{u}^{10},\phi^{10}$	(0,0,0)	(0,0)	(0,0,0,0,1,0)
$\mathbf{u}^{11},\phi^{11}$	(0,0,0)	(0,0)	(0,0,0,0,0,1)

5.2 Dynamic flexoelectricity at the macro scale

We consider a structure defined in an open domain $\Omega \subset \mathbb{R}^2$, with boundary $\partial\Omega$, and associated with the macro scale problem. At this scale, the composite is modeled by a homogeneous material whose effective properties have been defined with respect to a given microstructure geometry in section 5.1. Over the boundary of the domain $\partial\Omega$, mechanical displacements and tractions are prescribed over parts of the boundary denoted respectively by $\partial\Omega_u$ and $\partial\Omega_t$, as well as electric potential and surface charge density over portions $\partial\Omega_\phi$ and $\partial\Omega_D$, respectively. In addition, the strain gradients are associated with other types of boundary conditions defined over portions of the boundary $\partial\Omega_v$ and $\partial\Omega_r$. The boundary conditions are imposed such that $\partial\Omega_u \cup \partial\Omega_t = \partial\Omega_\phi \cup \partial\Omega_D = \partial\Omega_v \cup \partial\Omega_r = \partial\Omega$ and $\partial\Omega_u \cap \partial\Omega_t = \partial\Omega_\phi \cap \partial\Omega_D = \partial\Omega_v \cap \partial\Omega_r = \emptyset$. We define the electric enthalpy density $\hat{h}$ for a linear electromechanical system as:

$$\hat{h} = \frac{1}{2}\overline{C}_{ijkl}\varepsilon_{ij}\varepsilon_{kl} - \frac{1}{2}\overline{\alpha}_{ij}E_iE_j - \overline{e}_{ijk}E_k\varepsilon_{ij} - \overline{\mu}_{ijkl}E_i\nabla\varepsilon_{jkl} + \frac{1}{2}\overline{G}_{ijklmn}\nabla\varepsilon_{ijk}\nabla\varepsilon_{lmn} \tag{5.26}$$

where $\overline{C}$, $\overline{\alpha}$, $\overline{e}$ and $\overline{\mu}$ are the effective (homogenized) elastic, dielectric, piezoelectric and flexoelectric tensors, respectively, while $\overline{G}$ corresponds to the higher-order strain gradient elastic tensor (see a complete definition of these tensors in Chapter 3). For the sake of simplification, we assume here $\overline{G}$ in the form: $\overline{G}_{ijklmn} = \overline{C}_{ijlm}\ell_{kn}$, where ℓ_{kn} is material length parameters. Note that in this section, we do not use special notation to differ the quantities from microscopic ones in the previous section, to avoid burdening the notations.

The constitutive equations are derived as:

$$d_i = -\frac{\partial\hat{h}}{\partial E_i} = \overline{\alpha}_{ij}E_j + \overline{e}_{ijk}\varepsilon_{jk} + \overline{\mu}_{ijkl}\nabla\varepsilon_{jkl} \tag{5.27}$$

$$\sigma_{ij} = \frac{\partial\hat{h}}{\partial\varepsilon_{ij}} = \overline{C}_{ijkl}\varepsilon_{kl} - \overline{e}_{ijk}E_k \tag{5.28}$$

$$\tau_{ijk} = \frac{\partial\hat{h}}{\partial\nabla\varepsilon_{ijk}} = \overline{G}_{ijklmn}\nabla\varepsilon_{lmn} - \overline{\mu}_{ijkl}E_l \tag{5.29}$$

By integrating over Ω we obtain the electrical enthalpy as

$$H = \frac{1}{2}\int_\Omega (\sigma_{ij}\varepsilon_{ij} + \tau_{ijk}\nabla\varepsilon_{ijk} - D_iE_i)\mathrm{d}\Omega \tag{5.30}$$

The work W of external mechanical and electrical forces is given as

$$W^{ext} = \int_{\Omega_t} t_i^d u_i \mathrm{d}S - \int_{\Omega_D} D_n^b \phi \mathrm{d}S \tag{5.31}$$

The Rayleigh dissipation can be written as

$$\tilde{R} = \frac{1}{2}\int_{\Omega} V_{ij}\dot{u}_i\dot{u}_j \mathrm{d}\Omega \tag{5.32}$$

where V_{ij} is viscous damping coefficients and $\dot{(\cdot)}$ is time derivative.

The kinetic energy taking into account micro-inertial effect is defined by

$$K = \frac{1}{2}\int_{\Omega} \rho_0(\dot{u}_i\dot{u}_i + \ell_d^2\dot{u}_{i,j}\dot{u}_{i,j})\mathrm{d}\Omega \tag{5.33}$$

where ρ_0 is the density, ℓ_d is a dynamic scaling parameter (micro inertia characteristic length). The acceleration gradient term is generally introduced to obtain physically acceptable dispersive wave velocity [200] in strain-gradient models.

The governing differential equations for the electromechanical system are derived from the Hamiltons principle:

$$\delta\int_{t_1}^{t_2}(H - W - K)\mathrm{d}t = 0 \tag{5.34}$$

After algebraic manipulation, the weak form of balance equations are obtained as:

$$\int_{\Omega}\left(\rho_0\ddot{u}_i\delta u_i + \ell_d^2\ddot{u}_{i,j}\delta u_{i,j} + \sigma_{ij}\delta\varepsilon_{ij} + \tau_{ijk}\delta\nabla\varepsilon_{ijk} + V_{ij}\dot{u}_i\delta u_j\right)\mathrm{d}\Omega - \int_{\partial\Omega_t} t_i^d\delta u_i \mathrm{d}S = R_3 \tag{5.35}$$

$$\int_{\Omega} d_i\delta\phi_{,i}\mathrm{d}\Omega - \int_{\partial\Omega_D} D_n^d\delta\phi\mathrm{d}S = R_4 \tag{5.36}$$

The problem is completed with boundary conditions:

$$\phi = \phi^d \text{ on } \partial\Omega_\phi \tag{5.37}$$

$$d_i n_i = -D_n^d \text{ on } \partial\Omega_D \tag{5.38}$$

$$u_i = u^d \text{ on } \partial\Omega_{\mathrm{u}} \tag{5.39}$$

$$t_k = n_j\left(\sigma_{jk} - \tau_{ijk,i}\right) - D_j\left(n_i\tau_{ijk}\right) = t_k^d \text{ on } \partial\Omega_{\mathrm{t}} \tag{5.40}$$

$$u_{i,j}n_j = v_i^d \text{ on } \partial\Omega_v \tag{5.41}$$

$$n_i n_j \tau_{ijk} = r_k^d \text{ on } \partial\Omega_r \tag{5.42}$$

where ϕ^d, D_n^d, $\mathbf{u}^d$, $\mathbf{t}^d$, $\mathbf{v}^d$ and $\mathbf{r}_k^d$ are the prescribed electric potential, surface charge density, displacements, tractions, normal derivative of the displacement and the higher-order traction, respectively. $\mathbf{n}$ is the unitary normal vector to the boundary $\partial\Omega$ and $D_j(.) = \frac{\partial(.)}{\partial x_j} - n_j n_q \frac{\partial(.)}{\partial x_q}$. Here, we assume $\mathbf{v}^d = \mathbf{r}_k^d = 0$ on $\partial\Omega_v$ and $\partial\Omega_r$.

5.3 Topology optimization of flexoelectric micro and macro structures

We formulate a two-scale topology optimization of an electromechanical energy harvester made of non-piezoelectric material. At the microscale (see Fig. 5.2 (a)), the periodic microstructure of the material is optimized to maximize its flexoelectric effective properties. Then, homogenization is performed to obtain the corresponding coefficient of the macroscopic electromechanical properties. At the structural level (macro scale, see Fig. 5.2 (b)), a second topology optimization step is performed to maximize the electromechanical coupling factor (ECF) of the harvester under dynamic conditions. The overall procedure is summarized in Fig. 5.2.

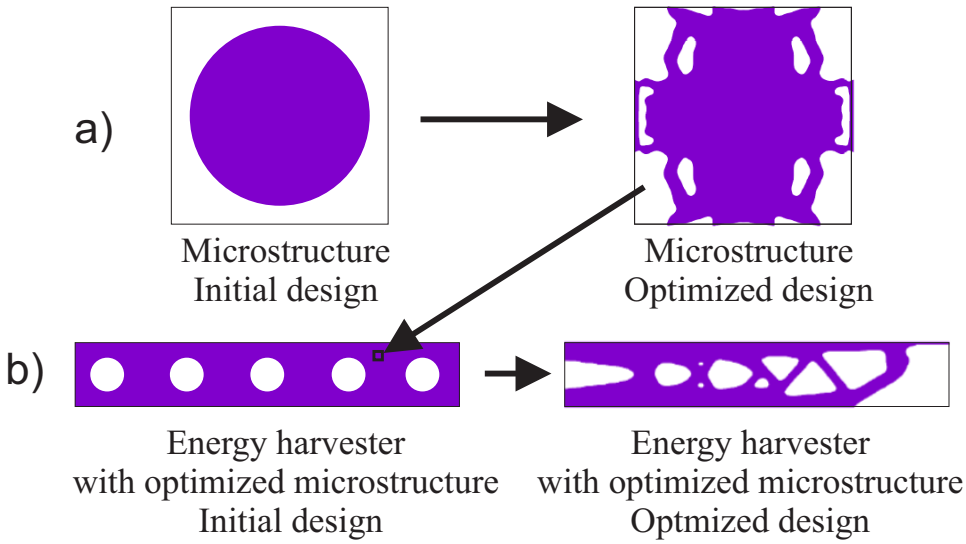

Figure 5.2: Multiscale topology optimization strategy for the design of the electromechanical energy harvester made of a non-piezoelectric material: (a) micro scale topology optimization problem; (b) macro scale topology optimization problem

5.3.1 SIMP framework with IGA

A SIMP topology optimization is adopted, where the geometry is defined within a design domain by means of densities ρ defined over the nodes of a mesh. In the present work, an Isogeometric Analysis (IGA) scheme is used both for solving equilibrium equations at micro and macro scales, but also to define the interpolation of densities within the topology optimization. The main advantage of IGA in the present framework is to allow C^1 continuity, which is required to solve the equations of the strain-gradient flexoelectric problems at both micro and macro scales. A complete description of the IGA discretization scheme can be found in Chapter 3. The density design variables are defined on control points, i.e. nodal densities. These densities are used to interpolate the material properties in a continuous manner, using penalty exponents to enforce local densities to values close to 0 or 1. In SIMP, the material properties: elastic tensor, flexoelectric tensor, dielelctric tensor and mass, are interpolated as follows:

$$C_{ijkl}(\rho) = C^{min}_{ijkl} + \rho^{p_c}(C^0_{ijkl} - C^{min}_{ijkl}) \tag{5.43}$$

$$\mu_{ijkl}(\rho) = \mu^{min}_{ijkl} + \rho^{p_\mu}(\mu^0_{ijkl} - \mu^{min}_{ijkl}) \tag{5.44}$$

$$\alpha_{ij}(\rho) = \alpha^{min}_{ij} + \rho^{p_a}(\alpha^0_{ij} - \alpha^{min}_{ij}) \tag{5.45}$$

$$m(\rho) = m^{min} + \rho(m^0 - m^{min}) \tag{5.46}$$

where the symbol $\square^{min}$ represents small numerical values assiated with void (no material). The same interpolation scheme is used to interpolate the other material tensors, at both micro and macro scales. The coefficients p_c, p_μ, p_a are a numerical penalty exponents. Different coefficients can be used for the other material properties.

5.3.2 Microstructure topology optimization problem

At the micro scale, the objective is to obtain the largest effective flexoelectric coefficients by designing the microstructure of the periodic flexoelectric composites. The topology optimization problem is then formulated so as to maximize one specific component of the effective flexoelectric tensor in (5.47).

$$\begin{aligned} \underset{\rho}{\text{Max}}: \quad & \overline{\mu}_{ijkl} \\ \text{Subject to}: \quad & \begin{cases} R_1(\rho) = 0 \\ R_2(\rho) = 0 \\ \int_{\Omega_m} \rho \mathrm{d}V \leq f^m \\ 0 \leq \rho \leq 1, \end{cases} \end{aligned} \tag{5.47}$$

where f^m is the micro volume fraction constraint, or density of the material.

5.3.3 Macroscopic dynamic electromechanical topology optimization

Once the microstructure is optimized from the previous section description, the obtained homogenized properties are used as material properties in the macro equations describing the behavior of the energy harverster in Eqs. (5.27)-(5.29), (5.35)-(5.36). Then, a second Topology Optimization step is performed at the macro structural level. Here, the objective is to maximize the dynamic electromechanical response of the structure. More specifically, the electromechanical coupling factor (ECF) of an electromechanical systems under harmonic excitation for a given frequency is defined as:

$$k^2_{eff} = \frac{\Pi_e(\omega)}{\Pi_m(\omega)} \tag{5.48}$$

$$\Pi_e(\omega) = \frac{1}{2}\int_\Omega E^*_i(\omega)\overline{\alpha}_{ij}E_j(\omega)\mathrm{d}\Omega \tag{5.49}$$

$$\Pi_m(\omega) = \frac{1}{2}\int_\Omega \varepsilon^*_{ij}(\omega)\overline{C}_{ijkl}\varepsilon_{kl}(\omega)\mathrm{d}\Omega \tag{5.50}$$

where the $\Pi_e(\omega)$ and $\Pi_m(\omega)$ are electric and mechanical energies, respectively, and $E^*_i = -\phi^*_{,i}$, with ϕ^* is the complex conjugate to ϕ, and $\varepsilon^*_{ij} = -\nabla^s_i u^*_j$, with u^*_j is the complex conjugate to u_j.

The topology optimization problem is formulated so as maximizing the ECF k^2_{eff} at a given excitation frequency, under volume and compliance constraints:

$$\begin{aligned} \underset{\rho}{\text{Min}}: \quad & J(\rho) = \tfrac{1}{k^2_{eff}(\rho)} = \tfrac{\Pi_m(\omega,\rho)}{\Pi_e(\omega,\rho)} \\ \text{Subject to}: \quad & \begin{cases} \int_{\Omega_M} \rho \mathrm{d}V \leq \frac{V^{max}}{V^0} \\ R_3(\rho) = 0 \\ R_4(\rho) = 0 \\ \hat{C}(\rho) \leq \hat{C}^{max} \\ 0 \leq \rho \leq 1, \end{cases} \end{aligned} \tag{5.51}$$

In the above, V^0 is the design domain volume and V^{max} is the maximum volume of the structure. In Eq. (5.51), $\hat{C}(\rho) = \Pi_m(0)$ is the static average compliance, which it is expected to eliminate disconnected domain by ensuring a minimal stiffness to the structure.

5.4 Sensitivity analysis

To solve the effective flexoelectric coefficients enhancement problemn (5.47) for microstructure and the electromechanical coupling efficiency optimization problem (5.35)-(5.36) for energy harvester based on the gradient-based mathematical programming method, The adjoint method is employed to derive both the numerical sensitivities.

5.4.1 Microstructure analysis

The effective flexoeletric tensor can be wirtten by compact form as

$$\overline{\boldsymbol{\mu}} = -\frac{1}{\Omega_m}\begin{bmatrix}\mathbf{V}_\phi \\ \mathbf{V}_u\end{bmatrix}^T \begin{bmatrix}\mathbf{K}_{\phi\phi} & \mathbf{K}_{\phi u} \\ \mathbf{K}_{\phi u}^T & \mathbf{K}_{uu}\end{bmatrix}\begin{bmatrix}\mathbf{W}_\phi \\ \mathbf{W}_u\end{bmatrix} \tag{5.52}$$

We define

$$\mathbf{K}_G = \begin{bmatrix}\mathbf{K}_{\phi\phi} & \mathbf{K}_{\phi u} \\ \mathbf{K}_{\phi u}^T & \mathbf{K}_{uu}\end{bmatrix} \tag{5.53}$$

By using the adjoint method, the corresponding Lagrangian L^m for the effective flexoelectric tensor components optimization problem (5.47) is formed by introducing adjoint vectors λ_1^m and λ_2^m as:

$$L^m = \overline{\boldsymbol{\mu}} - (\mathbf{V}^T\mathbf{K}_G - \mathbf{F}_V{}^T)\boldsymbol{\lambda}_1^m - (\boldsymbol{\lambda}_2^m)^T(\mathbf{K}_G\mathbf{W} - \mathbf{F}_W^T) \tag{5.54}$$

Where $\mathbf{V}^T\mathbf{K}_G - \mathbf{F}_V{}^T = 0$ and $\mathbf{K}_G\mathbf{W} - \mathbf{F}_W{}^T = 0$ are the IGA discrete forms of (5.11) with boundary condition shown in Table 5.1, and they hold for arbitrary vectors λ_1^m and λ_2^m. Differentiating the Lagrangian L^m with respect to the design variable ρ^m gives:

$$\frac{\partial L^m}{\partial \rho^m} = \frac{\partial \overline{\boldsymbol{\mu}}}{\partial \rho^m} - \frac{\partial(\mathbf{V}^T\mathbf{K}_G - \mathbf{F}_V{}^T)}{\partial \rho^m}\boldsymbol{\lambda}_1^m - (\boldsymbol{\lambda}_2^m)^T\frac{\partial(\mathbf{K}_G\mathbf{W} - \mathbf{F}_W{}^T)}{\partial \rho^m} \tag{5.55}$$

We finally obtain the adjoint sensitivity of effective flexoelectric components with respect to the density as

$$\frac{\partial \overline{\boldsymbol{\mu}}}{\partial \rho^m} = \frac{1}{\Omega_m}\begin{bmatrix}\mathbf{V}_\phi \\ \mathbf{V}_u\end{bmatrix}^T \cdot \frac{\partial}{\partial \rho^m}\left(\begin{bmatrix}\mathbf{K}_{\phi\phi} & \mathbf{K}_{\phi u} \\ \mathbf{K}_{\phi u}^T & \mathbf{K}_{uu}\end{bmatrix}\right)\cdot\begin{bmatrix}\mathbf{W}_\phi \\ \mathbf{W}_u\end{bmatrix} \tag{5.56}$$

5.4.2 Energy harvester analysis

For the energy harvester in dynamics, the first derivative of the objective function J with respect to the nodal design variable $\rho_{i,j}$ is calculated as

$$\frac{\partial J}{\partial \rho_{i,j}} = \frac{\frac{\partial \Pi_m}{\partial \rho_{i,j}}\Pi_e - \Pi_m\frac{\partial \Pi_e}{\partial \rho_{i,j}}}{\Pi_e^2} \tag{5.57}$$

The terms $\frac{\partial \Pi_m}{\partial \rho_{i,j}}$ and $\frac{\partial \Pi_e}{\partial \rho_{i,j}}$ are derived by chain rules, respectively

$$\frac{\partial \Pi_m}{\partial \rho_{i,j}} = \frac{\partial \Pi_m}{\partial \bar{\bar{\rho}}_{i,j}}\cdot\frac{\partial \bar{\bar{\rho}}_{i,j}}{\partial \bar{\rho}_{i,j}}\cdot\frac{\partial \bar{\rho}_{i,j}}{\partial \rho_{i,j}} \tag{5.58}$$

$$\frac{\partial \Pi_e}{\partial \rho_{i,j}} = \frac{\partial \Pi_e}{\partial \bar{\bar{\rho}}_{i,j}}\cdot\frac{\partial \bar{\bar{\rho}}_{i,j}}{\partial \bar{\rho}_{i,j}}\cdot\frac{\partial \bar{\rho}_{i,j}}{\partial \rho_{i,j}} \tag{5.59}$$

Furthermore, $\frac{\partial \Pi_m}{\partial \bar{\bar{\rho}}_{i,j}}$ and $\frac{\partial \Pi_e}{\partial \bar{\bar{\rho}}_{i,j}}$ is explicit calculated by introducing an adjoint vector $\boldsymbol{\lambda}^c$ and $\boldsymbol{\lambda}^e$, respectively. The corresponding Lagrangian equations are constructed as:

$$L_{\Pi_m} = \Pi_m - \boldsymbol{\lambda}_1^c(\mathbf{K}_{tot}\mathbf{U}_{tot} - \mathbf{F}_{tot}) - \boldsymbol{\lambda}_2^c(\overline{\mathbf{K}_{tot}\mathbf{U}_{tot}} - \overline{\mathbf{F}_{tot}}) \tag{5.60}$$

$$L_{\Pi_e} = \Pi_e - \boldsymbol{\lambda}_1^e(\mathbf{K}_{tot}\mathbf{U}_{tot} - \mathbf{F}_{tot}) - \boldsymbol{\lambda}_2^e(\overline{\mathbf{K}_{tot}\mathbf{U}_{tot}} - \overline{\mathbf{F}_{tot}}) \tag{5.61}$$

where the discrete system of coupling equilibrium equation $\mathbf{K}_{tot}\mathbf{U}_{tot} = \mathbf{F}_{tot}$ is defined in (5.35) and (5.36), while $\overline{\mathbf{K}_{tot}\mathbf{U}_{tot}} = \overline{\mathbf{F}_{tot}}$ is the corresponding conjugate counterpart. Both equilibrium equations hold for arbitrary $\boldsymbol{\lambda}^c$ and $\boldsymbol{\lambda}^e$. The sensitivities of the Lagrangian equations with respect to $\bar{\bar{\rho}}_{i,j}$ are written as

$$\frac{\partial L_{\Pi_m}}{\partial \bar{\bar{\rho}}_{i,j}} = \frac{\partial \Pi_m}{\partial \bar{\bar{\rho}}_{i,j}} + \frac{\partial \Pi_m}{\partial \mathbf{U}_{tot}} \cdot \frac{\partial \mathbf{U}_{tot}}{\partial \bar{\bar{\rho}}_{i,j}} + \frac{\partial \Pi_m}{\partial \overline{\mathbf{U}_{tot}}} \cdot \frac{\partial \overline{\mathbf{U}_{tot}}}{\partial \bar{\bar{\rho}}_{i,j}} - \boldsymbol{\lambda}_1^c \frac{\partial (\mathbf{K}_{tot}\mathbf{U}_{tot} - \mathbf{F}_{tot})}{\partial \bar{\bar{\rho}}_{i,j}} - \boldsymbol{\lambda}_2^c \frac{\partial (\overline{\mathbf{K}_{tot}\mathbf{U}_{tot}} - \overline{\mathbf{F}_{tot}})}{\partial \bar{\bar{\rho}}_{i,j}} \tag{5.62}$$

$$\frac{\partial L_{\Pi_e}}{\partial \bar{\bar{\rho}}_{i,j}} = \frac{\partial \Pi_e}{\partial \bar{\bar{\rho}}_{i,j}} + \frac{\partial \Pi_e}{\partial \mathbf{U}_{tot}} \cdot \frac{\partial \mathbf{U}_{tot}}{\partial \bar{\bar{\rho}}_{i,j}} + \frac{\partial \Pi_e}{\partial \overline{\mathbf{U}_{tot}}} \cdot \frac{\partial \overline{\mathbf{U}_{tot}}}{\partial \bar{\bar{\rho}}_{i,j}} - \boldsymbol{\lambda}_1^e \frac{\partial (\mathbf{K}_{tot}\mathbf{U}_{tot} - \mathbf{F}_{tot})}{\partial \bar{\bar{\rho}}_{i,j}} - \boldsymbol{\lambda}_2^e \frac{\partial (\overline{\mathbf{K}_{tot}\mathbf{U}_{tot}} - \overline{\mathbf{F}_{tot}})}{\partial \bar{\bar{\rho}}_{i,j}} \tag{5.63}$$

We finally obtain the sensitivities of mechanical and electrical energy w.r.t $\bar{\bar{\rho}}_{i,j}$,

$$\frac{d\Pi_m}{d\bar{\bar{\rho}}_{i,j}} = \frac{1}{2}\overline{\mathbf{U}}^T \frac{\partial \mathbf{K}_{uu}}{\partial \bar{\bar{\rho}}}\mathbf{U} - Re\left\{ (\boldsymbol{\lambda}_1^c)^T \frac{\partial \overline{\mathbf{K}_{tot}}}{\partial \bar{\bar{\rho}}} \overline{\mathbf{U}_{tot}} + (\boldsymbol{\lambda}_2^c)^T \frac{\partial \mathbf{K}_{tot}}{\partial \bar{\bar{\rho}}} \mathbf{U}_{tot} \right\} \tag{5.64}$$

$$\frac{d\Pi_e}{d\bar{\bar{\rho}}_{i,j}} = \frac{1}{2}\overline{\mathbf{\Phi}}^T \frac{\partial \mathbf{K}_{\phi\phi}}{\partial \bar{\bar{\rho}}}\mathbf{\Phi} - Re\left\{ (\boldsymbol{\lambda}_1^e)^T \frac{\partial \overline{\mathbf{K}_{tot}}}{\partial \bar{\bar{\rho}}} \overline{\mathbf{U}_{tot}} + (\boldsymbol{\lambda}_2^e)^T \frac{\partial \mathbf{K}_{tot}}{\partial \bar{\bar{\rho}}} \mathbf{U}_{tot} \right\} \tag{5.65}$$

where $Re\{\cdot\}$ means the real part of the complex. The adjoint vectors are calculated by the following adjoint equations

$$\overline{\mathbf{K}_{tot}}\boldsymbol{\lambda}_1^c = \frac{\partial \Pi_m}{\partial \overline{\mathbf{U}_{tot}}} \tag{5.66}$$

$$\mathbf{K}_{tot}\boldsymbol{\lambda}_2^c = \frac{\partial \Pi_m}{\partial \mathbf{U}_{tot}} \tag{5.67}$$

$$\overline{\mathbf{K}_{tot}}\boldsymbol{\lambda}_1^e = \frac{\partial \Pi_e}{\partial \overline{\mathbf{U}_{tot}}} \tag{5.68}$$

$$\mathbf{K}_{tot}\boldsymbol{\lambda}_2^e = \frac{\partial \Pi_e}{\partial \mathbf{U}_{tot}} \tag{5.69}$$

To solve the adjoint equations, we can use the same mechanical and electric boundary condition as the problem (5.35)-(5.36). The derivatives of material density distribution field $\bar{\bar{\rho}}$ with respect to nodal density field ρ presented in (5.58)-(5.59) can be obtained as

$$\frac{\partial \bar{\bar{\rho}}_{i,j}}{\partial \bar{\rho}_{i,j}} = R_{i,j}^{p,q}(\bar{\xi}, \bar{\eta}) \tag{5.70}$$

$$\frac{\partial \bar{\rho}_{i,j}}{\partial \rho_{i,j}} = \frac{w(r_{\bar{i},\bar{j}})}{\sum_{\hat{i}=1}^{n_s}\sum_{\hat{j}=1}^{m_s} w(r_{\hat{i},\hat{j}})} \tag{5.71}$$

Substituting (5.64)-(5.65)-(5.70)-(5.71) into (5.58) and (5.59), finally into (5.57), the explicit sensitivity of objection function with respect to nodal density variable ρ can therefore be obtained. The micro and macro optimization problems in (5.47) and (5.51) are solved by the conservative convex separable approximations (CCSAs) optimizer [144] based on the adjoint sensitivity.

5.5 Applications

In the following examples, we first design the microstructure of a periodic porous material made of a non-piezoelectric material, but possessing flexoelectric behavior, so as to maximize

its apparent flexoelectric properties. The resulting material has homogenized (apparent) non-zero piezoelectric properties. In a second step, we optimize the design of structures serving as energy harvesters in a dynamic regime and made with this material. The objective is to show that energy harversters using electromechanical transduction can be designed using fully non-piezoelectric materials.

5.5.1 Topology optimization of a non-piezoelectric microstructure made of a flexoelectric material

We first conduct the Topology Optimization (TO) of a microstructure made of a non-piezoelectric material, but having flexoelectric behavior. Since the energy harvester structures considered in this work mainly involve bending, we perform the TO of the microstructure so as to maximize the effective flexoelectric coefficient μ_{2112}, which characterizes the polarization under bending. The flexoelectric microstructure is made of centrosymmetric flexoelectric (non-piezoelectric) material $SrTiO_3$ (STO) [215], whose parameters are given in Table 5.2. The second phase is void (air). For this material, $\mu_{2112} \equiv \mu_{12} = 7$ nC/m and here, all penalty exponents used in the TO numerical procedure (see Eq. (5.43)-(5.45)) are chosen as equal to 3.

Table 5.2: Material properties of $SrTiO_3$ (STO)

Density	Elastic coefficients	Dielectric coefficients	Flexoelectric coefficients
$\rho_0 = 5.12$ g/cm^3	$c_{11} = c_{22} = 319$ GPa	$\alpha_{11} = 300\varepsilon_0$	$\mu_{11} = 0.2$ nC/m
	$c_{12} = 100$ GPa	$\alpha_{33} = 300\varepsilon_0$	$\mu_{12} = 7$ nC/m
	$c_{44} = 110$ GPa	$\varepsilon_0 = 8.854 \times 10^{-12}$C/V·m	$\mu_{44} = 5.8$ nC/m

The microstructural optimized topologies are provided for different volume fractions in Fig. 5.3. The optimized values of the flexoelectric component $\bar{\mu}_{2112}$ corresponding to the volume fractions f_1 =0.5, f_2 =0.6, f_3 =0.7 and f_4 =0.8 are respectively obtained as 7.14 nC/m, 9.19 nC/m, 10.10 nC/m and 12.15 nC/m, which represent a significant improvement as compared to STO of 2.00%, 31.29%, 44.29% and 73.57%, respectively. Note that even though non-piezoelectric, the material with optimized microstructure actually exhibits an apparent piezoelectric behavior due to local flexoelectricity. The respective values of the effective piezoelectric coefficient $\bar{e}_{211}$ corresponding to the volume fractions f_1, f_2, f_3 and f_4 are respectively obtained as 0.0032 nC/m^2, -0.0850 nC/m^2, -0.0201 nC/m^2, 0.3061 nC/m^2 . The piezoelectric coefficients $\bar{e}_{111}$, $\bar{e}_{211}$ and $\bar{e}_{222}$ of the microstructures for the different volume fractions are summarized in Table 5.3.

In the following, we will use the optimized microstructure corresponding to the volume fraction $f_4 = 0.8$ (see Fig. 5.3d) as a constitutive material for energy harvesters designs. The effective parameters corresponding to this optimized microstructure are provided in Eqs. (5.72)-(5.74). Note that such microstructures are complex, but may be fabricated with the recent advances in additive manufacturing, including 3D printing of ceramics (see e.g. [218]).

Table 5.3: Piezoelectric coefficients $\bar{e}_{111}$, $\bar{e}_{211}$ and $\bar{e}_{222}$ (unit: nC/m^2) of microstructures with different volume fractions

Volume fraction	$\bar{e}_{111}$	$\bar{e}_{211}$	$\bar{e}_{222}$
f_1 =0.5	0.0163	0.0032	-0.0271
f_2 =0.6	-0.4471	-0.0850	-0.1472
f_3 =0.7	0.0318	-0.0201	-0.0584
f_4 =0.8	-0.0209	0.3061	0.1456

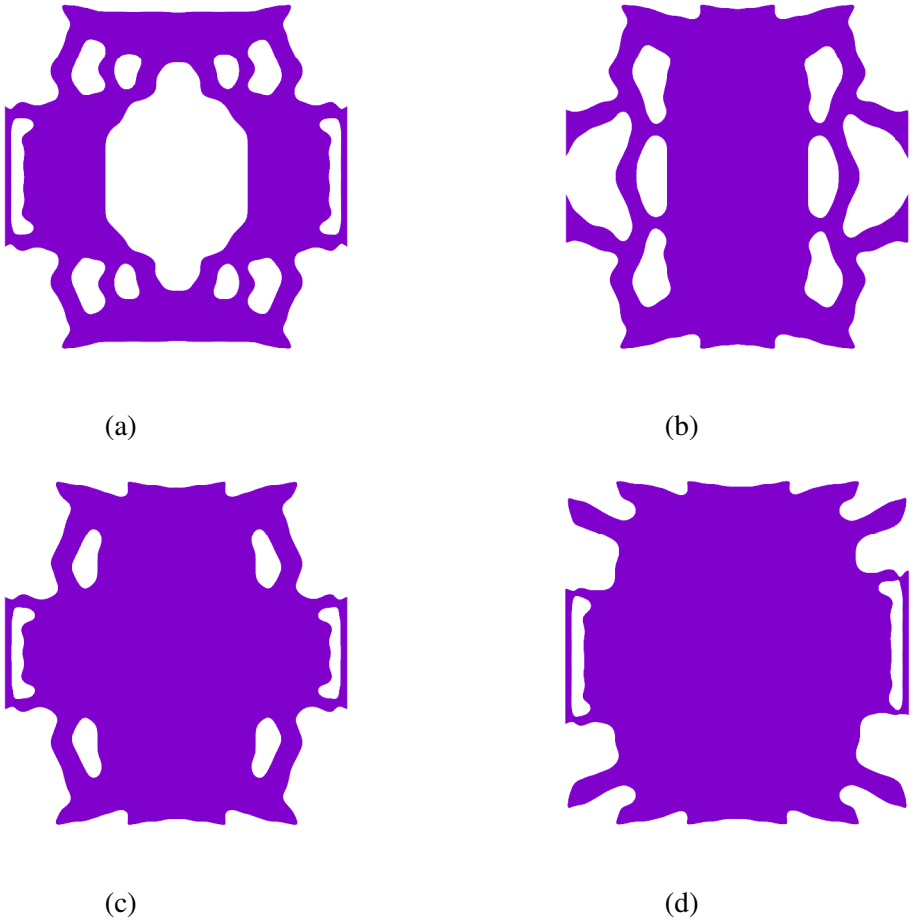

(a) (b)

(c) (d)

Figure 5.3: Optimized microstructure with respect to the apparent flexoelectric coefficient $\bar{\mu}_{2112}$ for different volume fractions: (a) $f_1 = 0.5$; (b) $f_2 = 0.6$; (c) $f_3 = 0.7$; (d) $f_4 = 0.8$.

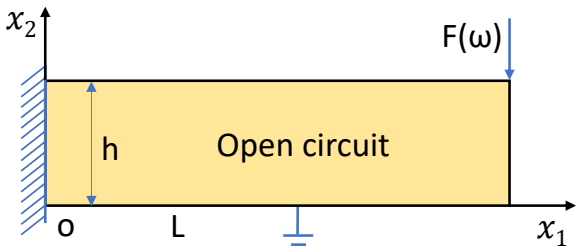

Figure 5.4: Beam-like energy harverster with open circuit boundary conditions: design domain

$$\mathbf{C} = \begin{bmatrix} 72.83 & 22.68 & 0 \\ 22.68 & 103.21 & 0 \\ 0 & 0 & 29.91 \end{bmatrix} (\text{GPa}), \quad \boldsymbol{\alpha} = \begin{bmatrix} 0.804 & 0 \\ 0 & 1.121 \end{bmatrix} (\text{nC/V} \cdot \text{m}) \tag{5.72}$$

$$\boldsymbol{e} = \begin{bmatrix} -0.0209 & 0.0512 & -0.0697 \\ 0.3061 & 0.1456 & -0.0608 \end{bmatrix} (\text{nC/m}^2) \tag{5.73}$$

$$\boldsymbol{\mu} = \begin{bmatrix} -0.16 & -0.18 & 0.64 & 0.06 & -0.05 & 2.38 \\ 0.07 & 12.15 & -0.05 & 1.37 & 0.62 & -0.05 \end{bmatrix} (\text{nC/m}) \tag{5.74}$$

5.5.2 Design of a dynamic beam-like energy harvester

In this example, we use the proposed methodology to design a dynamic beam-like energy harvester in open circuits boundary condition as shown as Fig. 5.4. The beam material is the one obtained from the optimized microstructure in the previous section, whose coefficients are provided in (5.72)-(5.74). The size of the beam is $h = 200$ nm, with an aspect ratio $L/h = 6$ and the micro inertial length $\ell_d = 10\ell$ in Eq. (5.33). The density of the optimized microstructure is $\rho_0 = 4.096$ g/cm^3. The internal length scale of higher-order elastic tensor (3.60) is $\ell = 1 \times 10^{-8}$ m. The modal damping ratios are taken as $\xi_1 = \xi_2 = 0.01$. The excitation frequency is $F(\omega) = F_0 e^{j\omega t}$ and $F_0 = -1$ N, applied along the x_2-direction on the top-right corner. The dynamic topology optimization is carried out for the excitation frequencies 0 MHz (static), 10 MHz, 12 MHz, 15 MHz and 16 MHz. The volume fraction constraint, defined as the quantity of material as compared to the design domain volume $L \times h$, is set as f =0.6 for all frequency cases. The compliance constraint is set as $\hat{C}^{max} = 8\overline{\Pi}_1(0)$, where $\overline{\Pi}_1(0)$ is the static strain energy of the undesigned flexoelectric beam. Here the undesigned structure means that the relative densities in the whole rectangular design domain are equal to 1. For comparison, a guess design consisting into a rectangular beam with 6 holes as depicted in Fig. 5.5(a) is analyzed. The holes radii are $R = 0.3568h$ corresponding to a volume fraction equal to 0.6. This structure will serve as a reference to be compared with the optimized designs. The penalty exponents used in the TO numerical procedure (see Eqs. (5.43)-(5.45)) are chosen here as $p_c = p_e = 3$, $p_a = 1$. These coefficients are different in this example for convergence reasons.

The dynamic topology optimization of the flexoelectric cantilever beam is performed for different excitation frequencies. Initialization of the densities is performed by setting them uniformly to $\rho_e = 0.6$ in the rectangular design domain defined in Fig. 5.4. The final optimized geometries, obtained respectively for the excitation frequencies 0 MHz, 10 MHz, 12 MHz, 15 MHz and 16 MHz, are depicted in Fig. 5.5. The corresponding electromechanical coupling

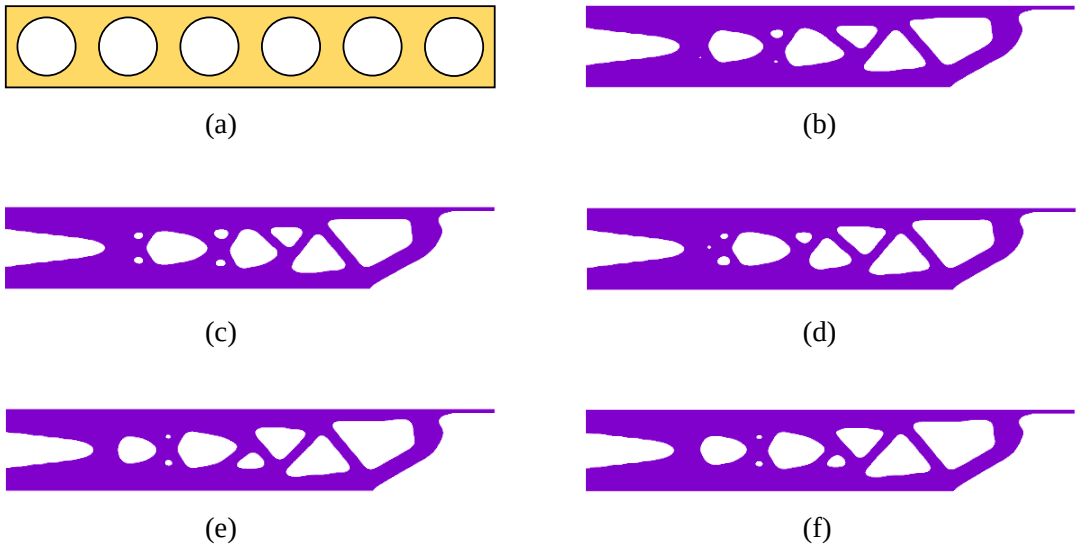

Figure 5.5: (a) Reference design for the beam-like energy harvester; Optimized designs corresponding to excitation frequencies: (b) Static conditions; (c) 10 MHz; (d) 12 MHz; (e) 15 MHz; (f) 16 MHz

factors (ECFs) are listed in Table 5.4. The ECFs of the optimized structures for excitation frequencies 0 MHz, 10 MHz, 12 MHz, 15 MHz and 16 MHz increase by factors of 20.18, 20.07, 20.04, 19.99 and 19.97 times, respectively, as compared to the reference design in Fig. 5.5(a). The influence of different upper limit values of the compliance constraint on the optimized structure and electromechanical coupling factors of the flexoelectric beam are also studied under static loading conditions, as presented in Fig. 5.6. It can be observed that the electromechanical coupling factors of the optimized structure firstly increase rapidly with the increase of the upper limit of the compliance constraint and finally tend to be stable. Meanwhile, the rods close to the load end in the optimized structural configuration are gradually getting longer.

The ECF frequency responses for the optimized geometries are compared to the reference response in Fig. 5.7, where the frequency ranges from 0 to 143 MHz. It is observed that the ECF frequency responses of all optimal designs obtained by different excitation frequencies are much larger (about 20 times) than the reference in a large frequency range (roughly between 0 and 100 MHz), while it drops for frequencies larger than 100 MHz. Using different excitation frequencies in the toplogy optimization does not modifiy significantly the ECF response of the otpimize structure. In conclusion, it is shown that the obtained optimized energy harvester structures have good performances both with respect to the reference (guess design) and considering that the constitutive material is not piezoelectric.

Table 5.4: electromechanical coupling factors (ECF) of optimal designs for flexoelectric nano beam under different excitation frequencies

Excitation Frequency	ECF (optimized)	ECF (reference)	Gain: ECF_{opt}/ECF_{ref}
0 MHz	0.03420	1.6149×10^{-3}	21.18
10 MHz	0.03406	1.6165×10^{-3}	21.07
12 MHz	0.03402	1.6171×10^{-3}	21.04
15 MHz	0.03397	1.6184×10^{-3}	20.99
16 MHz	0.03395	1.6189×10^{-3}	20.97

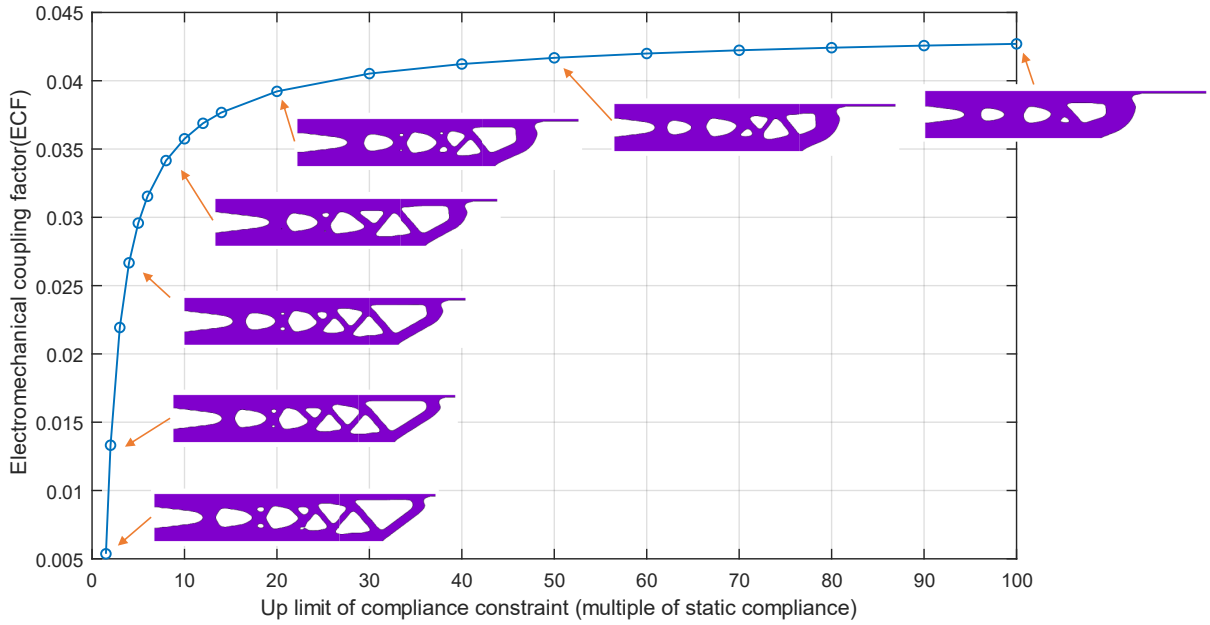

Figure 5.6: Influence of upper limit value of compliance constraint on optimized structures and electromechanical coupling factor of flexoelectric beams

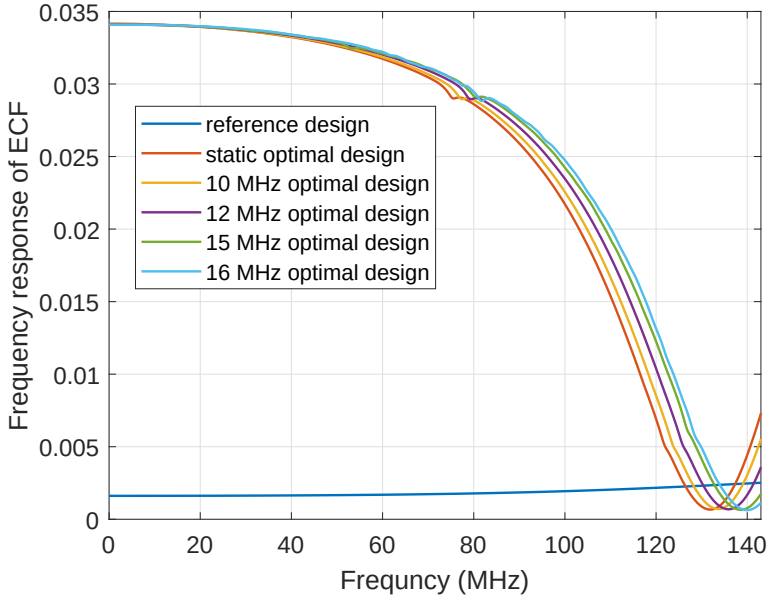

Figure 5.7: ECF frequency responses of reference and optimized designs for flexoelectric beam for different excitation frequencies

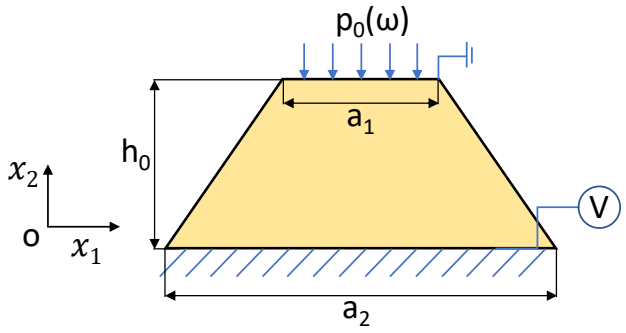

Figure 5.8: Energy harvester with truncated pyramid-shape under compression and open circuit conditions: design domain

5.5.3 Design of dynamic truncated pyramid-like energy harvester

In this example, we consider the design of an energy harvester with truncated pyramid shape and open circuit conditions, as shown in Fig. 5.8. This shape is often chosen in flexoelectric systems as inducing strain gradient in compression [93]. The initial design domain is defined by the geometrical parameters $a_1 = 400$ nm, $a_2 = 1200$ nm and $h_0 = 400$ nm. A spatially uniform and oscillating pressure $p_0(\omega) = -1e^{j\omega t}$ N is applied on the top surface along the x_2-direction and the displacement DOFs on the bottom surface are fixed. The material parameters and length scale ℓ, ℓ_d are same as in the previous example. The volume fraction constraint is here set as $f = 0.7$. The compliance constraint is set as $\hat{C}^{max} = 4\overline{\Pi}_2(0)$, where $\overline{\Pi}_2(0)$ is the static strain energy of the truncated pyramid design domain with $\rho = 1$. A reference guess design is defined in Fig. 5.9(a), consisting into a truncated pyramid including a circular void with radius $R' = 0.437h_0$. The penalty exponents used in the numerical TO procedure (see Eqs. (5.43)-(5.45)) are chosen as $p_c = p_e = 3$, $p_a = 1$.

We perform the topology optimization of the flexoelectric truncated pyramid under the excitation frequencies 0 MHz (static), 200 MHz, 600 MHz, 800 MHz and 1000 MHz. The final optimized structures obtained for the excitation frequencies mentioned above are presented in Fig. 5.9. We can see that the vertical lengths of the voids in the topologies of the optimized structures become shorter and the material is concentrated more towards the middle domain of the structures, with the increasing frequencies of excitation in optimization. The ECFs of the reference and optimized structures are summarized in Table 5.5. The ECFs of the optimized structures designed for excitation frequencies 0 MHz, 200 MHz, 600 MHz, 800 MHz and 1000 MHz increase respectively by 4.044, 3.293, 2.846, 2.403 and 2.089 times with respect to the reference design solutions. The ECFs frequency responses of reference structure and optimized designs obtained for the different excitation frequencies are shown in Fig. 5.10, where the frequency ranges from 0 to 3.16 GHz. Obviously, the ECF is improved by the optimized energy harvester as compared to the reference design, and this for the whole frequency range. As another observation, the designs obtained by the dynamic topology optimization (taking into account nonzero excitation frequencies), mainly improves the ECF as compared to the ones obtained by static TO. Finally, it seems that increasing the excitation frequency decreases the ECF at low frequencies, but for larger frequencies there is not clear trend. Globally, the dynamic TO leads to a clear ECF improvement as compared to the reference of static designs, showing the potential of this framework.

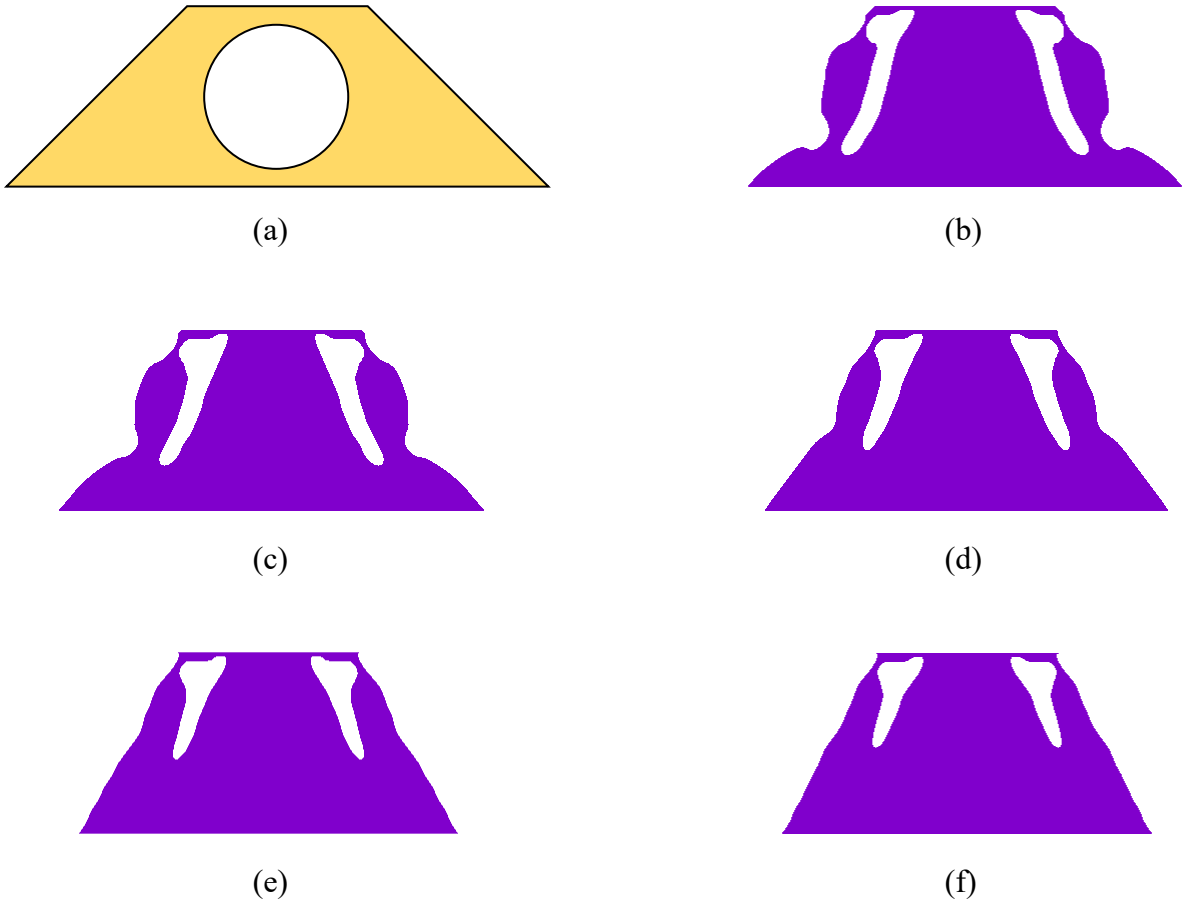

Figure 5.9: (a) Reference design for the truncated pyramid-like energy harvester; Optimized design corresponding to excitation frequencies: (b) Static conditions; (c) 200 MHz; (d) 600 MHz; (e) 800 MHz; (f) 1000 MHz

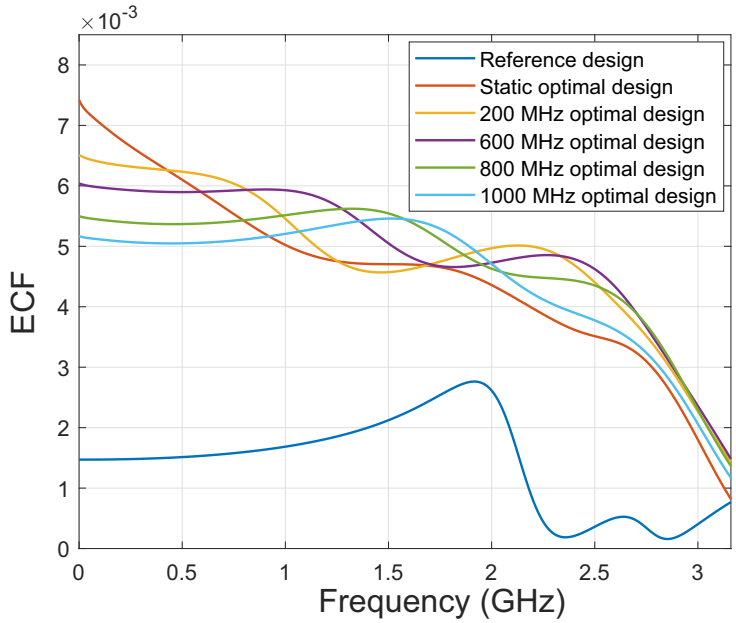

Figure 5.10: ECF frequency responses of reference and optimized designs for truncated pyramid for different excitation frequencies

Table 5.5: electromechanical coupling factors (ECF) of optimized designs for truncated pyramid obtained by different excitation frequencies

Excitation Frequency	ECF (optimized)	ECF (reference)	Gain: ECF_{opt}/ECF_{ref}
0 MHz	7.4203×10^{-3}	1.4712×10^{-3}	5.044
200 MHz	6.3395×10^{-3}	1.4766×10^{-3}	4.293
600 MHz	5.9021×10^{-3}	1.5346×10^{-3}	3.846
800 MHz	5.4302×10^{-3}	1.5956×10^{-3}	3.403
1000 MHz	5.2058×10^{-3}	1.6852×10^{-3}	3.089

5.6 Conclusions

A multiscale topology optimization method has been proposed for the design of electromechanical energy harvesting systems converting mechanical vibrations into electric currents made of non-piezoelectric materials. At the microscopic scale, the material is assumed to be periodic, porous and flexoelectric, although not piezoelectric. A first step of topology optimization is performed, in order to maximize the effective (homogenized) flexoelectric properties of the material. As a result, the effective material, although made of a non-piezoelectric material, has apparent piezoelectric properties. In a second step, these properties are used to model the behaviour of a dynamic electromechanical energy harvesting system structure. A second topology optimization step, this time performed at structure scale, aims to maximize the system Electromechanical Coupling Factor (ECF) for a given forced vibration frequency. We show that the optimized structure obtained offers significant gains in terms of ECF (by factors up to 20 times) compared with non-optimized structures of the same volume, over a wide range of excitation frequencies. The procedure could open up new possibilities in the design of energy recovery systems without the use of piezoelectric materials.

Chapter 6

Nonlinear topology optimization of flexoelectric soft dielectrics at large deformation

Macroscopic materials, typically rigid solids, face limitation in creating large strain gradients. Soft dielectrics have become a key focus of research due to their distinctive capability to undergo extensive deformations. This characteristic holds the potential for achieving more significant electric responses, attributed to the presence of larger strain gradients. The resulting mechanical deformations induced by applied electric fields create opportunities for applications such as flexible electronics, soft robotics, and sensing and actuation in various fields [219, 220, 221]. The reduction of structural dimensions to the micro- and nanoscale facilitates nonlinearity, enabling the more accessible production of large strain gradients, thereby contributing to the increasing improvement of the flexoelectric effect.

In this chapter, we propose a novel nonlinear topology optimization framework tailored for flexoelectric soft dielectrics undergoing large deformation. A numerical method based on Isogeometric analysis (IGA) is introduced to nonlinear soft dielectrics at finite strain, ensuring the C^1-continuity for flexoelectric problems. We outline the process of consistent linearizations and IGA discretizations. Additionally, we introduce an innovative and efficient Strain Density Function (SDF) interpolation scheme for optimizing electromechanical coupling factors, where the electromechanical and hyper-elastic energy terms are respectively interpolated based on SIMP model but the linear density model is employed on dielectric one. An energy remedy scheme [222] for void region is extended to optimization of soft dielectrics to avoid the distortion deformation in low-stiffness elements. The optimization solely based on the objective of the electromechanical coupling factor may lead to the formation of disconnected structures due to the neglect of mechanical stiffness considerations. To ensure the design of physically viable optimized structures, we incorporate a compliance constraint to regulate mechanical stiffness, thereby preventing the occurrence of disconnected domains. The influence of size effect on the optimization of flexoelectric soft materials is studied.

This chapter is adapted from the published articles [223].

6.1 Flexoelectricity for soft materials at finite strains

A solid domain $\Omega_0 \in \mathbb{R}^d$ is considered in the reference (undeformed) configuration, as schematically illustrated in Fig. 6.1. The boundary $\partial\Omega_0$ of Ω_0 is composed of mechanical and electrostatic boundary. The mechanical boundary includes Dirichlet and Neumann portions, represented respectively by $\partial\Omega_{0u}$ and $\partial\Omega_{0t}$, where the displacement and traction are imposed such that $\partial\Omega_{0u} \cup \partial\Omega_{0t} = \partial\Omega_0$ and $\partial\Omega_{0u} \cap \partial\Omega_{0t} = \emptyset$. While the electrostatic one is composed of electric Dirichlet boundary $\partial\Omega_{0\phi}$ and Robin boundary $\partial\Omega_{0D}$, which are prescribed such that

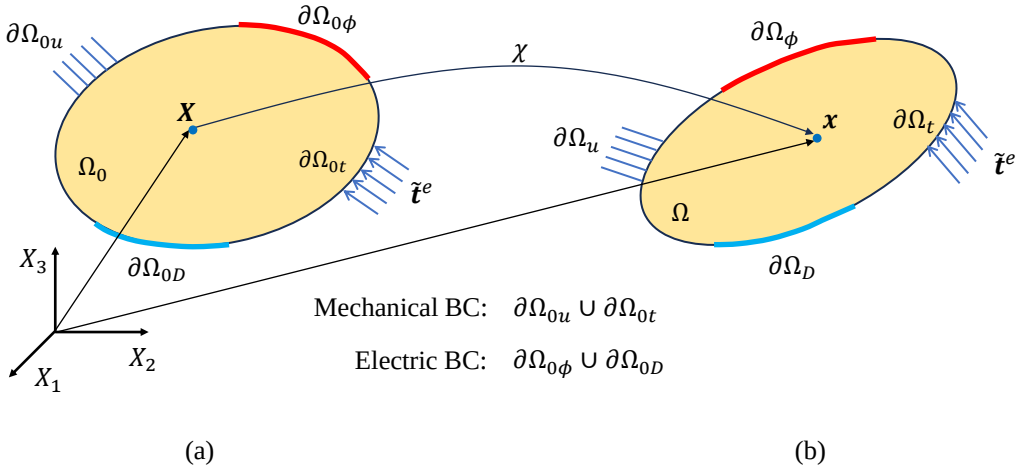

Figure 6.1: A solid domain: (a) reference (undeformed) configuration; (b) current (deformed) configuration

$\partial\Omega_{0\phi} \cup \partial\Omega_{0D} = \partial\Omega_0$ and $\partial\Omega_{0\phi} \cap \partial\Omega_{0D} = \emptyset$. The solid domain in current (deformed) configuration is denoted as Ω, and the counterparts of quantities are defined similarly by omitting the index 0. The deformation map $\chi : \Omega_0 \to \Omega$ maps every material point (or Lagrangian coordinate) $\boldsymbol{X} \in \Omega_0$ to the spatial point (or Eulerian coordinate) $\boldsymbol{x}$, i.e. $\boldsymbol{x} = \chi(\boldsymbol{X})$.

Here, the relevant quantities and notations are defined. The deformation gradient is defined as $\mathbf{F} = \nabla_X(\chi)$ and $\nabla_X(\cdot)$ denotes gradient with respect to reference configuration. $\mathbf{C} = \mathbf{F}^T\mathbf{F}$ is the right Cauchy-Green strain tensor. The Jacobian is defined as $J = \det(\mathbf{F})$. The divergence operator $Div = \nabla_X \cdot (\cdot)$ is related to reference configuration. The electric field, electric displacement, polarization and the first Piola-Kirchhoff stress in current configuration are denoted respectively as $\mathbf{E}$, $\mathbf{D}$, $\mathbf{P}$ and $\boldsymbol{\Sigma}$, while their counterparts in the reference configuration are expressed as $\tilde{\mathbf{E}}$, $\tilde{\mathbf{D}}$, $\tilde{\mathbf{P}}$ and $\tilde{\boldsymbol{\Sigma}}$, respectively. These quantities are related according to [79]:

$$\tilde{\mathbf{D}} = J\mathbf{F}^{-1}\mathbf{D}, \tilde{\mathbf{E}} = \mathbf{F}^T\mathbf{E}, \tag{6.1}$$

$$\tilde{\boldsymbol{\Sigma}} = J\boldsymbol{\Sigma}\mathbf{F}^{-T}, \tilde{\mathbf{P}} = J\mathbf{P} \tag{6.2}$$

and

$$\tilde{\mathbf{E}} = -\nabla_X\phi \tag{6.3}$$

$$\mathbf{F} = \mathbf{I} + \frac{\partial \mathbf{u}}{\partial \boldsymbol{X}} \tag{6.4}$$

with electric potential ϕ and unit matrix $\mathbf{I}$.

In this work, isotropic bulk flexoelectricity at finite strain is assumed, and surface effects are neglected. The total internal energy density of the system, encompassing contributions from elastic, flexoelectric, dielectric and linear gradient elastic portions, is provided as [108]:

$$\Psi = \Psi_{elast} + \Psi_{flexo} + \Psi_{diel} + \Psi_{elast}^{grad} \tag{6.5}$$

In this work, the Ψ_{elast} is considered as Mooney-Rivlin hyper-elastic model, and all the energy terms are given as

$$\Psi_{elast} = \frac{\mu}{2}(J^{-\frac{2}{3}}\Sigma_\alpha \lambda_\alpha^2 - 3) + \frac{\kappa}{2}(J-1)^2 \tag{6.6}$$

$$\Psi_{diel} = \frac{1}{2J}(\mathbf{R}^T \cdot \tilde{\mathbf{P}}) \cdot \mathbf{A} \cdot (\mathbf{R}^T \cdot \tilde{\mathbf{P}}) \tag{6.7}$$

$$\Psi_{flexo} = f_{ijkl}\tilde{P}_i G_{jkl} \tag{6.8}$$

$$\Psi_{elast}^{grad} = \frac{g_{ijklmn}}{2} G_{ijk} G_{lmn} \tag{6.9}$$

where μ and κ are the Lame's constants such that $\mu = \frac{E}{2(1+\nu)}$ and $\kappa = \frac{E}{3(1-2\nu)}$, with E is Young's modulus and ν is Poisson's ratio. λ_α^2 $(\alpha = 1,2,3)$ is the eigenvalue of right Cauchy-Green tensor $\mathbf{C}$. $\mathbf{G}$ is second order gradient of displacement and $\mathbf{G} = \nabla_X(\nabla_X(\mathbf{u}))$. $\mathbf{R}$ is rotation tensor with the property of $\mathbf{R} \cdot \mathbf{R}^T = \mathbf{I}$. f is the flexoelectric coefficient and g is the couple strain gradient constant. $\mathbf{A}$ is second order dielectric tensor. For an isotropic dielectric medium, it is defined as

$$\mathbf{A} = \frac{1}{\varepsilon - \varepsilon_0}\mathbf{I} \tag{6.10}$$

and ε_0 is the vacuum electric permittivity.

By the principle of frame indifference, the energy functions Ψ_{flexo} and Ψ_{elast}^{grad} satisfy [79]:

$$\Psi_{flexo}(\mathbf{G}, \tilde{\mathbf{P}}) = \Psi_{flexo}(\mathbf{RG}, \mathbf{R}\tilde{\mathbf{P}}), \forall \mathbf{R} \in So(3) \tag{6.11}$$

$$\Psi_{elast}^{grad}(\mathbf{G}, \mathbf{G}) = \Psi_{elast}^{grad}(\mathbf{RG}, \mathbf{RG}), \forall \mathbf{R} \in So(3) \tag{6.12}$$

where $So(3) \subset \mathbb{R}^{3\times3}$ is the group consisting of all rigid rotations. Then using the property of the material symmetry, we have

$$\Psi_{flexo}(\mathbf{G}, \tilde{\mathbf{P}}) = \Psi_{flexo}(\mathbf{RG}', \mathbf{R}\tilde{\mathbf{P}}'), \forall \mathbf{Q} \in \mathcal{G} \tag{6.13}$$

$$\Psi_{elast}^{grad}(\mathbf{G}, \mathbf{G}) = \Psi_{elast}^{grad}(\mathbf{RG}', \mathbf{RG}'), \forall \mathbf{Q} \in \mathcal{G} \tag{6.14}$$

where $\mathbf{G}'_{ijk} = \mathbf{G}_{imn}Q_{mj}Q_{nk}$ and $\tilde{\mathbf{P}}'_i = \tilde{\mathbf{P}}_j Q_{ji}$. Let $\mathcal{G} \subset \mathbb{R}^{3\times3}$ be the material symmetry group. For isotropic medium, i.e. $\mathcal{G} = So(3)$, any isotropic tensor, as well as higher-order tensors such as f_{ijkl} and g_{ijklmn}, can be represented as linear combinations of some isomers [224]. The general bilinear forms that fulfill the above identity (6.11)-(6.14) have been systematically derived in [224]. For simplicity, special forms for Ψ_{flexo} and Ψ_{elast}^{grad} with a single parameter, employed in [79] are used here:

$$\Psi_{flexo} = f\tilde{P}_i G_{ikk} \tag{6.15}$$

$$\Psi_{elast}^{grad} = \frac{g}{2} G_{ikk} G_{ill} \tag{6.16}$$

The first Piola-Kirchhoff stress $\tilde{\mathbf{\Sigma}}$ is expressed by:

$$\tilde{\mathbf{\Sigma}} = \frac{\partial \Psi_{elast}}{\partial \mathbf{F}} = -\frac{\mu}{3}J^{-\frac{2}{3}}\mathbf{F}^{-T}\Sigma_\alpha \lambda_\alpha^2 + \mu J^{-\frac{2}{3}}\mathbf{F} + \kappa(J-1)J\mathbf{F}^{-T} \tag{6.17}$$

The third-order hyperstress $\mathcal{S}$ is defined as

$$\begin{aligned}\mathcal{S}_{ijk} = \frac{\partial \Psi}{\partial G_{ijk}} &= \frac{g}{2}\delta_{mi}\delta_{kj}G_{mll} + \frac{g}{2}G_{mnn}\delta_{mi}\delta_{kj} + f\tilde{P}_m\delta_{mi}\delta_{jk} \\ &= gG_{ill}\delta_{jk} + f\tilde{P}_i\delta_{jk}\end{aligned} \tag{6.18}$$

where δ_{ij} is Kronecker delta.

The mechanical and electric equilibrium equations for flexoelectricity with boundary conditions are defined as [79]

$$\begin{cases} \mathbf{F}^{-T}\nabla_X\phi + \frac{\partial\Psi}{\partial\tilde{\mathbf{P}}} = 0 \text{ in } \Omega_0 \\ Div\,\tilde{\mathbf{D}} = \tilde{\rho}^e \text{ in } \Omega_0,\ \tilde{\mathbf{D}} = -\varepsilon_0 \mathbf{J}\mathbf{C}^{-1}\nabla_X\phi + \mathbf{F}^{-1}\tilde{\mathbf{P}} \\ Div(Div\frac{\partial\Psi}{\partial\mathbf{G}}) - Div\frac{\partial\Psi}{\partial\mathbf{F}} - \tilde{\mathbf{f}}^e = 0 \text{ in } \Omega_0 \end{cases} \tag{6.19}$$

with

$$\begin{cases} (\frac{\partial\Psi}{\partial\mathbf{F}})\mathbf{N} - (Div\ \frac{\partial\Psi}{\partial\mathbf{G}})\mathbf{N} - \tau - \tilde{\mathbf{t}}^e = 0 \text{ on } \partial\Omega_0 \\ (\frac{\partial\Psi}{\partial\mathbf{G}})\mathbf{N}\otimes\mathbf{N} = 0 \text{ on } \partial\Omega_0 \end{cases} \tag{6.20}$$

where $\mathbf{N}$ is the unitary normal vector to the boundary $\partial\Omega_0$. $\tilde{\mathbf{f}}^e$ and $\tilde{\mathbf{t}}^e$ denote body force and traction, respectively. The components of the vector field τ are given by [79]:

$$\tau_k = [\mathcal{S}_{kij}N_j(\delta_{im} - N_iN_m)]_{,m} - [\mathcal{S}_{kij}N_j - N_iN_m]_{,n}N_nN_m \tag{6.21}$$

Here, $\boldsymbol{\tau} = \mathbf{0}$. According to (6.7), we can obtain that

$$\frac{\partial\Psi}{\partial\tilde{\mathbf{P}}} = \frac{1}{J}\mathbf{R}\mathbf{A}\mathbf{R}^T\tilde{\mathbf{P}} \tag{6.22}$$

Substituting (6.10) and (6.22) into the first formula of (6.19), we have

$$\tilde{\mathbf{P}} = -J(\mathbf{R}\mathbf{A}\mathbf{R}^T)^{-1}[fG_{ikk} + \mathbf{F}^{-T}\nabla_X\phi] = -J(\varepsilon - \varepsilon_0)(fG_{ikk} + \mathbf{F}^{-T}\nabla_X\phi) \tag{6.23}$$

From the second row of (6.19) and (6.23), we arrive at

$$\tilde{\mathbf{D}} = -J\varepsilon\mathbf{C}^{-1}\nabla_X\phi - Jf(\varepsilon - \varepsilon_0)\mathbf{F}^{-1}G_{ikk} \tag{6.24}$$

The strong forms of the boundary values problems are provided as follows. The dielectric problem with Dirichlet and/or Robin boundary conditions is defined as:

$$\begin{cases} \nabla_X\cdot\tilde{\mathbf{D}} = \tilde{\rho}^e \text{ in } \Omega_0 \\ \phi = \phi^e \text{ on } \partial\Omega_{0\phi} \\ \tilde{N}\cdot\tilde{\mathbf{D}} = D^b \text{ on } \partial\Omega_{0\mathrm{D}} \end{cases} \tag{6.25}$$

The mechanical problem with Dirichlet and Neumann boundary conditions is expressed as:

$$\begin{cases} \nabla_X\cdot\tilde{\boldsymbol{\Sigma}} - \nabla_X\cdot(\nabla_X\cdot\mathcal{S}) + \tilde{\mathbf{f}}^e = 0,\ \text{in } \Omega_0 \\ \boldsymbol{\Sigma}\cdot\tilde{\mathbf{N}} - (\nabla_X\cdot\mathcal{S})\cdot\tilde{\mathbf{N}} - \tilde{\mathbf{t}} = 0 \text{ on } \partial\Omega_{0\mathrm{t}} \\ \mathcal{S}\tilde{\mathbf{N}}\otimes\tilde{\mathbf{N}} = 0 \text{ on } \partial\Omega_0 \\ u = u^b \text{ on } \partial\Omega_{0\mathrm{u}} \end{cases} \tag{6.26}$$

6.2 Weak forms of flexoelectric equilibrium equations

To be handled by discrete numerical methods, such as IGA method employed here, the above boundary values problem defined in (6.25)-(6.26) must be recast into weak forms. The weak formulations for electric and mechanical equilibrium are derived by employing the principle of virtual work. The electric potential is defined as $\phi \in \{\phi = \bar{\phi}^* \text{ on } \partial\Omega_{0\phi}, \phi \in H^1(\Omega_0)\}$ and its

corresponding test function as $\delta\phi \in \{\phi = 0 \text{ on } \partial\Omega_{0\phi}, \phi \in H^1(\Omega_0)\}$. Multiplying the first row of (6.25) by the test function $\delta\phi$ and integrating over Ω_0, we obtain the dielectric problem as

$$\int_{\Omega_0} \nabla_X \cdot \tilde{\mathbf{D}} \cdot \delta\phi \mathrm{d}\Omega_0 = \int_{\Omega_0} \tilde{\rho}^e \cdot \delta\phi \mathrm{d}\Omega_0 \tag{6.27}$$

By divergence theory, we have

$$\int_{\Omega_0} -\tilde{\mathbf{D}} \cdot \nabla_X(\delta\phi) \mathrm{d}\Omega_0 = \int_{\Omega_0} \tilde{\rho}^e \delta\phi \mathrm{d}\Omega_0 - \int_{\partial\Omega_0} \tilde{\mathbf{D}} \cdot \mathbf{N} \delta\phi \mathrm{d}\Omega_0 \tag{6.28}$$

As $\phi = 0$ on $\partial\Omega_{0\phi}$, introducing the last two rows of (6.25), we obtain

$$\int_{\Omega_0} -\tilde{\mathbf{D}} \cdot \nabla_X(\delta\phi) \mathrm{d}\Omega_0 = \int_{\Omega_0} \tilde{\rho}^e \delta\phi \mathrm{d}\Omega_0 - \int_{\partial\Omega_{0D}} D^b \delta\phi \mathrm{d}\Omega_0 \tag{6.29}$$

Substituting (6.24) into (6.29), we arrive at

$$\begin{aligned} &\int_{\Omega_0} J\varepsilon \mathbf{C}^{-1} \nabla_X \phi \cdot \nabla_X(\delta\phi) \mathrm{d}\Omega_0 + \int_{\Omega_0} Jf(\varepsilon - \varepsilon_0) \mathbf{F}^{-1} G_{ikk} \cdot \nabla_X(\delta\phi) \mathrm{d}\Omega_0 \\ &= \int_{\Omega_0} \tilde{\rho}^e \delta\phi \mathrm{d}\Omega_0 - \int_{\partial\Omega_{0D}} D^b \delta\phi \mathrm{d}\Omega_0 \end{aligned} \tag{6.30}$$

In the mechanical problem, we assume the displacement $\mathbf{u} \in \{\mathbf{u} = \bar{\mathbf{u}}^* \text{ on } \partial\Omega_{0u}, \mathbf{u} \in H^2(\Omega_0)\}$. Multiplying the first equation in (6.26) by the test function $\delta\mathbf{u} \in \{\mathbf{u} = 0 \text{ on } \partial\Omega_{0u}, \mathbf{u} \in H^2(\Omega_0)\}$, integrating over Ω_0, we have

$$\int_{\Omega_0} \nabla_X \cdot \tilde{\Sigma} \cdot \delta\mathbf{u} \mathrm{d}\Omega_0 - \int_{\Omega_0} \nabla_X \cdot (\nabla_X \cdot \mathcal{S}) \cdot \delta\mathbf{u} \mathrm{d}\Omega_0 + \int_{\Omega_0} \tilde{\mathbf{f}} \delta\mathbf{u} \mathrm{d}\Omega_0 = 0 \tag{6.31}$$

Using integral by part, we obtain

$$\begin{aligned} &\int_{\Omega_0} \nabla_X \cdot (\tilde{\Sigma} \delta\mathbf{u}) \mathrm{d}\Omega_0 - \int_{\Omega_0} \tilde{\Sigma} : \nabla_X \delta\mathbf{u} \mathrm{d}\Omega_0 - \int_{\Omega_0} \nabla_X \cdot ((\nabla_X \cdot \mathcal{S}) \delta\mathbf{u}) \mathrm{d}\Omega_0 \\ &+ \int_{\Omega_0} (\nabla_X \cdot \mathcal{S}) : \nabla_X \delta\mathbf{u} \mathrm{d}\Omega_0 + \int_{\Omega_0} \tilde{\mathbf{f}} \cdot \delta\mathbf{u} \mathrm{d}\Omega_0 = 0 \end{aligned} \tag{6.32}$$

By Gauss's theorem and $\nabla_X \delta\mathbf{u} = \delta\mathbf{F}$, we have

$$\int_{\Omega_0} \tilde{\Sigma} : \delta\mathbf{F} \mathrm{d}\Omega_0 - \int_{\Omega_0} (\nabla_X \cdot \mathcal{S}) : \delta\mathbf{F} \mathrm{d}\Omega_0 = \int_{\Omega_0} \tilde{\mathbf{f}} \cdot \delta\mathbf{u} \mathrm{d}\Omega_0 + \int_{\partial\Omega_0} (\tilde{\Sigma}\mathbf{N} - \nabla_X \cdot \mathcal{S}\mathbf{N}) \cdot \delta\mathbf{u} \mathrm{d}\Omega_0 \tag{6.33}$$

Considering the boundary condition defined in the second row of (6.26), it can be obtained as:

$$\int_{\Omega_0} \tilde{\Sigma} : \delta\mathbf{F} \mathrm{d}\Omega_0 - \int_{\Omega_0} (\nabla_X \cdot \mathcal{S}) : \delta\mathbf{F} \mathrm{d}\Omega_0 = \int_{\Omega_0} \tilde{\mathbf{f}} \cdot \delta\mathbf{u} \mathrm{d}\Omega_0 + \int_{\partial\Omega_{0t}} \tilde{\mathbf{t}} \cdot \delta\mathbf{u} \mathrm{d}\Omega_0 \tag{6.34}$$

The third-order tensor $\mathcal{U}$ and second-order tensor $\mathbf{V}$ have the property of $\nabla \cdot (\mathcal{U} : \mathbf{V}) = (\nabla \cdot \mathcal{U}) : \mathbf{V} + \mathcal{U} \vdots \nabla\mathbf{V}$. By introducing the property into the second term of (6.34), we arrive at

$$\int_{\Omega_0} \tilde{\Sigma} : \delta\mathbf{F} \mathrm{d}\Omega_0 + \int_{\Omega_0} \mathcal{S} \vdots \delta\mathbf{G} \mathrm{d}\Omega_0 - \int_{\partial\Omega_0} \mathcal{S}\mathbf{N} : \delta\mathbf{F} \mathrm{d}\Omega_0 = \int_{\Omega_0} \tilde{\mathbf{f}} \cdot \delta\mathbf{u} \mathrm{d}\Omega_0 + \int_{\partial\Omega_{0t}} \tilde{\mathbf{t}} \cdot \delta\mathbf{u} \mathrm{d}\Omega_0 \tag{6.35}$$

We assume the boundary condition $\mathcal{S}\mathbf{N} = 0$ on $\partial\Omega_0$, we finally obtain the weak form of the mechanical equilibrium equation as:

$$\int_{\Omega_0} \tilde{\Sigma} : \delta\mathbf{F} \mathrm{d}\Omega_0 + \int_{\Omega_0} \mathcal{S} \vdots \delta\mathbf{G} \mathrm{d}\Omega_0 = \int_{\Omega_0} \tilde{\mathbf{f}} \cdot \delta\mathbf{u} \mathrm{d}\Omega_0 + \int_{\partial\Omega_{0t}} \tilde{\mathbf{t}} \cdot \delta\mathbf{u} \mathrm{d}\Omega_0 \tag{6.36}$$

6.3 Consistent linearization of flexoelectric weak-form equations

The linearization is as follow. The residuals are calculated by,

$$\begin{cases} \mathbf{R}_\phi(\mathbf{u},\phi) = \mathbf{q}(\mathbf{u},\phi) - \mathbf{q}^{ext} = 0 \\ \mathbf{R}_u(\mathbf{u},\phi) = \mathbf{f}(\mathbf{u},\phi) - \mathbf{f}^{ext} = 0 \end{cases} \tag{6.37}$$

where

$$\begin{aligned} \mathbf{q}(\mathbf{u},\phi) &= \int_{\Omega_0} -\tilde{\mathbf{D}} \cdot \nabla_X(\delta\phi) \mathrm{d}\Omega_0 \\ &= \int_{\Omega_0} J\varepsilon \mathbf{C}^{-1} \nabla_X(\delta\phi) \cdot \nabla_X \phi \mathrm{d}\Omega_0 + \int_{\Omega_0} Jf(\varepsilon - \varepsilon_0)\mathbf{F}^{-1} G_{ikk} \cdot \nabla_X(\delta\phi) \mathrm{d}\Omega_0 \end{aligned} \tag{6.38}$$

$$\mathbf{f}(\mathbf{u},\phi) = \int_{\Omega_0} \tilde{\boldsymbol{\Sigma}} : \delta\mathbf{F} \mathrm{d}\Omega_0 + \int_{\Omega_0} \mathcal{S} \vdots \delta\mathbf{G} \mathrm{d}\Omega_0 \tag{6.39}$$

$$\mathbf{q}^{ext} = \int_{\Omega_0} \tilde{\rho}^e \delta\phi \mathrm{d}\Omega_0 - \int_{\partial\Omega_{0D}} D^b \delta\phi \mathrm{d}\Omega_0 \tag{6.40}$$

$$\mathbf{f}^{ext} = \int_{\Omega_0} \tilde{\mathbf{f}} \cdot \delta\mathbf{u} \mathrm{d}\Omega_0 + \int_{\partial\Omega_0} \tilde{\mathbf{t}} \cdot \delta\mathbf{u} \mathrm{d}\Omega_0 \tag{6.41}$$

Their Taylor expansions are respectively given as

$$\begin{cases} \mathbf{R}_\phi(\mathbf{u}+\Delta\mathbf{u},\phi+\Delta\phi) = \mathbf{R}_\phi(\mathbf{u},\phi) + D_{\Delta\mathbf{u}}\mathbf{R}_\phi(\mathbf{u},\phi) + D_{\Delta\phi}\mathbf{R}_\phi(\mathbf{u},\phi) = 0 \\ \mathbf{R}_u(\mathbf{u}+\Delta\mathbf{u},\phi+\Delta\phi) = \mathbf{R}_u(\mathbf{u},\phi) + D_{\Delta\mathbf{u}}\mathbf{R}_u(\mathbf{u},\phi) + D_{\Delta\phi}\mathbf{R}_u(\mathbf{u},\phi) = 0 \end{cases} \tag{6.42}$$

The solution for the next increment in an iterative Newton-like procedure consists in solving the linearized problems for $\Delta\mathbf{u}$ and $\Delta\phi$ and to update the field variables for the next iteration through $\mathbf{u}^{k+1} = \mathbf{u}^k + \Delta\mathbf{u}$ and $\phi^{k+1} = \phi^k + \Delta\phi$. For the sake of clarity, the superscript k is omitted. Let us group all unknown quantities, respectively the displacement vector $\mathbf{u}$ and the potential ϕ in a vector $\mathbf{v}$. The directional derivatives of $f(\mathbf{v})$ in the direction of $\Delta\mathbf{v}$ is defined as:

$$D_{\Delta\mathbf{v}} f(\mathbf{v}) = \left[\frac{d}{d\alpha} \{ f(\mathbf{v} + \alpha\Delta\mathbf{v}) \} \right]_{\alpha=0} \tag{6.43}$$

We obtain $\Delta\mathbf{F} = \nabla_X(\Delta\mathbf{u})$ and $\Delta\mathbf{G} = \nabla_X(\nabla_X(\Delta\mathbf{u}))$. Thus, the directional derivatives of the residuals $\mathbf{R}(\mathbf{u},\phi) = [\mathbf{R}_\phi(\mathbf{u},\phi); \mathbf{R}_u(\mathbf{u},\phi)]$ with respect to $\Delta\phi$ and $\Delta\mathbf{u}$ are calculated, respectively, as

$$\begin{cases} D_{\Delta\phi}\mathbf{R}(\mathbf{u},\phi) = \frac{\partial\mathbf{R}}{\partial\phi}\Delta\phi = \frac{\partial\mathbf{R}}{\partial\nabla_X\phi}\frac{\partial\nabla_X\phi}{\partial\phi}\Delta\phi = \frac{\partial\mathbf{R}_\phi}{\partial\nabla_X\phi}\nabla_X(\Delta\phi) \\ D_{\Delta\mathbf{u}}\mathbf{R}(\mathbf{u},\phi) = \frac{\partial\mathbf{R}}{\partial\mathbf{u}}\Delta\mathbf{u} = \frac{\partial\mathbf{R}}{\partial\mathbf{F}}\frac{\partial\mathbf{F}}{\partial\mathbf{u}}\Delta\mathbf{u} + \frac{\partial\mathbf{R}}{\partial\mathbf{G}}\frac{\partial\mathbf{G}}{\partial\mathbf{u}}\Delta\mathbf{u} = \frac{\partial\mathbf{R}}{\partial\mathbf{F}}\Delta\mathbf{F} + \frac{\partial\mathbf{R}}{\partial\mathbf{G}}\Delta\mathbf{G} \end{cases} \tag{6.44}$$

Substituting (6.37)-(6.42) into (6.44) and assuming constant external forces (dead load), we obtain

$$\begin{cases} D_{\Delta\phi}\mathbf{R}_\phi(\mathbf{u},\phi) = \int_{\Omega_0} \nabla_X(\delta\phi) \cdot \frac{\partial(-\tilde{\mathbf{D}})}{\partial\nabla_X\phi} \cdot \nabla_X(\Delta\phi) \mathrm{d}\Omega_0 \\ D_{\Delta\mathbf{u}}\mathbf{R}_\phi(\mathbf{u},\phi) = \int_{\Omega_0} \{ \nabla_X(\delta\phi) \cdot \frac{\partial(-\tilde{\mathbf{D}})}{\partial\mathbf{F}} : \Delta\mathbf{F} + \nabla_X(\delta\phi) \cdot \frac{\partial(-\tilde{\mathbf{D}})}{\partial\mathbf{G}} \vdots \Delta\mathbf{G} \} \mathrm{d}\Omega_0 \end{cases} \tag{6.45}$$

and

$$\begin{cases} D_{\Delta\phi}\mathbf{R}_u(\mathbf{u},\phi) = \int_{\Omega_0} \delta\mathbf{G} \vdots \frac{\partial\mathcal{S}}{\partial\nabla_X\phi} \cdot \nabla_X(\Delta\phi) \mathrm{d}\Omega_0 \\ D_{\Delta\mathbf{u}}\mathbf{R}_u(\mathbf{u},\phi) = \int_{\Omega_0} \delta\mathbf{F} : \frac{\partial\tilde{\boldsymbol{\Sigma}}}{\partial\mathbf{F}} : \Delta\mathbf{F} \mathrm{d}\Omega_0 + \int_{\Omega_0} \delta\mathbf{G} \vdots \frac{\partial\mathcal{S}}{\partial\mathbf{F}} : \Delta\mathbf{F} \mathrm{d}\Omega_0 + \int_{\Omega_0} \delta\mathbf{G} \vdots \frac{\partial\mathcal{S}}{\partial\mathbf{G}} \vdots \Delta\mathbf{G} \mathrm{d}\Omega_0 \end{cases} \tag{6.46}$$

Here, we recall the derivatives of deformation gradient $\mathbf{F}$, inverse deformation gradient $\mathbf{F}^{-1}$ and the right Cauchy-Green strain with respect to the deformation gradient that will be used in the following formulas:

$$\mathbb{F}_{ijkl} = \frac{\partial F_{ij}^{-1}}{\partial F_{kl}} = -F_{ik}^{-1}F_{lj}^{-1} \tag{6.47}$$

$$\tilde{\mathbb{F}}_{ijkl} = \frac{\partial F_{ij}^{-T}}{\partial F_{kl}} = -F_{li}^{-1}F_{jk}^{-1} \tag{6.48}$$

$$\tilde{\mathbb{A}}_{ijkl} = \frac{\partial C_{ij}^{-1}}{\partial F_{kl}} = -F_{ik}^{-1}C_{jl}^{-1} - C_{il}^{-1}F_{jk}^{-1} \tag{6.49}$$

For the polarization defined in (6.23), its derivatives with respect to the deformation gradient $\mathbf{F}$, electric potential gradient $\nabla_X\phi$ and the second-order gradient of displacement $\mathbf{G}$ can be obtained as:

$$\begin{cases} \frac{\partial \tilde{P}_i}{\nabla_m\phi} = -J(\varepsilon-\varepsilon_0)F_{mi}^{-1} \\ \frac{\partial \tilde{P}_i}{\partial F_{kl}} = -J(\varepsilon-\varepsilon_0)(fF_{lk}^{-1}G_{ipp} + F_{lk}^{-1}F_{mi}^{-1}\nabla_m\phi + \tilde{\mathbb{F}}_{imkl}\nabla_m\phi) \\ \frac{\partial \tilde{P}_i}{\partial G_{jkl}} = -J(\varepsilon-\varepsilon_0)f\delta_{ij}\delta_{kl} \end{cases} \tag{6.50}$$

The electric displacement in (6.24) with respect to the three fields $\mathbf{F}$, $\nabla_X\phi$ and $\mathbf{G}$, is derived as:

$$\begin{cases} \frac{\partial \tilde{D}_i}{\partial \nabla_m\phi} = -J\varepsilon C_{im}^{-1} \\ \frac{\partial \tilde{D}_i}{\partial F_{kl}} = -J\varepsilon(F_{lk}^{-1}C_{im}^{-1} - F_{ik}^{-1}C_{ml}^{-1} - C_{il}^{-1}F_{mk}^{-1})\nabla_m\phi - Jf(\varepsilon-\varepsilon_0)(F_{im}^{-1}F_{lk}^{-1} + \mathbb{F}_{imkl})G_{mpp} \\ \frac{\partial \tilde{D}_i}{\partial G_{jkl}} = -Jf(\varepsilon-\varepsilon_0)F_{ij}^{-1}\delta_{kl} \end{cases} \tag{6.51}$$

We obtain the derivatives of hyperstress given in (6.18) about the $\mathbf{F}$, $\nabla_X\phi$ and $\mathbf{G}$, as:

$$\begin{cases} \frac{\partial \mathcal{S}_{ijk}}{\partial \nabla_l\phi} = -Jf(\varepsilon-\varepsilon_0)F_{li}^{-1}\delta_{jk} \\ \frac{\partial \mathcal{S}_{ijk}}{\partial F_{lm}} = -f\delta_{jk}J(\varepsilon-\varepsilon_0)(fF_{ml}^{-1}G_{ipp} + F_{ml}^{-1}F_{ni}^{-1}\nabla_n\phi - F_{mi}^{-1}F_{nl}^{-1}\nabla_n\phi) \\ \frac{\partial \mathcal{S}_{ijk}}{\partial G_{lmn}} = g\delta_{il}\delta_{jk}\delta_{mn} - Jf^2(\varepsilon-\varepsilon_0)\delta_{il}\delta_{jk}\delta_{mn} \end{cases} \tag{6.52}$$

While the first Piola-Kirchhoff stress defined in (6.17) is only related to the deformation gradient $\mathbf{F}$, then we have

$$\begin{aligned} \frac{\partial \tilde{\Sigma}_{ij}}{\partial F_{kl}} = &\frac{2\mu}{9}J^{-\frac{2}{3}}F_{ji}^{-1}F_{lk}^{-1}\Sigma_\alpha\lambda_\alpha^2 + \frac{\mu}{3}J^{-\frac{2}{3}}F_{li}^{-1}F_{jk}^{-1}\Sigma_\alpha\lambda_\alpha^2 \\ &- \frac{2\mu}{3}J^{-\frac{2}{3}}F_{ji}^{-1}F_{kl} - \frac{2\mu}{3}J^{-\frac{2}{3}}F_{lk}^{-1}F_{ij} + \mu J^{-\frac{2}{3}}\delta_{ik}\delta_{jl} \\ &+ \kappa(2J-1)JF_{ji}^{-1}F_{lk}^{-1} - \kappa(J-1)JF_{li}^{-1}F_{jk}^{-1} \end{aligned} \tag{6.53}$$

6.4 IGA Discretization

The fundamental concept of Isogeometric Analysis is the use of NURBS not solely as a means of discretizing geometry, but also as a tool for discretizing the analysis itself [103, 202]. The NURBS basis functions with higher continuity are employed here to solve the fourth order flexoelectric PDEs. For the sake of simplicity, we restrict the developments to 2D, even though extension to 3D is straightforward. The basis function for NURBS surfaces has been defined in

(3.37). The polynomial orders of NURBS mesh are chosen as $p = q = 3$ here. The discretization of the electric potential ϕ and displacement $\mathbf{u}$ can be defined as

$$\phi(\mathbf{x}) = \sum_{i=1}^{n}\sum_{j=1}^{m} R_{i,j}^{p,q}(\xi,\eta)\phi^e = \mathbf{N}_\phi \phi^e \tag{6.54}$$

$$\mathbf{u}(\mathbf{x}) = \sum_{i=1}^{n}\sum_{j=1}^{m} R_{i,j}^{p,q}(\xi,\eta)u_{ij}^e = \mathbf{N}_u \mathbf{u}^e \tag{6.55}$$

The test function, potential increment and their corresponding gradient are approximated by

$$\begin{aligned} &\delta\phi = \mathbf{N}_\phi \delta\phi^e,\ \Delta\phi = \mathbf{N}_\phi \Delta\phi^e \\ &\nabla_X(\delta\phi) = \mathbf{B}_\phi \delta\phi^e,\ \nabla_X(\Delta\phi) = \mathbf{B}_\phi \Delta\phi^e \end{aligned} \tag{6.56}$$

Similarly, the test function, displacement increment and their corresponding gradient are obtained as:

$$\begin{aligned} &\delta\mathbf{u} = \mathbf{N}_u \delta\mathbf{u}^e,\ \Delta\mathbf{u} = \mathbf{N}_u \Delta\mathbf{u}^e \\ &\delta\mathbf{F} = \mathbf{B}_u \delta\mathbf{u}^e,\ \Delta\mathbf{F} = \mathbf{B}_u \Delta\mathbf{u}^e \end{aligned} \tag{6.57}$$

The vector forms of deformation gradient tensor and strain gradient are given as, respectively

$$[\Delta\mathbf{F}] = \begin{bmatrix} \Delta F_{11} \\ \Delta F_{21} \\ \Delta F_{12} \\ \Delta F_{22} \end{bmatrix} = \begin{bmatrix} \frac{\partial \Delta u_1}{\partial X_1} \\ \frac{\partial \Delta u_2}{\partial X_1} \\ \frac{\partial \Delta u_1}{\partial X_2} \\ \frac{\partial \Delta u_2}{\partial X_2} \end{bmatrix} \tag{6.58}$$

and

$$[\mathbf{G}(\Delta\mathbf{u})] = \begin{bmatrix} G_{111}(\Delta\mathbf{u}) \\ G_{112}(\Delta\mathbf{u}) \\ G_{211}(\Delta\mathbf{u}) \\ G_{122}(\Delta\mathbf{u}) \\ G_{212}(\Delta\mathbf{u}) \\ G_{222}(\Delta\mathbf{u}) \end{bmatrix} = \begin{bmatrix} \frac{\partial^2 \Delta u_1}{\partial X_1^2} \\ \frac{\partial^2 \Delta u_1}{\partial X_1 \partial X_2} \\ \frac{\partial^2 \Delta u_2}{\partial X_1^2} \\ \frac{\partial^2 \Delta u_1}{\partial X_2^2} \\ \frac{\partial^2 \Delta u_2}{\partial X_1 \partial X_2} \\ \frac{\partial^2 \Delta u_2}{\partial X_2^2} \end{bmatrix} \tag{6.59}$$

Then the discrete form of the strain gradient are obtained as:

$$[\mathbf{G}(\Delta\mathbf{u})] = \mathbf{H}_u \Delta\mathbf{u}^e,\ [\delta\mathbf{G}] = \mathbf{H}_u \delta\mathbf{u}^e \tag{6.60}$$

Above, $\mathbf{N}_\phi = \mathbf{N}_u$ are the discrete interpolation shape functions, their gradients $\mathbf{B}_\phi$ and $\mathbf{B}_u$, and second gradient $\mathbf{H}_u$. These matrices are defined as (n is the number of control points for every element):

$$\mathbf{B}_\phi = \begin{bmatrix} \frac{\partial N_\phi^1}{\partial X_1} & \cdots & \frac{\partial N_\phi^n}{\partial X_1} \\ \frac{\partial N_\phi^1}{\partial X_2} & \cdots & \frac{\partial N_\phi^n}{\partial X_2} \end{bmatrix},\ \mathbf{B}_u = \begin{bmatrix} \frac{\partial N_u^1}{\partial X_1} & \cdots & \frac{\partial N_u^n}{\partial X_1} & 0 & \cdots, & 0 \\ 0 & \cdots & 0 & \frac{\partial N_u^1}{\partial X_1} & \cdots & \frac{\partial N_u^n}{\partial X_1} \\ \frac{\partial N_u^1}{\partial X_2} & \cdots & \frac{\partial N_u^n}{\partial X_2} & 0 & \cdots, & 0 \\ 0 & \cdots & 0 & \frac{\partial N_u^1}{\partial X_2} & \cdots & \frac{\partial N_u^n}{\partial X_2} \end{bmatrix} \tag{6.61}$$

$$\mathbf{H}_u = \begin{bmatrix} \frac{\partial^2 N_u^1}{\partial X_1^2} & \cdots & \frac{\partial^2 N_u^n}{\partial X_1^2} & 0 & \cdots & 0 \\ \frac{\partial^2 N_u^1}{\partial X_1 \partial X_2} & \cdots & \frac{\partial^2 N_u^n}{\partial X_1 \partial X_2} & 0 & \cdots & 0 \\ 0 & \cdots & 0 & \frac{\partial^2 N_u^1}{\partial X_1^2} & \cdots & \frac{\partial^2 N_u^n}{\partial X_1^2} \\ \frac{\partial^2 N_u^1}{\partial X_1^2} & \cdots & \frac{\partial^2 N_u^n}{\partial X_1^2} & 0 & \cdots & 0 \\ 0 & \cdots & 0 & \frac{\partial^2 N_u^1}{\partial X_1 \partial X_2} & \cdots & \frac{\partial^2 N_u^n}{\partial X_1 \partial X_2} \\ 0 & \cdots & 0 & \frac{\partial^2 N_u^1}{\partial X_2^2} & \cdots & \frac{\partial^2 N_u^n}{\partial X_2^2} \end{bmatrix} \tag{6.62}$$

Introducing the approximation (6.54)-(6.57) and (6.60) into (6.45)-(6.46), then substituting into (6.42), we finally obtain the discrete form of the linearized equations:

$$\begin{bmatrix} \mathbf{K}_{\phi\phi}(\phi,\mathbf{u}) & \mathbf{K}_{\phi u}(\phi,\mathbf{u}) \\ \mathbf{K}_{u\phi}(\phi,\mathbf{u}) & \mathbf{K}_{uu}(\phi,\mathbf{u}) \end{bmatrix} \begin{bmatrix} \Delta\phi \\ \Delta\mathbf{u} \end{bmatrix} = - \begin{bmatrix} \mathbf{R}_\phi(\phi,\mathbf{u}) \\ \mathbf{R}_u(\phi,\mathbf{u}) \end{bmatrix} \tag{6.63}$$

where

$$\mathbf{K}_{\phi\phi}(\phi,\mathbf{u}) = \int_{\Omega_0} \mathbf{B}_\phi^T \frac{\partial(-\tilde{\mathbf{D}})}{\partial \nabla\phi} \mathbf{B}_\phi \mathrm{d}\Omega_0 \tag{6.64}$$

$$\mathbf{K}_{\phi u}(\phi,\mathbf{u}) = \int_{\Omega_0} \left\{ \mathbf{B}_\phi^T \frac{\partial(-\tilde{\mathbf{D}})}{\partial \mathbf{F}} \mathbf{B}_u + \mathbf{B}_\phi^T \frac{\partial(-\tilde{\mathbf{D}})}{\partial \mathbf{G}} \mathbf{H}_u \right\} \mathrm{d}\Omega_0 \tag{6.65}$$

$$\mathbf{K}_{u\phi}(\phi,\mathbf{u}) = \int_{\Omega_0} \mathbf{H}_u^T \frac{\partial \mathcal{S}}{\partial \nabla\phi} \mathbf{B}_\phi \mathrm{d}\Omega_0 \tag{6.66}$$

$$\mathbf{K}_{uu}(\phi,\mathbf{u}) = \int_{\Omega_0} \left\{ \mathbf{B}_u^T \frac{\partial \tilde{\mathbf{\Sigma}}}{\partial \mathbf{F}} \mathbf{B}_u + \mathbf{H}_u^T \frac{\partial \mathcal{S}}{\partial \mathbf{F}} \mathbf{B}_u + \mathbf{H}_u^T \frac{\partial \mathcal{S}}{\partial \mathbf{G}} \mathbf{H}_u \right\} \mathrm{d}\Omega_0 \tag{6.67}$$

6.5 Nonlinear topology optimization formulation for soft dielectrics with flexoelectricity

6.5.1 Strain Density Function (SDF) interpolation scheme by SIMP method and linear material interpolation model

Topology Optimization (TO) is to seek the optimal material distribution in a given structural domain and maximize the specific physical properties. The structural topology can be represented by the local material densities. In the employed SIMP framework, the material properties are interpolated with respect to the local density in a continuous manner, and penalty exponents are used to push the local densities to converge to 1 or 0 (so called 'black-white designs'). Then, the following interpolation scheme is adopted:

$$\begin{aligned} \Psi(\rho) =& [m_{in} + (1-m_{in})\rho^{p_c}](\Psi_{elast} + \Psi_{elast}^{grad}) + [m_{in} + (1-m_{in})\rho^{p_f}]\Psi_{flexo} \\ &+ [m_{in} + (1-m_{in})\rho]\Psi_{diel} \end{aligned} \tag{6.68}$$

It is worth noting that in the above, the interpolation related to the term Ψ_{diel} is linear. We have observed that this linear term improves the convergence of the topological optimization scheme in the present context. On the other hand, larger values of this exponent are not necessary to define a material density between zero and 1, as this property is provided by the exponents of the other terms.

While the electric displacement $\tilde{\mathbf{D}}$ defined in (6.24) is interpolated as:

$$\tilde{\mathbf{D}}(\rho) = -[\varepsilon_0 + (\varepsilon - \varepsilon_0)\rho] J \mathbf{C}^{-1} \nabla_X \phi - \rho^{p_f} J f (\varepsilon - \varepsilon_0) \mathbf{F}^{-1} G_{ikk} \tag{6.69}$$

where the small value $m_{in} = 1 \times 10^{-9}$ is employed to mimic the properties of void phase, ε is electric permittivity of solid material. ε_0 is the vacuum electric permittivity. p_c and p_f are penalty exponents, and taken as $p_c = p_f = 3$ in the following numerical examples.

6.5.2 Energy remedy for void region

To circumvent the numerical instability induced by distorted deformations in low stiffness regions, an energy remedy scheme proposed by Wang [222] is extended to nonlinear electromechanical system. The energy density is interpolated between the nonlinear energy density and the linear energy density. The energy remedy form can be defined as:

$$\widehat{\Psi}(\phi, \mathbf{u}) = \Psi^{NL}(\phi, \theta\mathbf{u}) - \Psi^{L}(\phi, \theta\mathbf{u}) + \Psi^{L}(\phi, \mathbf{u}) \tag{6.70}$$

where Ψ^{NL} is defined in terms of (6.5)-(6.9), and

$$\Psi^{L}(\phi, \mathbf{u}) = \underbrace{\frac{1}{2}\lambda\varepsilon_{kk}^2 + \mu\varepsilon_{ij}\varepsilon_{ij}}_{linear\ elast} + \underbrace{\frac{1}{2}A_{ij}P_i^L P_j^L}_{dielectric} + \underbrace{\frac{g}{2}G_{ikk}G_{ill} + fP_i^L G_{ikk}}_{flexoelectric} \tag{6.71}$$

$\lambda = \frac{E\nu}{1-\nu^2}$. By linear form of the first equation in (6.19), i.e. $\nabla_X \phi + \frac{\partial \Psi^L}{\partial \tilde{\mathbf{P}}^L} = 0$, we obtain the P_i^L as

$$P_i^L = -(\varepsilon - \varepsilon_0)(fG_{ikk} + \nabla_i \phi) \tag{6.72}$$

then

$$D_i^L = -\varepsilon\nabla_i\phi - f(\varepsilon - \varepsilon_0)G_{ikk} \tag{6.73}$$

$$\Sigma_{ij}^L = \lambda\varepsilon_{kk}\delta_{ij} + 2\mu\varepsilon_{ij} \tag{6.74}$$

$$\mathcal{S}_{ijk}^L = gG_{ipp}\delta_{jk} + f\tilde{P}_i^L\delta_{jk} \tag{6.75}$$

The interpolation parameter $\theta = 1$ for solid region and $\theta = 0$ for void region. It suggests that the stored electromechanical energy corresponds to the non-linear one for solid phase ($\theta = 1$) and the linear one for void phase ($\theta = 0$). To ensure differentiability, θ in (6.70) is defined by a smoothed Heaviside projection function,

$$\theta = \frac{\tanh(\beta_1\alpha) + \tanh(\beta_1(\tilde{\rho} - \alpha))}{\tanh(\beta_1\alpha) + \tanh(\beta_1(1 - \alpha))} \tag{6.76}$$

when $\beta_1 \to \infty$, $\theta = 1$ if $\tilde{\rho} > \alpha$, $\theta = 0$ if $\tilde{\rho} < \alpha$. We state that the symbols with subscript 'L' correspond to linear terms, while the symbols with subscript 'NL' correspond to non-linear ones, and the symbols with subscript 'θ' represent the terms where the displacement is interpolated by θ defined in (6.76).

Using (6.70), the flexoelectric boundary values problems are given:

$$\begin{cases} \nabla_X \cdot \widehat{\mathbf{D}} = \widehat{\rho}^e \text{ in } \Omega_0, \\ \nabla_X \cdot \widehat{\mathbf{\Sigma}} - \nabla_X \cdot (\nabla_X \cdot \widehat{\mathcal{S}}) + \widehat{\mathbf{f}}^e = 0, \text{ in } \Omega_0 \end{cases} \tag{6.77}$$

and

$$\widehat{\mathbf{D}} = \mathbf{D}^{NL,\theta} - \mathbf{D}^{L,\theta} + \mathbf{D}^{L} \tag{6.78}$$

$$\widehat{\mathbf{\Sigma}} = \mathbf{\Sigma}^{NL,\theta} - \mathbf{\Sigma}^{L,\theta} + \mathbf{\Sigma}^{L} \tag{6.79}$$

$$\widehat{\mathcal{S}} = \mathcal{S}^{NL,\theta} - \mathcal{S}^{L,\theta} + \mathcal{S}^{L} \tag{6.80}$$

where $\boldsymbol{\Sigma}^{NL,\theta}$, $\mathcal{S}^{NL,\theta}$ and $\mathbf{D}^{NL,\theta}$ are respectively defined in (6.17), (6.18) and (6.24) with the displacement $\mathbf{u}$ interpolated by θ. $\mathbf{D}^{L,\theta}$, $\boldsymbol{\Sigma}^{L,\theta}$ and $\mathcal{S}^{L,\theta}$ are respectively given in terms of (6.73), (6.74) and (6.75) with the displacement interpolation parameter θ.

The residuals are calculated by

$$\begin{cases} \widehat{\mathbf{R}}_{\phi}(\mathbf{u},\phi) = \widehat{\mathbf{q}}(\mathbf{u},\phi) - \widehat{\mathbf{q}}^{ext} = \mathbf{q}^{NL,\theta}(\mathbf{u},\phi) - \mathbf{q}^{L,\theta}(\mathbf{u},\phi) + \mathbf{q}^{L}(\mathbf{u},\phi) - \widehat{\mathbf{q}}^{ext} = 0 \\ \widehat{\mathbf{R}}_{u}(\mathbf{u},\phi) = \widehat{\mathbf{f}}(\mathbf{u},\phi) - \widehat{\mathbf{f}}^{ext} = \mathbf{f}^{NL,\theta}(\mathbf{u},\phi) - \mathbf{f}^{L,\theta}(\mathbf{u},\phi) + \mathbf{f}^{L}(\mathbf{u},\phi) - \widehat{\mathbf{f}}^{ext} = 0 \end{cases} \tag{6.81}$$

where

$$\mathbf{q}^{NL,\theta}(\mathbf{u},\phi) = \mathbf{q}(\theta\mathbf{u},\phi) \tag{6.82}$$

$$\mathbf{f}^{NL,\theta}(\mathbf{u},\phi) = \mathbf{f}(\theta\mathbf{u},\phi) \tag{6.83}$$

$$\mathbf{q}^{L}(\mathbf{u},\phi) = \int_{\Omega_0} -\mathbf{D}^{L}\cdot\nabla_X(\delta\phi)\mathrm{d}\Omega_0 \tag{6.84}$$

$$\mathbf{f}^{L}(\mathbf{u},\phi) = \int_{\Omega_0} \boldsymbol{\Sigma}^{L} : \delta\mathbf{u}\mathrm{d}\Omega_0 + \int_{\Omega_0} \mathcal{S}^{L}\vdots\delta\mathbf{G}\mathrm{d}\Omega_0 \tag{6.85}$$

We obtain the following discrete system associated with the linearized problem in the Newton algorithm:

$$\begin{bmatrix} \widehat{\mathbf{K}}_{\phi\phi}(\phi,\mathbf{u},\theta) & \widehat{\mathbf{K}}_{\phi u}(\phi,\mathbf{u},\theta) \\ \widehat{\mathbf{K}}_{u\phi}(\phi,\mathbf{u},\theta) & \widehat{\mathbf{K}}_{uu}(\phi,\mathbf{u},\theta) \end{bmatrix} \begin{bmatrix} \Delta\phi \\ \Delta\mathbf{u} \end{bmatrix} = - \begin{bmatrix} \widehat{\mathbf{R}}_{\phi} \\ \widehat{\mathbf{R}}_{u} \end{bmatrix} \tag{6.86}$$

where

$$\widehat{\mathbf{K}}_{\phi\phi}(\phi,\mathbf{u},\theta) = \frac{\partial\mathbf{q}^{NL,\theta}}{\partial\phi} - \frac{\partial\mathbf{q}^{L,\theta}}{\partial\phi} + \frac{\partial\mathbf{q}^{L}}{\partial\phi} = \mathbf{K}^{NL,\theta}_{\phi\phi} - \mathbf{K}^{L,\theta}_{\phi\phi} + \mathbf{K}^{L}_{\phi\phi} \tag{6.87}$$

$$\widehat{\mathbf{K}}_{\phi u}(\phi,\mathbf{u},\theta) = \frac{\partial\mathbf{q}^{NL,\theta}}{\partial\mathbf{u}} - \frac{\partial\mathbf{q}^{L,\theta}}{\partial\mathbf{u}} + \frac{\partial\mathbf{q}^{L}}{\partial\mathbf{u}} = \mathbf{K}^{NL,\theta}_{\phi u} - \mathbf{K}^{L,\theta}_{\phi u} + \mathbf{K}^{L}_{\phi u} \tag{6.88}$$

$$\widehat{\mathbf{K}}_{u\phi}(\phi,\mathbf{u},\theta) = \frac{\partial\mathbf{f}^{NL,\theta}}{\partial\phi} - \frac{\partial\mathbf{f}^{L,\theta}}{\partial\phi} + \frac{\partial\mathbf{f}^{L}}{\partial\phi} = \mathbf{K}^{NL,\theta}_{u\phi} - \mathbf{K}^{L,\theta}_{u\phi} + \mathbf{K}^{L}_{u\phi} \tag{6.89}$$

$$\widehat{\mathbf{K}}_{uu}(\phi,\mathbf{u},\theta) = \frac{\partial\mathbf{f}^{NL,\theta}}{\partial\mathbf{u}} - \frac{\partial\mathbf{f}^{L,\theta}}{\partial\mathbf{u}} + \frac{\partial\mathbf{f}^{L}}{\partial\mathbf{u}} = \mathbf{K}^{NL,\theta}_{uu} - \mathbf{K}^{L,\theta}_{uu} + \mathbf{K}^{L}_{uu} \tag{6.90}$$

$$\mathbf{K}^{NL,\theta}_{\phi\phi} = \int_{\Omega_0} B^{T}_{\phi}\frac{\partial(-\tilde{D}^{NL,\theta}_{i})}{\partial\nabla_m\phi}B_{\phi}\mathrm{d}\Omega_0 \tag{6.91}$$

$$\mathbf{K}^{NL,\theta}_{\phi u} = \int_{\Omega_0} \left\{ B^{T}_{\phi}\frac{\partial(-\tilde{D}^{NL,\theta}_{i})}{\partial F_{kl}}B_u + B^{T}_{\phi}\frac{\partial(-\tilde{D}^{NL,\theta}_{i})}{\partial G_{jkl}}H_u \right\}\theta\mathrm{d}\Omega_0 \tag{6.92}$$

$$\mathbf{K}^{NL,\theta}_{u\phi} = \int_{\Omega_0} H^{T}_{u}\frac{\partial\mathcal{S}^{NL,\theta}_{ijk}}{\partial\nabla_l\phi}B_{\phi}\mathrm{d}\Omega_0 \tag{6.93}$$

$$\mathbf{K}^{NL,\theta}_{uu} = \int_{\Omega_0} \left\{ B^{T}_{u}\frac{\partial\tilde{\Sigma}^{NL,\theta}_{ij}}{\partial F_{kl}}B_u + H^{T}_{u}\frac{\partial\mathcal{S}^{NL,\theta}_{ijk}}{\partial F_{lm}}B_u + H^{T}_{u}\frac{\partial\mathcal{S}^{NL,\theta}_{ijk}}{\partial G_{lmn}}H_u \right\}\theta\mathrm{d}\Omega_0 \tag{6.94}$$

$$\mathbf{K}^{L}_{\phi\phi} = \mathbf{K}^{L,\theta}_{\phi\phi} = \int_{\Omega_0} B^T_\phi \varepsilon \delta_{ij} B_\phi \mathrm{d}\Omega_0 \tag{6.95}$$

$$\mathbf{K}^{L}_{u\phi} = \mathbf{K}^{L,\theta}_{u\phi} = -\int_{\Omega_0} H^T_u f(\varepsilon - \varepsilon_0)\delta_{il}\delta_{jk} B_\phi \mathrm{d}\Omega_0 \tag{6.96}$$

$$\mathbf{K}^{L}_{\phi u} = \int_{\Omega_0} B^T_\phi f(\varepsilon - \varepsilon_0)\delta_{ij}\delta_{kl} H_u \mathrm{d}\Omega_0 \tag{6.97}$$

$$\mathbf{K}^{L}_{uu} = \int_{\Omega_0} \left\{ B^T_u [\lambda \delta_{ij}\delta_{kl} + \mu(\delta_{ik}\delta_{jl} + \delta_{il}\delta_{jk})] B_u + H^T_u [g - f^2(\varepsilon - \varepsilon_0)]\delta_{il}\delta_{mn}\delta_{jk} H_u \right\} \mathrm{d}\Omega_0 \tag{6.98}$$

$$\mathbf{K}^{L,\theta}_{\phi u} = \int_{\Omega_0} B^T_\phi f(\varepsilon - \varepsilon_0)\delta_{ij}\delta_{kl} H_u \theta \mathrm{d}\Omega_0 \tag{6.99}$$

$$\mathbf{K}^{L,\theta}_{uu} = \int_{\Omega_0} \left\{ B^T_u [\lambda \delta_{ij}\delta_{kl} + \mu(\delta_{ik}\delta_{jl} + \delta_{il}\delta_{jk})] B_u + H^T_u [g - f^2(\varepsilon - \varepsilon_0)]\delta_{il}\delta_{mn}\delta_{jk} H_u \right\} \theta \mathrm{d}\Omega_0 \tag{6.100}$$

After solving the linearized equation (6.86), the nodal electric potentials and displacements are updated through

$$\begin{aligned} \boldsymbol{\phi}^{k+1} &= \boldsymbol{\phi}^k + \Delta\boldsymbol{\phi} \\ \mathbf{u}^{k+1} &= \mathbf{u}^k + \Delta\mathbf{u} \end{aligned} \tag{6.101}$$

until a convergence criterion is reached. The algorithm for solving the nonlinear problem (6.81) is illustrated in Algorithm 2. It is important to note that the equations for the optimization model are calculated using the final converged state variables of the structural equilibrium residual vectors defined in (6.81).

Algorithm 2 The algorithm for nonlinear problem (6.81)

Initialize: $[\mathbf{u}^{(0)}; \boldsymbol{\phi}^{(0)}] = \mathbf{0}$, $tol = 10^{-8}$;
for $n = 1$ to N (Loop over all load increments) **do**
  Initialize: $err = 1$, $k = 0$;
  $\mathbf{u}^{(k,n)} = \mathbf{u}^{(n-1)}$, $\boldsymbol{\phi}^{(k,n)} = \boldsymbol{\phi}^{(n-1)}$;
  while $err > tol$ **do**
    Compute tangent stiffness $\widehat{\mathbf{K}}_{tan}(\boldsymbol{\phi}^{(k,n)}, \mathbf{u}^{(k,n)})$ from (6.87)-(6.100);
    Compute residual $\widehat{\mathbf{R}}(\boldsymbol{\phi}^{(k,n)}, \mathbf{u}^{(k,n)})$ from (6.81);
    Compute $\Delta\mathbf{u}^{(k,n)}$ and $\Delta\boldsymbol{\phi}^{(k,n)}$ from (6.86);
    Update $\mathbf{u}^{(k+1,n)} = \mathbf{u}^{(k,n)} + \Delta\mathbf{u}^{(k,n)}$, $\boldsymbol{\phi}^{(k+1,n)} = \boldsymbol{\phi}^{(k,n)} + \Delta\boldsymbol{\phi}^{(k,n)}$;
    $err = \|\widehat{\mathbf{R}}^{(k,n)}\|$;
    $k = k + 1$;
  end while
  $\mathbf{u}^{(n)} = \mathbf{u}^{(k,n)}$, $\boldsymbol{\phi}^{(n)} = \boldsymbol{\phi}^{(k,n)}$;
end for
return $\mathbf{u} = \mathbf{u}^{(k,N)}$, $\boldsymbol{\phi} = \boldsymbol{\phi}^{(k,N)}$;

6.5.3 Optimization problem formulation

Here we formulate the topology optimization problem to maximize the electromechanical coupling factor (ECF) of non-linear flexoelectric structures:

$$\begin{aligned} &\text{Minimize}: \quad J = \frac{1}{k_{eff}^2} = \frac{\Pi_m}{\Pi_e} \\ &\text{Subject to}: \quad \begin{cases} \frac{1}{|\Omega|}\int_{\Omega} \bar{\rho}\,\mathrm{d}\Omega - v_f \leq 0 \\ \widehat{\mathbf{R}}(\phi, \mathbf{u}) = 0 \\ \hat{C}(\rho) \leq \hat{C}^{max} \\ 0 \leq \rho_e \leq 1, \end{cases} \end{aligned} \tag{6.102}$$

where

$$\Pi_m = (\widehat{\mathbf{f}}^{ext})^T \mathbf{u} \tag{6.103}$$

$$\Pi_e = \frac{1}{2}\phi^T \widehat{\mathbf{K}}_{\phi\phi}\phi \tag{6.104}$$

and $\widehat{\mathbf{R}}(\phi, \mathbf{u}) = [\widehat{\mathbf{R}}_{\phi};\ \widehat{\mathbf{R}}_u]$ is the residual vector of the structural equilibrium defined by (6.81). $\hat{C}(\rho) = \Pi_m$ is the average compliance of the structure, which it is expected to eliminate disconnected domain by ensuring a minimal stiffness to the structure.

The continuous density design variable ρ in optimization formulation (6.102) yields a ill-posed problem, such as checkerboard and mesh-dependence. In order to enforce its well-posedness (smoothness and mesh-independence), a projection filter [143, 225] is defined by a convolution of the density ρ with a non-negative smooth kernel $h(\boldsymbol{x}, \bar{\boldsymbol{x}})$, such that ρ can inherit the smoothness characteristics of the kernel.

$$\bar{\rho}(\boldsymbol{x}) = \int_{\Omega} h(\boldsymbol{x}, \bar{\boldsymbol{x}})\rho(\bar{\boldsymbol{x}})\mathrm{d}\bar{\boldsymbol{x}}, \qquad \int_{\Omega} h(\boldsymbol{x}, \bar{\boldsymbol{x}})\mathrm{d}\bar{\boldsymbol{x}} = 1 \tag{6.105}$$

The discretization of projection in (6.105) can be expressed as:

$$\bar{\rho}_j = \sum_{\bar{i}=1}^{n_s} \psi(\rho_{\bar{i}})\rho_{\bar{i}} = \frac{\sum_{\bar{i}=1}^{n_s} w(r_{\bar{i}})\rho_{\bar{i}}}{\sum_{\hat{i}=1}^{n_s} w(r_{\hat{i}})} \tag{6.106}$$

and the weight function $w(r)$ can be defined as a compactly supported radial basis functions (RBFs) with the higher-order continuity and the non-negativity [226],

$$w(r) = (1-r)_+^6 \cdot (35r^2 + 18r + 3), \qquad r = d/r_{min} \tag{6.107}$$

where the symbol $(1-r)_+ = \max(0, 1-\mathrm{r})$. d is the Euclidean distances between the current nodal density and the neighborhood nodal density lying within the local support domain, and r_{min} means the specified radius of the local support domain.

A smoothed Heaviside projection is used to map the intermediate density to 1 or 0 by a prescribed threshold value, and it's defined as:

$$\tilde{\rho} = \frac{\tanh(\beta\rho_0) + \tanh(\beta(\bar{\rho} - \rho_0))}{\tanh(\beta\rho_0) + \tanh(\beta(1-\rho_0))} \tag{6.108}$$

where β controls the sharpness of the projection, and ρ_0 is the threshold value.

6.5.4 Sensitivity analysis

The adjoint method is employed to derive the sensitivity of electromechanical coupling factor with respect to local densities $\tilde{\rho}$.

$$\frac{\mathrm{dJ}}{\mathrm{d}\tilde{\rho}} = \frac{1}{\Pi_e^2}\left(\frac{\mathrm{d}\Pi_\mathrm{m}}{\mathrm{d}\tilde{\rho}}\Pi_e - \Pi_m\frac{\mathrm{d}\Pi_\mathrm{e}}{\mathrm{d}\tilde{\rho}}\right) \tag{6.109}$$

We construct the Lagrangian equations for mechanical and electric energy, respectively as:

$$\Pi_m = \Pi_m - \boldsymbol{\lambda}^T\widehat{\mathbf{R}} \tag{6.110}$$

$$\Pi_e = \Pi_e - \boldsymbol{\mu}^T\widehat{\mathbf{R}} \tag{6.111}$$

As the residual vector $\widehat{\mathbf{R}} = 0$ holds, the adjoint vectors $\boldsymbol{\lambda}$ and $\boldsymbol{\mu}$ are arbitrary vectors.

The derivatives of the Lagrangian equations with respect to density can be obtained as:

$$\begin{aligned}\frac{d\Pi_m}{d\tilde{\rho}} =& \frac{\partial\Pi_m}{\partial\tilde{\rho}} + \frac{\partial\Pi_m}{\partial\mathbf{Z}}\cdot\frac{\partial\mathbf{Z}}{\partial\tilde{\rho}} - \boldsymbol{\lambda}^T\left(\frac{\partial\widehat{\mathbf{R}}}{\partial\tilde{\rho}} + \frac{\partial\widehat{\mathbf{R}}}{\partial\theta}\cdot\frac{\partial\theta}{\partial\tilde{\rho}} + \frac{\partial\widehat{\mathbf{R}}}{\partial\mathbf{Z}}\cdot\frac{\partial\mathbf{Z}}{\partial\tilde{\rho}}\right)\\ =& -\boldsymbol{\lambda}^T\left(\frac{\partial\widehat{\mathbf{R}}}{\partial\tilde{\rho}} + \frac{\partial\widehat{\mathbf{R}}}{\partial\theta}\cdot\frac{\partial\theta}{\partial\tilde{\rho}}\right) + \left(\mathbf{f}^T - \boldsymbol{\lambda}^T\frac{\partial\widehat{\mathbf{R}}}{\partial\mathbf{Z}}\right)\frac{\partial\mathbf{Z}}{\partial\tilde{\rho}}\end{aligned} \tag{6.112}$$

$$\begin{aligned}\frac{d\Pi_e}{d\tilde{\rho}} =& \frac{\partial\Pi_e}{\partial\tilde{\rho}} + \frac{\partial\Pi_e}{\partial\mathbf{Z}}\cdot\frac{\partial\mathbf{Z}}{\partial\tilde{\rho}} - \boldsymbol{\mu}^T\left(\frac{\partial\widehat{\mathbf{R}}}{\partial\tilde{\rho}} + \frac{\partial\widehat{\mathbf{R}}}{\partial\theta}\cdot\frac{\partial\theta}{\partial\tilde{\rho}} + \frac{\partial\widehat{\mathbf{R}}}{\partial\mathbf{Z}}\cdot\frac{\partial\mathbf{Z}}{\partial\tilde{\rho}}\right)\\ =& \frac{1}{2}\boldsymbol{\phi}^T\frac{\partial\widehat{\mathbf{K}}_{\phi\phi}}{\partial\tilde{\rho}}\boldsymbol{\phi} - \boldsymbol{\mu}^T\left(\frac{\partial\widehat{\mathbf{R}}}{\partial\tilde{\rho}} + \frac{\partial\widehat{\mathbf{R}}}{\partial\theta}\cdot\frac{\partial\theta}{\partial\tilde{\rho}}\right)\\ &+ \left\{\left[\boldsymbol{\phi}^T\widehat{\mathbf{K}}_{\phi\phi},\ \frac{1}{2}\boldsymbol{\phi}^T\frac{\partial\widehat{\mathbf{K}}_{\phi\phi}(\mathbf{u})}{\partial\mathbf{u}}\boldsymbol{\phi}\right] - \boldsymbol{\mu}^T\frac{\partial\widehat{\mathbf{R}}}{\partial\mathbf{Z}}\right\}\frac{\partial\mathbf{Z}}{\partial\tilde{\rho}}\end{aligned} \tag{6.113}$$

where $\mathbf{Z} = [\boldsymbol{\phi};\mathbf{u}]$ and

$$\frac{\partial\widehat{\mathbf{R}}}{\partial\mathbf{Z}} = \begin{bmatrix}\widehat{\mathbf{K}}_{\phi\phi} & \widehat{\mathbf{K}}_{\phi u}\\ \widehat{\mathbf{K}}_{u\phi} & \widehat{\mathbf{K}}_{uu}\end{bmatrix} \tag{6.114}$$

$$\frac{\partial\widehat{\mathbf{R}}}{\partial\theta} = \begin{bmatrix}\mathbf{K}_{\phi u}^{NL,\theta} - \mathbf{K}_{\phi u}^{L,\theta}\\ \mathbf{K}_{uu}^{NL,\theta} - \mathbf{K}_{uu}^{L,\theta}\end{bmatrix}\mathbf{u} \tag{6.115}$$

The adjoint vectors can be calculated by the following adjoint equations, in order to eliminate the implicit term $\frac{\partial\mathbf{Z}}{\partial\tilde{\rho}}$ in (6.112) and (6.113):

$$\boldsymbol{\lambda}^T\frac{\partial\widehat{\mathbf{R}}}{\partial\mathbf{Z}} = \mathbf{f}^T \tag{6.116}$$

$$\boldsymbol{\mu}^T\frac{\partial\widehat{\mathbf{R}}}{\partial\mathbf{Z}} = \left[\boldsymbol{\phi}^T\widehat{\mathbf{K}}_{\phi\phi},\ \frac{1}{2}\boldsymbol{\phi}^T\frac{\partial\mathbf{K}_{\phi\phi}^{NL,\theta}(\mathbf{u})}{\partial\mathbf{u}}\boldsymbol{\phi}\right] \tag{6.117}$$

where

$$\frac{\partial\mathbf{K}_{\phi\phi}^{NL,\theta}(\mathbf{u})}{\partial\mathbf{u}} = \int_{\Omega_0} B_\phi^T\frac{\partial^2(-\tilde{D}_i^{NL,\theta})}{\partial(\nabla_j\phi)\partial u_k}B_\phi\,\mathrm{d}\Omega_0 \tag{6.118}$$

and

$$\frac{\partial^2(-\tilde{D}_i^{NL,\theta})}{\partial(\nabla_j\phi)\partial u_k} = J\varepsilon\theta(C_{ij}^{-1}F_{lk}^{-1} - F_{ik}^{-1}C_{jl}^{-1} - C_{il}^{-1}F_{jk}^{-1})\nabla_l \tag{6.119}$$

6.6 Numerical examples

6.6.1 Bending cantilever beam

In this first example, we consider a cantilever beam subjected to bending deformation, as shown in Fig. 6.2. The left end is fixed and the bottom is grounded, while the force is imposed on the top-right point. The dimension of the beam is $h_1 \times L_1 = 0.2\mu\text{m} \times 0.8\mu\text{m}$. The material of the beam is polyvinylidene fluoride (PVDF), which is a widely studied polymer in soft dielectrics and nonlinear flexoelectricity [81, 88, 111, 170]. Its parameters are [81]: Young's modulus $E = 3.7$ GPa, Poisson's ratio $\nu = 0.3$, dielectric permittivity $\varepsilon = 9.2\varepsilon_0$, flexoelectric coefficient $f = 179$ V. Here, the couple strain constant is taken as $g = 4 \times 10^{-6}$ N. The vacuum electric permittivity is $\varepsilon_0 = 8.854 \times 10^{-12}$ F/m. The isotropic material assumption is taken account. The IGA discretization for beam is 124×31 control points. The variation of electromechanical coupling factors (ECFs) for bending cantilever beam with respect to the mesh refinement is analyzed in Fig. 6.3. We can note a tendency to convergence, even though this one is quite slow, in view of the low difference between the initial and final values.

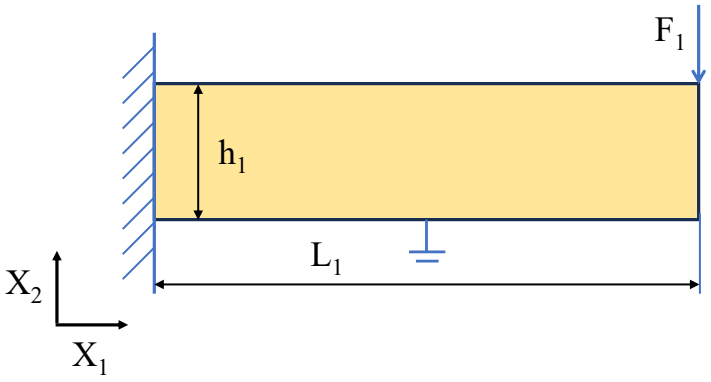

Figure 6.2: Bending beam-like soft dielectrics with open circuit boundary conditions: design domain

The topology optimization of the cantilever beam is performed under the force magnitudes F_1=-0.1 N, F_1=-1 N, F_1=-2 N, F_1=-2.5 N and F_1=-3 N, respectively. The volume fraction constraint, defined as the quantity of material as compared to the design domain volume $h_1 \times L_1$ is set as v_f =0.6 for all load cases. The parameters of Heaviside projection function (6.76) in energy remedy formulation are chosen as $\alpha = 0.1$ and $\beta_1 = 500$. The compliance constraint in (6.102) is set as $\hat{C}^{max} = 4\overline{\Pi}_1$, where $\overline{\Pi}_1$ is the strain energy of the undesigned flexoelectric beam, i.e. the beam with all the relative densities $\rho = 1$. For comparison, a guess design consisting into a rectangular beam with 4 holes as depicted in Fig. 6.4(a) is analyzed. The holes radii are $R = 0.3568h_1$ corresponding to a volume fraction equal to 0.6. This structure will serve as a reference to be compared with the optimized designs. The penalty exponents used in the TO numerical procedure (see Eqs. (6.68)-(6.69)) are chosen here as $p_c = p_f = 3$.

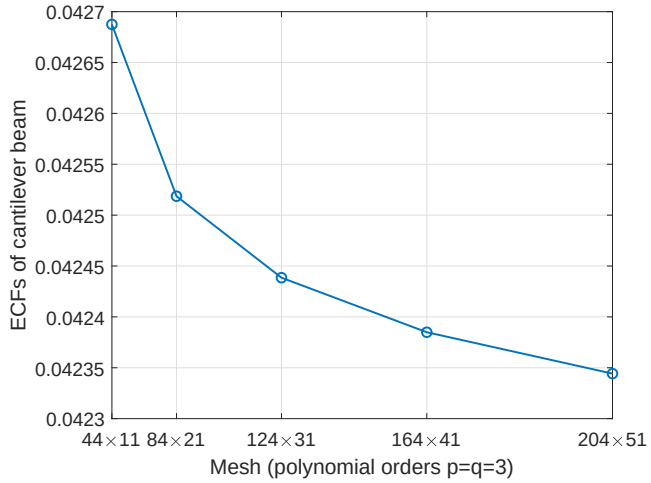

Figure 6.3: Electromechanical coupling factors (ECFs) for bending cantilever beam with respect to the mesh refinement

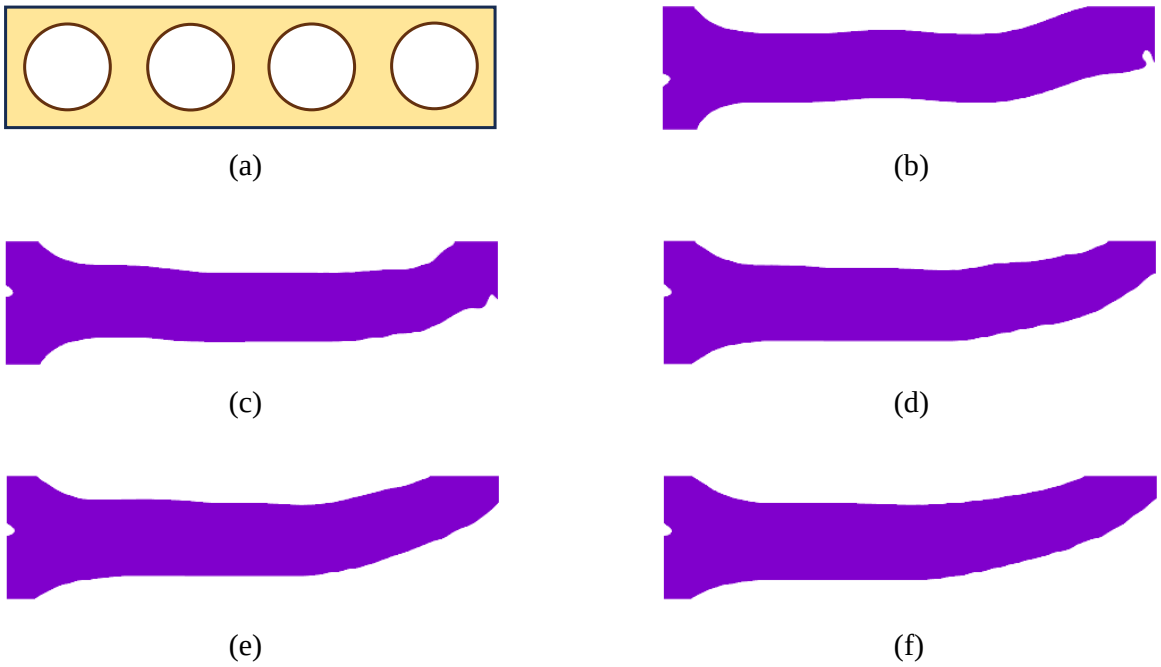

Figure 6.4: Reference structure and optimized designs for beam-like soft dielectrics by different loads, with beam size $h_1 \times L_1 = 0.2\mu\text{m} \times 0.8\mu\text{m}$: (a) reference structure; (b) optimal design by load $F_1 = -0.1$ N; (c) optimal design by load $F_1 = -1$ N; (d) optimal design by load $F_1 = -2$ N; (e) optimal design by load $F_1 = -2.5$ N; (f) optimal design by load $F_1 = -3$ N

We carry out the optimization of the cantilever beam, where the initialization of the densities is performed by setting them uniformly to $\rho_i = 0.6$, $(i = 1, ..., N_{cp})$ in the rectangular design domain defined in Fig. 6.2. N_{cp} denotes the number of control points in IGA. At the initial optimization stage, the uniform structural densities lead to a significant deterioration in the overall mechanical behavior of the material, making it prone to excessive deformation or rendering it incapable of optimization as the force increases. To address this issue, a heuristic continuation scheme is implemented on the mechanical penalty factor p_c. In this study, the updating scheme

for the mechanical penalty factor p_c is set as $p_c = \min(p_c + \Delta p, 3)$ every 3 steps after the iteration surpasses 10, with $\Delta p = 0.1$ and initial $p_c = 1$. The final optimized geometries, obtained respectively for the force magnitudes F_1=-0.1 N, F_1=-1 N, F_1=-2 N, F_1=-2.5 N and F_1=-3 N, are depicted in Fig. 6.4. Observing the topology figures, we can see that there is no hole feature in the optimal structures, and their material distribution is more concentrated, resembling the characteristics of shape optimization. Different initializations have been tested: uniform densities and circular voids. Both finally converged to the same topology. The optimization process of electromechanical coupling factors (ECFs) for different forces is given in Fig. 6.5. All the iteration curves present that the optimization process is stable. The corresponding electromechanical coupling factors (ECFs) are listed in Table 6.1. The ECFs of the optimized structures for forces F_1=-0.1 N, F_1=-1 N, F_1=-2 N, F_1=-2.5 N and F_1=-3 N increase by factors of 9.2638, 9.4201, 9.1106, 8.9157 and 8.7066 times, respectively, as compared to the reference design in Fig. 6.4(a). It can be seen that the optimal electromechanical coupling factors first increase and subsequently decrease as the external forces applied for optimization escalate.

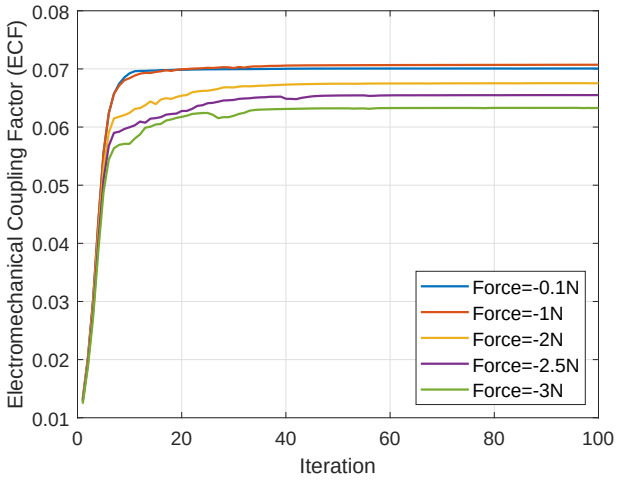

Figure 6.5: Iteration process of Electromechanical coupling factors (ECF) for bending beam-like soft dielectrics under different loads

Table 6.1: Electromechanical coupling factors (ECF) of optimal designs for flexoelectric nano beam under different loads

Force	ECF (optimized)	ECF (reference)	Gain: ECF_{opt}/ECF_{ref}
-0.1 N	0.07007	6.8272×10^{-3}	10.2638
-1 N	0.07072	6.7865×10^{-3}	10.4201
-2 N	0.06754	6.6801×10^{-3}	10.1106
-2.5 N	0.06550	6.6056×10^{-3}	9.9157
-3 N	0.06329	6.5200×10^{-3}	9.7066

The distribution of electric potentials and deformed configurations for optimal structures under different forces is illustrated in Fig. 6.6. We can intuitively see that the optimized structure produces very large deformations under the increased loads. Notably, the potential in the upper left part of the beam is more pronounced. Furthermore, it is evident that the magnitudes of the distributed electric potentials increase with the escalating applied forces.

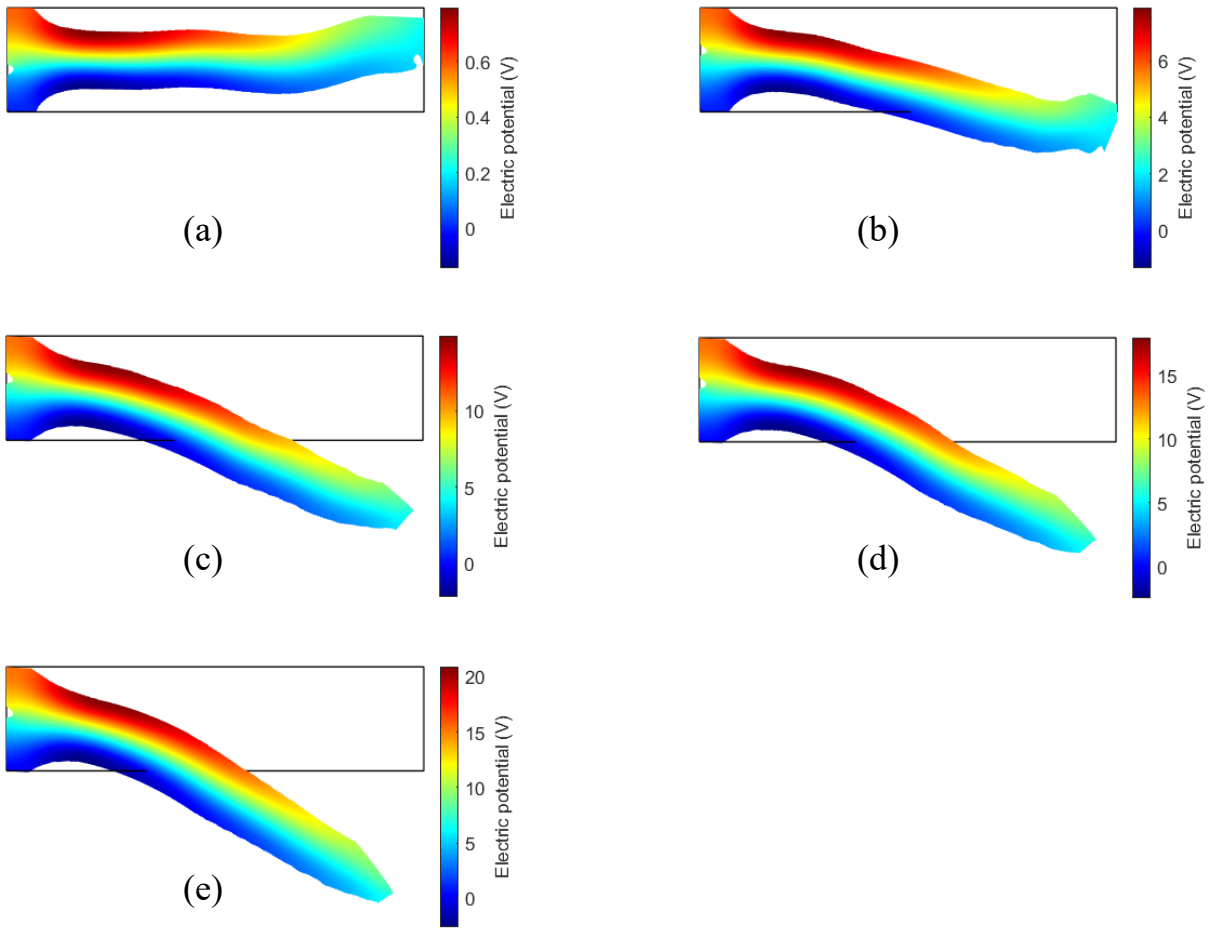

Figure 6.6: Distribution of electric potentials and deformed configuration for optimal structures of flexoelectric nano beam under different forces, with beam size $h_1 \times L_1 = 0.2\mu\text{m} \times 0.8\mu\text{m}$: (a) optimal design by load $F_1 = -0.1\text{N}$; (b) optimal design by load $F_1 = -1$ N; (c) optimal design by load $F_1 = -2$ N; (d) optimal design by load $F_1 = -2.5$ N; (e) optimal design by load $F_1 = -3$ N

(a) (b)

Figure 6.7: Optimal designs of flexoelectric nano beam with size $h_1 \times L_1 = 1\mu\text{m} \times 4\mu\text{m}$, optimized by different loads: (a) optimal design by load $F_1 = -3$ N; (c) optimal design by load $F_1 = -5$ N

The influence of size effect on the topology optimization of nonlinear soft dielectrics under large deformation is also examined in the context of a flexoelectric cantilever beam. We perform the optimization for the flexoelectric beam under the same boundary conditions, but the dimension of the beam is changed as $h_1 \times L_1 = 1\mu\text{m} \times 4\mu\text{m}$. The optimal designs achieved by forces $F_1 = -3$ N and $F_1 = -5$ N are depicted in Fig. 6.7. There are some holes in the optimal topology, and they present a significant geometric difference from the optimal structures of beam with size $h_1 \times L_1 = 0.2\mu\text{m} \times 0.8\mu\text{m}$. The electromechanical coupling factors (ECFs) of optimal structures by the forces $F_1 = -3$ N and $F_1 = -5$ N are obtained as 0.04641 and 0.04887, respectively. Compared to the previously mentioned smaller-sized beam, the ECFs are smaller for this larger-sized beam, which shows size effect of the optimization for flexoelectric energy harvesters.

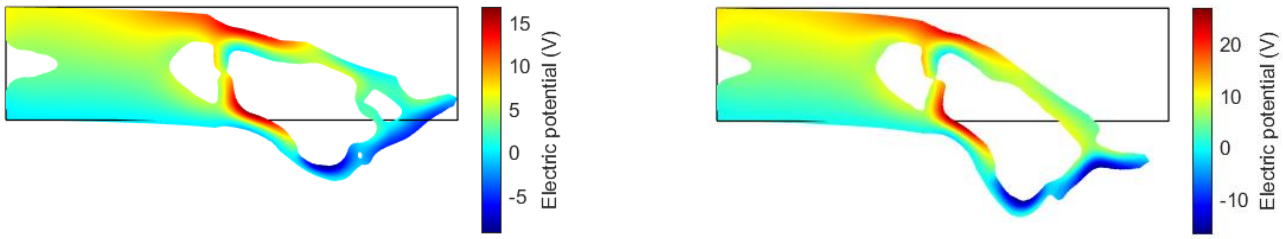

(a) (b)

Figure 6.8: Distribution of electric potentials and deformed configuration for optimal structures of flexoelectric nano beam with dimension $h_1 \times L_1 = 1\mu\text{m} \times 4\mu\text{m}$, under different forces: (a) optimal design by load $F_1 = -3$ N; (c) optimal design by load $F_1 = -5$ N

The distribution of electric potentials and deformed configuration for optimal structures of beam with size $h_1 \times L_1 = 1\mu\text{m} \times 4\mu\text{m}$ is illustrated in Fig. 6.8. We observe that the magnitudes of electric potential for both sizes of beams are similar when the imposed loads are the same. A beam with a smaller size can produce deformations that are significantly larger in magnitude compared to the structural dimensions. The size effect in continuum mechanics imparts increased stiffness to structures at the micro scale to some extent. However, in flexoelectricity, the size effect plays a beneficial role in enhancing the electromechanical response. Striking a balance between both the effects is essential for optimal performance. Soft materials capable of large deformations can serve as a bridge in achieving this equilibrium. Larger deformations contribute to the enhancement of electromechanical coupling factors. Consequently, the improvement in electromechanical coupling factors for optimized structures stems from the interplay of size effects and large deformations.

6.6.2 Bending double-clamped beam

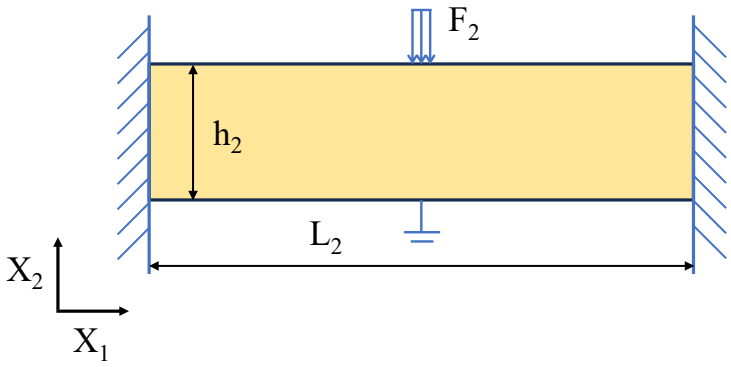

Figure 6.9: Bending double-clamped beam-like soft dielectrics with open circuit boundary conditions: design domain

In this example, the double-clamped beam undergoing bending deformation is investigated, as illustrated in Fig. 6.9. The size of beam is $h_2 \times L_2 = 2\mu\text{m} \times 8\mu\text{m}$. Both the ends are fixed, the load is imposed in the middle three points while the bottom surface is connected to the ground. The material is same as the previous example, i.e. PVDF. The volume fraction constraint is here set as $f_2 = 0.6$. The compliance constraint in (6.102) is set as $\hat{C}^{max} = 4\overline{\Pi}_2$, where $\overline{\Pi}_2$ is the strain energy of the double-clamped beam design domain with all $\rho = 1$. The parameters for energy remedy formulation are set as $\alpha = 0.2$ and $\beta_1 = 500$. It is worthwhile noted that an increase in α to 0.2 enhances the load-carrying capacity of control points characterized by weak densities, thereby enabling optimization under larger deformations without excessive distortion. A reference guess design is outlined in Fig. 6.10(a), comprising a double-clamped beam with four circular voids each having a radius $R = 0.3568h_2$, equivalent to a volume fraction of 0.6. The penalty exponents for the SDF interpolation scheme in Eqs. (6.68)-(6.69) are also chosen as $p_c = p_f = 3$.

Table 6.2: Electromechanical coupling factors (ECF) of optimal designs for flexoelectric double-clamped beam under different loads

Force	ECF (optimized)	ECF (reference)	Gain: $\text{ECF}_{opt}/\text{ECF}_{ref}$
-1 N	0.02420	0.01441	1.6806
-10 N	0.02820	0.01367	2.0630
-20 N	0.03278	0.01220	2.6878
-25 N	0.03325	0.01146	2.9005
-30 N	0.03290	0.01079	3.0496
-35 N	0.03274	0.01018	3.2166

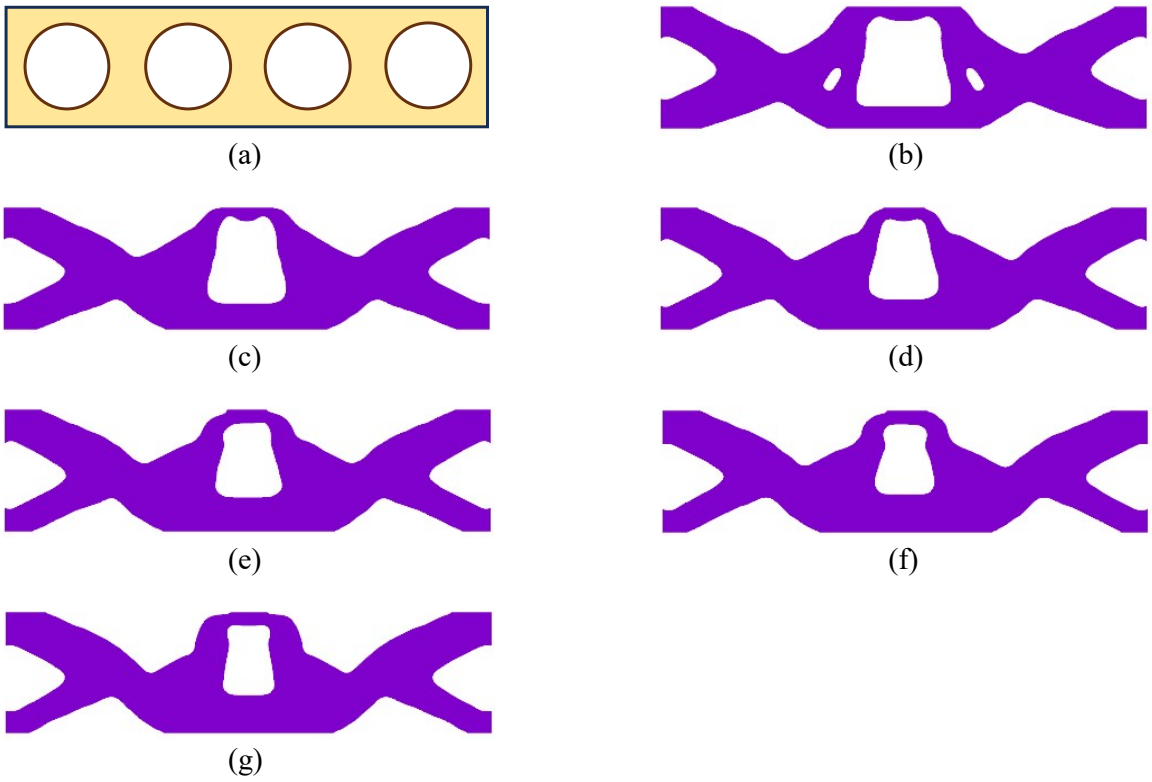

Figure 6.10: Reference structure and optimized designs for flexoelectric double-clamped beam under different forces: (a) reference structure; (b) optimal design by load $F_2 = -1$ N; (c) optimal design by load $F_2 = -10$ N; (d) optimal design by load $F_2 = -20$ N; (e) optimal design by load $F_2 = -25$ N; (f) optimal design by load $F_2 = -30$ N; (g) optimal design by load $F_2 = -35$ N

We perform the topology optimization of the double-clamped beam under the forces F_2=-1 N, F_2=-10 N, F_2=-20 N, F_2=-25 N, F_2=-30 N and F_2=-35 N, respectively. As an initial step in the optimization algorithm, the design variables are uniformly assigned values of $\rho_i = 0.6$ $(i = 1,...,N_{cp})$. The same continuation scheme of the mechanical penalty factor p_c is utilized. The final optimal designs obtained by the forces F_2=-1 N, F_1=-10 N, F_2=-20 N, F_2=-25 N, F_2=-30 N and F_2=-35 N, respectively, are presented in Fig. 6.10. We can observe the variation of topology, where the holes in the optimal designs decreases in size, and the rods at the bottom-left and right become thinner as the force increases. The electromechanical coupling factors (ECFs) of optimal structures under different forces are presented in Table. 6.2. Notably, the ECFs of the reference structure in Fig. 6.10(a) increase with the increase of force magnitude. Specifically, for the forces F_2=-1 N, F_2=-10 N, F_2=-20 N, F_2=-25 N, F_2=-30 N, and F_2=-35 N, the ECFs improve by factors of 0.6806 1.0630, 1.6878, 1.9005, 2.0496, and 2.2166, respectively, compared to the reference design. The gain in ECFs raises with the increase in force.

We also illustrate the distribution of electric potentials and deformed configuration for optimal structures of flexoelectric double-clamped beam obtained by different forces in Fig. 6.11. We can see that the local large deformation or strain occurs, due to the concentration force imposed on the top-mid area. The localized nature of the strain typically gives rise to substantial deformations and significant strain gradients occurring within the specific region. It also results in the concentrated distribution of large electric potentials. Similarly, an increase in the force applied on optimization will elevate the amplitude of the distributed electric potentials.

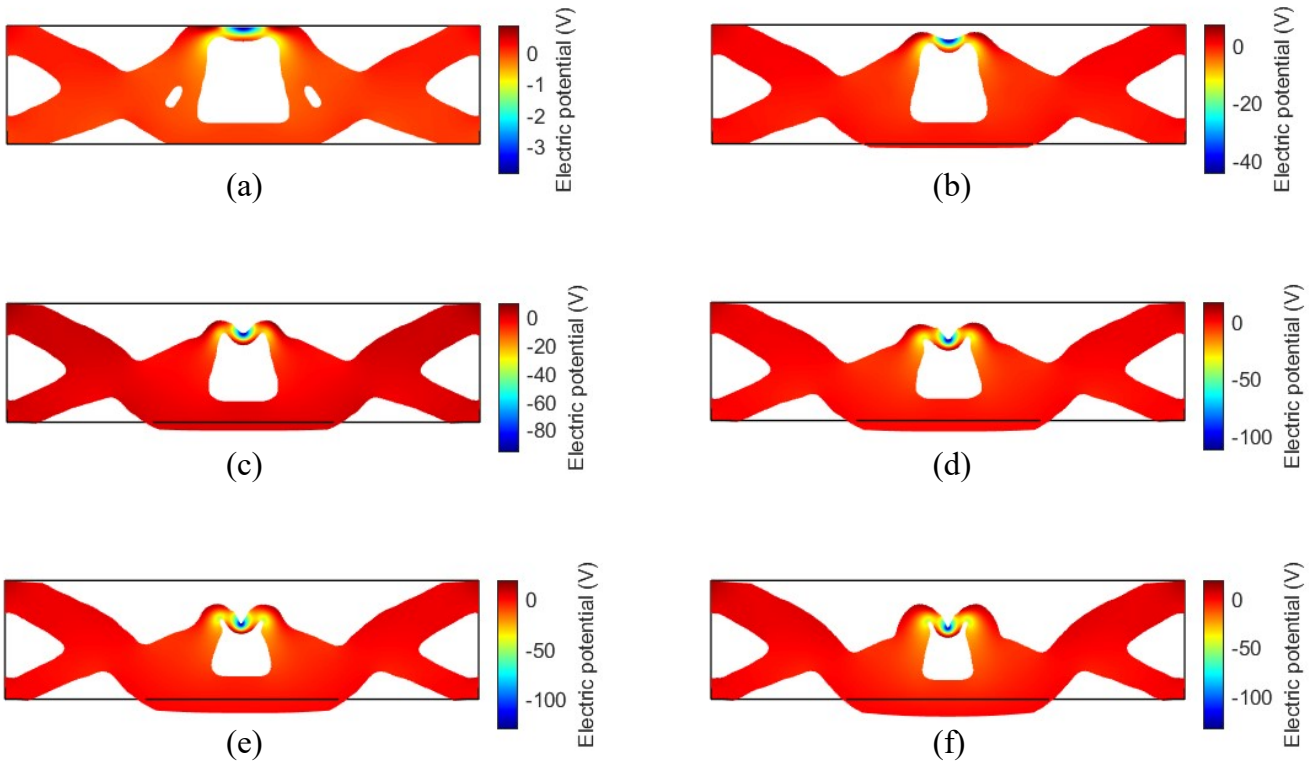

Figure 6.11: Distribution of electric potentials and deformed configuration for optimal structures of flexoelectric double-clamped beam under different forces: (a) optimal design by load $F_2 = -1$ N; (b) optimal design by load $F_2 = -10$ N; (c) optimal design by load $F_2 = -20$ N; (d) optimal design by load $F_2 = -25$ N; (e) optimal design by load $F_2 = -30$ N; (f) optimal design by load $F_2 = -35$ N

To further investigate the mechanism behind the improvement in the electromechanical coupling factors (ECFs) of the flexoelectric double-clamped beam, we depict the variation of ECFs for the optimized structures in relation to the volume fraction. This analysis is conducted for the case of the force $F_2 = -10$ N, as shown in Fig. 6.12, where the topology configuration, distribution of electric potentials and deformations are illustrated. We observe an increase in the ECFs for the optimized structures of the flexoelectric double-clamped beam as the volume fraction rises. Significant local deformation and electric potential are concentrated near the load sites. When the volume fraction is minimal, the support configuration near the loading site on the optimized structure takes on a triangular shape, leading to challenges in generating large deformations at that specific site. As the volume fraction increases, the hole of support structure adjacent to the loading site approximates a polygonal shape (quadrilateral or hexagonal), facilitating the generation of substantial local deformations.

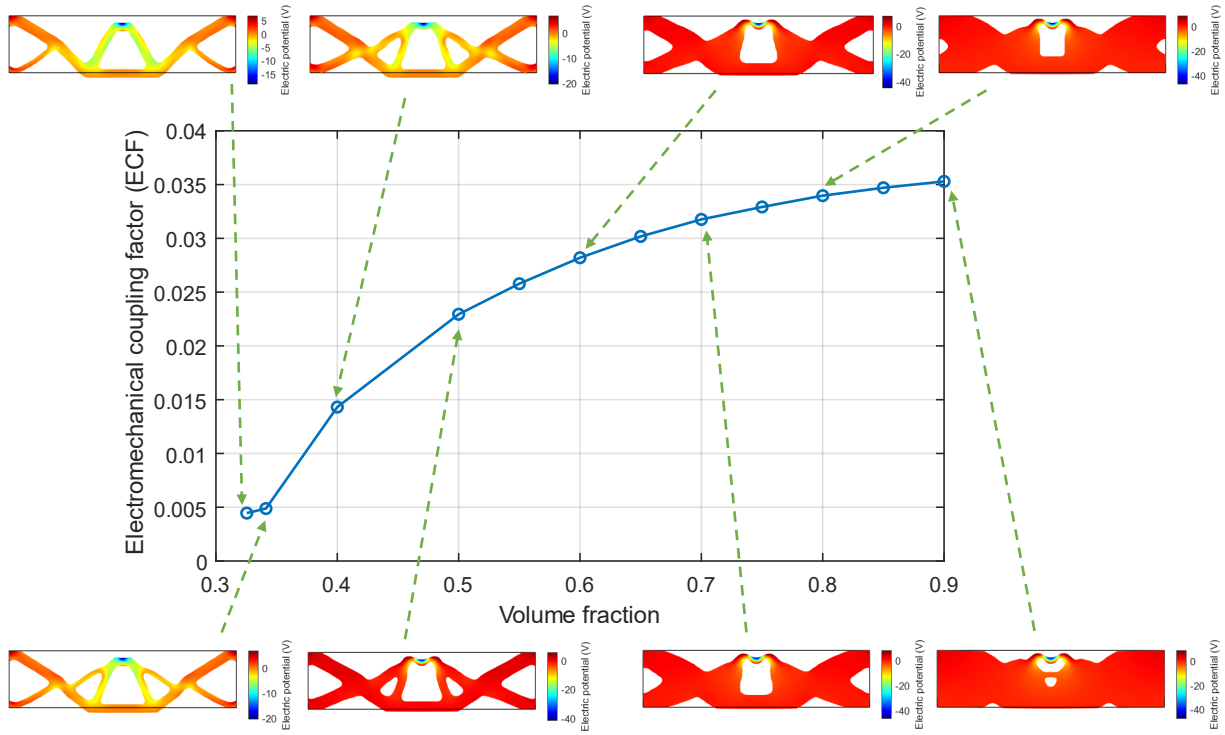

Figure 6.12: Electromechanical coupling factors for optimized structures of flexoelectric double-clamped beam with respect to the volume fraction, and the force $F_2 = -10$ N

6.6.3 Compressed truncated pyramid

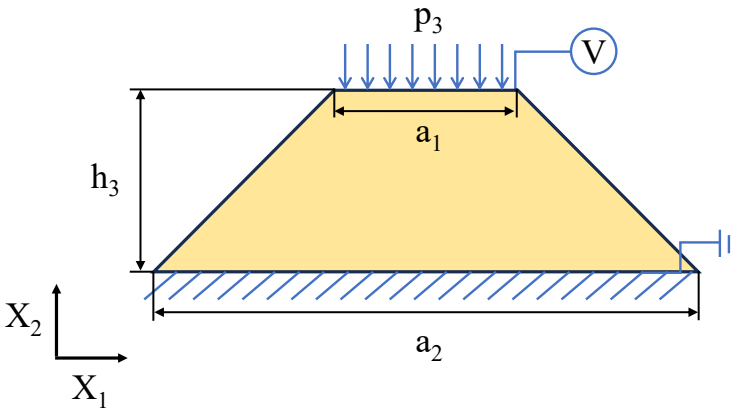

Figure 6.13: Compressed truncated pyramid-like soft dielectrics with open circuit boundary conditions: design domain

In this example, we consider the design of a truncated pyramid-like soft dielectrics, as shown in Fig. 6.13. This particular shape is frequently selected in flexoelectric systems to induce strain

gradient in compression [93]. The size of the truncated pyramid is $h_1 = 2\mu$m, $a_1 = 2\mu$m and $a_2 = 6\mu$m. A spatially uniform pressure is applied on the top surface along the X_2-direction and the displacement DOFs on the bottom surface are fixed. The material parameters of PVDF are also employed here. The volume fraction constraint is set as $f_3 = 0.7$. The compliance constraint defined in (6.102) is here chosen as $\hat{C}^{max} = 3\overline{\Pi}_3$, where $\overline{\Pi}_3$ is the strain energy of the truncated pyramid design domain with all $\rho = 1$. The parameters for energy remedy formulation in (6.70) are set as $\alpha = 0.2$ and $\beta_1 = 500$. A reference guess design is depicted in Fig. 6.13(a), representing a truncated pyramid with semi-circular voids on the bottom surface, with a radius $R = 0.6180h_3$, corresponding to a volume fraction of 0.7. The penalty exponents for the SDF interpolation scheme in Eqs. (6.68)-(6.69) are set as $p_c = p_f = 3$.

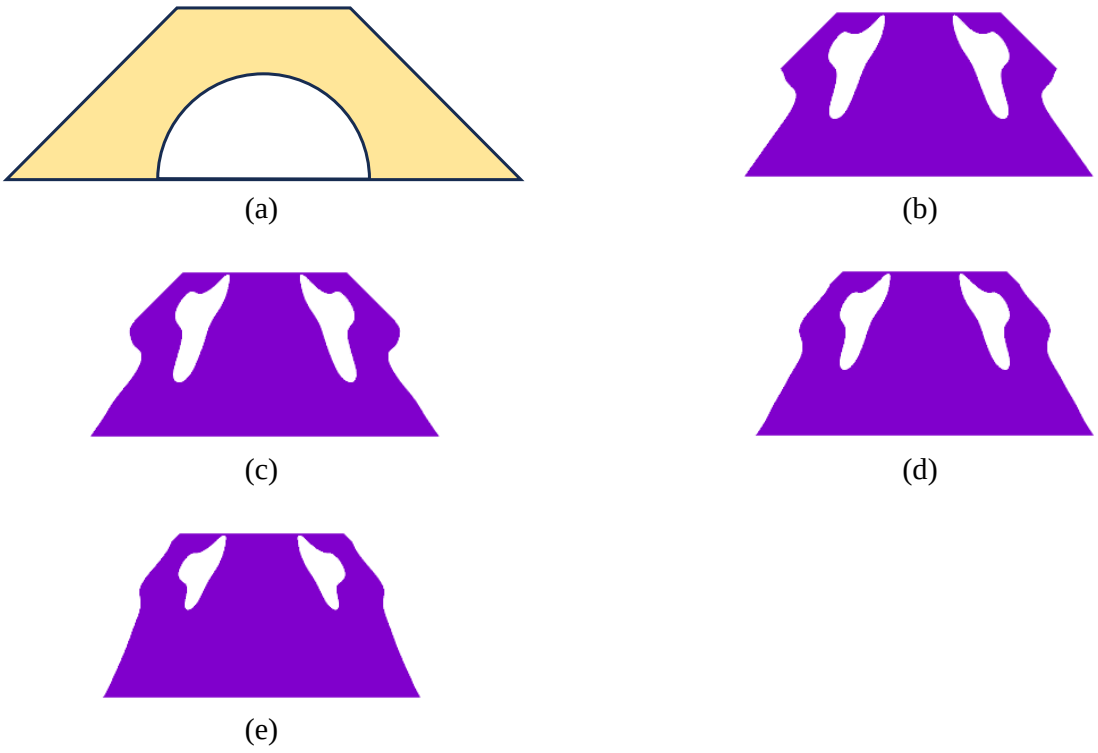

Figure 6.14: Reference structure and optimized designs for truncated pyramid obtained by different loads: (a) reference structure; (b) optimal design by load $p_3 = -0.5$N; (c) optimal design by load $p_3 = -1$N; (d) optimal design by load $p_3 = -2$N; (e) optimal design by load $p_3 = -2.5$N

We perform the topology optimization of the truncated pyramid-like soft dielectrics under the forces F_3=-0.5 N, F_3=-1 N, F_3=-2 N and F_3=-2.5 N, respectively. As an initial step in the optimization algorithm, the design variables are uniformly assigned values of $\rho_i = 0.7$ $(i = 1,...,N_{cp})$. The same continuation scheme of the mechanical penalty factor p_c is also utilized here. The final optimal designs obtained by the forces F_3=-0.5 N, F_3=-1 N, F_3=-2 N and F_3=-2.5 N, respectively, are presented in Fig. 6.14. It is observed that the height and area of the holes in the optimal designs decreases as the force increases. The electromechanical coupling factors (ECFs) of optimal structures under different forces are summarized in Table. 6.3. In this example, the ECFs of the reference structure in Fig. 6.14(a) decrease when the magnitude of the force increases. The ECFs of the optimized structures increase by factors of 6.3446, 6.0646, 6.1426 and 4.7234 for the forces F_3=-0.5 N, F_3=-1 N, F_3=-2 N and F_3=-2.5 N, respectively, compared to the reference design.

We notice that in some situations (beam problem, Table 6.1, and truncated pyramid, Table

6.3), the gain increases then decreases in Table 6.1 and decreases in Table 6.3 as the magnitude of the force increases, while we observe an opposite trend for the double-clamped beam problem (Table 6.2).

Table 6.3: Electromechanical coupling factors (ECF) of optimal designs for flexoelectric truncated pyramid under different loads

Force	ECF (optimized)	ECF (reference)	Gain: $\mathrm{ECF}_{opt}/\mathrm{ECF}_{ref}$
-0.5 N	0.01877	2.5551×10^{-3}	7.3446
-1 N	0.01970	2.7881×10^{-3}	7.0646
-2 N	0.02108	3.4313×10^{-3}	6.1426
-2.5 N	0.02242	3.9178×10^{-3}	5.7234

The distribution of electric potentials and deformed configuration for optimal structures of flexoelectric truncated pyramid achieved by different forces are presented in Fig. 6.15. It is evident that localized large deformations occurring on the top surface of the holes leads to a concentrated distribution of large electric potentials. An increase in the force applied during optimization will amplify the amplitude of the distributed electric potentials.

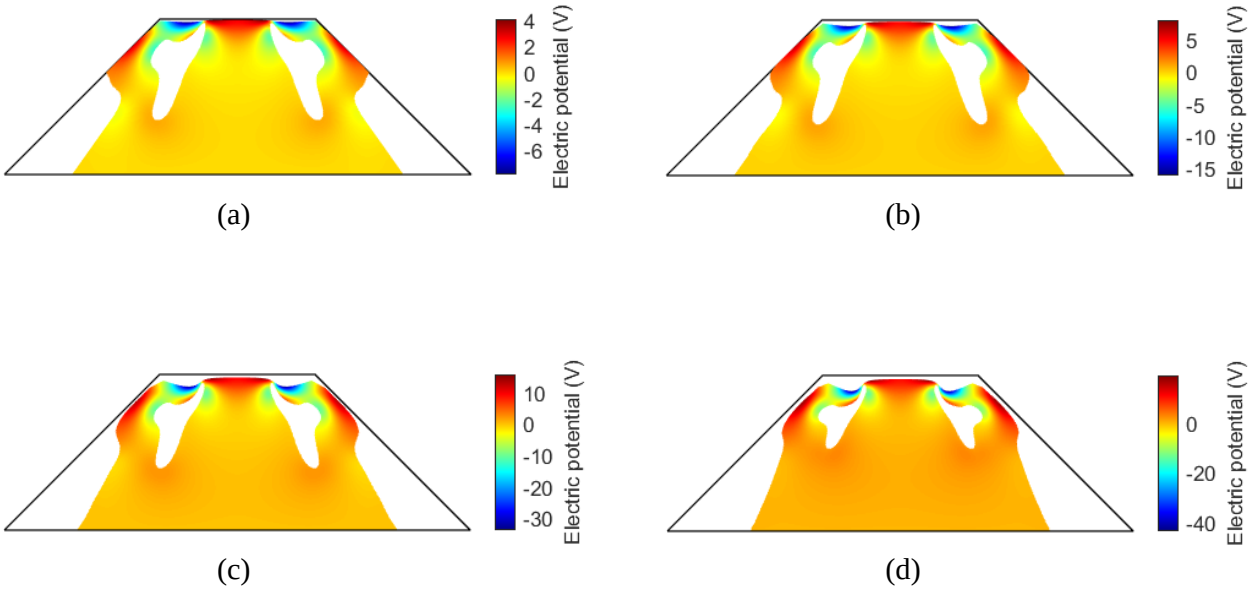

Figure 6.15: Distribution of electric potentials and deformed configuration for optimal structures of truncated pyramid under different forces: (a) optimal design by pressure $p_3 = -0.5$N; (b) optimal design by pressure $p_3 = -1$N; (c) optimal design by pressure $p_3 = -2$N; (d) optimal design by pressure $p_3 = -2.5$N

6.7 Conclusion

In this study, we proposed a nonlinear topology optimization framework for flexoelectric soft dielectrics undergoing large deformation. We start by deriving a numerical framework for non-

linear dielectrics at finite strain, ensuring C^1-continuity for flexoelectric fourth-order partial differential equations using Isogeometric analysis (IGA). We outlined the procedure for consistent linearizations and IGA discretizations. At the topology optimization stage, we formulate an innovative and efficient Strain Density Function (SDF) interpolation scheme. In this scheme, the electromechanical and hyper-elastic SDFs are interpolated based on the SIMP model, while a linear density interpolation model is employed for the dielectric component. The mechanical stiffness penalization is sufficient to guarantee the convergence of the final topology to 1 or 0.

Throughout our numerical analysis, we showcased the good performance of the proposed Strain Density Function (SDF) interpolation scheme in nonlinear electromechanical optimization scenarios. We extend an energy remedy scheme [222] for void regions, to the optimization of soft dielectrics, preventing distortion deformations in low-stiffness elements. Additionally, optimization solely based on the electromechanical coupling factor objective may lead to the formation of disconnected structures due to the oversight of mechanical stiffness considerations. To ensure the generation of physically viable optimal structures, we introduce a compliance constraint to regulate mechanical stiffness, preventing the occurrence of disconnected domains. Finally, the electromechanical coupling factors (ECFs) of the optimized structures in all the aforementioned cases exhibit improvements up to 9 times compared to the reference guess designs.

The influence of large deformations on the optimization of flexoelectric soft materials has been demonstrated, as well as their effects on the gains obtained. Size effects have also been shown in this context. The topology optimization framework we have proposed for nonlinear flexoelectric soft materials takes full advantage of large deformations, resulting in a significant improvement in the electromechanical coupling factors in the optimized structures. The electromechanical coupling factors (ECF) of optimized structures in all the above cases show improvements of up to 9 times over those of reference designs. It has been shown that in some situations, non-linear effects, i.e. the magnitude of the prescribed load, can increase the gains in electromechanical coupling factors, while they can reduce them in other cases. Proposing a framework for generally improving ECFs as a function of applied forces is an interesting avenue to explore in future studies.

Conclusion and Perspectives

Contributions and conclusion

In this thesis, several developments have been made for the modeling and design of energy harvesting systems based on flexoelectric materials. The main contributions are summarized as follows:

In Chapter 2, we have proposed a computational homogenization framework for composites composed of piezoelectric phases with apparent flexoelectric behavior. The effective model takes into account direct and converse flexoelectric effects, as well as all other higher-order electromechanical coupling terms related to electricity and the electrical gradient. In contrast to previous work, the present framework allows the evaluation of direct anisotropic flexoelectric tensors associated with electric fields and electric gradients. We show that the apparent converse flexoelectric coefficients in a composite of periodic triangular inclusions are of the same order of magnitude as the direct flexoelectric coefficients. We have shown that a significant improvement in flexoelectric effects can be achieved by appropriate selection of inclusion shapes and orientations. In addition, we have indicated that other higher-order coupling terms, i.e. those linking the electric field to an applied electric field gradient and the deformation (bending) gradient to the electric field, have non-negligible values compared to the flexoelectric coefficients and can contribute significantly to the electromechanical response of composites electromechanical composites.

In Chapter 3, we have developed a C^1-continuous isogeometric analysis (IGA) framework with one or more patches for the dynamic frequency response of flexoelectric structures with complex geometries. The inertial effect of deformation gradients was taken into account in the isogeometric analysis. The IGA method was used to satisfy the C^1 continuity requirement of the approximate displacement field for the fourth-order PDE. Next, the flexoelectric dynamic response with the inertial effect of the deformation gradient was solved under open and closed circuit conditions. Multi-patch constructions for complex geometries in isogeometric analysis are at most C^0-continuity between common patch boundaries. By ensuring that the graph surfaces corresponding to the isogeometric functions have the same order of geometric smoothness, the C^1 continuity of the isogeometric functions at the common boundary of the multiple patched has been ensured. The method of constructing the C^1 continuous multi-patch structure has then been validated. Finally, the sensitivity of different parameters (e.g., load resistance, geometrical parameters, flexoelectric coefficients, and dynamic scaling effects) to the frequency response of the output voltage, power, and displacement of beam-like structures with complex geometrical features has been evaluated. The advantages of the C^1-continuous one/multi-patch isogeometric analysis framework for solving flexoelectric dynamic problems of complex structures has been demonstrated.

In Chapter 4, a topology optimization framework has been proposed to maximize the effective, direct and converse flexoelectric properties of composites composed of piezoelectric phases. The original contribution here is to combine computational homogenization for flexoelectric materials with topological optimization of microstructures. We have develop a homogenization method for estimating direct and converse flexoelectric properties from the local

phase distribution in a representative volume element (RVE), avoiding the need to optimize the whole structure. We show that in several cases (piezo-piezo, piezo-polymer and porous piezo-composites), the present topology optimization scheme increases direct and converse properties by up to 1-2 orders of magnitude compared with a "naive" design. We have highlighted various mechanisms for improving flexoelectric properties, and electromechanical coupling. Specifically, piezo-piezo composites (hard/hard) generated a better electromechanical response thanks to improved effective piezoelectric properties. On the other hand, piezo-polymer composites (hard/soft) generated a better electromechanical response thanks to an interplay between piezoelectric and polymer properties. The result is a better electromechanical response thanks to the interaction between electromechanical (piezoelectric) and electrical (dielectric) properties, improved electromechanical (piezoelectric) and electrical (dielectric) properties, and reduced mechanical compliance, resulting from local electric fields, a significant increase in local electric fields and deformation gradients along the hard/soft interface.

In Chapter 5, a multiscale topology optimization method for designing flexoelectric metamaterials made of non-piezoelectric materials and electromechanical energy harvesting systems has been proposed to efficiently convert mechanical vibrations into electrical energy. First, based on computational homogenization, we have developed a representative volume element (RVE) model for the flexoelectric microstructure made of non-piezoelectric materials, which enables the estimation of the effective flexoelectric tensor of microstructures containing arbitrarily shaped inclusion phases. The microstructures were optimized by topology optimization combined with homogenization, in order to maximize the effective flexoelectric properties of the materials. Periodic, porous, and non-piezoelectric flexoelectric metamaterials have been obtained. The flexoelectric metamaterials with optimal electromechanical coupling properties were used to model the behavior of a dynamic electromechanical energy harvesting system structure. Then, a second topology optimization step was performed at the structural scale, aiming to maximize the system Electromechanical Coupling Factor (ECF) for a given forced vibration frequency. We showed that the optimized structure obtained offers significant gains in terms of ECF (by factors up 20 times) compared with non-optimized structures of the same volume, over a wide bandwidth of excitation frequencies.

In Chapter 6, a nonlinear topology optimization framework for flexoelectric soft dielectrics at finite strain has been established. A numerical computational framework for nonlinear flexoelectric soft dielectrics under finite strain was firstly derived, and the linearization process of the nonlinear electromechanical coupled equilibrium equations as well as the IGA discretization approach were detailed. In the topology optimization stage, a novel and effective energy interpolation scheme was proposed. In this scheme, the electromechanical coupling and hyperelastic energy terms employ penalty interpolation based on the SIMP model, while the dielectric term is interpolated by linear density model. An energy remedy scheme is applied to void regions to eliminate the instability of nonlinear optimization, effectively preventing distortion deformations in low-stiffness elements. To ensure the design of physically viable optimal structures, we incorporated a compliance constraint to regulate mechanical stiffness, thereby avoiding the occurrence of disconnected domains. Our proposed topology optimization framework for nonlinear flexoelectric soft materials fully leverages the interplay between size effects and large deformation, thereby increasing the electromechanical coupling factors (ECFs) of the optimized structure up to 9 times.

Perspectives

To extend this dissertation, some research works could be developed:

1. In the present thesis, the multiscale topology optimization was performed sequentially, first optimizing the microstructure, then the macro structure. A concurrent approach, i.e.

performing the topology at both scales and allowing different local microstructures, could be investigated.

2. We established a topology optimization framework for the electromechanical coupling factors of flexoelectric structures under single-frequency excitation. However, the next step could be to consider the topology optimization of the electromechanical coupling factors of flexoelectric structures in a certain frequency domain, so as to design flexoelectric structures with wider bandwidth.

3. Finally, a dynamic analysis model for nonlinear flexoelectric structures could be proposed, as well as a nonlinear topology optimization framework for designing nonlinear flexoelectric structures under dynamic loads.

Bibliography

[1] Vullers R.J.M, Schaijk R.V, Visser H.J, Penders J, and Hoof C.V. Energy harvesting for autonomous wireless sensor networks. *IEEE Solid-State Circuits Magazine*, 2(2):29–38, 2010.

[2] Puccinelli D and Haenggi M. Wireless sensor networks: applications and challenges of ubiquitous sensing. *IEEE Circuits and Systems Magazine*, 5(3):19–31, 2005.

[3] Sun H, Yin M, Wei W, Li J, Wang H, and Jin X. Mems based energy harvesting for the internet of things: a survey. *Microsystem Technologies*, 24:2853–2869, 2018.

[4] Mateu L and Moll F. Review of energy harvesting techniques and applications for microelectronics. In *VLSI Circuits and Systems II*, volume 5837, pages 359–373. SPIE, 2005.

[5] Tan Y, Dong Y, and Wang X. Review of mems electromagnetic vibration energy harvester. *Journal of Microelectromechanical Systems*, 26(1):1–16, 2017.

[6] Tian W, Ling Z, Yu W, and Shi J. A review of mems scale piezoelectric energy harvester. *Applied Sciences*, 8(4):645, 2018.

[7] Paradiso J.A and Starner T. Energy scavenging for mobile and wireless electronics. *IEEE Pervasive Computing*, 4(1):18–27, 2005.

[8] Mitcheson P.D, Yeatman E.M, Rao G.K, Holmes A.S, and Green T.C. Energy harvesting from human and machine motion for wireless electronic devices. *Proceedings of the IEEE*, 96(9):1457–1486, 2008.

[9] Knight C, Davidson J, and Behrens S. Energy options for wireless sensor nodes. *Sensors*, 8(12):8037–8066, 2008.

[10] Elfrink R, Kamel T.M, Goedbloed M, Matova S, Hohlfeld D, Andel Y.V, and Schaijk R.V. Vibration energy harvesting with aluminum nitride-based piezoelectric devices. *Journal of Micromechanics and Microengineering*, 19(9):094005, aug 2009.

[11] Liu H, Tay C.J, Quan C, Kobayashi T, and Lee C. Piezoelectric mems energy harvester for low-frequency vibrations with wideband operation range and steadily increased output power. *Journal of Microelectromechanical Systems*, 20(5):1131–1142, 2011.

[12] Peano F and Tambosso T. Design and optimization of a mems electret-based capacitive energy scavenger. *Journal of Microelectromechanical Systems*, 14(3):429–435, 2005.

[13] Lo H and Tai Y-C. Parylene-based electret power generators. *Journal of Micromechanics and Microengineering*, 18(10):104006, 2008.

[14] Naifar S, Bradai S, Viehweger C, and Kanoun O. Survey of electromagnetic and magnetoelectric vibration energy harvesters for low frequency excitation. *Measurement*, 106:251–263, 2017.

[15] Deng Q, Kammoun M, Erturk A, and Sharma P. Nanoscale flexoelectric energy harvesting. *International Journal of Solids and Structures*, 51(18):3218–3225, 2014.

[16] Wang B, Gu Y, Zhang S, and Chen L.Q. Flexoelectricity in solids: Progress, challenges, and perspectives. *Progress in Materials Science*, 106:100570, 2019.

[17] Ma W and Cross L.E. Large flexoelectric polarization in ceramic lead magnesium niobate. *Applied Physics Letters*, 79(26):4420–4422, 2001.

[18] Ma W and Cross L.E. Strain-gradient induced electric polarization in lead zirconate titanate ceramics. *Applied Physics Letters*, 82(19):3923–3925, 2003.

[19] Zubko P, Catalan G, Buckley A, Welche P.R.L, and Scott J.F. Strain-gradient-induced polarization in srtio$_3$ single crystals. *Physical Review Letters*, 99:167601, Oct 2007.

[20] Cross L.E. Flexoelectric effects: Charge separation in insulating solids subjected to elastic strain gradients. *Journal of materials science*, 41:53–63, 2006.

[21] Bendsøe M.P. Optimal shape design as a material distribution problem. *Structural optimization*, 1(4):193–202, 1989.

[22] Rozvany G.I.N, Zhou M, and Birker T. Generalized shape optimization without homogenization. *Structural optimization*, 4(3-4):250–252, 1992.

[23] Bendsøe M.P and Sigmund O. Material interpolation schemes in topology optimization. *Archive of applied mechanics*, 69(9-10):635–654, 1999.

[24] Sharma N.N, Maranganti R, and Sharma P. On the possibility of piezoelectric nanocomposites without using piezoelectric materials. *Journal of the Mechanics and Physics of Solids*, 55(11):2328–2350, 2007.

[25] Fousek J, Cross L.E, and Litvin D.B. Possible piezoelectric composites based on the flexoelectric effect. *Materials Letters*, 39(5):287–291, 1999.

[26] Mashkevich V.S and Tolpygo K.B. Electrical, optical and elastic properties of diamond type crystals. *Soviet Physics JETP*, 5(3), 1957.

[27] Scott J.F. Lattice perturbations in cawo4 and camoo4. *The Journal of Chemical Physics*, 48(2):874–876, 09 1968.

[28] Bursian E.V and Zaikovsk O.I. Changes in curvature of a ferroelectric film due to polarization. *Soviet Physics Solid State, USSR*, 10(5):1121, 1968.

[29] Kogan S.M. Piezoelectric effect during inhomogeneous deformation and acoustic scattering of carriers in crystals. *Soviet Physics-Solid State*, 5:197 – 224, 1964.

[30] Harris P. Mechanism for the shock polarization of dielectrics. *Journal of Applied Physics*, 36(3):739–741, 1965.

[31] Mindlin R.D. Polarization gradient in elastic dielectrics. *International Journal of Solids and Structures*, 4(6):637–642, 1968.

[32] Askar A, Lee P.C.Y, and Cakmak A.S. Lattice-dynamics approach to the theory of elastic dielectrics with polarization gradient. *Physical Review B*, 1:3525–3537, Apr 1970.

[33] Osipov M.A Indenbom V.L, Loginov E.B. Flexoelectric effect and crystal-structure. *Kristallografiya*, 26:1157–62, 1981.

[34] Tagantsev A.K. Theory of flexoelectric effect in crystals. *Soviet Physics JETP*, 61(6):1246, 1985.

[35] Tagantsev A.K. Piezoelectricity and flexoelectricity in crystalline dielectrics. *Physical Review B*, 34(8):5883–5889, 1986.

[36] Tagantsev A.K. Pyroelectric, piezoelectric, flexoelectric, and thermal polarization effects in ionic crystals. *Soviet Physics Uspekhi*, 30(7):588, 1987.

[37] Bursian E.V and Trunov N.N. Nonlocal piezo-effect. *Fizika Tverdogo Tela*, 16(4):1187–1190, 1974.

[38] Ma W and Cross L.E. Flexoelectric polarization of barium strontium titanate in the paraelectric state. *Applied Physics Letters*, 81(18):3440–3442, 2002.

[39] Ma W and Cross L.E. Flexoelectricity of barium titanate. *Applied Physics Letters*, 88(23):232902, 2006.

[40] Resta R. Towards a bulk theory of flexoelectricity. *Physical Review Letters*, 105:127601, 2010.

[41] Hong J, Catalan G, Scott J.F, and Artacho E. The flexoelectricity of barium and strontium titanates from first principles. *Journal of Physics: Condensed Matter*, 22(11):112201, mar 2010.

[42] Stengel M. Flexoelectricity from density-functional perturbation theory. *Physical Review B*, 88:174106, 2013.

[43] Ma W and Cross L.E. Observation of the flexoelectric effect in relaxor pb(mg1/3nb2/3)o3 ceramics. *Applied Physics Letters*, 78(19):2920–2921, 05 2001.

[44] Fu J.Y, Zhu W, Li N, and Cross L.E. Experimental studies of the converse flexoelectric effect induced by inhomogeneous electric field in a barium strontium titanate composition. *Journal of Applied Physics*, 100(2):024112, 2006.

[45] Zhang S, Xu M, Ma G, Xu L, and Shen S. Experimental method research on transverse flexoelectric response of poly(vinylidene fluoride). *Japanese Journal of Applied Physics*, 55(7):071601, 2016.

[46] Shu L, Huang W, Ryung Kwon S, Wang Z, Li F, Wei X, Zhang S, Lanagan M, Yao X, and Jiang X. Converse flexoelectric coefficient f1212 in bulk ba0.67sr0.33tio3. *Applied Physics Letters*, 104(23):232902, 06 2014.

[47] Ma W and Cross L.E. Flexoelectric effect in ceramic lead zirconate titanate. *Applied Physics Letters*, 86(7):072905, 02 2005.

[48] Baskaran S, He X, Chen Q, and Fu J.Y. Experimental studies on the direct flexoelectric effect in -phase polyvinylidene fluoride films. *Applied Physics Letters*, 98(24):242901, 06 2011.

[49] Baskaran S, Ramachandran N, He X, Thiruvannamalai S, Lee H.J, Heo H, Chen Q, and Fu J.Y. Giant flexoelectricity in polyvinylidene fluoride films. *Physics Letters A*, 375(20):2082–2084, 2011.

[50] Chu B and Salem D.R. Flexoelectricity in several thermoplastic and thermosetting polymers. *Applied Physics Letters*, 101(10):103905, 09 2012.

[51] Zhang S, Liang X, Xu M, Feng B, and Shen S. Shear flexoelectric response along 3121 direction in polyvinylidene fluoride. *Applied Physics Letters*, 107(14):142902, 10 2015.

[52] Narvaez J, Saremi S, Hong J, Stengel M, and Catalan G. Large flexoelectric anisotropy in paraelectric barium titanate. *Physical Review Letters*, 115:037601, Jul 2015.

[53] Narvaez J and Catalan G. Origin of the enhanced flexoelectricity of relaxor ferroelectrics. *Applied Physics Letters*, 104(16):162903, 04 2014.

[54] Shu L, Wang T, Jiang X, and Huang W. Verification of the flexoelectricity in barium strontium titanate through d33 meter. *AIP Advances*, 6(12):125003, 12 2016.

[55] Biancoli A, Fancher C.M, Jones J.L, and Damjanovic D. Breaking of macroscopic centric symmetry in paraelectric phases of ferroelectric materials and implications for flexoelectricity. *Nature materials*, 14(2):224–229, 2015.

[56] Zhang X, Pan Q, Tian D, Zhou W, Chen P, Zhang H, and Chu B. Large flexoelectriclike response from the spontaneously polarized surfaces in ferroelectric ceramics. *Physical Review Letters*, 121:057602, 2018.

[57] Beainou R.El, Rauch J-Y, Dembélé S, Lehmann O, Hirsinger L, and Devel M. Qualitative evidence of the flexoelectric effect in a single multi-wall carbon nanotube by nanorobotic manipulation. *Applied Physics Letters*, 120(3):033101, 01 2022.

[58] Jiawang Hong and David Vanderbilt. First-principles theory and calculation of flexoelectricity. *Physical Review B*, 88:174107, 2013.

[59] Stengel M. Surface control of flexoelectricity. *Physical Review B*, 90:201112, Nov 2014.

[60] Abdollahi A, Millán D, Peco C, Arroyo M, and Arias I. Revisiting pyramid compression to quantify flexoelectricity: A three-dimensional simulation study. *Physical Review B*, 91:104103, Mar 2015.

[61] Yurkov A.S and Tagantsev A.K. Strong surface effect on direct bulk flexoelectric response in solids. *Applied Physics Letters*, 108(2):022904, 01 2016.

[62] Yang Y, Hirsinger L, and Devel M. Computation of flexoelectric coefficients of a mos2 monolayer with a model of self-consistently distributed effective charges and dipoles. *The Journal of Chemical Physics*, 156(17):174104, 05 2022.

[63] Abdollahi A, Vásquez-Sancho F, and Catalan G. Piezoelectric mimicry of flexoelectricity. *Physical Review Letters*, 121:205502, Nov 2018.

[64] Morozovska A.N and Eliseev E.A. Size effect of soft phonon dispersion in nanosized ferroics. *Physical Review B*, 99:115412, Mar 2019.

[65] Yudin P.V and Tagantsev A.K. Fundamentals of flexoelextricity in solids. *Nanotechnology*, 24:432001, 2013.

[66] Hong J and Vanderbilt D. First-principles theory of frozen-ion flexoelectricity. *Physical Review B*, 84:180101, Nov 2011.

[67] Martin R.M. Piezoelectricity. *Physical Review B*, 5:1607–1613, 1972.

[68] Born M and Huang K. *Dynamical theory of crystal lattices*. Oxford university press, 1996.

[69] Dumitric T, Landis C.M, and Yakobson B.I. Curvature-induced polarization in carbon nanoshells. *Chemical Physics Letters*, 360(1):182–188, 2002.

[70] Kalinin S.V and Meunier V. Electronic flexoelectricity in low-dimensional systems. *Physical Review B*, 77:033403, Jan 2008.

[71] Springolo M, Royo M, and Stengel M. Direct and converse flexoelectricity in two-dimensional materials. *Physical Review Letters*, 127:216801, Nov 2021.

[72] Royo M and Stengel M. Lattice-mediated bulk flexoelectricity from first principles. *Physical Review B*, 105:064101, 2022.

[73] Catalan G, Noheda B, McAneney J, Sinnamon L.J, and Gregg J.M. Strain gradients in epitaxial ferroelectrics. *Physical Review B*, 72:020102, Jul 2005.

[74] Eliseev E.A, Morozovska A.N, Glinchuk M.D, and Blinc R. Spontaneous flexoelectric/flexomagnetic effect in nanoferroics. *Physical Review B*, 79:165433, Apr 2009.

[75] Catalan G, Sinnamon L.J, and Gregg J.M. The effect of flexoelectricity on the dielectric properties of inhomogeneously strained ferroelectric thin films. *Journal of Physics: Condensed Matter*, 16(13):2253, mar 2004.

[76] Shen S and Hu S. A theory of flexoelectricity with surface effect for elastic dielectrics. *Journal of the Mechanics and Physics of Solids*, 58(5):665–677, 2010.

[77] Maranganti R, Sharma N.D, and Sharma P. Electromechanical coupling in nonpiezoelectric materials due to nanoscale nonlocal size effects: Greens function solutions and embedded inclusions. *Physical Review B*, 74(1):014110, 2006.

[78] Toupin R.A. The elastic dielectric. *Journal of Rational Mechanics and Analysis*, 5(6):849–915, 1956.

[79] Liu L. An energy formulation of continuum magneto-electro-elasticity with applications. *Journal of the Mechanics and Physics of Solids*, 63:451–480, 2014.

[80] Giannakopoulos A.E and Rosakis A.J. Dynamic magneto-flexoelectricity and seismo-electromagnetic phenomena: Connecting mechanical response to electromagnetic signatures. *Journal of the Mechanics and Physics of Solids*, 168:105058, 2022.

[81] Deng Q, Liu L, and Sharma P. Flexoelectricity in soft materials and biological membranes. *Journal of the Mechanics and Physics of Solids*, 62:209–227, 2014. Sixtieth anniversary issue in honor of Professor Rodney Hill.

[82] Deng Q and Shen S. The flexodynamic effect on nanoscale flexoelectric energy harvesting: a computational approach. *Smart Materials and Structures*, 27(10):105001, sep 2018.

[83] Baroudi S, Najar F, and Jemai A. Static and dynamic analytical coupled field analysis of piezoelectric flexoelectric nanobeams: a strain gradient theory approach. *International Journal of Solids and Structures*, 135:110–124, 2018.

[84] Yan Z. Modeling of a nanoscale flexoelectric energy harvester with surface effects. *Physica E: Low-dimensional Systems and Nanostructures*, 88:125–132, 2017.

[85] Yan Z and Jiang L. Size-dependent bending and vibration behaviour of piezoelectric nanobeams due to flexoelectricity. *Journal of Physics D: Applied Physics*, 46(35):355502, 2013.

[86] Zhang D.P, Lei Y.J, and Adhikari S. Flexoelectric effect on vibration responses of piezoelectric nanobeams embedded in viscoelastic medium based on nonlocal elasticity theory. *Acta Mechanica*, 229(6):2379–2392, 2018.

[87] Nguyen B.H, Nanthakumar S.S, Zhuang X, Wriggers P, Jiang X, and Rabczuk T. Dynamic flexoelectric effect on piezoelectric nanostructures. *European Journal of Mechanics - A/Solids*, 71:404–409, 2018.

[88] Wang K.F and Wang B.L. Non-linear flexoelectricity in energy harvesting. *International Journal of Engineering Science*, 116:88–103, 2017.

[89] Baroudi S and Najar F. Dynamic analysis of a nonlinear nanobeam with flexoelectric actuation. *Journal of Applied Physics*, 125(4):044503, 2019.

[90] Zarepour M, Hosseini S.A.H, and Akbarzadeh A.H. Geometrically nonlinear analysis of timoshenko piezoelectric nanobeams with flexoelectricity effect based on eringen's differential model. *Applied Mathematical Modelling*, 69:563–582, 2019.

[91] Ajri M, Rastgoo A, and Fakhrabadi M.M.S. How does flexoelectricity affect static bending and nonlinear dynamic response of nanoscale lipid bilayers? *Physica Scripta*, 95(2):025001, 2019.

[92] Chen L, Pan S, Fei Y, Zhang W, and Yang F. Theoretical study of micro/nano-scale bistable plate for flexoelectric energy harvesting. *Applied Physics A*, 125(4):1–11, 2019.

[93] Zhu W, Fu J.Y, Li N, and Cross L.E. Piezoelectric composite based on the enhanced flexoelectric effects. *Applied Physics Letters*, 89(19):192904, 2006.

[94] Wang K.F and Wang B.L. An analytical model for nanoscale unimorph piezoelectric energy harvesters with flexoelectric effect. *Composite Structures*, 153:253–261, 2016.

[95] Hu S.D andLi H andTzou H. Sensing signal and energy generation analysis on a flexoelectric beam. In *ASME International Mechanical Engineering Congress and Exposition*, volume 45226, pages 523–531. American Society of Mechanical Engineers, 2012.

[96] Zhang Z, Yan Z, and Jiang L. Flexoelectric effect on the electroelastic responses and vibrational behaviors of a piezoelectric nanoplate. *Journal of Applied Physics*, 116(1):014307, 2014.

[97] Shingare K.B and Kundalwal S.I. Static and dynamic response of graphene nanocomposite plates with flexoelectric effect. *Mechanics of Materials*, 134:69–84, 2019.

[98] Abdollahi A, Peco C, Millán D, Arroyo M, and Arias I. Computational evaluation of the flexoelectric effect in dielectric solids. *Journal of Applied Physics*, 116(9):093502, 09 2014.

[99] Abdollahi A, Peco C, Millán D, Arroyo M, Catalan G, and Arias I. Fracture toughening and toughness asymmetry induced by flexoelectricity. *Physical Review B*, 92:094101, 2015.

[100] Mao S, Purohit P.K, and Aravas N. Mixed finite-element formulations in piezoelectricity and flexoelectricity. *Proceedings of the Royal Society A: Mathematical, Physical and Engineering Sciences*, 472(2190):20150879, 2016.

[101] Deng F, Deng Q, and Shen S. A three-dimensional mixed finite element for flexoelectricity. *Journal of Applied Mechanics*, 85(3):031009, 01 2018.

[102] Nanthakumar S.S, Zhuang X, Park H.S, and Rabczuk T. Topology optimization of flexoelectric structures. *Journal of the Mechanics and Physics of Solids*, 105:217 – 234, 2017.

[103] Hughes T.J.R, Cottrell J.A, and Bazilevs Y. Isogeometric analysis: Cad, finite elements, nurbs, exact geometry and mesh refinement. *Computer Methods in Applied Mechanics and Engineering*, 194(39):4135–4195, 2005.

[104] Ghasemi H, Park H.S, and Rabczukk T. A level-set based iga formulation for topology optimization of flexoelectric materials. *Computer Methods in Applied Mechanics and Engineering*, 313:239 – 258, 2017.

[105] Thai T.Q, Rabczuk T, and Zhuang X. A large deformation isogeometric approach for flexoelectricity and soft materials. *Computer Methods in Applied Mechanics and Engineering*, 341:718–739, 2018.

[106] Nguyen B.H, Zhuang X, and Rabczuk T. Numerical model for the characterization of maxwell-wagner relaxation in piezoelectric and flexoelectric composite material. *Computers & Structures*, 208:75–91, 2018.

[107] Chen X, Yao S, and Yvonnet J. Dynamic analysis of flexoelectric systems in the frequency domain with isogeometric analysis. *Computational Mechanics*, 71(2):353–366, 2023.

[108] Yvonnet J and Liu L.P. A numerical framework for modeling flexoelectricity and maxwell stress in soft dielectrics at finite strains. *Computer Methods in Applied Mechanics and Engineering*, 313:450 – 482, 2017.

[109] Thai T.Q, Zhuang X, Park H.S, and Rabczuk T. A staggered explicit-implicit isogeometric formulation for large deformation flexoelectricity. *Engineering Analysis with Boundary Elements*, 122:1–12, 2021.

[110] Codony D, Gupta P, Marco O, and Arias I. Modeling flexoelectricity in soft dielectrics at finite deformation. *Journal of the Mechanics and Physics of Solids*, 146:104182, 2021.

[111] Deng F, Yu W, Liang X, and Shen S. A mixed finite element method for large deformation of flexoelectric materials. *Applied Mathematical Modelling*, 118:303–321, 2023.

[112] Michell A.G.M. Lviii. the limits of economy of material in frame-structures. *The London, Edinburgh, and Dublin Philosophical Magazine and Journal of Science*, 8(47):589–597, 1904.

[113] Rozvany G.I.N. Grillages of maximum strength and maximum stiffness. *International Journal of Mechanical Sciences*, 14(10):651–666, 1972.

[114] Prager W and Rozvany G.I.N. Optimal layout of grillages. *Journal of Structural Mechanics*, 5(1):1–18, 1977.

[115] Cheng K-T and Olhoff N. An investigation concerning optimal design of solid elastic plates. *International Journal of Solids and Structures*, 17(3):305–323, 1981.

[116] Cheng K-T and Olhoff N. Regularized formulation for optimal design of axisymmetric plates. *International Journal of Solids and Structures*, 18(2):153–169, 1982.

[117] Kohn R.V and Strang G. Optimal design and relaxation of variational problems, i. *Communications on Pure and Applied Mathematics*, 39(1):113–137, 1986.

[118] Bendsøe M.P and Kikuchi N. Generating optimal topologies in structural design using a homogenization method. *Computer Methods in Applied Mechanics and Engineering*, 71(2):197 – 224, 1988.

[119] Xie Y.M and Steven G.P. A simple evolutionary procedure for structural optimization. *Computers and Structures*, 49(5):885 – 896, 1993.

[120] Wang M.Y, Wang X, and Guo D. A level set method for structural topology optimization. *Computer Methods in Applied Mechanics and Engineering*, 192(1):227 – 246, 2003.

[121] Allaire G, Jouve F, and Toader A-M. Structural optimization using sensitivity analysis and a level-set method. *Journal of computational physics*, 194(1):363–393, 2004.

[122] Bourdin B and Chambolle A. Design-dependent loads in topology optimization. *ESAIM: Control, Optimisation and Calculus of Variations*, 9:19–48, 2003.

[123] Guo X, Zhang W, and Zhong W. Doing topology optimization explicitly and geometricallya new moving morphable components based framework. *Journal of Applied Mechanics*, 81(8):081009, 05 2014.

[124] Zhang W, Chen J, Zhu X, Zhou J, Xue D, Lei X, and Guo X. Explicit three dimensional topology optimization via moving morphable void (mmv) approach. *Computer Methods in Applied Mechanics and Engineering*, 322:590–614, 2017.

[125] Rozvany G.I.N. A critical review of established methods of structural topology optimization. *Structural and multidisciplinary optimization*, 37:217–237, 2009.

[126] Huang X and Xie Y.M. A further review of eso type methods for topology optimization. *Structural and Multidisciplinary Optimization*, 41:671–683, 2010.

[127] Xia L, Xia Q, Huang X, and Xie Y.M. Bi-directional evolutionary structural optimization on advanced structures and materials: a comprehensive review. *Archives of Computational Methods in Engineering*, 25:437–478, 2018.

[128] Van Dijk N.P, Maute K, Langelaar M, and Van Keulen F. Level-set methods for structural topology optimization: a review. *Structural and Multidisciplinary Optimization*, 48:437–472, 2013.

[129] Sigmund O and Kurt M. Topology optimization approaches. *Structural and Multidisciplinary Optimization*, 48(6):1031–1055, Dec 2013.

[130] Deaton J.D and Grandhi R.V. A survey of structural and multidisciplinary continuum topology optimization: post 2000. *Structural and Multidisciplinary Optimization*, 49:1–38, 2014.

[131] Wang C, Zhao Z, Zhou M, Sigmund O, and Zhang X.S. A comprehensive review of educational articles on structural and multidisciplinary optimization. *Structural and Multidisciplinary Optimization*, pages 1–54, 2021.

[132] Osanov M and Guest J.K. Topology optimization for architected materials design. *Annual Review of Materials Research*, 46(1):211–233, 2016.

[133] Xia L and Breitkopf P. Recent advances on topology optimization of multiscale nonlinear structures. *Archives of Computational Methods in Engineering*, 24:227–249, 2017.

[134] Wu J, Sigmund O, and Groen J.P. Topology optimization of multi-scale structures: a review. *Structural and Multidisciplinary Optimization*, 63:1455–1480, 2021.

[135] Zhu J, Zhou h, Wang C, Zhou L, Yuan S, and Zhang W. A review of topology optimization for additive manufacturing: Status and challenges. *Chinese Journal of Aeronautics*, 34(1):91–110, 2021.

[136] M.P Bendsøe. Optimal shape design as a material distribution problem. *Structural optimization*, 1:193–202, 1989.

[137] Zhou M and Rozvany G.I.N. The coc algorithm, part ii: Topological, geometrical and generalized shape optimization. *Computer Methods in Applied Mechanics and Engineering*, 89(1):309 – 336, 1991. Second World Congress on Computational Mechanics.

[138] Sigmund O. Design of multiphysics actuators using topology optimization part ii: Two-material structures. *Computer Methods in Applied Mechanics and Engineering*, 190(49):6605–6627, 2001.

[139] Sigmund O and Petersson J. Numerical instabilities in topology optimization: a survey on procedures dealing with checkerboards, mesh-dependencies and local minima. *Structural optimization*, 16:68–75, 1998.

[140] Lazarov B.S and Sigmund O. Filters in topology optimization based on helmholtz-type differential equations. *International Journal for Numerical Methods in Engineering*, 86(6):765–781, 2011.

[141] Wang F, Lazarov B.S, and Sigmund O. On projection methods, convergence and robust formulations in topology optimization. *Structural and multidisciplinary optimization*, 43:767–784, 2011.

[142] Sigmund O. A 99 line topology optimization code written in matlab. *Structural and multidisciplinary optimization*, 21:120–127, 2001.

[143] Bendsoe M.P and Sigmund O. *Topology optimization: theory, methods, and applications*. Springer Science & Business Media, 2013.

[144] Svanberg K. A class of globally convergent optimization methods based on conservative convex separable approximations. *SIAM Journal on Optimization*, 12(2):555–573, 2002.

[145] Osher S and Sethian J.A. Fronts propagating with curvature-dependent speed: Algorithms based on hamilton-jacobi formulations. *Journal of Computational Physics*, 79(1):12–49, 1988.

[146] Allaire G, Jouve F, and Toader A.M. Structural optimization using sensitivity analysis and a level-set method. *Journal of Computational Physics*, 194(1):363–393, 2004.

[147] Wang X, Wang M.Y, and Guo D. Structural shape and topology optimization in a level-set-based framework of region representation. *Structural and Multidisciplinary Optimization*, 27:1–19, 2004.

[148] Burger M, Hackl B, and Ring W. Incorporating topological derivatives into level set methods. *Journal of Computational Physics*, 194(1):344–362, 2004.

[149] Luo J, Luo Z, Chen L, Tong L, and Wang M.Y. A semi-implicit level set method for structural shape and topology optimization. *Journal of Computational Physics*, 227(11):5561–5581, 2008.

[150] Wang S and Wang M.Y. Radial basis functions and level set method for structural topology optimization. *International Journal for Numerical Methods in Engineering*, 65(12):2060–2090, 2006.

[151] Amstutz S and Andrä H. A new algorithm for topology optimization using a level-set method. *Journal of Computational Physics*, 216(2):573–588, 2006.

[152] Haber E. A multilevel, level-set method for optimizing eigenvalues in shape design problems. *Journal of Computational Physics*, 198(2):518–534, 2004.

[153] Yamada T, Izui K, Nishiwaki S, and Takezawa A. A topology optimization method based on the level set method incorporating a fictitious interface energy. *Computer Methods in Applied Mechanics and Engineering*, 199(45):2876–2891, 2010.

[154] Young V, Querin O.M, Steven G.P, and Xie Y.M. 3d and multiple load case bi-directional evolutionary structural optimization (beso). *Structural optimization*, 18:183–192, 1999.

[155] Burger M and Stainko R. Phasefield relaxation of topology optimization with local stress constraints. *SIAM Journal on Control and Optimization*, 45(4):1447–1466, 2006.

[156] Wang M.Y and Zhou S. Phase field: a variational method for structural topology optimization. *Comput Model Eng Sci*, 6(6):547–566, 2004.

[157] Kreissl S and Maute K. Level set based fluid topology optimization using the extended finite element method. *Structural and Multidisciplinary Optimization*, 46:311–326, 2012.

[158] Van Miegroet L and Duysinx P. Stress concentration minimization of 2d filets using x-fem and level set description. *Structural and Multidisciplinary Optimization*, 33:425–438, 2007.

[159] Yamasaki S, Nomura T, Kawamoto A, Sato K, and Nishiwaki S. A level set-based topology optimization method targeting metallic waveguide design problems. *International Journal for Numerical Methods in Engineering*, 87(9):844–868, 2011.

[160] Shojaee S, Mohamadian M, and Valizadeh N. Composition of isogeometric analysis with level set method for structural topology optimization. *Int J Optim Civil Eng*, 2(1):47–70, 2012.

[161] Wang Y and Benson D.J. Isogeometric analysis for parameterized lsm-based structural topology optimization. *Computational Mechanics*, 57:19–35, 2016.

[162] Sigmund O. On the usefulness of non-gradient approaches in topology optimization. *Structural and Multidisciplinary Optimization*, 43:589–596, 2011.

[163] Zhang Z, Li Y, Zhou W, Chen X, Yao W, and Zhao Y. Tonr: An exploration for a novel way combining neural network with topology optimization. *Computer Methods in Applied Mechanics and Engineering*, 386:114083, 2021.

[164] Ghasemi H, Park H.S, and Rabczuk T. A multi-material level set-based topology optimization of flexoelectric composites. *Computer Methods in Applied Mechanics and Engineering*, 332:47 – 62, 2018.

[165] López J, Valizadeh N, and Rabczuk T. An isogeometric phasefield based shape and topology optimization for flexoelectric structures. *Computer Methods in Applied Mechanics and Engineering*, 391:114564, 2022.

[166] Zhang W, Yan X, Meng Y, Zhang C, Youn S-K, and Guo X. Flexoelectric nanostructure design using explicit topology optimization. *Computer Methods in Applied Mechanics and Engineering*, 394:114943, 2022.

[167] Chen X, Yvonnet J, Yao S, and Park H.S. Topology optimization of flexoelectric composites using computational homogenization. *Computer Methods in Applied Mechanics and Engineering*, 381:113819, 2021.

[168] Chen X, Yvonnet J, Park H.S, and Yao S. Enhanced converse flexoelectricity in piezoelectric composites by coupling topology optimization with homogenization. *Journal of Applied Physics*, 129(24):245104, 2021.

[169] Greco F, Codony D, Mohammadi H, Fernández-Méndez S, and Arias I. Topology optimization of flexoelectric metamaterials with apparent piezoelectricity. *Journal of the Mechanics and Physics of Solids*, 183:105477, 2024.

[170] Zhuang X, Thai T.Q, and Rabczuk T. Topology optimization of nonlinear flexoelectric structures. *Journal of the Mechanics and Physics of Solids*, 171:105117, 2023.

[171] Ortigosa R, Martínez-Frutos J, and Gil A.J. A computational framework for topology optimisation of flexoelectricity at finite strains considering a multi-field micromorphic approach. *Computer Methods in Applied Mechanics and Engineering*, 401:115604, 2022.

[172] Chen P, Zhang H, and Chu B. Strain gradient induced thermal-electrical response in paraelectric $Na_{0.5}Bi_{0.5}Tio_3$-based ceramics. *Physical Review Materials*, 2:034401, Mar 2018.

[173] Yang M.M, Kim D.J, and Alexe M. Flexo-photovoltaic effect. *Science*, 360(6391):904–907, 2018.

[174] Mardana A, Bai M, Baruth A, Ducharme S, and Adenwalla S. Magnetoelectric effects in ferromagnetic cobalt/ferroelectric copolymer multilayer films. *Applied Physics Letters*, 97(11):112904, 09 2010.

[175] Kwon S.R, Huang W.B, Zhang S.J, Yuan F.G, and Jiang X.N. Flexoelectric sensing using a multilayered barium strontium titanate structure. *Smart Materials and Structures*, 22(11):115017, oct 2013.

[176] Hu S, Li H, and Tzou H. Flexoelectric Responses of Circular Rings. *Journal of Vibration and Acoustics*, 135(2):021003, 02 2013.

[177] Wang K.F and Wang B.L. Energy gathering performance of micro/nanoscale circular energy harvesters based on flexoelectric effect. *Energy*, 149:597–606, 2018.

[178] Huang W, Kwon S.R, Zhang S, Yuan F.G, and Jiang X. A trapezoidal flexoelectric accelerometer. *Journal of Intelligent Material Systems and Structures*, 25(3):271–277, 2014.

[179] Yvonnet J, Chen X, and Sharma P. Apparent flexoelectricity due to heterogeneous piezoelectricity. *Journal of Applied Mechanics*, 87(11):111003, 2020.

[180] Mawassy N, Reda H, Ganghoffer J-F, Eremeyev VA, and Lakiss H. A variational approach of homogenization of piezoelectric composites towards piezoelectric and flexoelectric effective media. *International Journal of Engineering Science*, 158:103410, 2021.

[181] Mawassy N, Reda H, Ganghoffer J-F, and Lakiss H. Control of the piezoelectric and flexoelectric homogenized properties of architected materials by tuning their inner topology. *Mechanics Research Communications*, 127:104034, 2023.

[182] Nasimsobhan M, Ganghoffer J-F, and Shamshirsaz M. Construction of piezoelectric and flexoelectric models of composites by asymptotic homogenization and application to laminates. *Mathematics and Mechanics of Solids*, 27(4):602–637, 2022.

[183] Qi Y, Jafferis N.T, Lyons J.K, Lee C.M, Ahmad H, and McAlpine M.C. Piezoelectric ribbons printed onto rubber for flexible energy conversion. *Nano letters*, 10(2):524–528, 2010.

[184] Qi Y, Kim J, Nguyen T.D, Lisko B, Purohit P.K, and McAlpine M.C. Enhanced piezoelectricity and stretchability in energy harvesting devices fabricated from buckled pzt ribbons. *Nano letters*, 11(3):1331–1336, 2011.

[185] Feng X, Yang B.D, Liu Y, Wang Y, Dagdeviren C, Liu Z, Carlson A, Li J, Huang Y, and Rogers J.A. Stretchable ferroelectric nanoribbons with wavy configurations on elastomeric substrates. *Acs Nano*, 5(4):3326–3332, 2011.

[186] Gitman I.M, Askes H, and Sluys L.J. Representative volume: Existence and size determination. *Engineering Fracture Mechanics*, 74(16):2518–2534, 2007.

[187] Zohdi T.I and Wriggers P. *An introduction to computational micromechanics*, volume 20. Springer Science & Business Media, 2004.

[188] Kanit T, Forest S, Galliet I, Mounoury V, and Jeulin D. Determination of the size of the representative volume element for random composites: statistical and numerical approach. *International Journal of Solids and Structures*, 40(13):3647–3679, 2003.

[189] Yvonnet J. *Computational homogenization of heterogeneous materials with finite elements*, volume 258. Springer, 2019.

[190] Michel J.C, Moulinec H, and Suquet P. Effective properties of composite materials with periodic microstructure: a computational approach. *Computer Methods in Applied Mechanics and Engineering*, 172(1):109–143, 1999.

[191] Forest S, Pradel F, and Sab K. Asymptotic analysis of heterogeneous cosserat media. *International Journal of Solids and Structures*, 38(26):4585 – 4608, 2001.

[192] Forest S. and Trinh D.K. Generalized continua and non-homogeneous boundary conditions in homogenisation methods. *ZAMM - Journal of Applied Mathematics and Mechanics / Zeitschrift für Angewandte Mathematik und Mechanik*, 91(2):90–109, 2011.

[193] Li J and Zhang X.B. A numerical approach for the establishment of strain gradient constitutive relations in periodic heterogeneous materials. *European Journal of Mechanics - A/Solids*, 41:70–85, 2013.

[194] Monchiet V, Auffray N, and Yvonnet J. Strain-gradient homogenization: A bridge between the asymptotic expansion and quadratic boundary condition methods. *Mechanics of Materials*, 143:103309, 2020.

[195] Yvonnet J, Auffray N, and Monchiet V. Computational second-order homogenization of materials with effective anisotropic strain gradient behavior. *International Journal of Solids and Structures*, 191-192:434–448, 2020.

[196] Kapl M, Vitrih V, Jüttler B, and Birner K. Isogeometric analysis with geometrically continuous functions on two-patch geometries. *Computers & Mathematics with Applications*, 70(7):1518–1538, 2015. High-Order Finite Element and Isogeometric Methods.

[197] Chan C.L, Anitescu C, and Rabczuk T. Isogeometric analysis with strong multipatch c1-coupling. *Computer Aided Geometric Design*, 62:294–310, 2018.

[198] Chan C.L, Anitescu C, and Rabczuk T. Strong multipatch c1-coupling for isogeometric analysis on 2d and 3d domains. *Computer Methods in Applied Mechanics and Engineering*, 357:112599, 2019.

[199] Sladek J, Sladek V, Repka M.V, and Deng Q. Flexoelectric effect in dielectrics under a dynamic load. *Composite Structures*, 260:113528, 2021.

[200] Askes H and Aifantis E.C. Gradient elasticity in statics and dynamics: An overview of formulations, length scale identification procedures, finite element implementations and new results. *International Journal of Solids and Structures*, 48(13):1962–1990, 2011.

[201] Maranganti R and Sharma P. A novel atomistic approach to determine strain-gradient elasticity constants: Tabulation and comparison for various metals, semiconductors, silica, polymers and the (ir) relevance for nanotechnologies. *Journal of the Mechanics and Physics of Solids*, 55(9):1823–1852, 2007.

[202] Cottrell J.A, Hughes T.J.R, and Bazilevs Y. *Isogeometric analysis: toward integration of CAD and FEA*. John Wiley & Sons, 2009.

[203] Nguyen V.P and Bordas S. *Extended Isogeometric Analysis for Strong and Weak Discontinuities*, pages 21–120. Springer Vienna, Vienna, 2015.

[204] Carl D.B. *A practical guide to splines*, volume 27. springer-verlag New York, 1978.

[205] Kapl M and Vitrih V. Space of c2-smooth geometrically continuous isogeometric functions on two-patch geometries. *Computers & Mathematics with Applications*, 73(1):37–59, 2017.

[206] Majdoub M.S, Sharma P, and T Çağin. Erratum: Enhanced size-dependent piezoelectricity and elasticity in nanostructures due to the flexoelectric effect. *Physical Review B*, 79:119904, Mar 2009.

[207] Fan M and Tzou H. Vibration control with the converse flexoelectric effect on the laminated beams. *Journal of Intelligent Material Systems and Structures*, 30(17):2556–2566, 2019.

[208] Gitman I.M, Askes H, Kuhl E, and Aifantis E.C. Stress concentrations in fractured compact bone simulated with a special class of anisotropic gradient elasticity. *International Journal of Solids and Structures*, 47(9):1099–1107, 2010.

[209] Wang L and Hu H. Flexural wave propagation in single-walled carbon nanotubes. *Physical Review B*, 71:195412, May 2005.

[210] Felippa C.A. Introduction to finite element methods. *University of Colorado*, 885, 2004.

[211] Kim J.E, Kim D.S, Ma P.S, and Kim Y.Y. Multi-physics interpolation for the topology optimization of piezoelectric systems. *Computer Methods in Applied Mechanics and Engineering*, 199(49):3153 – 3168, 2010.

[212] Arrison J.S and Ounaies Z. Piezoelectric polymers encyclopedia of polymer science and technology, 2002.

[213] Komkov V, Choi K.K, and Haug E.J. *Design Sensitivity Analysis of Structural Systems*. Mathematics in science and engineering. Elsevier Science, 1986.

[214] Brenner R. Numerical computation of the response of piezoelectric composites using fourier transform. *Physical Review B*, 79(18):184106, 2009.

[215] Zubko P, Catalan G, and Tagantsev A.K. Flexoelectric effect in solids. *Annual Review of Materials Research*, 43(1):387–421, 2013.

[216] Ramadan K.S, Sameoto D, and Evoy S. A review of piezoelectric polymers as functional materials for electromechanical transducers. *Smart Materials and Structures*, 23(3):033001, 2014.

[217] Chen X, Yao S, and Yvonnet J. Multiscale topology optimization of an electromechanical dynamic energy harvester made of non-piezoelectric material. *Structural and Multidisciplinary Optimization*, 67(5):66, 2024.

[218] Cholleti E.R. A review on 3d printing of piezoelectric materials. In *IOP conference series: materials science and engineering*, volume 455, page 012046. IOP Publishing, 2018.

[219] Pelrine R, Kornbluh R, Pei Q, and Joseph J. High-speed electrically actuated elastomers with strain greater than 100%. *Science*, 287(5454):836–839, 2000.

[220] Zhao X and Suo Z. Theory of dielectric elastomers capable of giant deformation of actuation. *Physical Review Letters*, 104:178302, 2010.

[221] Gupta U, Qin L, Wang Y, Godaba H, and Zhu J. Soft robots based on dielectric elastomer actuators: a review. *Smart Materials and Structures*, 28(10):103002, 2019.

[222] Wang F, Lazarov B.S, Sigmund O, and Jensen J.S. Interpolation scheme for fictitious domain techniques and topology optimization of finite strain elastic problems. *Computer Methods in Applied Mechanics and Engineering*, 276:453–472, 2014.

[223] Chen X, Yao S, and Yvonnet J. Nonlinear topology optimization of flexoelectric soft dielectrics at large deformation. *Computer Methods in Applied Mechanics and Engineering*, 427:117005, 2024.

[224] Jarić J.P, Kuzmanović D, and Golubović Z. On tensors of elasticity. *Theoretical and Applied Mechanics*, 35(1-3):119–136, 2008.

[225] Wang F, Lazarov B.S, and Sigmund O. On projection methods, convergence and robust formulations in topology optimization. *Structural and multidisciplinary optimization*, 43:767–784, 2011.

[226] Gao J, Gao L, Luo Z, and Li P. Isogeometric topology optimization for continuum structures using density distribution function. *International Journal for Numerical Methods in Engineering*, 119(10):991–1017, 2019.